UNIVERSITÉ DE GRENOBLE

THÈSE

Pour obtenir le grade de
DOCTEUR DE L'UNIVERSITÉ DE GRENOBLE
Spécialite: **Matériaux, Mécanique, Génie Civil, Electrochimie**
Arrêté ministériel: 7 août 2006
et
DOCTEUR DE L'UNIVERSITÉ DE LIÈGE
Spécialite: **Architecture, Génie Civil et Géologie**

Présentée par

Bram van den Eijnden

Thèse dirigée en cotutelle par **Pierre BÉSUELLE** et **Frédéric COLLIN**
et codirigée par **René CHAMBON**

préparée au sein du **Laboratoire 3SR - Grenoble, France**
dans **l'École Doctorale Ingénierie - Matériaux Mécanique Environnement Energétique Procédés Production (I-MEP^2)**
et au sein de l´**Institut de Mécanique et Génie civil - Liège, Belgique**
dans **l'École Doctorale Architecture - Géologie - Construction**

Multi-scale modelling of the hydromechanical behaviour of argillaceous rocks

Thèse à soutenir publiquement le **13.07.2015**,
devant le jury composé de:

Prof. Claudio TAMAGNINI
Professeur, Università degli studi di Perugia, Rapporteur
Prof. Thierry MASSART
Professeur, Université Libre de Bruxelles, Rapporteur
Prof. Robert CHARLIER
Professeur, Université de Liège, Invité
Prof. Djimédo KONDO
Professeur, Université UPMC, Examinateur
Dr. Darius SEYEDI
HDR, Andra, Examinateur
Dr. Pierre BÉSUELLE
CR HDR, CNRS UMR 5521, Directeur de Thèse
Prof. Frédéric COLLIN
Professeur, Université de Liège, Directeur de Thèse
Prof. René CHAMBON
Professeur Émérite, Université Joseph Fourier Grenoble, Co-encadrant

Version : August 2015

ABSTRACT

Feasibility studies for deep geological radioactive waste disposal facilities have led to an increased interest in the geomechanical modelling of its host rock. In France, a potential host rock is the Callovo-Oxfordian claystone. The low permeability of this material is of key importance, as the principle of deep geological disposal strongly relies on the sealing capacity of the host formation. The permeability being coupled to the mechanical material state, hydromechanical coupled behaviour of the claystone becomes important when mechanical alterations are induced by gallery excavation in the so-called excavation damaged zone (EDZ).

In materials with microstructure such as the Callovo-Oxfordian claystone [Robinet et al., 2012], the macroscopic behaviour has its origin in the interaction of its micromechanical constituents. In addition to the coupling between hydraulic and mechanical behaviour, a coupling between the micro (material microstructure) and macro scale will be made. By means of the development of a framework of computational homogenization for hydromechanical coupling, a doublescale modelling approach is formulated, for which the macroscale constitutive relations are derived from the microscale by homogenization.

An existing model for the modelling of hydromechanical coupling based on the distinct definition of grains and intergranular pore space [Frey, 2010] is adopted and modified to enable the application of first order computational homogenization for obtaining macroscale stress and fluid transport responses. This model is used to constitute a periodic representative elementary volume (REV) that allows the representation of the local macroscopic behaviour of the claystone. As a response to deformation loading, the behaviour of the REV represents the numerical equivalent of a constitutive relation at the macroscale.

For the required consistent tangent operators, the framework of computational homogenization by static condensation [Kouznetsova et al., 2001] is extended to hydromechanical coupling. The theoretical developments of this extension are implemented in the finite element code Lagamine (Liège) as an independent constitutive relation. For the modelling of localization of deformation, which in classical FE methods suffers from the well-known mesh dependency, the doublescale approach of hydromechanical coupling is combined with a local second gradient model [Collin et al., 2006] to control the internal length scale of localized deformation. By accepting the periodic boundary conditions as a regularization of the microscale deformation, the use of the multiscale model in combination with the local second gradient model can be used for modelling localization phenomena in HM-coupled settings with material softening.

The modelling capacities of the approach are demonstrated by means of simulations of oedometer tests and biaxial compression tests. The approach is demonstrated to be a powerful way to model anisotropy in the mechanical as well as the hydraulic behaviour of the material both in the initial material state and as

an effect of hydromechanical alterations. For the application to the modelling of Callovo-Oxfordian claystone, microstructural REVs are calibrated to geometrical characteristics of the inclusion that form the microstructure under consideration and to macroscale experimental results of the mechanical behaviour. The calibrated constitutive relation is used in the simulation of gallery excavation processes. These computations give a proof of concept of the doublescale assessment of the hydromechanical behaviour of the excavation damaged zones around galleries in the context of nuclear waste disposal.

Keywords : Multiscale modelling, hydromechanical coupling, computational homogenization, coupled local second gradient model, excavation damaged zone, anisotropy, strain localization.

RÉSUMÉ

Les études de faisabilité concernant le stockage géologique profond des déchets radioactifs ont conduit un intérêt accru concernant la modélisation géomécanique de la roche hte. En France, une roche hte potentielle est l'argilite du Callovo-Oxfordien du site de Meuse/Haute Marne. Etant donné que le principe de stockage géologique profond repose fortement sur la capacité de confinement de la formation hte, sa faible perméabilité est d'une importance clé. La perméabilité étant dépendante de la microstructure du matériau et de son évolution sous chargement, le comportement couplé hydro-mécanique de l'argilite est important. En effet, des modifications mécaniques sont induites par le creusement de la galerie d'entreposage, générant une zone endommagée (EDZ), pouvant conduire une modification de la perméabilité dans le voisinage de la galerie.

Dans les matériaux microstructure complexe comme l'argilite du Callovo-Oxfordien [Robinet, 2008], le comportement macroscopique trouve son origine dans l'interaction des constituants micro-mécaniques. En plus du couplage entre le comportement hydraulique et mécanique, un couplage entre les échelles micro (au niveau de la microstructure) et macro existe. Par le biais de l'élaboration d'un cadre d'homogénéisation du couplage hydro-mécanique, une approche de modélisation deux échelles est développée dans ce travail, dans laquelle la relation constitutive macroscopique découle directement du comportement à l'échelle microscopique.

Un modèle existant du couplage hydro-mécanique, reposant sur l'identification de grains et d'espaces poreux intergranulaires à l'échelle micro [Frey, 2010] est adopté comme point de départ. Ce modèle repose sur une homogénéisation numérique du comportement à la petite échelle afin d'obtenir à l'échelle macroscopique la réponse en contrainte et de transport du fluide interstitiel. Ce modèle est basé sur un volume élémentaire représentatif (VER) périodique qui permet de déduire le comportement macroscopique local de l'argilite. En réponse, en un point d'intégration macro donné, à un incrément de la déformation et du gradient de pression, la réponse du VER permet d'exprimer l'incrément de contrainte et de flux associé, constituant de fait un équivalent numérique de la relation constitutive.

Les problèmes aux conditions limites macro et micro sont traités simultanément par la méthode élément fini. Pour obtenir les opérateurs tangents consistants à l'échelle macro, la méthode d'homogénéisation par condensation statique [Kouznetsova et al., 2001] des opérateurs tangeants micro est étendu au cas avec couplage hydro-mécanique. L'implémentation du modèle double échelle et la mise en uvre des développements théoriques d'homogénéisation ont été effectués dans le code élément fini Lagamine (Université de Liège). Pour la modélisation de la localisation de la déformation à l'échelle macro, qui, dans un formalisme de milieu continu classique, souffre de la dépendance au maillage, l'approche double-échelle a été utilisée dans un formalisme de milieu enrichi de type milieu de second gradi-

ent pour matériau poreux saturé [Collin et al., 2006]. Ceci permet d'introduire une échelle de longueur interne, régularisant ainsi le problème de localisation de la déformation (objectivité vis-à-vis du maillage).

Les capacités du modèle homogénéisé numériquement, utilisé dans un cadre de milieu de second gradient, sont ensuite démontrées par des simulations d'essais dométriques et d'essais de compression biaxiaux. L'approche se confirme être un moyen puissant pour modéliser l'anisotropie initiale et induite du comportement mécanique et du comportement hydraulique. Pour la modélisation du comportement de l'argilite du Callovo-Oxfordien, des VER sont construits en tenant compte des travaux de caractérisation de la géométrie des inclusions microscopiques et des résultats expérimentaux d'essais macroscopiques sur le comportement hydro-mécanique. La loi de comportement homogénéisée numériquement ainsi calibrée est utilisée dans des simulations de creusement de galerie jusqu'à des niveaux d'endommagement générant une localisation de la déformation. Ces calculs montrent à la fois la pertinence et l'applicabilité du concept double échelle pour l'évaluation du comportement hydro-mécanique des zones endommagées autour des galeries dans un contexte du stockage des déchets radioactifs.

CONTENTS

LIST OF FIGURES

LIST OF TABLES

NOMENCLATURE

x_i	component of position vector $\vec{x}$
∇^M	macroscale gradient operator
$[.]^+$	upper side of interface (opposite to $[.]^-$)
$[.]^-$	lower side of interface (opposite to $[.]^+$)
$[.]^0$	variable at reference configuration (no displacement)
$[.]^\star$	virtual quantity
$[.]^F$	follow DOF; dependent on one lead DOF
$[.]^L$	lead DOF
$[.]^M$	variable related to the macroscale reference frame
$[.]^t$	variable at updated configuration at time t
$[.]^{ext}$	related to external boundaries (the REV boundaries)
$[.]^{int}$	related to interfaces
$[.]^{ps}$	plane-strain equivalent of 3D material parameters
$[.]^{REV}$	variable related to the REV reference frame under symmetric deformation (polar decomposition)
$[.]_h$	hydraulic equivalent to normal component $[.]_n$ $[m]$
$[.]_n$	normal component
$[.]_t$	tangential component
$[.]_{(n)}$	indication of the length of a column vector
$[.]_{(n\times n)}$	indication of the size of a matrix
$\bar{p}$	REV average pressure
$\bar{q}$	boundary fluid flux $\bar{q} = m_i n_i$
$\bar{t}_i$	component of domain boundary traction $\vec{t} = \boldsymbol{\sigma}\vec{n}$
β	grain orientation
$\boldsymbol{\sigma}$	Cauchy stress tensor

$\boldsymbol{F}$	deformation gradient tensor
$\boldsymbol{P}$	First Piola-Kirchhoff stress tensor
${}^{\mathbf{4}}\boldsymbol{A} \cdot \vec{b}$	inner product of fourth order tensor and vector $A_{ijkl}b_l$
${}^{\mathbf{4}}\boldsymbol{C}$	consistent tangent stiffness matrix with respect to the current
$\boldsymbol{A} : \boldsymbol{B}$	inner product of two tensors $A_{ij}B_{ij}$
$\boldsymbol{A} \cdot \boldsymbol{B}$	dot product between two tensors $A_{ik}B_{kj}$
$\boldsymbol{A} \cdot \vec{b}$	dot product between tensor and vector $A_{ij}b_j$
Δ	interface relative displacement
$\delta[.]$	variation of variable
$\dot{M}$	fluid storage (time derivative of fluid mass)
ϵ	small value
ϵ_{ij}	components of the small strain tensor, defined as $\epsilon_{ij} = \frac{\partial x_i^{m,t}}{2\partial x_j^{m,0}} + \frac{\partial x_j^{m,t}}{2\partial x_i^{m,0}}$
Γ	domain boundary (1D surface)
$\hat{p}$	micromechanical pressure variation (relative to $\bar{p}$)
κ	hydromechanical coupling term of the interfaces
λ	Lamé parameter (shear modulus)
λ^p	exponential pressure term $\exp(p/k^w)$
λ_{ij}	Lagrange multipliers for weak constraint of the local second gradient formalism
μ	Lamé parameter
μ	dynamic viscosity
∇	gradient operator $\frac{\partial}{\partial x_i}$
ν	Poisson's ratio
Ω	Domain (2D volume)
ϕ	(effective) friction angle
ϕ	total interface hydraulic transmissivity term
ρ	material density
ρ^w	fluid density
σ_p	peak stress (to biaxial loading)
θ	angle of rotation

ε	alternative small strain tensor, defined as $\boldsymbol{U} - \boldsymbol{I}$
ϖ	interface total mass flux
$\vec{a} \cdot \vec{b}$	scalar product $a_i b_i$
$\vec{a} \otimes \vec{b}$	tensor product $a_i b_j$
$\vec{t}$	stress vector or boundary traction
$\vec{y}$	periodicity vector $\vec{x}^F - \vec{x}^L$
A	grain orientation anisotropy
c	(effective) cohesion
D	interface cohesion state parameter
E	Young's modulus
e	elongation index
f_i	external body force
F_{ij}	components of deformation gradient tensor $\boldsymbol{F} = \frac{\partial \vec{x}^t}{\partial \vec{x}^0}$
k^w	fluid bulk modulus $[Pa]$
k_{ij}	components of permeability tensor $\boldsymbol{k}$
M	fluid mass per unit volume
m_i	components of local fluid mass flux $\vec{m}$
R_{ij}	components of the rotation tensor $\boldsymbol{R} = \boldsymbol{F} \cdot \boldsymbol{U}^{-1}$
s	1D coordinate in interface
T_i	components of the interface cohesive force $\vec{T}$
U_{ij}	components of the symmetric stretch tensor $\boldsymbol{U} = \boldsymbol{R}^T \cdot \boldsymbol{F}$
V	Volume
V	volume (2D×depth in the plane strain sense)
v_i	components of the (fluid) velocity $\vec{v}$
W	work $\boldsymbol{\sigma} : \varepsilon$
${}^2W$	second order work $\dot{\boldsymbol{\sigma}} : \dot{\boldsymbol{\varepsilon}}$

ACKNOWLEDGEMENTS

Like any thesis, this work relies on the contributions of many, contributing in different ways and resulting in the final version of this manuscript. I therefore would like to acknowledge my sincere gratitude to the following people:

My supervisors; Pierre for the care of my good arrival in Grenoble, the years of guidance and our many tough wednesday-after-lunch meetings and discussions; René for his motivating enthusiasm for numerical difficulties; Frédéric for his supportive cheerfulness and guidance through Lagamine.

Andra, for the financial support that has made this work possible; Darius Seyedi for following the work and taking seat in the jury. The members of the jury; as president of the jury Djimédo Kondo for presiding the defence; as the rapporteurs Claudio Tamagnini for his detailed comments on the manuscript and Thierry Massart for his clear and precise remarks.

The 3SR lab and more precisely the GDR/Géomécanique team for having me around in Grenoble and providing the varied working environment; in the same way one of the GEO's of the GEO^3 section for my year in Liège.

The (former) PhD students of GDR and GEO(mcanique); especially Nando for his great care for introducing me in the different finite element codes and Albert for our many discussions over lunch; Max, Raphael and Viviana for the climbing trips around Grenoble; Simon and Benoit for the mid-day runs in Lige; Patrizia and Ghonwa for sharing an office during the final years of our theses; ...

Finally, my gratitude goes to all those outside the lab who helped me forget my work during evenings weekends and holidays in, around and far away from Grenoble. You've made my stay here an unforgettable time. It's been a pleasure!

Bram van den Eijnden

Grenoble, August 2015

CONTEXT AND OBJECTIVES

Different scales of observations can be defined in basically any type of geomaterial. On the finer scales of observation these materials contain heterogeneities, the arrangements of which define the microstructure of the material. The combined effect of the microstructural elements in the material behaviour can generally be characterized by an effective continuum at larger scales of observation. Classically, the behaviour of this macroscale continuum is described by phenomenological constitutive models in which the homogenized effect of some of the micromechanical features is assumed to be accounted for. Improving these macroscale phenomenological models by taking into account more and more micromechanical effects makes it more and more difficult to formulate the macromechanical constitutive relations and alternative descriptions are required. One of these alternatives is to model the micromechanical effects explicitly on their specific length scale and couple their homogenized effects to the macroscale behaviour. In this way, the global response of an assembly of micromechanical features can provide an alternative formulation for the multiphysical behaviour of the material at the macro scale.

Making a coupling between different scales in the description of the behaviour of materials has seen a developing trend in the last decennia. This trend has its origin in the need to express the macroscale behaviour as a direct effect of micromechanical processes and many approaches have been proposed for these scale transitions of upscaling the micromechanical response to deformation to a macroscale constitutive behaviour. Early developments mainly concerned the elastic behaviour of inclusions, such as the effective medium approach [Eshelby, 1957] or the self-consistent method [Hill, 1965], followed by asymptotic homogenization theory [Bensoussan et al., 1978, Sanchez-Palencia, 1980] for periodic media with simple microstructures and the use of a representative cell for more complex structures and constitutive relations that has led to local-global modelling, also known as the framework of homogenization [Suquet, 1985, Lee and Ghosh, 1995, 1996, Feyel and Chaboche, 2000, Kouznetsova et al., 2001].

The modelling of the excavation of tunnels (referred to as galleries from here on) for the construction of deep geological waste repositories is a field of studies in which both the coupling of different scales and the coupling of different physical processes are involved. The principle of the nuclear waste disposal in deep geological repositories relies strongly on the low permeability of the host rock, which can provide a sealing capacity against the transport of radioactive nuclides into the atmosphere. Changes in this sealing capacity can take place in the zone around the gallery, usually referred to as the excavation damaged zone (EDZ), due to deformations induced by the gallery excavation. Although different definitions can be found in literature, this zone is generally characterized as follows:

> *"The EDZ is a zone in which hydromechanical and geochemical modifications induce significant changes in flow and transport properties. These changes can, for example, include one or more orders-of-magnitude increase in flow permeability" [Tsang et al., 2005].*

The coupling between mechanical alteration on one hand and the transport and flow properties on the other, is therefore of vital importance in the feasibility studies of deep geological repositories, comprising the characterization of the hydromechanical coupled behaviour and subsequently its numerical modelling for predicting the performance of future repositories. As the transport phenomena take place at the fine scales, and macroscale damage has its origin in micromechanical action, the link to the fine scale phenomena of the host rock need an adequate representation in the characterization. In this context the modelling of hydromechanical coupling in a multiscale framework is studied here. Objectives of this work are to develop a doublescale model for studying localization problems with hydromechanical coupling, and in specific the modelling of problems related to gallery excavations in argillaceous rocks.

The choice for a doublescale model is based on the desire to derive macroscopic material behaviour directly from microstructural effects, without relying on phenomenological macroscale relations. As the direct modelling of the microstructure is usually not possible due to its high computational expense, an alternative formulation is needed to take into account the micromechanical effects. The use of a fine scale representative elementary volume (REV) provides a tool for constructing a detailed model of the microstructure without modelling the microstructural details for the full domain. The response to deformation loading of such a REV can be linked to the macroscale and serve as a numerical constitutive relation in the framework of periodic computational homogenization [Kouznetsova et al., 2001]. In this way, the macromechanical modelling is directly linked to the micromechanical processes, which fully dictates the macromechanical behaviour. When solving the boundary value problems (BVP) at both scales using a finite element method, we speak of the finite element squared (FE^2) method.

This work presents the development of a FE^2 method for hydromechanical coupling and its application to localization problems related to gallery excavation in argillaceous rocks.

From the development point of view the microscale model for hydromechanical coupling [Frey, 2010] is combined here with computational homogenization by static condensation [Kouznetsova et al., 2001, Özdemir et al., 2008a] to facilitate an efficient scale transition from micro to macroscale. This method, generally used for purely mechanical problems, is extended to hydromechanical coupling. The implementation of the computational homogenization for hydromechanical coupling allows an efficient implementation in the existing finite element code Lagamine [Charlier, 1987]. Because the purpose is to study localization phenomena, a regularization technique is needed to avoid macroscale mesh dependency. Therefore, the doublescale method is combined with a local second gradient model for hydromechanical coupling [Chambon et al., 2001, Collin et al., 2006].

This thesis was financed by the French national radioactive waste management agency (Andra) in the context of the ongoing research on the feasibility of deep geological repositories for high- and mid-level long-lived radioactive waste

in France. It focuses on the possibilities of the construction of a repository in the Callovo-Oxfordian claystone, in line with the research currently being conducted in the underground research laboratory (URL) in Bure (Meuse/Haute-Marne, France). Part of this research focuses on the evolution of transport phenomena in the EDZ as an effect of the mechanical material alteration such as localized strain and material damage.

An objective of this thesis is to apply the developed method to the modelling of the localization of deformation around gallery excavations in Callovo-Oxfordian claystone, more specifically those related to the URL in Bure.

Outline and presentation

The work presented in tis thesis concerns the development of a doublescale model for hydromechanical coupling in a FE^2 framework, its implementation in the existing finite elements code Lagamine and its application on the modelling of hydromechanical behaviour of claystones in the setting of gallery excavations. The development of the code is the continuation of the work by Bilbie et al. [2008],Frey [2010] and Marinelli [2013]. Building upon the results of these works and theory available in literature (notably the computational homogenization [Kouznetsova et al., 2001, Özdemir et al., 2008a] and local second gradient modelling [Chambon et al., 2001, Collin et al., 2006]), the following parts are considered original in this work;

- The extension of computational homogenization by static condensation to hydromechanical coupling to use an existing microscale model [Frey, 2010] for obtaining a homogenized macroscale constitutive relation to be used in doublescale finite element computations. Key aspect is the consistent homogenization of the REV responses to kinematical constraints and its consistent tangent operators.

- The implementation of the hydromechanical coupled model in the finite element code Lagamine as independent constitutive laws for mechanical and HM-coupled behaviour

- The application of the doublescale FE^2 method to localization problems using a local second gradient model. The main doublescale computations concern the modelling of biaxial compression tests and gallery excavation problems.

This work is subdivided in five parts;

- Part I introduces the setting of the research for the development of the doublescale model and introduces existing modelling approaches that form the starting point of this work.

- Part II contains the development of the microscale model and its computational homogenization procedure required for the scale transition, including the upscaling of consistent tangent operators.

- Part III deals with the implementation and validation of the developed microscale model in the finite element code Lagamine. Aspects of computational efficiency, numerical accuracy and consistency are discussed, after

which a validation of the doublescale model is given based on analytical results. The purpose of the results presented in this Part is the validation of the code and the demonstration of its possibilities.

- Part IV contains examples of the application of the model to true doublescale computations in the modelling of localization in anisotropic material, the calibration of the model against experimental results of laboratory tests on Callovo-Oxfordian claystone and the application of the model to the simulation of gallery excavation.
- Part V summarizes the results and states some points that requires further study for the correct application of the proposed framework.

Several appendices with complementary information are added. Some of these appendices give additional results or derivations as an extension to the main text, some contain developments with respect to different versions of the micromechanical model. These latter developments need to be seen as independent from the main part of the text. One of these developments is an alternative version of the HM-coupled model with computational homogenization. This version resembles more the model presented in Frey [2010], but has become obsolete after changes in the formulation of the hydraulic system, as will be discussed in this work.

Part I

INTRODUCTION – MULTISCALE MODELLING OF HYDROMECHANICAL BEHAVIOUR IN GEOMATERIALS

1. CALLOVO-OXFORDIAN CLAYSTONE - DESCRIPTION AND EXPERIMENTAL RESULTS

As part of the Paris Basin, the Callovo-Oxfordian claystone (COx) formation of Bure can be found at depths between 420 and 550 meters below surface level [Andra, 2005a]. As a potential host rock for deep geological nuclear waste disposal sites, this formation is subject of an extensive research program into the feasibility of the construction of underground disposal facilities. As a major part of this program, the Andra Underground Research Laboratory (URL) is constructed at a depth of 490 meters in the COx formation in Bure (Marne/Haute-Meuse, France), providing means for both in-situ and laboratory testing of the host material [Andra, 2005a,b].

Different facies can be identified in the Callovo-Oxfordian claystone, for which the general characteristics are those of a mudstone. The claystone consists of a fine-grained clay matrix embedded with carbonate and tectosilicate grains and has low permeability. From the length scale of the formation to the finest scales of clay minerals, different scales of interest can be identified on which formation-specific properties can be studied. Four scales are identified in the COx claystone by Robinet [2008]:

- **Microscopic scale** ($< \mu m$) the structure of clay minerals forms a complex microstructure on different subscales (sheets, particles, grains...)
- **Mesoscopic scale** ($\mu m - cm$) On this scale mineral grains (quartz, carbonates, sulphides) embedded in a clay matrix can be observed
- **Macroscopic scale** ($cm - dm$) On this scale the mineralogy is considered to be homogeneous and porosity is uniformly distributed
- **Formation scale** ($> dm$) Different facies can be identified on this scale. This is the scale of the geological and geotechnical (galleries) structures.

In the following sections, the characteristics of the material at these scales that are relevant to the current work are presented.

1.1 The microscopic scale ($< \mu m$)

The Callovo-Oxfordian claystone consists mainly of three groups of minerals; clays (20-60%), tectosilicates (10-40%) and carbonates (22-37%). The clay minerals form a matrix in which carbonate (mainly calcite) and tecto-silicate (mainly quartz) grains are embedded. In additions, small fraction of heavy minerals can be found, predominantly pyrite (up to 3 %), see [Andra, 2005a] and the references therein.

As the inclusions all have dimensions bigger than the microscale characteristic length, the main interest on this scale is the structure of the clay particles

and aggregations that form the clay matrix on the mesoscale. The clay mass is composed of mainly illite and interstratified illite/smectite, kaolinite, mica, and chlorite minerals [Pellenard and Deconinck, 2006]. The pore space at this scale (infra-micro and nano scale) is between the clay particles and around secondary minerals, forming a connected pore network [Yven et al., 2007]. The clay particles themselves consist of layers of clay minerals, each consisting of two or three sheets with tetrahedral or octahedral atomic structure.

In this work, the clay particles and nano-pore network will not be modelled in detail and treated as a homogeneous matrix. Possible hydraulic transport through the nano-pore network will be considered as diffusive flow in the matrix, which is in itself a phenomenological model for the hydromechanical processes taking place at the underlying scales of the clay matrix.

1.2 Mesoscopic characterization

The experimental characterization of (fluid) transport phenomena in claystone is not easily obtained and the effect of microstructure on its behaviour is therefore mainly based on microstructure imaging in combination with numerical modelling of fluid transport in equivalent pore networks [Robinet et al., 2012]. An example of the result of imaging the microstructure and discretization into non-porous and diffusive zones is given in Figure 1.1, based on X-ray computed tomography (performed at the European Synchrotron Radiation Facility) with a spatial resolution (voxel size) of 0.7 μm.

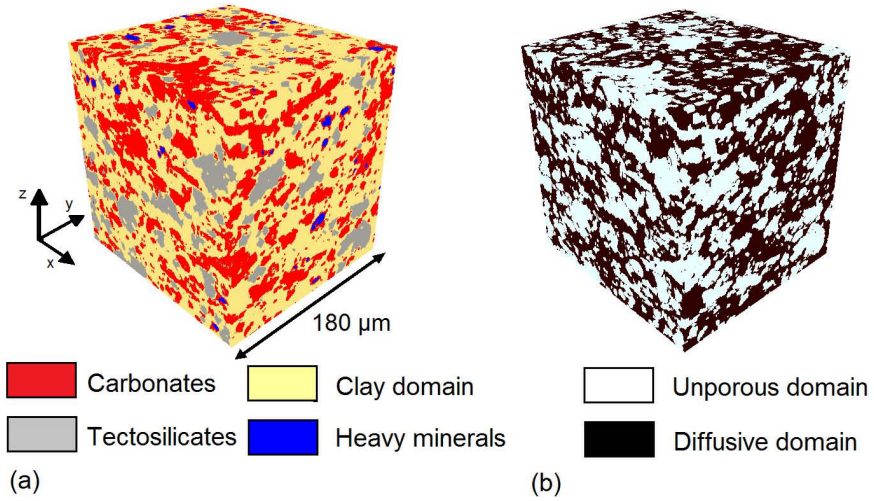

Fig. 1.1: a). Three-dimensional spatial distribution of mineral groups obtained using X-ray synchrotron tomography. b). Imposition of diffusive properties [Robinet et al., 2012]

The shape of the inclusions at the mesoscale was investigated by Robinet [Robinet, 2008, Robinet et al., 2012] by means of digital image analysis. The images were obtained by two different techniques; scanning electron microscopy using backscattered electron imaging mode (SEM BSEi) and X-ray computed tomography (micro-CT), where in the case of micro-CT images 2D slices of 3D

images were used. After gray-scale segmentation to distinguish between clay matrix and the different types of inclusions, the grain elongation and the grain orientation were computed from the shape of a best fit of an ellipse to the grain intersection in the image. The dimensionless grain elongation index e is defined as the ratio between minimum diameter $l2$ and maximum diameter $l1$ of the ellipse:

$$e = \frac{l_2}{l_1} \tag{1.1}$$

The angle between the orientation in which $l1$ is measured and the positive horizontal axis defines the grain orientation angle β between 0° and 180° (see Figure 1.2).

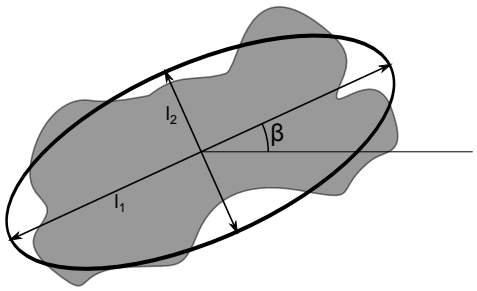

Fig. 1.2: Grain geometry equivalent ellipse for the characterization of grain elongation e and orientation β.

A histogram of the orientation of the grains is given in Figure 1.3 (see also Figures 14.1 and 14.2) which gives a measure of the anisotropy and the distribution of the orientation. A dimensionless anisotropy parameter A was defined by Robinet [2008], Robinet et al. [2012] as the ratio between the highest and lowest frequency $f(\beta)$ at which a certain orientation is observed to quantify the orientation distribution. Results for elongation e and orientation anisotropy A obtained from sample images normal and parallel to the bedding plane are reported in Table 1.1.

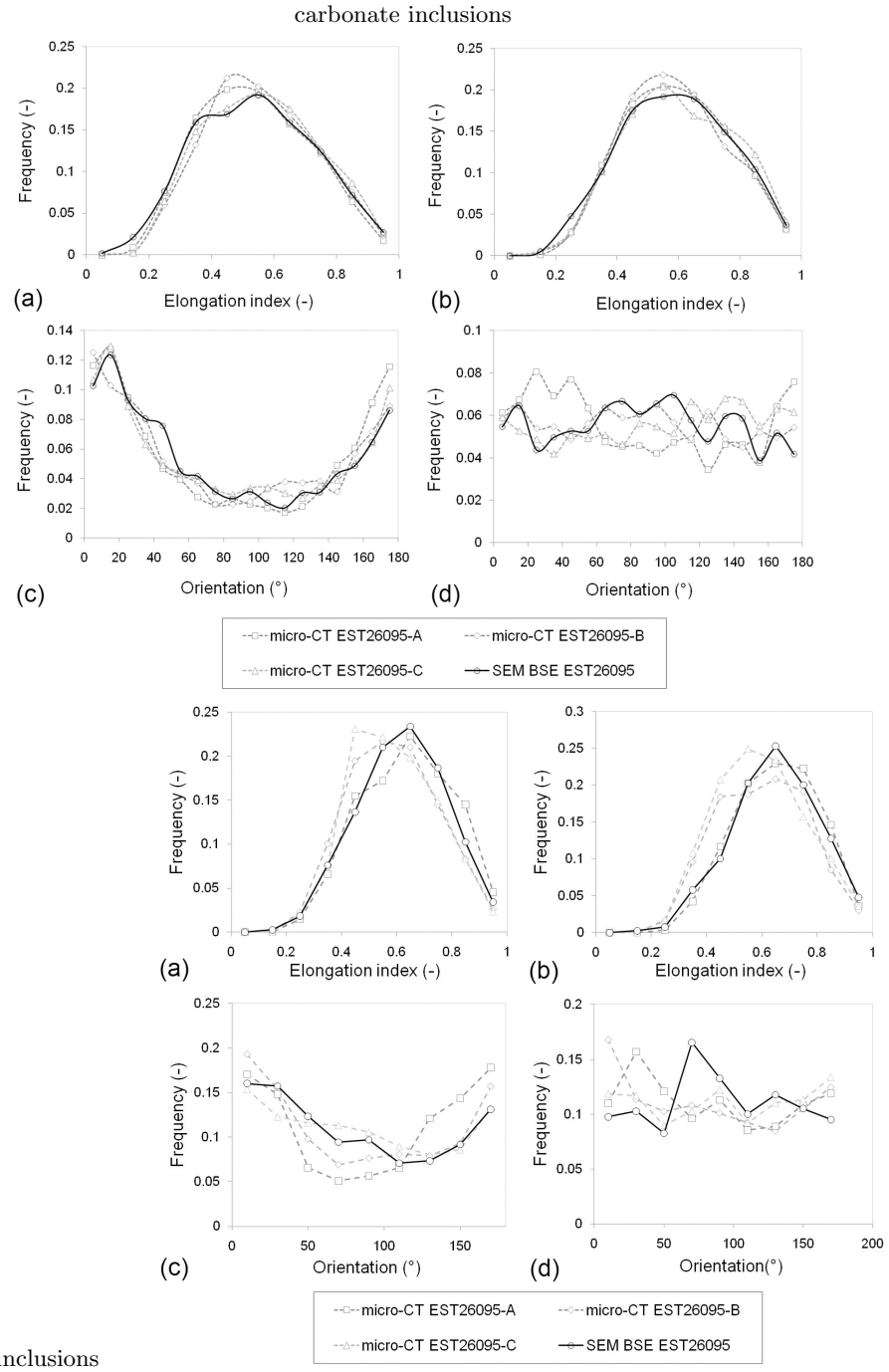

Fig. 1.3: Statistical characterization of the elongation index e and orientation β of carbonate (top) and tectosilicate inclusions (bottom) in the bedding plane (b,d) and in the plane parallel to the bedding (a,c) [Robinet et al., 2012].

Mesoscale observations of the evolution of deformation of the Callovo-Oxfordian claystone are scarce in literature and the development of the cracks from a meso-

Technique	Sample Ref.	Carbonates A	Carbonates e	Carbonates %	Tectosilicates A	Tectosilicates e	Tectosilicates %	Clays %
SEM BSEi	EST26065⊥	6.04	0.54	25.1	2.26	0.61	8.9	67.0
	EST26095‖	1.79	0.59	26.6	2.00	0.64	12.0	60.4
Micro-CT	EST26095⊥	4.66	0.55	25.1*	2.52	0.60	14.7*	60.2*
	EST26095‖	1.35	0.59		1.55	0.62		

Tab. 1.1: Geometrical characterization of the inclusions in C0x claystone. After Robinet et al. [2012]. * = volumetric percentages obtained from 3D images.

scopic point of view is something that has not yet been fully characterized. Nevertheless, results on the initiation and developments of fractures at this scale have been obtained from X-ray tomography on triaxial compression tests [Lenoir et al., 2007, Bésuelle, 2014] and images of triaxial [Bornert et al., 2010] and biaxial compression tests [Bésuelle et al., 2010, Wang et al., 2014].

In Figure 1.4 a slice of a 3D image of the state of a claystone sample under triaxial loading is presented. This image was obtained by synchrotron radiation micro tomography that was used for imaging the sample throughout the loading test. Full-field measurements obtained from the time evolution of such 3D images can provide a better insight in the initiation and continuation of micro cracks and can give qualitative information on the cohesion between inclusions and clay matrix.

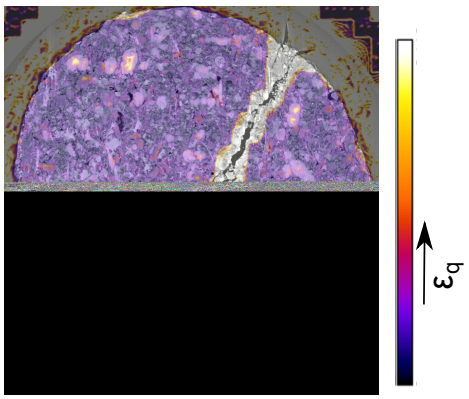

Fig. 1.4: Horizontal slice of 3D nanoCT image (synchrotron) of triaxial compression test performed on a $\varnothing$ $1.3mm$ sample at 10 MPa confining pressure. 3D image correlation is used to follow the development of (micro)crack during compression. Colored overlay shows deviatoric strain Bésuelle [2014].

Porosity at the mesoscale is found in the form of isolated meso-pores ($> 1\mu m$), located mainly around the inclusions. Their interconnection is through the nano-pore network [Yven et al., 2007].

1.3 Macroscopic material characterization

Besides the purely mechanical and fully saturated hydromechanical behaviour, studies were performed on the chemical, thermal, mineralogical and non-saturated

behaviour of the COx, as well as the migration of gas and the coupling between these different effects. Since this work is restricted to the development of a model for hydromechanical coupling in fully saturated conditions, only these properties of the COx are discussed, although it should be noted that hydromechanical behaviour is strongly influenced by the degree of saturation [Pham et al., 2007, Andra, 2011, Zhang, 2011] and a clear separation between dry, non-saturated and saturated material conditions in experiments is not easily obtained.

AT the centimeter scale, on which the material can be considered homogeneous, the material behaviour is characterized by means of the results of laboratory tests. A range of laboratory test were performed by different laboratories, from which results are summarized in two reports by Andra [2005a, 2011]. From these experimental campaigns, the following can be concluded regarding the macroscopic behaviour of the COx:

- preliminary evidence for anisotropy in the peak stress σ_p has been observed, with a slightly higher peak stress for compression in the direction of the bedding plane compared to perpendicular to the bedding plane and a reduction up to 50% in the direction 45° to the bedding plane [Auvray, 2011].
- anisotropy of the Young's modulus can be observed, with a 20-30% higher stiffness in the bedding direction [Zhang, 2011]. This anisotropy however, is not observed in the triaxial tests shown in Figure 1.5.
- Initial (intrinsic) permeability is in the order of $1 \times 10^{-20}\ m^2$. This intrinsic permeability corresponds to a hydraulic conductivity in the order of $1 \times 10^{-13} m/s$.
- Total porosity ranges between 14% and 19.5% [Yven et al., 2007].

A series of triaxial compression tests was performed by different laboratories [Andra, 2013], for which samples were stabilized under a relative humidity of 90% before testing. This stabilization leads to a partially saturated state of the sample and the measured response is influenced by this degree of saturation. Therefore, the response should be interpreted as a total stress. Although globally no fluid pressure was applied, the (partial) saturation might play an important role in the stress response, as demonstrated experimentally by Zhang [2011].

The nominal stress response to triaxial compression at different confining stress for this series of tests is given in Figure 1.5. These results will serve in this work as reference experimental results for the macroscopic behaviour of drained conditions. Drained conditions in this sense is defined as the absence of influences of hydraulic pressure on the mechanical response, which means both locally and globally drained conditions at zero fluid pressure and the absence of any unsaturated effects.

Rock parameter	Ind	Value
mass of unit volume (wet)	ρ	2.39 g/cm^3
Porosity	n	18 ± 1 %
Young modulus	E	4000 ± 1470 MPa
Poisson ratio	ν	0.29 ± 0.05
Uniaxial compressive strength	UCS	21 ± 6.8 MPa
Hoek-Brown criteria	S	0.43
	m	2.5
	σ_c	33.5 MPa
Intrinsic permeability	k_{ii}	$5 \times 10^{-21} - 5 \times 10^{-20} m^2$
Water content	M	$7.2 \pm 1.4\%$

Tab. 1.2: Main characteristics of the Callovo-Oxfordian claystone at the URL level (-490m). After Armand et al. [2014]

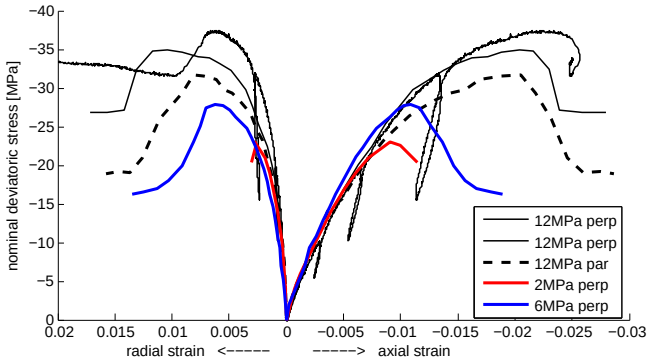

Fig. 1.5: Nominal deviatoric stress response to triaxial compression at 2, 6 and 12MPa confinement stress, perpendicular (perp) and parallel (par) to the bedding plane [Andra, 2013].

By adopting the assumption of a Mohr-Coulomb failure criterion, a friction angle ϕ and cohesion c can be found based on the peak response of the triaxial tests. This gives a friction angle of $\phi = 24°$ and a cohesion of $c = 6.4MPa$. In addition, the Poisson's ratio ν and Young's modulus E can be obtained from the initial slopes of the stress-strain relations and fall well within the range of $\nu = 0.29 \pm 0.05$ and $E = 4.0 \pm 1.47GPa$ respectively, as can be found in literature (Table 1.2). More macroscale material properties can be found in literature, notable in Andra [2005a,b] and the references therein. A range of material parameters can be found, depending on the mineral content, which varies with the depth at which the samples for testing were taken. Table 1.2 gives reference values of the main hydromechanical parameters of the COx to be used in this work. In this table, the failure criteria are given in the form of the Hoek-Brown criteria [Hoek and Brown, 1997], which can be translated into equivalent cohesion c' and friction angle ϕ' for a Mohr-Coulomb criterion [Hoek et al., 2002] (the conversion procedure used here is presented in this specific 2002-version of the publication). When using the Bure URL in-situ stress state, this results in $\phi' = 22.1°$ and $c' = 6.8MPa$, which is in good agreement with the results obtained from the triaxial tests presented above.

1.4 Formation scale observation in the EDZ

At the formation scale (>1 dm), the Callovo-Oxfordian shows a variation in the distribution of the mineral content, of which the variation of the carbonate content is the most important parameters. At the URL level (-490m) the variation is relatively low and the mineral content can be considered constant with depth. The in-situ stress regime is related to the tectonic regime of alpine orogenesis with a major principal stress direction in the horizontal plane at a $NE150°$ strike. The stress regime can therefore be characterized by means of a vertical stress component σ_v and a major and minor horizontal stress component σ_H and σ_h. Vertical stress corresponds to the weight of the overburden $\rho g h \approx 12 MPa$:

$$\begin{aligned} \sigma_h &= 12.40 \text{ MPa} \\ \sigma_H &= 16.12 \text{ MPa} \\ \sigma_v &= 12.70 \text{ MPa} \end{aligned}$$

A detailed study of the geometry of the EDZ around gallery drifts at the URL level is documented in Armand et al. [2014]. Based on this work, the main features for the characterization can be derived:

For a detailed observation of the fracture network, dyed resin was injected in the rock around the gallery from a borehole horizontally drilled from the gallery wall. The extraction of the injected material allowed the detailed identification of the fracture network in the characterization of the distribution of the different types of fractures (Figure 1.6).

In the excavation damaged zone, two types of localized failure are observed; and extension fractures (mode I) and shear fractures (mode II). In the proximity of the gallery wall, extensional fractures are observed with a heterogeneous distribution of orientation with respect to the gallery wall. These fractures have a discrete nature. The chevron shear fractures have more the characteristics of a zone in which smaller fractures form a band. The width of these bands is is the order of a decimeter. The chevron fractures extend beyond the zone in which the extension fractures are observed.

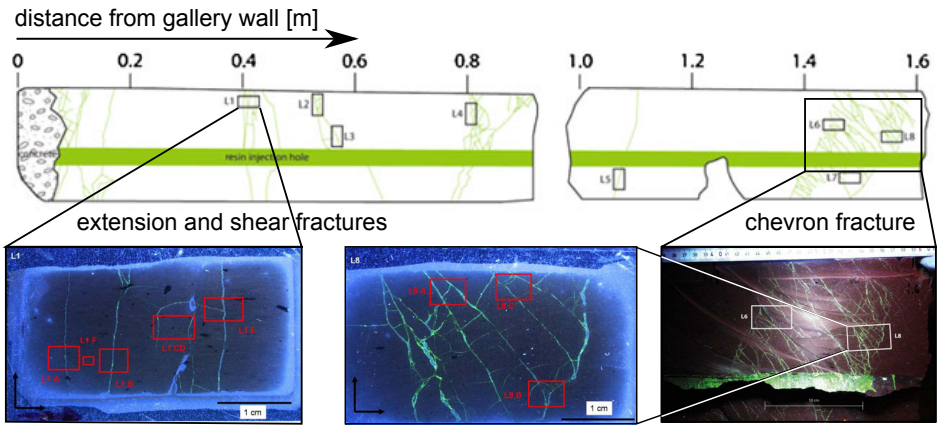

Fig. 1.6: Fracture observation under fluorescent light after dyed resin injection in a horizontal borehole drilled from the gallery wall. Top: interpretation of fracture pattern drilled around resin injection. Bottom left: thin section with details of extension/shear fractures. Bottom right: picture under fluorescent light of chevron fracture. Bottom center: thin section of detail of chevron fracture. Images taken from Armand et al. [2014]

Two models of the EDZ are defined; a model for galleries with an orientation along the minor and along the major principal stress directions respectively. A graphical representation of these models is given in Figure 1.7. It can be observed that for the model of the gallery along the mayor principal stress direction, the geometry of the excavation damaged zone is does not show a spherical pattern around the gallery, although the (initial) stress state is close to axisymmetric ($\sigma_2 : \sigma_3 = 12.7 : 12.4$). This indicates that anisotropic behaviour is likely to be induced by the host rock, either at the local scale (present in the constitutive behaviour) or at the global scale (formation-scale heterogeneity, effect of geological layering,...).

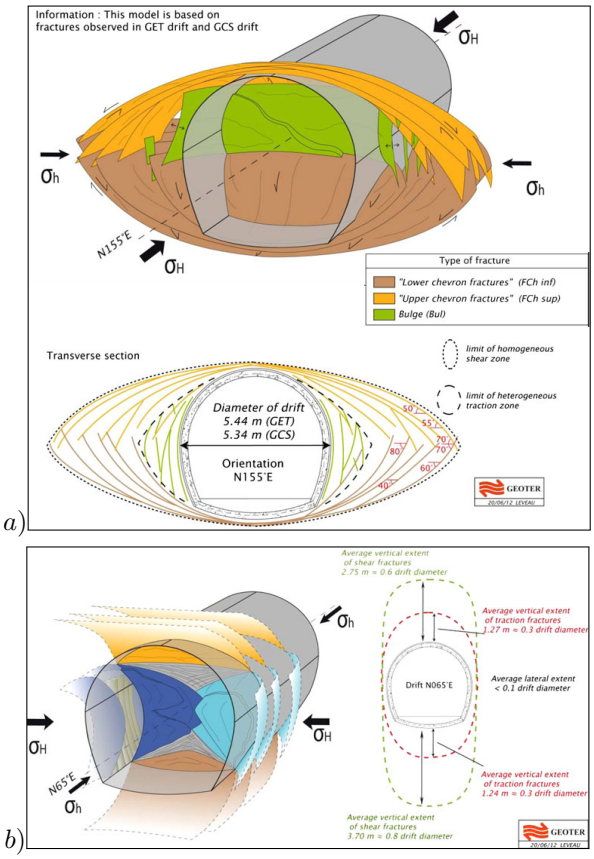

Fig. 1.7: Conceptual model of the fractures in the EDZ for drifts in the direction of *a*) the major principal stress and *b*) the minor principal stress [Armand et al., 2014].

Other observations related to the hydromechanical behaviour at the formation scale are [Armand et al., 2014]:

- In the 'homogeneous shear zone', no big changes in hydraulic conductivity was observed. The observed variations in hydraulic conductivity fall within the range of one order of magnitude.
- In the 'heterogeneous traction zone', a strong change in hydraulic conductivity was observed, with an increase up to 4 orders of magnitude. This increase is related to the fracture transmissivity and not to a change in permeability of the matrix.

2. MODELLING APPROACH FOR GALLERIES IN CALLOVO-OXFORDIAN CLAYSTONE

The choice of appropriate constitutive models is a key factor in the modelling of geomaterials and many constitutive models have been proposed in the classical way of modelling material behaviour through the formulate of phenomenological descriptions in macroscale constitutive relations. These models can generally be divided in the family of elastic-plastic models [Vermeer and de Borst, 1984] and hypoplastic models [Kolymbas, 1991], although many variations can be found, allowing the direct introduction of a wide range of phenomena of material behaviour such as plasticity, viscosity and coupling between multiple physical processes that can directly be formulated. Examples of such phenomenological models applied on the modelling of the hydromechanical behaviour of claystone can be found in Shao et al. [2006], Arson and Gatmiri [2009], Cariou et al. [2013], Charlier et al. [2013].

However, this way of phenomenological macroscale modelling can lead to difficulties when

- anisotropy has to be introduced for different phenomena
- a full loading history has to be taken into account
- material behaviour based on micromechanical observations needs to be taken into account
- non-linear responses for principal stress rotation are to be considered

The incorporation of micromechanical phenomena in the formulation of the macroscale behaviour can therefore hardly be avoided. An alternative to phenomenological macro scale constitutive models is taking into account the material microstructure underlaying the macroscopic constitutive behaviour in a direct simulation. However, the full incorporation of the microstructure in the computation is often restricted to relatively simple computations as an effect of the limitations in computation power. Instead, a selection of the microstructure can be modelled from which the homogenized response represents macroscopic behaviour. Many approaches are available with different levels of microstructural detail. One family of such models for anisotropic damage derives the macro scale behaviour from micro scale damage related to the nucleation and growth of microcracks Andrieux et al. [1986], Pensée et al. [2002]. These methods have seen a range of applications and extensions, notably to poromechanical modelling Dormieux et al. [2002, 2006]. This family of microcrack models does however not represent a complete microstructure that takes into account for example the full interaction between the micromechanical constituents such as inclusions, crystals or grains and more complex micromechanical models with different homogenization schemes are required for this extend.

2.1 Finite element squared – FE^2

Another approach of microscale-based modelling can be found in double-scale finite element methods [Lee and Ghosh, 1995, 1996, Smit et al., 1998] or the finite element squared (FE^2) method [Feyel and Chaboche, 2000, Kouznetsova et al., 2001, Miehe and Koch, 2002, Schröder, 2014], where the material behaviour at the macro scale is modelled by means of a representative elementary volume (REV), containing a detailed model of the material microstructure. The boundary value problem related to the deformation of the REV is solved by means of a finite element method. The global response of the REV to the deformation, dictated by the macroscale local deformation tensor $\boldsymbol{F}^M = \nabla_0^M \vec{x}$, serves as a numerical constitutive law for the macro scale (Figure 2.1).

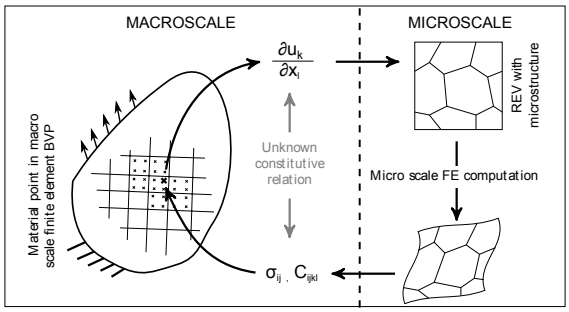

Fig. 2.1: Schematic representation of the FE^2 method. Macro response σ_{ij}, together with tangent operator C_{ijkl}, forms the numerical constitutive relation derived from the REV boundary value problem by computational homogenization.

The translation from the macroscale deformation gradient $\boldsymbol{F}$ to the REV boundary value problem, which is discussed in more detail in Section 4, is most efficiently done through periodic boundary conditions at the REV [Terada et al., 2000, van der Sluis et al., 2000]. Once the boundary value problem at the microscale is solved up to an acceptable degree of accuracy, the stress response to the deformation loading is sent back to the macroscale. In the framework of computational homogenization, this scale transition is obtained from the condition of equal work on the micro and the macroscale, better known as the Hill-Mandel macro-homogeneity condition [Hill, 1965, Mandel, 1972] (Equation 2.1). In combination with the divergence theorem, the integral over the microscale domain can be linked to the boundary conditions of the microscale:

$$\boldsymbol{P}^M : \boldsymbol{F}^{\star M} = \frac{1}{V} \int_{\Omega} \boldsymbol{P} : \boldsymbol{F}^{\star} d\Omega = \frac{1}{V} \int_{\partial\Omega} \vec{t} \cdot \vec{x}^{\star} d\Gamma \tag{2.1}$$

Here $\partial\Omega$ is the boundary of domain Ω and $\vec{t}$ is the traction acting on this boundary at coordinate $\vec{x}$.

These classical methods of first order computational homogenization are based on the assumption of scale separability; the scale of fluctuation in the macroscopic fields is large compared to the microstructure and its REV, such that the boundary conditions of the microscale BVP can be properly dictated by the local macroscale deformation gradient. The method of computational homogenization

has become a generally applied method in the analysis of the behaviour of material with microscale heterogeneity, see for example Geers et al. [2010] and the references therein. However, the method has it restrictions, notably linked to the capacity of modelling localization phenomena. This is summarized in Geers et al. [2010] as follows:

- *The method complies with the principle of local action and the material point concept and is therefore in a non-modified form limited to a standard continuum mechanics theory at the macroscale.*
- *The aforementioned principle of separation of scales clearly sets limits for the first-order case. As a consequence, large spatial gradients at the macro-scale cannot be resolved. The method is therefore not suited for the analysis of localization problems [Geers et al., 2010]*

For obtaining objective results in case of softening response and localization problems, the first-order computational homogenization was extended to second-order computational homogenization [Kouznetsova et al., 2002, 2004, Luscher et al., 2010], in which a length scale was derived from micromechanical computations by adding the gradient of the macroscopic deformation tensor $\nabla_0 \boldsymbol{F}^M$ to the boundary conditions of the REV. By linking this strain gradient to the macroscale strain gradient, a second gradient model can be obtained which is directly dependent on the microscale deformation. Others have extended the computational homogenization to micromorphic media [Jänicke et al., 2009], obtaining a length scale at the macrolevel through additional boundary conditions at the microscale. In these ways, the continuity at the macroscale can be guaranteed for loading beyond the peak response. However, the derivation of a length scale from the microscale REV requires defining a length scale at the REV level and the separation of scales is no longer valid.
An alternative approach is to extend the macroscale framework with discontinuities to allow localization of deformation at the microscale develop into fracture-like discontinuities at the macroscale. For this purpose, a decomposition of the macroscale deformation into a homogeneous unloading and a discrete fracture part has been introduced in a continuous-discontinuous framework by Massart et al. [2007]. Following a similar philosophy of tensorial decomposition of the deformation was used to model localization along a-priori defined macroscale cracks [Kulkarni et al., 2010, Nguyen et al., 2011]. Other methods have been proposed, using multi-level computations combining multiscale modelling with direct modelling of the microstructure to account for damage in zones where discontinuities are likely to occur (see for example Ghosh et al. [2007], Bai [2008])
Recently, a continuous/discontinuous approach without a priori defined localization paths using the so-called 'percolation-path aligned' boundary conditions was proposed by Coenen et al. [2011a,b]. Here the periodicity is rotated to align with localization paths in order to decompose into continuous and discontinuous deformation. This method has been applied in the modelling macroscale localization in cellular material due to micro-buckling of cell walls in a discontinuous Galerkin methods by Nguyen [2014], Nguyen and Noels [2014].

When it comes to multiphysical coupling in doublescale computations, the FE^2 method has seen few applications, with the first notable formulation of multiphys-

ics couplings the introduction of thermo-mechanical coupling by Özdemir et al. [2008a,b]. Computational homogenization was later used for deriving the effective porosity from microstructures captured in a REV [Massart and Selvadurai, 2012, 2014]. In these approaches, first order computational homogenization was used, which implies that the separation of scales was honoured and no length scale was supposed to be present at the microscale. A variational homogenization was introduced by Su et al. [2011] for solving transient hydromechanical coupled problems, taking into account the transient effects in both macro and microscale computations. This requires the introduction of an internal length scale in the REV. For the incorporation of such a physical length scale, hydromechanical coupling in a computational homogenization framework for micropolar media was proposed by Jänicke et al. [2015] for the modelling of poroelastic media.

Computational homogenization of the hydromechanical coupling in porous media was presented in Mercatoris et al. [2014] for the modelling of anisotropic hydromechanical coupling in heterogeneous porous media.

2.2 Strain localization in finite element models; regularization techniques

We investigate here an approach for the modelling of localization phenomena while maintaining the continuum at the macro scale. It is well-known that the classical finite element method will lead to spurious mesh dependency in case of strain localization and an enhancement is required to obtain objective results. Several regularization enhancements are available for this purpose, such as nonlocal damage models Pijaudier-Chabot and Bažant [1987] or gradient models Muhlhaus and Alfantis [1991] in which damage parameters are smeared out through spatial averaging or through dependency on strain gradients. In this way mesh objectivity is obtained. However, this introduces a non-local dependency of (damage) parameters in the constitutive law, which is not compatible with the envisioned double scale approach. For this reason local second gradient models Mindlin [1965], Germain [1973] are required, since its framework is based on the assumption of a microstructure with small dimensions compared to the macro scale. This allows constraining the microkinematic field such that the constitutive behaviour is strictly local. A local second gradient model has been developed for geomaterials Chambon et al. [2001], Matsushima et al. [2002] and the modelling of localization in shear bands has been investigated and presented in works Bésuelle et al. [2006].

A consequence of the use of a local second gradient model on the macroscale, is that a continuum approach is maintained throughout the computation and macroscale discontinuities can not be taken into account. This requires the constitutive behaviour to represent local continuous behaviour with a diffuse character of deformation. This requirement might be very strong and is closely related to the periodicity of the material behaviour. Section 11.2 will investigate this requirement in more detail.

3. STATE OF ART : EXISTING MODELS TO START FROM

In this chapter, two existing approaches for the modelling of hydromechanical coupling at the macro and micro level are discussed. These approaches form the starting point of this work.

3.1 Large strain formulation of a poromechanical continuum with a local second gradient model

On the macro scale a poromechanical continuum is defined for which the field equations describing equilibrium under quasi-static conditions are solved for field variables u_i (displacement) and p (fluid pressure). Since localization due to softening will be studied, an enhancement is required to avoid either the well known mesh dependency or the strain localization into bands with vanishing width and energy dissipation upon mesh refinement [Pijaudier-Chabot and Bažant, 1987]. This enhancement is introduced by considering the material as a micromorphic material with a microkinematical gradient ν_{ij}, in addition to the macro displacement field u_i. As a particular case of micromorphic continuum, the microkinematical gradient ν_{ij} is assumed to be identical to the gradient of the macro displacement $\partial u_i/\partial x_j$ in accordance with the second gradient theory [Mindlin, 1965, Germain, 1973, Chambon et al., 1998, Matsushima et al., 2002].

The introduction of the kinematical gradient ν_{ij} as a variable in the framework of second gradient theory requires double stress $\mathbf{\Sigma}$ (with components Σ_{ijk}) as a static dual to the gradient of $\boldsymbol{\nu}$. This allows writing the field equations in a virtual work formulation for any kinematically admissible field of displacement $u_i^\star$ and $\nu_{ij}^\star = \partial u_i^\star/\partial x_j$ as:

$$\int_{\Omega^t} \left(\sigma_{ij}^t \frac{\partial u_i^\star}{\partial x_j^t} + \Sigma_{ijk}^t \frac{\partial^2 u_i^\star}{\partial x_j^t \partial x_k^t} \right) d\Omega - \bar{W}_e^\star = 0 \tag{3.1}$$

with Ω^t the configuration at time t, σ_{ij}^t the classical Cauchy stress and $\bar{W}_e^\star$ the external virtual work. The external virtual work is assumed to contain no body double forces and therefore can be given by:

$$\bar{W}_e^\star = \int_{\Omega^t} \rho^t f_i^t u_i^\star d\Omega + \int_{\Gamma_{\sigma'}} \left(p_i^t u_i^\star + P_i^t \frac{\partial u_i^\star}{\partial x_k^t} n_k \right) d\Gamma \tag{3.2}$$

where f_i^t is the body force per unit mass, ρ^t is the mass density, p_i^t the external (classical) forces per unit area, and P_i^t an additional external (double) force per unit area. All these force densities are applied on part Γ_σ^t of boundary Γ^t.

Solving for the second gradient of displacement in (3.1) by a finite element method requires continuously-differentiable (class C1) elements when the constraint on the microkinematical gradient is strong. As an alternative to the use

of this class of elements, a field of Lagrange multipliers λ_{ij} can be introduced to weaken the constraint on ν_{ij}:

$$\int_{\Omega^t} \lambda^\star_{ij} \left(\frac{\partial u^t_i}{\partial x^t_j} - \nu^t_{ij} \right) d\Omega = 0 \tag{3.3}$$

with $\lambda^\star_{ij}$ a virtual field of Lagrange multipliers. This allows rewriting Equation (3.1) into

$$\int_{\Omega^t} \left(\sigma^t_{ij} \frac{\partial u^\star_i}{\partial x^t_k} + \Sigma^t_{ijk} \frac{\partial \nu^\star_{ij}}{\partial x^t_k} \right) d\Omega - \int_{\Omega^t} \lambda_{ij} \left(\frac{\partial u^\star_i}{\partial x^t_j} - \nu^\star_{ij} \right) d\Omega - \bar{W}^\star_e = 0 \tag{3.4}$$

For the fluid pressure, the field equations are written in terms of a fluid mass balance equation in weak form as

$$\int_{\Omega^t} \left(\dot{M}^t p^\star - m^t_i \frac{\partial p^\star}{\partial x^t_i} \right) d\Omega = \int_{\Omega^t} Q^t p^\star d\Omega - \int_{\Gamma^t} \bar{q}^t p^\star d\Gamma \tag{3.5}$$

with M^t the fluid mass in the current configuration, m^t_i the mass flow density, Q^t a sink term and $\bar{q}^t = m^t_i n^t_i$ the boundary input flux per unit area as the product of m^t_i and the boundary surface normal n^t_i.

The non-linear field equations (3.3), (3.4) and (3.5) have to hold for the boundary value problem related to a loading path that is followed for a certain time. To solve this boundary value numerically, a discretization into time steps is required, for which the solutions to the BVP are computed by a full Newton-Raphson scheme. The fields u_i and p are solved for, together with the fields ν_{ij} for regularization and λ_{ij} to provide a weakening in the constraints between u_i and ν_{ij}.

The linearization of the 3 types of field equations (3.3)-(3.5) for finding the iterative updates $\mathrm{d}u^t_i$, $\mathrm{d}\lambda^t_{ij}$, $\mathrm{d}\nu^t_{ij}$ and $\mathrm{d}p^t$ through the definition of a linear auxiliary problem is given in Collin et al. [2006]. This linearization results in a linear system of field equations to be solved in the form of a 25×25 matrix equation with $\tau 1$ referring to configuration $\Omega^{t,n-1}$after iteration $n-1$:

$$\int_{\Omega^{\tau 1}} [U^{\star,\tau 1}_{(x,y)}]^T [E^{\tau 1}][\mathrm{d}U^{\tau 1}] \mathrm{d}\Omega = -R^{\tau 1} \tag{3.6}$$

$R^{\tau 1}$ is the out-of-balance term at the last computation, which needs to be corrected for in the iteration, $[U^{\tau 1}_{(x,y)}]$ is a 25-term array, with subsequently the components of $\frac{\partial du_i}{\partial x_j}$, $du^{\tau 1}_1$, $\frac{\partial dp^{\tau 1}}{\partial x^{\tau 1}_i}$,$dp^{\tau 1}$,$\frac{\partial d\nu^{\tau 1}_{ij}}{\partial x^{\tau 1}_k}$, $d\lambda^{\tau 1}_{ij}$ and $d\nu^{\tau 1}_{ij}$. Matrix $[E^{\tau 1}]$ has the following structure:

$$[E^{t_n}] = \begin{bmatrix} C^{t_n}_{(4\times4)} + E1^{t_n}_{(4\times4)} & 0_{(4\times4)} & K^{t_n}_{hm(4\times3)} & 0_{(4\times8)} & 0_{(4\times4)} & -I_{(4\times4)} \\ G1^{t_n}_{(2\times4)} & 0_{(2\times2)} & G2^{t_n}_{(2\times3)} & 0_{(2\times8)} & 0_{(2\times4)} & 0_{(2\times4)} \\ K^{t_n}_{mh(3\times4)} & 0_{(3\times2)} & K^{t_n}_{hh(3\times3)} & 0_{(3\times8)} & 0_{(3\times4)} & 0_{(3\times4)} \\ E2^{t_n}_{(8\times4)} & 0_{(4\times4)} & 0_{(4\times4)} & D^{t_n}_{(8\times8)} & 0_{(8\times4)} & 0_{(8\times4)} \\ E3^{t_n}_{(4\times4)} & 0_{(4\times4)} & 0_{(4\times4)} & 0_{(4\times8)} & 0_{(4\times4)} & I_{(4\times4)} \\ E4^{t_n}_{(4\times4)} & 0_{(4\times4)} & 0_{(4\times4)} & 0_{(4\times8)} & -I_{(4\times4)} & 0_{(4\times4)} \end{bmatrix}$$

(3.7)

Matrices $[C^{t_n}_{(4\times4)}]$ and $[D^{t_n}_{(8\times8)}]$ are the consistent linearizations of the classical and the second gradient mechanical constitutive relations respectively. Matrix $[K_{hh}]$ is the linearization of the hydraulic constitutive behaviour, relating variations of p^M and ∇p^M to variations in $\dot{M}$ and $\vec{m}$. Matrices $[K_{hm}]$ and $[K_{mh}]$ contain the coupling between the mechanical and hydraulic systems.

The second gradient tangent stiffness matrix $[D_{(8\times8)}]$ is obtained from a consistent linearization of the second gradient constitutive behaviour at the macro level (see Section 3.1). The first order tangent stiffness matrices $[C_{(4\times4)}]$, $[K_{hh}]$, $[K_{hm}]$ and $[K_{mh}]$ are obtained by a consistent linearization of the classical constitutive behaviour, either by a numerical approximation such as a finite difference approximation or in the form of an analytical expression through the partial derivatives of the constitutive relation. To solve the linearized problem of Equation (3.6) for displacement updates $[\mathrm{d}U]$ the problem is spatially discretized using a finite element method for large strains. The 9-node elements with 4 integration points used for the discretization is given in figure 3.1.

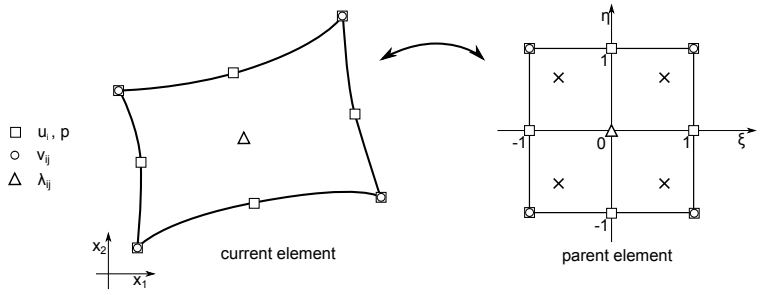

Fig. 3.1: Quadrilateral element and parent element used on the macro scale.

The numbers of nodes per element imply a quadratic shape function ϕ for u_i and p (8 nodes), a linear shape function ψ for ν_{ij} (four nodes) and λ_{ij} assumed constant over the element (one node). Using the four integration points in a finite element procedure, the field equations (3.4) and (3.5) are approximated on the element domain as a function of the column vector $[\mathrm{d}U^{\tau_1}_{node}]$ containing all variables defined on the different element nodes, using the weakened constraint of (3.3) on the second gradient of displacement. An identical discretization is done with respect to the residual $R^{\tau_1\star}_{elem}$ on the element domain [Matsushima et al., 2002, Collin et al., 2006]. The constitutive law for the second gradient model is explicitly defined on the macro level. A special case of the isotropic linear model by Mindlin [1964] is used here. This gives the relation between double stress Σ_{ijk} and double strain $\frac{\partial^2 u_l}{\partial x_m \partial x_n}$ by a single parameter D as given in Equation (3.8)

[Bésuelle et al., 2006].

$$\begin{bmatrix} \overset{\triangledown}{\Sigma}_{111} \\ \overset{\triangledown}{\Sigma}_{112} \\ \overset{\triangledown}{\Sigma}_{121} \\ \overset{\triangledown}{\Sigma}_{122} \\ \overset{\triangledown}{\Sigma}_{211} \\ \overset{\triangledown}{\Sigma}_{212} \\ \overset{\triangledown}{\Sigma}_{221} \\ \overset{\triangledown}{\Sigma}_{222} \end{bmatrix} = \begin{bmatrix} D & 0 & 0 & 0 & 0 & D/2 & D/2 & 0 \\ 0 & D/2 & D/2 & 0 & -D/2 & 0 & 0 & D/2 \\ 0 & D/2 & D/2 & 0 & -D/2 & 0 & 0 & D/2 \\ 0 & 0 & 0 & D & 0 & -D/2 & -D/2 & 0 \\ 0 & -D/2 & -D/2 & 0 & D & 0 & 0 & 0 \\ D/2 & 0 & 0 & -D/2 & 0 & D/2 & D/2 & 0 \\ D/2 & 0 & 0 & -D/2 & 0 & D/2 & D/2 & 0 \\ 0 & D/2 & D/2 & 0 & 0 & 0 & 0 & D \end{bmatrix} \begin{bmatrix} \frac{\partial \dot{\nu}_{11}}{\partial x_1} \\ \frac{\partial \dot{\nu}_{11}}{\partial x_2} \\ \frac{\partial \dot{\nu}_{12}}{\partial x_1} \\ \frac{\partial \dot{\nu}_{12}}{\partial x_2} \\ \frac{\partial \dot{\nu}_{21}}{\partial x_1} \\ \frac{\partial \dot{\nu}_{21}}{\partial x_2} \\ \frac{\partial \dot{\nu}_{22}}{\partial x_1} \\ \frac{\partial \dot{\nu}_{22}}{\partial x_2} \end{bmatrix} \tag{3.8}$$

Here $\dot{\nu}_{ij}$ is the material derivative of ν_{ij} and $\overset{\triangledown}{\Sigma}_{ijk}$ is the Jaumann double stress derivative defined as:

$$\overset{\triangledown}{\Sigma}_{ijk} = \dot{\Sigma}_{ijk} + \Sigma_{ljk}\omega_{li} + \Sigma_{ilk}\omega_{lj} + \Sigma_{ijl}\omega_{lk} \tag{3.9}$$

with ω_{ij} the spin tensor. The consistent linearization $[D_{(8\times8)}]$ defined in equation (3.7) is derived by a forward finite difference approximation based on the constitutive relation of equation (3.8).

3.2 The Frey microscale model for hydromechanical coupling

A starting point for the modelling of hydromechanical coupling at the microscale is the microscale model developed by Frey [2010], Frey et al. [2013]. This model, developed in large strain formulation, has been modified on several aspects. Before continuing with the development of the computational homogenization framework, the main characteristics of the original model are given, after which a discussion validates the proposed changes of the model.

3.2.1 The Frey-model in a large-strain formulation

The microscale model assumes the material to be composed of an assembly of deformable grains connected by cohesive interfaces. These interfaces form a network of pore channels saturated by a fluid. The fluid can percolate through the network as an effect of the pressure gradients in the interface channels (see Figure 3.2), for which the hydraulic transmissivity is controlled by the normal opening between the grains. The fluid pressure and the pressure gradient act on the grains as normal and tangential tractions. In addition, mechanical cohesive forces act over the interfaces depending on the history of the interface opening.

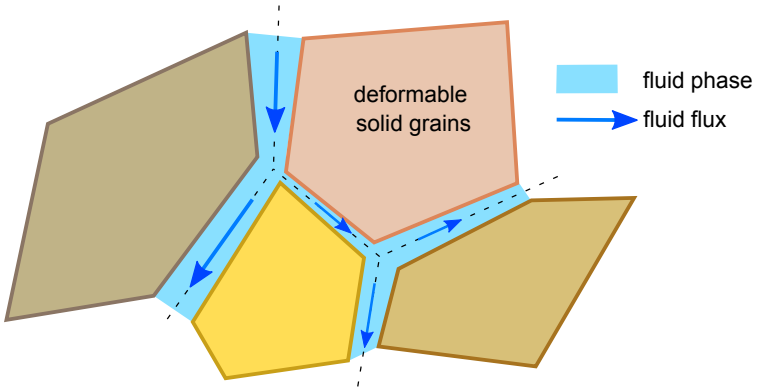

Fig. 3.2: Micromechanical model of the fluid-saturated microstructure in the Frey-model.

By assigning different properties to the solids and the cohesive interfaces, a model for the microstructure of claystone is obtained. Inclusions can be simulated by introducing large grains with high stiffness embedded in a matrix of grains to represent the clay matrix. The interfaces between the grains are therefore used to simulate the border between the inclusions and the clay matrix or the potential fractures in the clay matrix. The variation of interface cohesive parameters can be used to introduce the different types of interfaces, for example the interfaces between different inclusions or the interfaces between inclusions and clay matrix.

A hyperelastic constitutive relation provides the Cauchy stress $\boldsymbol{\sigma}$ inside the grains at a given time t as a function of the deformation, expressed in terms of the left Cauchy-Green strain tensor $\boldsymbol{b}^{0t} = \boldsymbol{F} \cdot \boldsymbol{F}^T$:

$$\sigma_{ij}^t = \frac{\mu}{J^{0t}}(b_{ij}^{0t} - \delta_{ij}) + \frac{\lambda}{J^{0t}} \ln(J^{0t})\delta_{ij} \tag{3.10}$$

with J^{0t} the Jacobian of the deformation gradient tensor $\boldsymbol{F}^t$ at time t and δ_{ij} the components of unit tensor $\boldsymbol{I}$. The material constants in this relation are the Lamé parameters λ and μ. The interfaces that separate the grains allow a finite displacement of the opposite grain boundaries. Cohesive forces between opposite sides of the interfaces are directed normally (T_n) and tangentially (T_t) to the interface orientation and are defined as a function of the history of normal and tangential relative displacement of the opposite interface boundaries Δu_n and Δu_t respectively. This means that a full decoupling between normal and tangential components in the $\vec{T}(\Delta\vec{u})$-relation is assumed. Figure 3.3 shows the model of the interface with the components of the cohesive forces, acting antisymmetrically on opposite interface boundaries

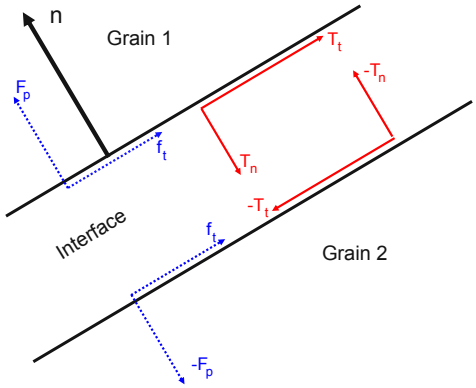

Fig. 3.3: Interface model with components of cohesive forces T_t and T_n and fluid-on-solid forces f_t and F_p. [Frey et al., 2013]

The interfaces form a network of channels allowing fluid percolation. Taking into account fluid bulk modulus k^w, the fluid density ρ^w can be expressed as:

$$\rho^w = \rho^0 \exp\left(\frac{1}{k^w}(p - p^0)\right) \tag{3.11}$$

where ρ^w is the fluid density at reference pressure p^0. The fluid mass flux ϖ in the interface as a function of the pressure gradient $\frac{dp}{ds}$ is found by an integration of the Navier-Stokes equation for laminar flow between smooth parallel plates as

$$\varpi = \rho^w \kappa \frac{dp}{ds} \tag{3.12}$$

with κ a function of the dynamic viscosity of the fluid and the normal opening of the interfaces Δu_n. The integration of Equation (3.12) over the length of an interface channel provides a solution for the mass flux between two points for a given pressure difference Δp between these points. Reduction of Stokes equation with some minor simplifying assumptions gives

$$\varpi = \left(\exp\left(\frac{1}{k^w}p^0\right)\rho^0 \int_{s^-}^{s^+} \frac{1}{\kappa(s)} ds\right)^{-1} \left(\exp\left(\frac{1}{k^w}p^+\right) - \exp\left(\frac{1}{k^w}p^-\right)\right) \tag{3.13}$$

with p^+ and p^- the fluid pressure at the extremities of the fluid channel. When a given configuration of the REV is known, the integral over κ can be solved by a Gauss quadrature, leading to an equation linear in the exponential of the fluid pressure p. Introducing λ^p as the exponential of the fluid pressure p as

$$\lambda^p = \exp\left(\frac{p}{k^w}\right) \tag{3.14}$$

and interface conductivity term ϕ as

$$\phi = \left(\exp\left(\frac{1}{k^w}p^0\right)\rho^0 \int_{s^-}^{s^+} \frac{1}{\kappa(s)} ds\right)^{-1} \tag{3.15}$$

Equation (3.13) can be rewritten in the linear form to describe the fluid mass flux in a single interface channel as:

$$\varpi = \phi(\lambda^{p^+} - \lambda^{p^-}) \tag{3.16}$$

A mass balance equation at the intersection of interfaces can be written

$$\sum \varpi = 0 \tag{3.17}$$

Periodic boundary condition $p^F = p^L + \Delta p$, where $[]^F$ are the 'follow' degrees of freedom, depending on a homologous 'lead' degree of freedom $[]^L$, is enforced through

$$\lambda^{p^F} - \lambda^{\Delta p}\lambda^{p^L} = 0 \tag{3.18}$$

where $\Delta p = \nabla^M p \cdot (\vec{x}^F - \vec{x}^L)$ is the difference between the periodic couples p^L and p^F and $\lambda^{\Delta p} = \exp\left(\frac{1}{k^w}\Delta p\right)$. The definition of a degree of freedom p at each intersection of interfaces allows writing the global system of equations in λ^p by the global assembly of (3.17) and (3.18):

$$[\Phi]\{\Lambda\} = \{0\} \tag{3.19}$$

where $[\Phi]$ is a $n \times n$ matrix and $\{\Lambda\}$ is the column vector containing the n degrees of freedom λ. One additional constraint is added by the penalization of one degree of freedom in order to obtain a well-posed system of equations from Equation (3.19);

$$\lambda^{pen} = \lambda^{\hat{p}} \tag{3.20}$$

The value of penalization is used to iteratively update the pressure profile over the REV in order to satisfy the third hydraulic boundary condition

$$\frac{1}{V^w}\int_{\Omega^w} p d\Omega = p^M \tag{3.21}$$

with Ω^w the part of domain Ω occupied by the fluid phase, which in this case is equal to the domain of the interfaces. Given a certain mechanical configuration to provide the information for κ, the fluid system is solved for this specific configuration, after which the fluid pressure and pressure gradients in the channels are used to determine the hydraulic forces F_p and f_t acting as respectively normal and tangential forces on the interface boundaries as shown in Figure 3.3. These hydraulic forces take part in the equilibrium of the mechanical system, which is solved for in a Newton-type iterative scheme (the tangent operators are only consistent to the mechanical part of the problem, whereas the equilibrium involves both mechanical and hydraulic components due to the grain boundary traction by the fluid pressure). For each iterative update of the mechanical configuration (nodal positions), the hydraulic system is solved to update the hydraulic back coupling on the grains. This staggered scheme of subsequently taking a mechanical iteration and solving the hydraulic system of equations generally leads to an efficient convergence due to the relatively low coupling from hydraulics to mechanics [Frey, 2010].

Once equilibrium is obtained for the mechanical system, the macroscopic properties are obtained from the REV by volume averaging by the following equations;

$$\boldsymbol{\sigma}^M = \frac{1}{V^{REV}} \left(\int_{\Omega^s} \boldsymbol{\sigma} d\Omega + \int_{\Omega^w} p\boldsymbol{I} d\Omega \right) \tag{3.22}$$

$$\vec{m} = \frac{1}{V^{REV}} \int_{\Gamma^+} (\vec{x}^F - \vec{x}^L) \bar{q} d\Gamma \tag{3.23}$$

$$M = \frac{1}{V^{REV}} \int_{\Omega^w} \rho^w d\Omega \tag{3.24}$$

where the solid domain Ω^s is defined as the grain domain and Ω^w as the interface element, $\bar{q}$ is the interface fluid flux to be integrated over the upper REV boundary Γ^+.

3.2.2 Proposed modifications of the Frey model

The model presented above, for which the numerical details can be found in Frey [2010] and Marinelli [2013], can provides a fully-coupled poromechanical macroscale constitutive relation when combined with a homogenization framework to provide the consistent tangent operators relating the increments in response to increments in macroscale kinematical constraints. The staggered approach of separately solving the microscale hydraulic and mechanical problems provides a computationally efficient numerical scheme to solve the coupled problem. The efficiency of this scheme is due to the relatively small coupling of the hydraulic system on the mechanical system, allowing to omit the coupling terms in the Newton-Raphson scheme for the mechanical problem.

However, for the implementation of this model in the framework of computational homogenization several difficulties arise:

- The first order computational homogenization is based on the separation of scales. This implies that the REV represents local macroscale material behaviour and a length scale at the microscale level should not be present in order to be able to correctly prescribe the periodic boundary conditions. The variation of fluid pressure over the REV violates this assumption. When the variation in fluid pressure as an effect of the pressure gradient is taken into account in the REV, an absolute REV size is required to translate the macroscale pressure gradient to a pressure difference between the homologous points on the periodic boundaries. Through the hydromechanical coupling, the choice of the REV length not only has an effect on the hydraulic response, but also on the mechanical response of the REV.

- The definition of the macroscale stress tensor as the volume average of the Cauchy stress over the deformed REV, with no mechanical stress components in the interfaces, is not compatible with the Hill-Mandel principle of macro-homogeneity, which requires the macroscopic work to be equal to the

microscopic work. A possible alternative and more consistent way of taking into account the macro homogeneity is to consider the first Piola-Kirchhoff stress for the scale transition and obtain the macroscale Cauchy stress as

$$\sigma^M = \frac{1}{V^0 \det(\boldsymbol{F})} \int_{\Omega^0} \boldsymbol{P} d\Omega \cdot \boldsymbol{F}^T \tag{3.25}$$

In addition, the application of the Gauss-Ostrogradsky (or divergence) theorem for the integral over the domain boundary is required in the computational homogenization later on;

$$\boldsymbol{P}^M = \frac{1}{V^0} \int_{\Omega^0} \boldsymbol{P} d\Omega = \frac{1}{V^0} \int_{\Gamma^0} \vec{t} \otimes \vec{x}^0 d\Gamma \tag{3.26}$$

However, this might result in a non-symmetric Cauchy stress tensors, as no requirements on the balance of moments is evaluated over the interfaces. A similar problem arises when the macro stress is evaluated by means of the boundary integral, either in the current or the reference configuration; the undefined stress state in the interfaces either give rise to non-symmetric Cauchy stress tensor or the internal grain boundaries have to be taken into account in the integral. This prevents the direct application of the model in the framework of computational homogenization.

- The consistent modelling of contact problems in large deformation formulation by the finite element method is not straightforward and might require a redistribution of the grain contacts or a least a remeshing of the contact interfaces for a proper transmission of the intergranular forces. As the purpose of this model is to provide a simple and efficient way of modelling micromechanical constituents, these contacts are modeled by interface elements, for which no remeshing or redistribution of contacts is considered. For large deformations, the contact forces acting between the different particles loose their physical meaning as contacts are no longer well-aligned. In addition to the physical meaning of these interface elements under large local displacements, the definition of the interface channel fluid volume suffers from a similar limitation as the intersections of several in interface elements needs to be taken into account. The same would apply for a possible reformulation in which a consistent interface stress state is applied.

To overcome the aforementioned problems the following conceptual modifications of the Frey model are introduced, facilitating a more consistent implementation in the framework of computational homogenization.

A first modification is to change from a large deformation formulation to small strain assumption at the microscale, through which stress tensors $\boldsymbol{P}$ and $\boldsymbol{\sigma}$ can be assumed approximately equal, as the deformation gradient tensor $\boldsymbol{F}$ is assumed to be approximately equal to identity matrix $\boldsymbol{I}$. Moreover, the macroscale stress state σ_{ij}^M is now found as

$$\sigma_{ij}^M = \frac{1}{V} \int_{\Omega} \sigma_{ij} d\Omega = \frac{1}{V} \int_{\Gamma} t_i x_j d\Gamma \tag{3.27}$$

A second modification is related to the spatial variation of the fluid pressure and density inside the REV. To be consistent in the separation of scales, the fluid pressure and density are considered to be constant over the REV. This means that the drag forces acting on the grain interfaces f_t disappear from the model and the normal hydraulic forces F_p become equal to the macroscale fluid pressure as the fluid pressure variation is small. Except the conceptual point of view, this modification has some advantages compared to the original model: First of all, the resulting hydraulic system of equations becomes linear in p instead of the exponential pressure term λ, which provides a numerically more precise formulation due to the independence of the fluid compressibility. A second advantage from numerical point of view is that at the microscale the mechanical system can be solved separate from the hydraulic system, since the hydraulic-to-mechanic couplings are a-priori known. This makes the staggered procedure of solving the hydraulic system of equations during each mechanical microscale iteration obsolete. Finally, the periodic computational homogenization can be implemented more efficiently for the new version of the model, as the new formulation of the hydromechanical coupled microscale problem is easier to differentiate for condensing into consistent tangent operators.

With the above mentioned modifications, the microscale model in the framework of first order periodic computational homogenization for hydromechanical coupling will be redeveloped in the following chapters.

CONCLUSIONS PART I: TOWARD FE^2 MODEL FOR HYDROMECHANICAL COUPLING WITH A LOCAL SECOND GRADIENT MODEL

In this part, the context of hydromechanical behaviour of claystone on multiple scales and the challenges in the description of its behaviour in excavation problems were presented. From this description, the coupling between the mesoscale of microstructure with discrete characteristics and the macroscale with a (initially) continuous behaviour is seen as an important modelling challenge and a coupling between the different scales as well as the different physical phenomena is required. To be more specific, the following phenomena are considered to be taken into account:

- The macroscale modelling of the behaviour of claystone based on the explicit description of its micromechanical constituents and their arrangement in the microstructure;
- the modelling of the hydromechanical coupling through the evolving microsctructure under deformation;
- the incorporation of the full loading history in the material behaviour;
- a natural way of introducing macroscale material anisotropy based on micromechanical observations;
- the modelling of the onset of localizations of macroscale deformation in poromechanical continuum.

For the modelling of the microstructure, a model for hydromechanical coupling on the microscale level was introduced by Frey [2010]. This model is able to take into account the hydromechanical coupling at the microscale and provides a primary way of modelling the actual mesoscopic structure of the claystone with inclusions and discrete openings between its constituents. For the modelling of localization problems in a poromechanical continuum, a poromechanical formulation for saturated porous media combined with the local second gradient model [Collin et al., 2006] was summarized as a model that can deal with the macroscale localizations and evolving relations in hydromechanical coupled constitutive relations. Computational homogenization was presented as a framework in which the modelling of microstructural processes can be used to obtain the macromechanical constitutive behaviour, which comes best into its own in a finite element squared (FE^2) modelling approach.

This work will combine these two models through the scale transition provided by a computational homogenization framework. This work is motivated by the ambition of developing a multi-scale modelling approach to take into account

the aforementioned characteristics of the behaviour of claystone. For a consistent implementation, some modifications of the model were presented. The full development of the merged models is given in the following parts.

The resulting modelling approach is summarized in Figure 3.4

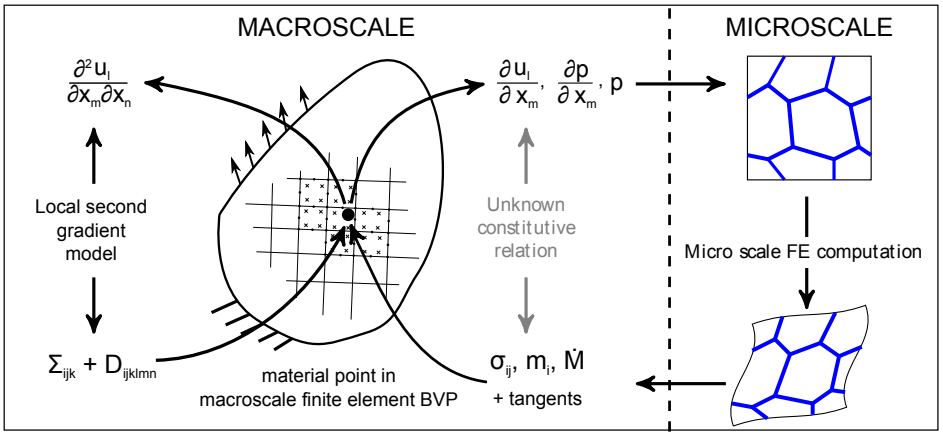

Fig. 3.4: Schematic representation of the hydromechanically coupled doublescale model with local second gradient model.

Part II

A DOUBLESCALE MODEL FOR HYDROMECHANICAL COUPLING

The starting point of the developments described in this work is the doublescale model for hydromechanical coupling by [Frey, 2010], which is based on a mechanical version developed by Bilbie [2007] and followed by the first doublescale computations by Marinelli [2013]. Several modifications of this model have been made to facilitate the implementation of computational homogenization by static condensation and to guarantee the consistency in the doublescale framework as discussed in section 3.2.2.

Chapter 5 describe the development of the microscale numerical model. With respect to the Frey model the following contributions have been made:

- The change from large strain to a small-strain large-rotation formulation
- The separation of scales for the fluid problem
- A complete reformulation of the fluid flow model
- The introduction of diffusive fluid mass transport in the grains, combined with the interface flow model

The last sections describe the homogenization procedure for obtaining the macroscale response and the tangent operators. For the mechanical part of the model, this is the application the computational homogenization available in literature [Kouznetsova et al., 2001] to the mechanical part of the microscale model. The theory is therefore not original, although the reformulation using the periodicity vector generalizes the approach to arbitrary periodic frames and is considered to be more straightforward. The developments of the extension of the computational homogenization to hydromechanical coupling for the microstructure is an original contribution, inspired on the computational homogenization of thermomechanical coupled problems by Özdemir et al. [2008a].

From an implementation point of view, the following contributions were made on the microscale ;

- a restructuring of the larger part of the code
- the implementation of the above-mentioned modifications of the model
- the complete implementation of the computational homogenization, both for mechanical and HM coupled problems and both by numerical perturbation and computational homogenization by static condensation.

4. THE PERIODIC FRAMEWORK FOR HYDROMECHANICAL COUPLED PROBLEMS

4.1 Decomposition of the microkinematics

The doublescale modelling approach distinguishes between a microscale and a macroscale. The kinematics fields on these scales are u_i^m, p^m and u_i^M, p^M respectively and are not necessarily the same; given a point $\hat{x}_i$ with a displacement $u_i^M(\hat{x})$, the microkinematics can be defined to be identical; $u_i^m(\hat{x}) = u_i^M(\hat{x})$. A Taylor expansion can be used to define the macro displacement of a point $\vec{x}$ close to $\vec{\hat{x}}$ as

$$u_i(x) = u_i(\hat{x}) + \frac{\partial u_i(\hat{x})}{\partial x_j}(x_j - \hat{x}_j) + ... \tag{4.1}$$

For points $\vec{x}$ in a macroscale continuum very close to point $\vec{\hat{x}}$, only a first order expansion is required and the higher-order terms of the expansion can be neglected. For the microkinematics, these higher order terms can not be neglected, as no continuity restriction is made to the displacement field at the micro level.

The micromechanical displacement field $u_i^m(x)$ is therefore decomposed in the macromechanical field $u_i^M(x)$ and further decomposition into microkinematical gradients [Germain, 1973]:

$$u_i^m(x) = u_i^M(\hat{x}) + \frac{\partial u_i^M(\hat{x})}{\partial x_j}x'_j + \chi_{ijk}(\hat{x})x'_j x'_k + \chi_{ijkl}(\hat{x})x'_j x'_k x'_l + ... \tag{4.2}$$

with $x'_i = x_i - \hat{x}_i$ and $\chi_{ijk}, \chi_{ijkl}, ...$ the higher order gradients of the microscale displacement fields. Rather than working with the full expansion, the higher order terms are replaced by a micromechanical fluctuation field $u_i^f(x)$, which leads to

$$u_i^m(x) = u_i^M(\hat{x}) + \frac{\partial u_i^M}{\partial x_j}x'_j + u_i^f(x) \tag{4.3}$$

This micro fluctuation field can be discontinuous (as a result of the infinite decomposition), but has to be kinematically admissible. Moreover, the requirement $u_i^m(\hat{x}) = u_i^M(\hat{x})$ has to hold for any point in the macroscopic formulation. From (4.2) it follows that this expression holds approximately, and only for $x_i - \hat{x}_i << u_i^M(\hat{x})$. In this way the requirement for separation of scales is obtained, in which the length scale of the representative elementary volume containing the microstructure with its microkinematics is much smaller than the macroscale problem.

In the same way as for the microscale displacements, the microscale pressure fields can be decomposed into a macroscale components an a microkinematical fluctuation field:

$$p^m(x) = p^M(\hat{x}) + \frac{\partial p^M(\hat{x})}{\partial x_j}x'_j + p^f \tag{4.4}$$

As a consequence of the requirement of the separation of scales, it is found that

$$\frac{\partial p^M}{\partial x_j}(x_j - \hat{x}_j) + p^f << p^M(\hat{x}) \tag{4.5}$$

4.2 REV with periodic boundary conditions

In this section, a framework for the BVP on the REV is outlined. Different types of boundary conditions can be chosen to translate the macroscale deformation, pressure and pressure gradient to the microscale, of which the three main types are;

- Dirichlet boundary conditions, where equal displacement of the boundaries is enforced to apply the macroscale deformation,
- Neumann boundary conditions, where equals traction is applied on the boundaries,
- Periodic boundary conditions, where the relative displacement between opposite boundaries is enforced and boundary traction on opposite boundaries is antisymmetric.

It is well-known that Dirichlet and Neumann boundary conditions provide an upper and lower bound solution, as they tend to respectively overestimate and underestimate the equivalent material strength when the REV is not large enough to be fully representative [Hill, 1963, Terada et al., 2000, van der Sluis et al., 2000]. The periodic boundary conditions give a results bounded by these upper and lower bounds. The convergence towards a representative response with increasing REV sample size is therefore more efficient with periodic boundary conditions. For this reason and its suitability for homogenization applications, periodic boundary conditions are adopted for transferring the macroscale deformation to the microscale REV. In this section, the framework for the REV with periodic boundary conditions is presented.

Next to the periodicity of the boundary conditions, periodicity of material can be considered [Gitman et al., 2007]. Although not strictly necessary for the application of periodic boundary conditions of the REV (see for example V.-D. Nguyen and Noels [2012] for an alternative formulation of the periodic boundary conditions), the material periodicity provides a natural accordance with the periodic boundary conditions, as periodicity of the microscopic deformation is initially obtained regardless the boundary conditions. This periodicity of the material behaviour can be lost when softening phenomena occur and the localization of deformation does not honor the periodicity of the microstructure. Numerical examples, using a REV with periodic microstructure and a microscale model very similar to the one presented in this work, were given by Bilbie et al. [2008] who showed that the response to deformation loading can become REV-dependent when softening of the material takes place and localized deformation can occur. This loss of material periodicity leads to dependency on the REV boundary conditions whenever these conditions are not enhanced to deal with this non-periodicity of deformation. In these cases the boundary conditions can become part of the material behaviour, leading to a spurious REV-size and -shape dependency.

This being noted, the aim is to develop a homogenization procedure that provides a constitutive relation for a continuous macroscale medium. This restricts the REV to representing continuous macroscale response. As a proper enhancement for fully continuous macroscale might not exist, the periodic boundary conditions are accepted as a way of enforcing the local periodicity of the microscale material behaviour. Although it provides a certain regularization of microscale localized deformation, this will have implications on the macroscale material behaviour that cannot be ignored. They will be discussed in Section 11.2.

The boundary value problem to be formulated on the REV is enforced through periodic boundary conditions under the assumption that the material can be characterized by a microstructure with a local periodicity. Local periodic media can locally be subdivided in periodic domains Ω^p enclosed by periodic boundaries Γ^p, each of which contains a single realization of each microstructural phenomenon. In the definition of a periodic representative elementary volume (REV) a section of the periodic media is chosen such that it contains n times the entire domain Ω^p. The choice of the position and shape of the frame for cutting out the REV from the locally periodic medium is arbitrary as long as the n realizations of domain Ω^p fill the domain Ω, which has to be simply connected (that is, Ω should have a single continuous boundary Γ). For the definition of the boundary value problem on the REV it is convenient to choose a periodic frame with a simple geometry, for which a rectangular frame aligned along the coordinate axes is the most straightforward. An example of a locally periodic medium with the definition of a periodic frame is given in Figure 4.1

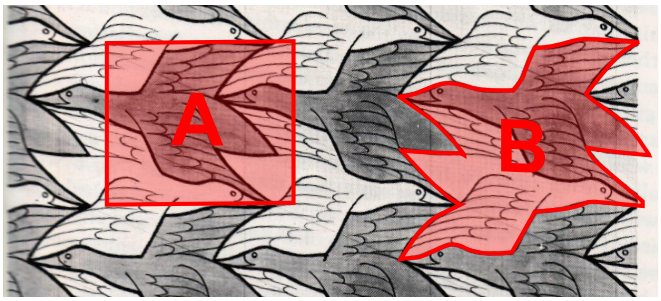

Fig. 4.1: Periodic structure by M.C. Escher (1938) with examples of a convenient periodic frame A and inconvenient periodic frame B.

For periodic frames with finite dimensions, the periodic boundary Γ enclosing Ω can be subdivided into two parts: a lead part Γ^L and a follow part Γ^F (see Figure 4.2). The kinematics of any point x^F on the follow boundary Γ^F dependents on the kinematics its homologous counterpart x^L on the lead boundary Γ^L. The distance between points x^L and x^F is defined by a vector $\vec{y}$. The vector $\vec{y}$ will be called the periodic vector and provides the mechanical part of the periodic boundary conditions for the REV through the relation between the homologous couple:

$$\vec{x}^F = \vec{x}^L + \vec{y} \tag{4.6}$$

In the reference configuration Ω^0 of rectangular $y_1 \times y_2$ periodic frames aligned along the coordinate axes, the periodic vector $\vec{y}^0$ is either $[y_1; 0]$ or $[0; y_2]$, although

the periodic frame can have any geometrically periodic shape characterized by other periodic vectors and different points on the boundary might have different periodic vectors. In a deformed configuration, the deformation of the REV is enforced through the periodic vector by the global deformation gradient tensor:

$$x_i^{F,t} = x_i^{L,t} + \frac{\partial x_i^{M,t}}{\partial x_j^0} y_j^0 \tag{4.7}$$

This expression can be written in terms of displacements as

$$u_i^{F,t} = u_i^{L,t} + \frac{\partial u_i^{M,t}}{\partial x_j^0} y_j^0 \tag{4.8}$$

Comparing this expression with (4.3) shows that the microkinematical displacement field u^f is constrained by the periodicity of the microstructure and the relative microkinematical displacement between the lead and follow is zero:

$$u_i^{f\,F} - u_i^{f\,L} = 0 \tag{4.9}$$

One point on the lead boundary is fixed to prevent rigid body motion, for which the most practical choice is to fix the lower left corner of the REV to the origin of the coordinate axis of the REV.

When these boundary conditions are enforced, equilibrium of the REV is obtained in a classical way for mechanical problems. In a formulation for virtual displacements $u_i^\star$ this writes

$$\int_\Omega \sigma_{ij} \frac{\partial u_i^\star}{\partial x_j} d\Omega + \int_\Gamma \bar{t}_i u_i^\star d\Gamma - \int_\Omega \rho f_i u_i^\star d\Omega = 0 \tag{4.10}$$

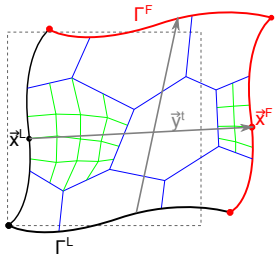

Fig. 4.2: Schematic representation of deformed REV with fixed lead •, lead REV boundary ——, follow REV boundary ——, periodic vectors ⟶, initial REV boundaries - - -, interface elements —— and solid element mesh ——.

With the REV small enough to neglect body forces f_i and the field of virtual displacements constrained by the periodic boundary conditions, this leads to the requirement of antisymmetric boundary traction $\vec{t}_i$, completing the boundary periodic boundary conditions of the REV.

$$\vec{t}^F + \vec{t}^L = 0 \tag{4.11}$$

When hydromechanical coupling is considered, the number of degrees of freedom in a point x in domain Ω^p is augmented by 1 with respect to the purely

mechanical case, as the fluid pressure p is introduced. For the pressure, the same periodicity conditions apply and the boundary condition for pressure is given by

$$p^F = p^L + \nabla^M p \cdot \vec{y} \tag{4.12}$$

considering the balance equation for fluid using the virtual pressure field $p^\star$, equilibrium of the hydraulic system in the REV is described by

$$\int_\Omega m_i \frac{\partial p^\star}{\partial x_i} d\Omega + \int_\Gamma \bar{q} p^\star d\Gamma = 0 \tag{4.13}$$

where m_j is the local fluid mass flux, $\bar{q}$ the fluid mass flux over the domain boundary $\bar{q} = m_i n_i$. Again, $p^\star$ is constrained by the periodic boundary conditions of Equation (4.12), which leads to the requirement of anti-periodic boundary flux completing the fluid pressure boundary conditions.

$$\bar{q}^F + \bar{q}^L = 0 \tag{4.14}$$

The requirement for the average pressure is easily obtained from the assumption of scale separability, which allows the assumption of equal pressure over the REV, or

$$\nabla p^M \cdot \vec{y} << p^M \tag{4.15}$$

Similar to fixing one point to a fixed pressure, the pressure degree of freedom in a single point can be fixed to the mean pressure obtain the correct REV pressure.

An additional result of the separation of scales is that transient effects can be neglected on the microscale. This means that steady state flow can be considered on the microscale.

4.3 Small strain - large rotation: stretch-rotation decomposition

Motivated by the implementation of the microscale model in a computational homogenization framework, the REV boundary value problem will be formulated under small strain assumptions. In order to obtain a small strain deformation tensor, a transformation of the macroscale deformation gradient tensor is required. The general approach of defining the small strain tensor $\boldsymbol{\varepsilon}$ as $(\nabla\vec{u} + \nabla\vec{u}^T)/2$ does not allow large rotation of the REV to be taken into account and a less strong restriction on the deformation of the REV can be obtained by taking into account large rotation of material. This can be obtained by decomposing the deformation gradient tensor into a rotation component $\boldsymbol{R}$ and a stretch component $\boldsymbol{U}$ as follows

$$F_{ij}^M = R_{ik}^M U_{kj}^{REV} \tag{4.16}$$

This decomposition introduces a rotation of the REV with respect to the coordinate system of the macroscale problem. To be able to distinguish between the macroscale coordinate system and the REV coordinate system, superscripts $[]^M$ and $[]^{REV}$ will be used respectively.

The symmetric stretch tensor $\boldsymbol{U}$ is then assumed to represent the small strain deformation gradient tensor to be enforced on the REV and the small strain tensor $\boldsymbol{\varepsilon}$ is then defined as

$$\boldsymbol{\varepsilon} = \boldsymbol{U}^{REV} - \boldsymbol{I} \tag{4.17}$$

It should be noted that in this formulation that:

$$\mathrm{diag}(\boldsymbol{\varepsilon}) \neq \mathrm{diag}(\boldsymbol{F}) - \mathbf{1} \tag{4.18}$$

As a consequence of the decomposition of the deformation gradient tensor, the pressure gradient needs to be rotated equally:

$$\frac{\partial p^M}{\partial x_i} = R_{ij}^M \frac{\partial p^{REV}}{\partial x_j} \tag{4.19}$$

Moreover, homogenized responses of the REV need to be rotated back into the configuration corresponding to the macroscale kinematics. This involves the rotation of the Cauchy stress tensor:

$$\boldsymbol{\sigma}^M = \boldsymbol{R}^M \cdot \boldsymbol{\sigma}^{REV} \cdot \boldsymbol{R}^{M^T} \tag{4.20}$$

The rotation of the macroscale fluid mass flux is done as follows:

$$\vec{m}^M = \boldsymbol{R} \cdot \vec{m}^{REV} \tag{4.21}$$

So far, only rotation-objective vectors and tensors were dealt with. For the incremental relation between the stress and strain, the rotation introduces some additional terms to be taken into account:

$$\delta\boldsymbol{F} = \delta(\boldsymbol{R} \cdot \boldsymbol{U}) = \delta\boldsymbol{R} \cdot \boldsymbol{U} + \boldsymbol{R} \cdot \delta\boldsymbol{U} \tag{4.22}$$

$$\begin{aligned} \delta\boldsymbol{\sigma}^M &= \delta(\boldsymbol{R} \cdot \boldsymbol{\sigma}^{REV} \cdot \boldsymbol{R}^T) \\ &= \delta\boldsymbol{R} \cdot \boldsymbol{\sigma}^{REV} \cdot \boldsymbol{R}^T + \boldsymbol{R} \cdot \delta\boldsymbol{\sigma}^{REV} \cdot \boldsymbol{R}^T + \boldsymbol{R} \cdot \boldsymbol{\sigma}^{REV} \cdot \delta\boldsymbol{R}^T \end{aligned} \tag{4.23}$$

The same applies for the variation of the pressure gradient and the fluid mass flux;

$$\delta\nabla p^M = \delta\boldsymbol{R} \cdot \nabla p^{REV} + \boldsymbol{R} \cdot \delta\nabla p^{REV} \tag{4.24}$$

$$\delta\vec{m}^M = \delta\boldsymbol{R} \cdot \vec{m}^{REV} + \boldsymbol{R} \cdot \delta\vec{m}^{REV} \tag{4.25}$$

These relations need to be taken into account when tangent operators, relating variations of the REV response to variations of the macroscale kinematics, are transferred from the REV with symmetric deformation to the macroscale later on.

5. THE MICROSCALE MODEL

In the model development from the original Frey model to the final microscale model, different versions have been defined. Two of these versions were extended with computational homogenization for obtaining the consistent tangent operator:

- The Frey model for hydromechanical coupling. This is the model presented in Section 3.2 with the only modification being the change from large strain formulation to small strain/large rotation formulation. This version is not consistent with respect to the separation of scales for the fluid and contains contradictions in the way the fluid pressure distribution in a periodic REV is taken into account. Nevertheless, an important part of the developments of the computational homogenization by static condensation for hydromechanical coupling was devoted to this version of the model. The developments of the computational homogenization of this version are therefore given in Appendix C, together with the introduction of the diffusive fluid transport in the grains.
- The microscale model for hydromechanical coupling. This is the 'final' version of the developments discussed in this work and contains all proposed modifications. The developments of this version are given in this chapter. Moreover, the developments in the following chapters and the results presented in Part III and Part IV all correspond to this version.

5.1 The microscale model - mechanical part

To model the material microstructure, a material is defined on the micro level that is built of solid particles separated by cohesive interfaces. To concentrate possible softening phenomena purely at the particle interfaces, the solid particles are modelled as elastic solids, although the constitutive behaviour could be extended to more complex behaviour as well.
Interfaces are defined as the open space between two grains and its opening is derived from the relative position of opposite grain boundaries (Figure 5.1). In the initial (undeformed) configuration Ω^0, the interfaces are closed, which means the upper and lower boundaries Γ^{int+} and Γ^{int-} coincide. The cohesive forces act between the opposite sides of the interfaces as a function of the history of normal and tangential relative displacements Δu_n and Δu_t between the two boundaries, which will be referred to as the interface state parameters D_n and D_t, although an arbitrary number of state parameters could be used if required. For the cohesive force vector $\vec{T}$ a normal component T_n and a tangential component T_t are defined as indicated in Figure 5.1, which gives the general relation for the

interface cohesive forces as:

$$\dot{T}_n^t = f(\Delta u_n^t, \Delta u_t^t, D_n^t, D_t^t; \Delta \dot{u}_n, \Delta \dot{u}_t) \tag{5.1}$$

$$\dot{T}_t^t = f(\Delta u_n^t, \Delta u_t^t, D_n^t, D_t^t; \Delta \dot{u}_n, \Delta \dot{u}_t) \tag{5.2}$$

These general relations need to take into account the full mechanical behaviour of the interfaces, including contact behaviour in compression (grains should not overlap) and all other forces acting between the two grains on the opposite sides of the interface as a function of (the history of) their relative displacement.

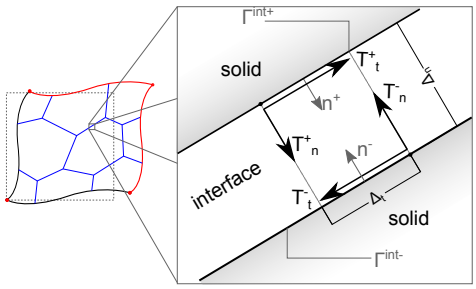

Fig. 5.1: Cohesive interface forces acting on the boundaries of the two opposite solids in a deformed configuration.

The micro mechanical model described above is used to constitute a REV with grains separated by cohesive interfaces. The field equation for the conservation of momentum of this boundary value problem is written in the weak form for any kinematically admissible virtual field of displacement $u^\star$ as follows:

$$\int_\Omega \sigma_{ij} \frac{\partial u_i^\star}{\partial x_j} d\Omega + \int_\Gamma \bar{t}_i u_i^\star d\Gamma - \int_\Omega \rho f_i u_i^\star d\Omega = 0 \tag{5.3}$$

with $\bar{t}$ the boundary traction on any boundary Γ. The boundary Γ can be divided in external boundaries Γ^{ext} (the periodic REV boundaries) and internal boundary Γ^{int} (the interfaces). The external boundary is conditioned by Equations (4.8) and (4.11) for periodicity from which follows that the integral over the external boundary is zero due to the antisymmetry of the external boundary traction ($\bar{t}_i^F u_i^{\star F} = -\bar{t}_i^L u_i^{\star L}$). With $T_i^{+/-}$ the global components of the cohesive interface forces acting on the upper/lower part of the interface and $\Gamma^{int,+}$ and $\Gamma^{int,-}$ the opposite grain boundaries, this gives

$$\int_\Omega \sigma_{ij} \frac{\partial u_i^\star}{\partial x_j} d\Omega - \int_{\Gamma_{int,+}} T_i^+ u_i^{\star +} d\Gamma - \int_{\Gamma_{int,-}} T_i^- u_i^{\star -} d\Gamma = 0 \tag{5.4}$$

Note that the definition of the upper ($^+$) and lower ($^-$) part of the interface is arbitrary as long as the corresponding outward normal vectors are consistent with the definition.

This nonlinear field equation is solved using a full Newton-Raphson iterative scheme by a linearization of the problem. After spatial discretization by a finite element method, this scheme yields solving the following linear system of equations

$$\{u^\star\}^T [K^{n_i}] \{\mathrm{d}u^{n_i}\} \approx -R^{\star n_i} \tag{5.5}$$

with $[K^{n_i}]$ the global finite element matrix and $\{\mathrm{d}u^{n_i}\}$ column vector to update the nodal positions from configuration Ω^{n_i} to $\Omega^{n_{i+1}}$.

5.1.1 Discretization of the continuum

The discretization of the field equations by the finite element are obtained as follows:

For the grains, a four-node element with 4 integration points is used for the spatial discretization. The element has a parent element in coordinate system $[\xi_1, \xi_2]$ with nodal coordinates $[\pm 1, \pm 1]$ as presented in Figure 5.2.

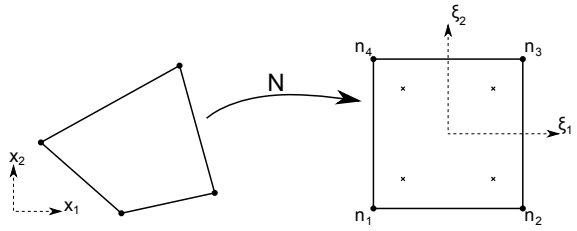

Fig. 5.2: Mechanical 4-node element with 4 integration points for modelling the mechanical behaviour of the solid grains

The nodal positions in global coordinates x_i are written as column vector $\{X_{Node}\}$ and its displacements as $\{U_{Node}\}$ with $[]^{(i)}$ the element numbering of nodes:

$$\{X_{Node}\} = \begin{Bmatrix} x_1^{(1)} \\ x_2^{(1)} \\ x_1^{(2)} \\ x_2^{(2)} \\ x_1^{(3)} \\ x_2^{(3)} \\ x_1^{(4)} \\ x_2^{(4)} \end{Bmatrix} \qquad \{U_{Node}\} = \begin{Bmatrix} u_1^{(1)} \\ u_2^{(1)} \\ u_1^{(2)} \\ u_2^{(2)} \\ u_1^{(3)} \\ u_2^{(3)} \\ u_1^{(4)} \\ u_2^{(4)} \end{Bmatrix} \tag{5.6}$$

Shape functions $N^{(i)}$ are defined for the bilinear interpolation between the nodal values as the contribution of the individual nodes (i) on the position $[\xi_1, \xi_2]$ in the parent element:

$$\begin{aligned} N^{(1)} &= \frac{1}{4}(1-\xi_1)(1-\xi_2) \\ N^{(2)} &= \frac{1}{4}(1+\xi_1)(1-\xi_2) \\ N^{(3)} &= \frac{1}{4}(1+\xi_1)(1+\xi_2) \\ N^{(4)} &= \frac{1}{4}(1-\xi_1)(1+\xi_2) \end{aligned} \tag{5.7}$$

These shape functions are used to define the strain $(\frac{\partial u_i}{\partial x_j})$ in the integration points as a function of $\{U_{Node}\}$ through defining the matrices of partial derivatives

$\frac{\partial \xi_i}{\partial x_j}$ and $\frac{\partial N^{(i)}}{\partial \xi_j}$ as $[T]$ and $[B]$:

$$[T] = \begin{bmatrix} \frac{\partial \xi_1}{\partial x_1} & \frac{\partial \xi_2}{\partial x_1} & 0 & 0 \\ \frac{\partial \xi_1}{\partial x_2} & \frac{\partial \xi_2}{\partial x_2} & 0 & 0 \\ 0 & 0 & \frac{\partial \xi_1}{\partial x_1} & \frac{\partial \xi_2}{\partial x_1} \\ 0 & 0 & \frac{\partial \xi_1}{\partial x_2} & \frac{\partial \xi_2}{\partial x_2} \end{bmatrix} \tag{5.8}$$

$$[B] = \begin{bmatrix} \frac{\partial N^{(1)}}{\partial \xi_1} & 0 & \frac{\partial N^{(2)}}{\partial \xi_1} & 0 & \frac{\partial N^{(3)}}{\partial \xi_1} & 0 & \frac{\partial N^{(4)}}{\partial \xi_1} & 0 \\ \frac{\partial N^{(1)}}{\partial \xi_2} & 0 & \frac{\partial N^{(2)}}{\partial \xi_2} & 0 & \frac{\partial N^{(3)}}{\partial \xi_2} & 0 & \frac{\partial N^{(4)}}{\partial \xi_2} & 0 \\ 0 & \frac{\partial N^{(1)}}{\partial \xi_1} & 0 & \frac{\partial N^{(2)}}{\partial \xi_1} & 0 & \frac{\partial N^{(3)}}{\partial \xi_1} & 0 & \frac{\partial N^{(4)}}{\partial \xi_1} \\ 0 & \frac{\partial N^{(1)}}{\partial \xi_2} & 0 & \frac{\partial N^{(2)}}{\partial \xi_2} & 0 & \frac{\partial N^{(3)}}{\partial \xi_2} & 0 & \frac{\partial N^{(4)}}{\partial \xi_2} \end{bmatrix} \tag{5.9}$$

The terms $\frac{\partial \xi_i}{\partial x_j}$ in $[T]$ are obtained from the inverse of the individual terms of $\{\frac{\partial x}{\partial \xi}\} = [B]\{X_{Node}\}$

$$\{\xi_{Node}\} = \begin{Bmatrix} \xi_1^{(1)} \\ \xi_2^{(1)} \\ \xi_1^{(2)} \\ \xi_2^{(2)} \\ \xi_1^{(3)} \\ \xi_2^{(3)} \\ \xi_1^{(4)} \\ \xi_2^{(4)} \end{Bmatrix} \tag{5.10}$$

The strain tensor in an integration point can be found as the function of its local coordinated ξ_i and the nodal displacements $\{U_{Node}\}$:

$$\begin{Bmatrix} \frac{\partial u_1}{\partial x_1} \\ \frac{\partial u_1}{\partial x_2} \\ \frac{\partial u_2}{\partial x_1} \\ \frac{\partial u_2}{\partial x_2} \end{Bmatrix} = [T][B]\{U_{Node}\} \tag{5.11}$$

The variation of a stress tensor $\boldsymbol{\sigma}^t$ in a certain configuration at time t can now be written as

$$\{\delta\sigma^t\} = \begin{Bmatrix} \delta\sigma_{11}^t \\ \delta\sigma_{12}^t \\ \delta\sigma_{21}^t \\ \delta\sigma_{22}^t \end{Bmatrix} = [C^t][T][B]\{\delta U_{Node}\} \tag{5.12}$$

It is now possible to write the components of the balance equation (5.4) as

$$\int_\Omega \{U_{Node}^\star\}^T [B]^T [T]^T [C^\tau][T][B]\{\delta U_{Node}\} d\Omega \tag{5.13}$$

For individual elements this can be further rewritten into

$$\{U^{\star}_{Node}\}^T \int_{\Omega^e} [E^{\tau}] d\Omega \{\delta U_{Node}\} \tag{5.14}$$

with

$$[E]^{\tau} = [B]^T [T]^T [C^{\tau}][T][B] \tag{5.15}$$

The column vector of residual forces on the nodes of the solid elements is given by;

$$\{f^e\} = \int_{\Omega^e} [B]^T [T]^T [\sigma] d\Omega = \int_{\omega^{pe}} [B]^T [T]^T [\sigma] \det\left(J^{\Omega\omega}\right) d\omega \tag{5.16}$$

with ω^{pe} the parent element domain, $\{f^e\}$ the element nodal force column vector:

$$\{f^e\} = \begin{Bmatrix} f_1^{(1)} \\ f_2^{(1)} \\ f_1^{(2)} \\ f_2^{(2)} \\ f_1^{(3)} \\ f_2^{(3)} \\ f_1^{(4)} \\ f_2^{(4)} \end{Bmatrix} \tag{5.17}$$

and $J^{\Omega\omega}$ the Jacobian of the transformation from the parent element to the global element

$$J^{\Omega\omega} = \begin{bmatrix} \frac{\partial x_1}{\partial \xi_1} & \frac{\partial x_1}{\partial \xi_2} \\ \frac{\partial x_2}{\partial \xi_1} & \frac{\partial x_2}{\partial \xi_2} \end{bmatrix} \tag{5.18}$$

The stiffness matrix relating the variation of nodal displacement to the variation of these nodal forces can be found as:

$$[k^e] = \int_{\Omega^e} [E^t] d\Omega = \int_{\omega^{pe}} [E^t] \det(J^{\Omega\omega}) d\omega \tag{5.19}$$

Replacing the integrals of (5.16) and (5.19) over the element by a numerical integration, the residual nodal forces and stiffness matrix are obtained as:

$$[f^e] = \sum_{i=1}^{npi} \sum_{j=1}^{npi} [B(\xi_1^i, \xi_2^j)]^T [T(\xi_1^i, \xi_2^j)]^T [\sigma(\xi_1^i, \xi_2^j)] \det\left(J^{\Omega\omega}(\xi_1^i, \xi_2^j)\right) W^i W^j \tag{5.20}$$

$$[k^e] = \sum_{i=1}^{npi} \sum_{j=1}^{npi} [E(\xi_1^i, \xi_2^j)] \det(J^{\Omega\omega}) W^i W^j \tag{5.21}$$

with W^i the weights of the Gauss quadrature, depending on the type of element. $W^i = 1$ in case of the element with 4 integration points.

5.1.2 Discretization of the interfaces

For the interfaces a four node element with 2 integration points is used (see Figure 5.3). The nodes of the parent elements have coordinates $[\xi_1, \xi_2] = [\pm 1, 0]$:

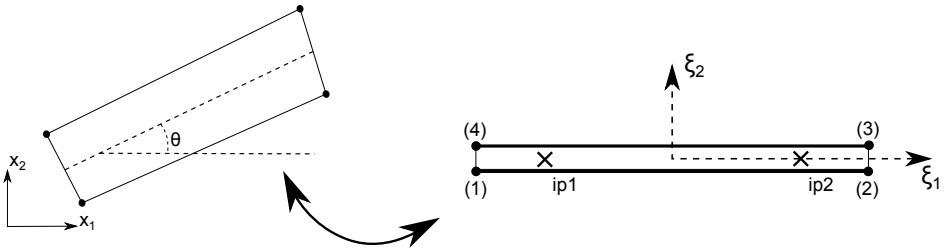

Fig. 5.3: Mechanical part of the interface element with parent element in local coordinates.

For the four nodes of the elements $[X_{Node}]$ and $[U_{Node}]$ can be used in the same way as for the quadrilateral grain element. The shape functions for the interface elements $N^{(i)}$ are different, because the parent element has only one dimension ξ_1. ξ_2 merely serves as the orientation normal to the interface element and for any point in the interface element $\xi_2 = 0$:

$$\begin{aligned} N^{(1)} &= \frac{1}{4}(1-\xi_1) \\ N^{(2)} &= \frac{1}{4}(1+\xi_1) \\ N^{(3)} &= \frac{1}{4}(1+\xi_1) \\ N^{(4)} &= \frac{1}{4}(1-\xi_1) \end{aligned} \tag{5.22}$$

Rather than defining a strain in the integration points, the relative opening of the interface Δu_t and Δu_n is required. This means that $[T^I]$ and $[B^I]$ can be defined as:

$$[B^I] = \begin{bmatrix} -N^{(1)} & 0 & -N^{(2)} & 0 & N^{(3)} & 0 & N^{(4)} & 0 \\ 0 & -N^{(1)} & 0 & -N^{(2)} & 0 & N^{(3)} & 0 & N^{(4)} \end{bmatrix} \tag{5.23}$$

$$[T^I] = \begin{bmatrix} \frac{\partial x_t}{\partial \xi_1} & 0 \\ 0 & \frac{\partial x_n}{\partial \xi_2} \end{bmatrix} \begin{bmatrix} \frac{\partial \xi_1}{\partial x_1} & \frac{\partial \xi_1}{\partial x_2} \\ \frac{\partial \xi_2}{\partial x_1} & \frac{\partial \xi_2}{\partial x_2} \end{bmatrix} = \begin{bmatrix} \cos(\theta) & \sin(\theta) \\ -\sin(\theta) & \cos(\theta) \end{bmatrix} \tag{5.24}$$

with θ the orientation of the interface with respect to the global horizontal axis. This leads to

$$\begin{Bmatrix} \Delta u_t \\ \Delta u_n \end{Bmatrix} = [T^I][B^I]\{U_{Node}\} \tag{5.25}$$

and for a consistent linearization $[C^I]$ of the interface cohesive forces defined as

$$\begin{Bmatrix} \delta T_t \\ \delta T_n \end{Bmatrix} = \begin{bmatrix} C^I_{tt} & C^I_{tn} \\ C^I_{nt} & C^I_{nn} \end{bmatrix} \begin{Bmatrix} \delta \Delta u_t \\ \delta \Delta u_n \end{Bmatrix} = \left[C^I\right][T^I][B^I]\{\delta U_{Node}\} \tag{5.26}$$

It is now possible to write the last 2 components of the balance equation (5.4) as

$$\int_{\Gamma} \{U^{\star}_{Node}\}^T [B^I]^T [T^I]^T [C^{I^\tau}][T^I][B^I]\{\delta U_{Node}\} d\Gamma \tag{5.27}$$

For individual elements this can be further rewritten into

$$\{U^{\star}_{Node}\}^T \int_{\Gamma^e} [E^{I^\tau}] d\Omega \{\delta U_{Node}\} \tag{5.28}$$

with

$$[E^I]^\tau = [B^I]^T [T^I]^T [C^{I^\tau}][T^I][B^I] \tag{5.29}$$

The column vector of residual forces on the nodes of the interface elements is given by;

$$\{f^{ie}\} = \int_{\Gamma^{ie}} [B^I]^T [T^I]^T [T^\tau] d\Gamma = \int_{\gamma^{ipe}} [B]^T [T]^T [t^\tau] J^{\Gamma\gamma} d\gamma \tag{5.30}$$

with γ^{ipe} the interface parent element domain, $\{f^{ie}\}$ the interface element nodal forces and $J^{\Gamma\gamma}$ the Jacobian of the transformation from the parent element to the global element

$$J^{\Gamma\gamma} = \frac{\partial s}{\partial \xi_1} \tag{5.31}$$

and s the length along the interface element in the global coordinate system. The stiffness matrix relating the variation of nodal displacement to the variation of these nodal forces can be found as:

$$[k^{ie}] = \int_{\Gamma^{ie}} [E^{I^\tau}] d\Gamma = \int_{\gamma^{ipe}} [E^{I^\tau}] J^{\Gamma\gamma} d\gamma \tag{5.32}$$

Replacing the integrals of (5.30) and (5.32) over the element by a numerical integration, the residual nodal forces and stiffness matrix are obtained as:

$$\{f^{ie}\} = \sum_{i=1}^{npi} [B^I(\xi_1^i)]^T [T^I(\xi_1^i)]^T [t^\tau(\xi_1^i)] J^{\Gamma\gamma}(\xi_1^i)) W^i \tag{5.33}$$

$$[k^{ie}] = \sum_{i=1}^{npi} [E^{I^t}(\xi_1^i)] J^{\Gamma\gamma}) W^i \tag{5.34}$$

with W^i the weights of the Gauss quadrature, depending on the type of element. $W^i = 1$ in case of the interface element with 2 integration points.

5.1.3 Global assembly

The global stiffness matrix $[K]$ yields the incremental relation between the column vector of nodal displacement components $\{u\}$ and nodal force components $\{f\}$:

$$[K]\{\delta u\} = \{\delta f\} \tag{5.35}$$

This global system of equations is obtained by an assembly of the element stiffness matrices $[k^e]$ and $[k^{ie}]$ and the column vectors of nodal element forces $\{f^e\}$ and $\{f^{ie}\}$. Periodic boundary conditions are enforced by penalization of nodal displacement in Equation (5.35).

5.2 Hydromechanical coupling: the channel flow model

When fluid pressure is taken into account, the fluid pressure in the interfaces acts normally on the grain boundaries. This introduces an additional force term f_n (the global equivalent of to the nodal balance equation. Because of the stationarity of the microscale problem these hydraulic pressure forces only depend on the macroscale fluid pressure. Due to the separation of scales between micro and macro, the spatial variation of the fluid pressure has not to be taken into account for solving the microscale problem. Nevertheless, the fluid pressures acting on the grain boundaries are introduced as an additional (constant) nodal force in the nodal balance equation for obtaining the nodal out-of-balance forces, since these fluid pressures are active in the mechanical equilibrium form the hydraulics-to-mechanics coupling.

The interfaces between the grains form a pore channel network and provide a flow paths for fluid transport between the grains. The hydraulic transmissivity of a channel is a function of the dynamic viscosity of the constitutive relation of the fluid and the shape of the channel through which the fluid is percolating. The variable for the coupling from the mechanical to the hydraulic system is the normal openings of the interfaces and (if required) its history. Assumptions on the shape of the interface channels as a function of the relative openings and the associated flow regime determined by the pressure or the pressure gradient allows the definition of a hydraulic transmissivity κ:

$$\kappa = \kappa(\Delta u_n, \Delta u_t, p^M, \nabla p^M) \tag{5.36}$$

In this work, the assumption on the interface geometry will be that of two closely-space parallel plates, for which a hydraulic aperture Δu_h is defined as a function of the normal opening of the interface Δu_n. This hydraulic opening allows the translation from Δu_n which is relative to the REV size (as a length scale with undefined unit) and can be slightly negative, to a hydraulic non-negative equivalent opening with a physical dimension in order to derive the fluid transport properties of the interface channel.

As introduced in Section 3.2.2, the separation of scales validates the assumption of fluid incompressibility at the microscale level, which allows modelling of the fluid flow in the interfaces starting from the Navier-Stokes equations for incompressible flow;

$$\rho^w \left(\frac{\partial v_i}{\partial t} + v_j \frac{\partial v_i}{\partial x_j} \right) = -\frac{\partial p}{\partial x_i} + \mu \frac{\partial^2 v_i}{\partial x_j \partial x_j} + f_i \tag{5.37}$$

Only small interface openings with low pressure gradients are considered in the domain of application of the model. It is therefore reasonable to assume laminar flow conditions. The microscale problem is solved under steady state conditions, which has the following consequences for the fluid flow velocity $\vec{v}$

$$\frac{\partial v_i}{\partial x_i} = 0 \qquad \text{(fluid incompressibility)} \tag{5.38}$$

$$\frac{\partial v_i}{\partial t} = 0 \qquad \text{(steady state)} \tag{5.39}$$

$$v_j \frac{\partial v_i}{\partial x_j} = 0 \qquad \text{(laminar flow)} \tag{5.40}$$

When no body forces are considered, this allows reducing Equation (5.37) into

$$\frac{\partial^2 v_i}{\partial x_j \partial x_j} = \frac{1}{\mu} \frac{\partial p}{\partial x_i} \tag{5.41}$$

Given a channel along the x_1-axis with hydraulic opening Δu_h (Figure 5.4), solving for boundary conditions $v(x_2 = \pm \Delta u_h/2) = 0$ and $\partial p/\partial x_2 = 0$ gives

$$v_1(x_2) = -\frac{1}{2\mu} \left(\frac{{\Delta u_h}^2}{4} - {x_2}^2 \right) \frac{dp}{dx_1} \tag{5.42}$$

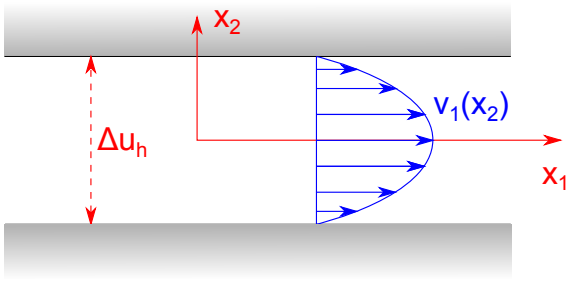

Fig. 5.4: Laminar fluid flow profile in an interface along the x_1-axis with hydraulic opening Δu_h

The integration of the mass flux $\rho^w \vec{v}$ over the cross-section of the interface gives the interface fluid mass flux ϖ as the following cubic function of the hydraulic opening Δu_h:

$$\varpi = \int_{-\frac{1}{2}\Delta u_h}^{\frac{1}{2}\Delta u_h} \rho^w v_1 dx_2 = -\rho^w \frac{{\Delta u_h}^3}{12\mu} \frac{\partial p}{\partial x_1} = -\rho^w \kappa \frac{dp}{ds} \tag{5.43}$$

s is the distance along the channel, to generalize the expression from the example of a channel along the x_1-axis to the case of an arbitrary interface orientation.

With the local fluid mass flux in an interface channel defined as a function of hydraulic transmissivity κ and the fluid density ρ^w, the pressure gradient can be integrated over a channel section. Repeating the scale separability (i.e. the very small spatial variation of fluid density with respect to the REV size, validating the local assumption of the REV with respect to fluid density gradient), the fluid pressure variation in the REV will have a negligible effect on the fluid density ρ^w which thus can be taken constant over the REV and becomes directly dependent on the REV average fluid pressure $\bar{p} = p^M$;

$$\rho^w = \rho_0^w \exp\left(\frac{\bar{p} - p_0}{k^w}\right) \tag{5.44}$$

with ρ_0^w the fluid density at ambient pressure p_0. This gives a relation between the pressure gradient along the channel and the channel mass flux ϖ;

$$\frac{dp}{ds} = -\frac{1}{\kappa(s)} \frac{1}{\rho_0^w \exp\left(\frac{\bar{p}-p_0}{k^w}\right)} \varpi \tag{5.45}$$

with s the position in the (1-dimensional) channel. The notion of steady state flow at the micro scale provides the required conservation of fluid mass in the channels, which means that ϖ is constant over the length of a channel. This allows the integration of (5.45) over a channel between locations s^i and s^j as follows:

$$p(s^j) - p(s^i) = \int_{s^i}^{s^j} \frac{1}{\kappa(s)} ds \frac{1}{\rho_0^w \exp\left(\frac{\bar{p}-p_0}{k^w}\right)} \bar{\omega} \tag{5.46}$$

or

$$\varpi^l = \rho^w \phi^l \left(p(s^j) - p(s^i)\right) \tag{5.47}$$

were ϕ^l is a hydraulic transmissivity term for channel l at given fluid density, linearly relating the channel fluid mass flux ϖ^l to the pressure difference;

$$\phi^l = \rho^w \left(\int_{s^i}^{s^j} \frac{1}{\kappa(s)} ds \right)^{-1} \tag{5.48}$$

Given the pressures at the end and the beginning of a channel section and the REV fluid density, the fluid flow in individual channels is completely described by (5.47). In order to solve for this, the fluid coupling term κ in equation (5.48) need to be integrated over the channel section. Discretization of the channel by means of one-dimensional finite elements allows the integration by means of a Gauss quadrature. In the interface elements introduced for the mechanical part of the model in 5.1, an equivalent one-dimensional hydraulic element with two integration points is introduced (Figure 5.5).

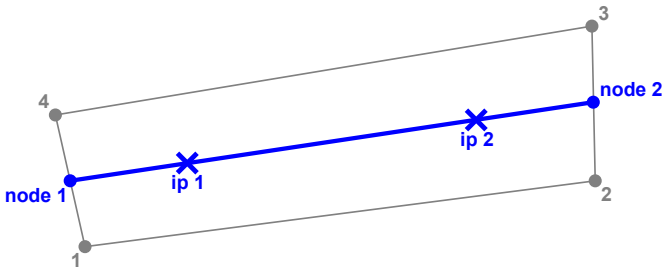

Fig. 5.5: Hydraulic interface element (blue) with two integration points in its equivalent mechanical interface element (gray).

The pore channel network can be discretized by means of these hydraulic elements, resulting in a pore network with a degree of freedom at each interface node defined at the channel intersection point. A schematic example of such a network is given in Figure 5.6.

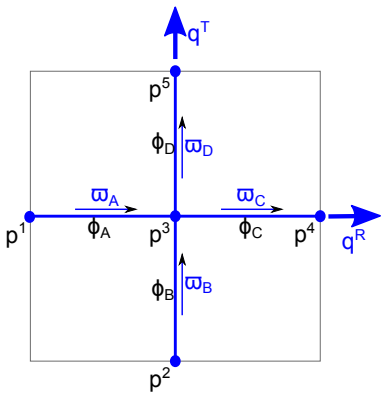

Fig. 5.6: Example mesh of a unit-length REV for the example of hydraulic system with 5 hydraulic degrees of freedom.

With the fluid mass flux over individual interface elements defined, the mass balance equations in the intersection points of the channels are written for all channels l connected to this intersection, thereby taking into account the homologous connectivity of lead and follow node couples over the periodic boundaries:

$$\sum_{l} \varpi_{(i)}^{l} = 0 \tag{5.49}$$

This nodal mass balance provides an equation for each independent degree of freedom p^i. The additional equations needed to obtain a $n \times n$ system of equations to solve the REV boundary value problem of n degrees of freedom are provided by the periodic boundary conditions:

$$p^F = p^L + \nabla p \cdot \vec{y} \tag{5.50}$$

A penalization of one of the nodal pressures to prevent the global variation of the fluid pressure (the fluid pressure equivalent of rigid body movement in case

of displacements) gives a well-posed system of equations in the form of Equation (5.51). As the pressure over the REV can be considered constant, the penalization pressure $\bar{p}$ can be taken equal to the macroscale pressure p^M. The matrix $[\Phi]$ is the global assembly of nodal mass conservation (5.49) and the constraints of the periodicity (5.50).

$$[\Phi]\{p\} = \{R\} \tag{5.51}$$

The n terms in column vector $\{R\}$ are the penalization pressure $\bar{p}$ (for one of the independent degrees of freedom), 0 (for all other independent degrees of freedom) or the periodic pressure difference $\nabla p \cdot \vec{y}$ (for all follow degrees of freedom p^F). If needed, the individual equations assembled in (5.51) can be multiplied by a penalization term to avoid ill-posed system of equations.

For the microstructure in Figure 5.6 this would give the following system of equations:

$$\begin{bmatrix} \phi_A & 0 & -\phi_A - \phi_C & \phi_c & 0 \\ 0 & \phi_B + c_2 & -\phi_B - \phi_D & 0 & \phi_D \\ -\phi_A & -\phi_B & \phi_A + \phi_B + \phi_C + \phi_D & -\phi_C & -\phi_D \\ -c_1 & 0 & 0 & c_1 & 0 \\ 0 & -c_1 & 0 & 0 & c_1 \end{bmatrix} \begin{Bmatrix} p_1 \\ p_2 \\ p_3 \\ p_4 \\ p_5 \end{Bmatrix} = \begin{Bmatrix} 0 \\ c_2\bar{p} \\ 0 \\ c_1\Delta p_1 \\ c_1\Delta p_2 \end{Bmatrix} \tag{5.52}$$

with c_1 and c_2 the penalization terms for the pore pressure and pore pressure gradient respectively. Solving this system of equations provides the pore pressure distribution from which the local fluid fluxes can be recomputed using Equation (5.47).

An alternative approach for solving the REV hydraulic boundary value problem is to follow the approach of the computational homogenization that will be used in the next chapter. This approach consists of writing the reduced system of equations; when the homologous connectivity is initially not taken into account, Equation (5.49) provides n mass balance equations for all n fluid degrees of freedom, leading to the system of equations:

$$[G]\left\{p\right\} = \left\{\Sigma\varpi\right\}. \tag{5.53}$$

$\Sigma\varpi$ indicates the mass balance in the interface hydraulic nodes as a summation of the contributions of fluid mass fluxes ϖ in the elements connected to the interface hydraulic node on which degree of freedom p is defined.

In case of the example REV in Figure 5.6 , this gives;

$$\begin{bmatrix} \phi_A & 0 & -\phi_A & 0 & 0 \\ 0 & \phi_B + 1 & -\phi_B & 0 & 0 \\ -\phi_A & -\phi_B & \phi_A + \phi_B + \phi_C + \phi_D & -\phi_C & -\phi_D \\ 0 & 0 & -\phi_C & \phi_C & 0 \\ 0 & 0 & -\phi_D & 0 & \phi_D \end{bmatrix} \begin{Bmatrix} p_{(1)} \\ p_{(2)} \\ p_{(3)} \\ p_{(4)} \\ p_{(5)} \end{Bmatrix} = \begin{Bmatrix} \Sigma\varpi_{(1)} \\ \Sigma\varpi_{(2)} + \hat{p} \\ \Sigma\varpi_{(3)} \\ \Sigma\varpi_{(4)} \\ \Sigma\varpi_{(5)} \end{Bmatrix} \tag{5.54}$$

replacing the sum of the interface mass flux towards a node $\sum \varpi$ by the nodal fluid balance q, the periodic boundary conditions for fluid fluxes is written as

$$\Sigma\varpi^F + \Sigma\varpi^L = q^F + q^L = 0 \tag{5.55}$$

System of equations (5.53) can be extended with the macroscale gradient of pressure. This gives the following extended system of equations:

$$\begin{bmatrix} 0_{(2\times 2)} & 0_{(2\times m)} \\ 0_{(m\times 2)} & G_{(m\times m)} \end{bmatrix} \begin{Bmatrix} \nabla p \\ p_{(m)} \end{Bmatrix} = \begin{Bmatrix} 0_{(2)} \\ q_{(m)} \end{Bmatrix} \tag{5.56}$$

where m is the number of fluid pressure degrees of freedom in the interface channel network. Two additional equations are required to provide dual terms for ∇p for which the flux on the follow boundary ϖ^F can be used, expressed as the macroscale mass fluid flux:

$$m_i^{REV} = \frac{1}{V^{REV}} \sum_{\Gamma^F} q^F y_i \tag{5.57}$$

with q^F the residual of the mass balance in the hydraulic interface nodes on the follow boundary. Adding these constraints to the extended system of equations (which is simply done by a summation of the equations of degrees of freedom q^F) provides a first intermediate system of equations:

$$\begin{bmatrix} 0_{(2\times 2)} & G1_{(2\times m)} \\ 0_{(m\times 2)} & G1_{(m\times m)} \end{bmatrix} \begin{Bmatrix} \nabla p \\ p_{(n)} \end{Bmatrix} = \begin{Bmatrix} m_{(2)}^{REV} \\ q_{(n)} \end{Bmatrix} \tag{5.58}$$

This system of equations is then reduced by eliminating the dependent degrees of freedom and their static duals by means of the periodic boundary conditions (5.50) and (5.55), which can be repeated here as:

$$p^F = p^L + \nabla p \cdot \vec{y} \qquad (5.50) \qquad (5.59)$$

and

$$q^F + q^L = 0 \qquad (5.55) \qquad (5.60)$$

First, the elimination of the follow degrees of freedom is obtained by transferring their corresponding columns to those of their leads and the macro pressure gradient. This leads to the second intermediate system of equations:

$$\begin{bmatrix} G2_{(2\times 2} & G2_{2\times m^i} \\ G2_{(m\times 2} & G2_{m\times m^i} \end{bmatrix} \begin{Bmatrix} \nabla p \\ p_{(m^i)} \end{Bmatrix} = \begin{Bmatrix} m_{(2)}^{REV} \\ q_{(n)} \end{Bmatrix} \tag{5.61}$$

with m^i the number of independent pressure degrees of freedom, which is equal to the number of nodes not on the follow boundary. The elimination of the dependent mass fluxes q^F by means of (5.60), which is simply the addition of the equations for q^F to those of q^L, gives the final reduced system of equations:

$$\begin{bmatrix} G_{(2\times 2)}^{\star pp} & G_{(2\times m^i)}^{\star pi} \\ G_{(m^i\times 2)}^{\star ip} & G_{(m^i\times m^i)}^{\star ii} \end{bmatrix} \begin{Bmatrix} \nabla p_{(2)} \\ p_{(m^i)} \end{Bmatrix} = \begin{Bmatrix} m_{(2)} \\ 0_{(m^i)} \end{Bmatrix} \tag{5.62}$$

This system is singular, as the average pressure has not been defined and a penalization is required to be able to solve the system of equations. This is done by penalizing one of the independent fluid pressures to the macroscale fluid pressure $\bar{p} = p^M$. Because the main interest here is solving for the macroscale hydraulic behaviour and not the microscale local fluid pressures fluctuation field p^f, the

choice of the penalization pressure $\hat{p}$ for the penalization is arbitrary and it is convenient to take $\hat{p} = 0$.

For obtaining the relation between the macroscale fluid pressure gradient $\nabla^{REV} p$ and the macroscale flux m_i^{REV} the independent degrees of freedom p^i are reduced from the system by static condensation to find:

$$[K^\star]\{\nabla p\} = \{m\}, \qquad [K^\star] = [G^{\star pp}] - [G^{\star pi}][G^{\star ii}]^{-1}[G^{\star ip}] \tag{5.63}$$

with $[K^\star]$ a 2×2 matrix, $\{\nabla p\}$ the macroscale pressure gradient and $\{m\}$ the homogenized fluid mass flux. Because $\boldsymbol{K}^\star$ is only dependent on nodal coordinates $\vec{x}$ and average pressure $\bar{p} = p^M$ (the fluid pressure fluctuation has been eliminated from the equation), the variational relation is directly found as

$$\boldsymbol{K}^\star \cdot \delta \nabla p^M = \delta \vec{m} \tag{5.64}$$

which makes perturbation or additional computational homogenization for a variational formulation obsolete. Finally, the permeability tensor is given as

$$\boldsymbol{k}^{REV} = -\frac{1}{\rho\mu} \boldsymbol{K}^\star \tag{5.65}$$

The permeability $\boldsymbol{k}$ as a second order tensor is now obtained purely from the microstructure configuration defined by the micromechanical nodal positions $\{\vec{x}\}$ and is a local material property. Darcian flow is obtained as a result, in contrast with the Frey microsacle model for hydromechanical coupling in which the fluid flow is non-Darcian as an effect of the variation of fluid density within the REV (see for more details Section 3.2 and Frey [2010]). Note that the macroscale rotation of the REV needs to be taken into account in order to distinguish between $\boldsymbol{k}^{REV}$ and $\boldsymbol{k}^M$.

Unlike the purely mechanical problem, the REV for hydromechanical coupled problems requires the definition of a length scale related to the opening of the interfaces to obtain a physically meaningful permeability tensor that can be used on the macroscale, as the hydraulic interface aperture has to provide a physical dimension for the permeability. This size introduction can be done by assigning explicit REV dimensions (which gives Δu_n) a physical dimension), or by an artificial translation from dimensionless normal interface openings Δu_n to a hydraulic interface opening Δu_h with a physical dimension. Moreover, to guarantee well-posed systems of equations (5.52) and (5.54), a minimum hydraulic transmissivity to each node is required so that $\phi \neq 0$. Both requirements of a physical dimension of Δu_h and $\Delta u_h > 0$ are obtained by defining the hydraulic opening Δu_h as follows:

$$\Delta u_h = \max\left(\Delta u_h^{min}, \Delta u_h^0 + a_h \Delta u_n\right) \tag{5.66}$$

Parameters Δu_h^{min}, Δu_h^0 and a_h all have a length scales (in $[m]$) and can be used to define the translation from a unitless mechanical normal opening to a physical hydraulic opening. The resulting dependency on the normal mechanical interface opening is given in Figure 5.7.

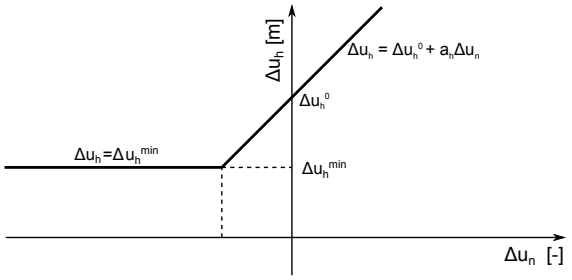

Fig. 5.7: Relation between normal mechanical interface opening Δu_n $[-]$ and hydraulic equivalent opening Δu_h $[m]$.

5.3 Hydromechanical coupling with diffusive flow in the grain

The hydraulic model presented in Section 5.2 has a macroscale initial permeability defined by the minimum interface opening and fluid transport is only taking place in the grain interfaces. As the purpose of the model is to capture the behaviour of claystone, with a clay matrix material through which fluid transport has a diffusive character, the hydraulic model might not represent the correct physical phenomena. For this reason, the hydraulic model is extended in this section to take into account diffusive flow in the grains, such that it can be used to simulate the diffusive flow in the clay matrix.

Within the presented framework of doublescale modelling, different approaches can be followed for the introduction of diffusive fluid transport phenomena in the grains. In order not to intervene with the steady-state formulation of the scale transition, transient formulations are not applicable and only steady-state formulations can be applied. Apart from this a full poromechanical approach could be followed for the modelling of the HM-coupled behaviour of individual grains under microscale steady-state conditions, but as a first extension of the existing model towards diffusive flow, some restrictions are made to maintain the general structure of the numerical formulation of the microscale problem. The concept of the diffusive flow introduced in the grains can be characterized by the following restrictions:

- Transient effects are, in line with the steady-state formulation of the microscale model, not considered in the diffusive flow. This implies that the diffusive flow does not introduce a double porosity effect as it would require the definition of different timescales in the microscale model
- No coupling between the deformation and the diffusive flow model are considered; permeability and pore volume are considered constant in the grains and fluid pressure in the grains does not effect the deformation of the grains.
- The microkinematical fluctuation field p^f is considered continuous over the full REV domain. This means that all grains are considered permeable and the fluid pressure is equal on both sides of the grain interface.
- Hydromechanical coupling is not taken into account in the diffusive part of the model; only fluid flow and (time-independent) fluid mass storage in the grains are considered. The variation of the fluid density in the diffusive part

is (in the same way as for the interfaces) due to the macroscale variation of pore pressure.

These restrictions lead to a complete decoupling of the deformation and the fluid flow in the grains, which is favorable for the application of computational homogenization by static condensation.

As presented in 5.2 a minimum hydraulic interface opening is required in the interface flow model to guarantee the connectivity between all degrees of freedom in a general way. With the introduction of diffusive flow in the grains, the connectivity can be obtained through the grains as well and a minimum interface opening is no longer needed. However, to maintain the generality of well-connected degrees of freedom, this requires a minimum permeability of all grains and impermeable inclusions must be modelled as grains with a low permeability with respect to the other grains. Moreover, the definition of a permeability for all grains allows using the same finite element mesh for the mechanical and hydraulic parts of the model. In the following developments, all grains are considered to have a minimum permeability to constitute a well-posed system of equations.

The diffusive flow in the grains has to interact with the pore channel flow in the interfaces. This interaction takes place at the grain boundaries for which the channel flow model prescribes equal pressure at opposite sides of the interface element. The linearity of the combined fluid problem allows addressing the diffusive flow problem separately from the interface flow problem. This will be done by deriving an expression relating the pore fluid pressure on the grain boundaries to the grain boundary residual fluxes related to the diffusive flow in the grains. Once this expression is derived, it can be merged with the system of equations of the channel flow model do obtain the combined mass balance equations.

5.3.1 The microscale model for diffusive flow in the grains

A microscopic permeability tensor $\boldsymbol{k}^m$ is introduced to describe the microscale permeability of the grain material:

$$\boldsymbol{k} = \begin{bmatrix} k_{11} & k_{12} \\ k_{12} & k_{22} \end{bmatrix} \tag{5.67}$$

This leads to a mass flux m_i:

$$m_i = -\rho^w \frac{k_{ij}}{\mu} \frac{\partial p}{\partial x_j} \tag{5.68}$$

with μ the fluid phase dynamic viscosity and $\frac{\partial p}{\partial x_j}$ the local pressure gradient. Starting from the conservation of mass using a virtual work formulation in steady-state conditions

$$\int_\Omega \frac{\partial p^*}{\partial x_i} m_i d\Omega - \int_\Gamma p^\star \bar{q} d\Gamma = 0 \tag{5.69}$$

where $\bar{q} = m_i n_i$ is the domain boundary mass flux along outward boundary vector $\vec{n}$. Ω is here an arbitrary domain enclosed by domain boundary Γ. As we consider an arbitrary configuration $\tau 1$ during the Newton-Raphson iteration, equilibrium has not been obtained and a residual $R^{\tau 1}$ will be present;

$$\int_\Omega \frac{\partial p^*}{\partial x_i} m_i^{\tau 1} d\Omega - \int_\Gamma p^* \bar{q}^{\tau 1} d\Gamma = R^{\tau 1} \tag{5.70}$$

A next configuration $\tau 2$ is needed, for which $R = 0$. Including the substitution of m_i and assuming $\bar{q}$ does not change, this gives;

$$\int_\Omega \frac{\partial p^*}{\partial x_i} \left(\rho_w^{\tau 2} \frac{k_{ij}^{\tau 2}}{\mu} \frac{\partial p^{\tau 2}}{\partial x_j} - \rho_w^{\tau 1} \frac{k_{ij}^{\tau 1}}{\mu} \frac{\partial p^{\tau 1}}{\partial x_j} \right) d\Omega = -R^{\tau 1} \tag{5.71}$$

Introducing the notation

$$\mathrm{d}\rho_w^{\tau 1} = \rho_w^{\tau 2} - \rho_w^{\tau 1} = \frac{\partial \rho_w^{\tau 1}}{\partial p} \mathrm{d}p^{\tau 1} + \frac{\partial^2 \rho_w^{\tau 1}}{\partial p^2} (\mathrm{d}p^{\tau 1})^2 + ... \tag{5.72}$$

$$\mathrm{d}k_{ij}^{\tau 1} = k_{ij}^{\tau 2} - k_{ij}^{\tau 1} = \frac{\partial k_{ij}^{\tau 1}}{\partial p} \mathrm{d}p^{\tau 1} + \frac{\partial^2 k_{ij}^{\tau 1}}{\partial p^2} (\mathrm{d}p^{\tau 1})^2 + ... \tag{5.73}$$

$$\mathrm{d}p^{\tau 1} = p^{\tau 2} - p^{\tau 1} \tag{5.74}$$

allows substitution of the unknowns for $\tau 2$ and gives the general expression

$$\int_\Omega \frac{\partial p^*}{\partial x_i} \left((\rho_w^{\tau 1} + \mathrm{d}\rho_w^{\tau 1}) \frac{(k_{ij}^{\tau 1} + \mathrm{d}k_{ij}^{\tau 1})}{\mu} \frac{\partial (p^{\tau 1} + \mathrm{d}p^{\tau 1})}{\partial x_j} - \rho_w^{\tau 1} \frac{k_{ij}^{\tau 1}}{\mu} \frac{\partial p^{\tau 1}}{\partial x_j} \right) d\Omega = -R^{\tau 1} \tag{5.75}$$

Local fluid pressure independency of the material ($\frac{\partial k_{ij}}{\partial p} = 0$) and the fluid density ($\frac{\partial \rho_w}{\partial p^f} = 0$) makes most terms drop out simplifying the problem into a linear system:

$$\int_\Omega \frac{\partial p^*}{\partial x_i} \rho_w^t \frac{k_{ij}}{\mu} \frac{\partial \mathrm{d}p^{\tau 1}}{\partial x_j} d\Omega = -R^{\tau 1} \tag{5.76}$$

This system, which is linear in p, can be solved directly, and iterations in a Newton-Raphson scheme are not needed. Linearity of the problem means that the formulation for a solution at time t becomes

$$\int_\Omega \frac{\partial p^*}{\partial x_i} \rho_w^t \frac{k_{ij}}{\mu} \frac{\partial p^t}{\partial x_j} d\Omega = 0 \tag{5.77}$$

which can be solved after constraining the problem through boundary conditions corresponding to time t.

5.3.2 Discretization of the diffusive flow in the grains

For the discretization, the 4-node quadrilateral element are used. These are the same elements as were used for the discretization of the grains in mechanical problem. In classical poromechanical computations of transient problems, these elements are known to lead to numerical problems and introduce oscillations in the numerical results. By the restriction to steady-state problems at the microscale, with a decoupling between the mechanical and hydraulic problem in the grains, these problems are avoided and the Q4 elements can be used.

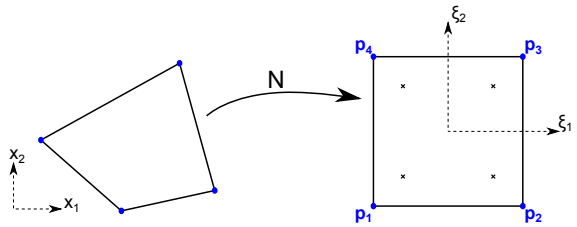

Fig. 5.8: Element for discretization of the hydraulic pressure field to solve for, equivalent to the mechanical element in Figure 5.2

Equation (5.77) can be further rewritten using matrix notation to allow spatial discretization;

$$\int_{\Omega} \{P^*\}^T [K^p] \{P\} d\Omega = 0 \tag{5.78}$$

with

$$\{P\} = \begin{Bmatrix} \frac{\partial p}{\partial x_1} \\ \frac{\partial p}{\partial x_2} \end{Bmatrix} \tag{5.79}$$

$$[K^p] = -\frac{\rho_w^t}{\mu} \begin{bmatrix} k_{11} & k_{12} \\ k_{21} & k_{22} \end{bmatrix} \tag{5.80}$$

Using finite element discretization in the same way as for the mechanical part, the vectors $\{P\}$ and $\{P^*\}^T$ can be found by

$$\{P\} = [B^p][T^p]\{P_{Node}\} \tag{5.81}$$

with

$$\{P_{Node}\} = \begin{Bmatrix} p^{(1)} \\ p^{(2)} \\ p^{(3)} \\ p^{(4)} \end{Bmatrix}, \tag{5.82}$$

$$[B^p] = \begin{bmatrix} \frac{\partial x_1}{\partial \xi_1} & \frac{\partial x_1}{\partial \xi_2} \\ \frac{\partial x_2}{\partial \xi_1} & \frac{\partial x_2}{\partial \xi_2} \end{bmatrix}. \tag{5.83}$$

and

$$[T^p] = \begin{bmatrix} \frac{\partial N^{(1)}}{\partial \xi_1} & \frac{\partial N^{(2)}}{\partial \xi_1} & \frac{\partial N^{(3)}}{\partial \xi_1} & \frac{\partial N^{(4)}}{\partial \xi_1} \\ \frac{\partial N^{(1)}}{\partial \xi_2} & \frac{\partial N^{(2)}}{\partial \xi_2} & \frac{\partial N^{(3)}}{\partial \xi_2} & \frac{\partial N^{(4)}}{\partial \xi_2} \end{bmatrix} \tag{5.84}$$

With $N^{(i)}$ the shape functions for element nodes (i) according to (5.8), Equation (5.78) can be further rewritten into

$$\int_{\Omega} \{P^{\star}_{Nodes}\}^T [T^p]^T [B^p]^T [K^p] [B^p] [T^p] \{P_{Nodes}\} d\Omega = 0 \tag{5.85}$$

In a single element, the left-hand side of this expression becomes

$$\{P^{\star}_{Nodes}\}^T \int_{\Omega^e} [E^p] d\Omega \{P_{Nodes}\} \tag{5.86}$$

with

$$[E^p] = [T^p]^T [B^p]^T [K^p] [B^p] [T^p] \tag{5.87}$$

The residual element fluxes $\{q^e\}$ can be obtained as

$$\{q^e\} = \int_{\Omega^e} [T^p]^T [B^p]^T \{m\} d\Omega \tag{5.88}$$

$$= \int_{\omega^{pe}} [T^p]^T [B^p]^T \{m\} \det(J^{\Omega\omega}) d\omega \tag{5.89}$$

with

$$\{q^e\} = \begin{Bmatrix} q^{(1)} \\ q^{(2)} \\ q^{(3)} \\ q^{(4)} \end{Bmatrix} \tag{5.90}$$

The fluid element 'stiffness' matrix $[K^p]^e$ as

$$[K^p]^e = \int_{\omega^e} [E^p] \det(J^{\Omega\omega}) d\omega \tag{5.91}$$

Transformation into numerical integration then leads to

$$[K^p]^e = \sum_{i=1}^{npi} \sum_{j=1}^{npi} [E^p(\xi_1, \xi_2)] \det(J^{\Omega\omega}(\xi_1, \xi_2)) W^i W^j \tag{5.92}$$

$$\{q^e\} = \sum_{i=1}^{npi} \sum_{j=1}^{npi} [T^p(\xi_1, \xi_2)]^T [B^p(\xi_1, \xi_2)]^T \{m(\xi_1, \xi_2)\} \det(J^{\Omega\omega}(\xi_1, \xi_2)) W^i W^j \tag{5.93}$$

Global assembly of element 'stiffness' matrices $[K^p]^e$ and column vectors of element nodal residual fluxes $\{q^e\}$ leads to a system of equations describing the variation of the nodal fluid pressure degrees of freedom p in the grains and its nodal fluid mass balance q in mass per time:

$$[K^p]\{p\} = \{q\} \tag{5.94}$$

The unknown boundary conditions at the grain boundaries can not be addressed directly as they interact with the interface hydraulic system. Therefore, system of equations 5.94 is partitioned for degrees of freedom p^b on the grain boundaries

and internal degrees of freedom p^i (for all nodes not on the grain boundaries). This gives the following system:

$$\begin{bmatrix} K^{pii} & K^{pib} \\ K^{pbi} & K^{pbb} \end{bmatrix} \begin{Bmatrix} p^i \\ p^b \end{Bmatrix} = \begin{Bmatrix} q^i \\ q^b \end{Bmatrix} \tag{5.95}$$

The dependent degrees of freedom (those on a REV follow boundary in Γ^F) in $\{p^i\}$ can be eliminated using the periodic boundary conditions given in equations (4.12) and (4.14). Together with the conservation of mass being satisfied for all other grain internal degrees of freedom, this gives the reduced system of equations

$$\begin{bmatrix} K^{p^\star ii} & K^{p^\star ib} & K^{p^\star ip} \\ K^{p^\star bi} & K^{p^\star bb} & K^{p^\star bp} \\ K^{p^\star pi} & K^{p^\star pb} & K^{p^\star pp} \end{bmatrix} \begin{Bmatrix} p^i \\ p^b \\ \nabla p^M \end{Bmatrix} = \begin{Bmatrix} 0 \\ q^b \\ m^{\star i} \end{Bmatrix} \tag{5.96}$$

where superscript $[]^p$ refers to the prescribed degrees of freedom through the boundary conditions. $\{q^{\star i}\}$ is here the fluid mass flow over the periodic boundaries through the internal grain nodes. Condensation of this system of equations on the boundary and prescribed degrees of freedom gives a new system of equations:

$$\begin{bmatrix} H^{bb} & H^{bp} \\ H^{pb} & H^{pp} \end{bmatrix} \begin{Bmatrix} p^b \\ \nabla p^M \end{Bmatrix} = \begin{Bmatrix} q^b \\ m^{\star i} \end{Bmatrix} \tag{5.97}$$

with

$$\begin{bmatrix} H^{bb} & H^{bp} \\ H^{pb} & H^{pp} \end{bmatrix} = \begin{bmatrix} K^{p^\star bb} & K^{p^\star bp} \\ K^{p^\star pb} & K^{p^\star pp} \end{bmatrix} - \begin{bmatrix} K^{p^\star bi} \\ K^{p^\star pi} \end{bmatrix} \left[K^{p^\star ii}\right]^{-1} \begin{bmatrix} K^{p^\star ib} & K^{p^\star ip} \end{bmatrix} \tag{5.98}$$

5.3.3 Merging the interface flow model and the diffusive grain flow model

For merging the system of equations for the grain boundary flux as a function of the grain boundary pressure in Equation (5.97) with the pore channel flow system of equations (5.53), a reassembly of the former system of equations is needed. From the pore channel flow model follows that the fluid pressure on opposite grain boundaries is identical. Hence, the hydraulic interface node on the axis of the interface has the same pressure as the two node on opposite interface sides between which it is located. To be able to define a mass balance equation for the nodes with equal pressures, the mass balance is evaluated for the combination of points of equal microscale pressures p^m. This is done by defining a single shared hydraulic degree of freedom p^h for the nodes with identical pore pressure (see Figure 5.9). The fluid mass flux as the dual to this degree of freedom is the sum of the mass flux over the shared nodes:

$$\sum \varpi + \sum q^b = 0 \tag{5.99}$$

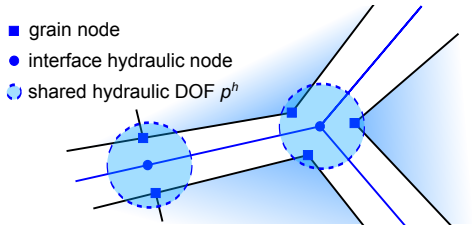

Fig. 5.9: Shared hydraulic degrees of freedom p^h for nodes with equal fluid pressure to merge the diffusive grain flow and the interface channel flow.

The number of degrees of freedom p^h is equal to the number of hydraulic interface nodes for which the degrees of freedom are taken into account in (5.53). Moreover, all condensed degrees of freedom p^b in (5.97) are related to nodes for which a shared degree of freedom is defined. This means that in practice, a reassembly of system of equations (5.97) on the degrees of freedom p^h can be used to merge the diffusive flow problem and the interface flow problem. Reassembling (5.97) and addition of (5.53) will lead to the combined system of equations for degrees of freedom p^h:

$$\begin{bmatrix} G + H^{\star hh} & H^{\star hp} \\ H^{\star ph} & H^{\star pp} \end{bmatrix} \begin{Bmatrix} p^h \\ \nabla p^{REV} \end{Bmatrix} = \begin{Bmatrix} \sum \varpi + q^{\star h} \\ m^{\star diff} \end{Bmatrix} \tag{5.100}$$

with $[H^*]$ and $\{q^h\}$ the reassembled equivalent of $[H]$ and $\{q^b\}$ in (5.97) and $[G]$ and $\sum \varpi$ the contribution of (5.53). Subscript $[]^p$ refers to the prescribed macro degrees of freedom. This system of equations is again a system of equations of degrees of freedom with the connectivity of the interface hydraulic nodes. A subsequent condensation following the procedure of Section 5.2 gives the relations between the macro gradient of pressure and the macroscale fluid mass flux of Equations (5.63) and (5.64). Moreover; as long as the diffusive fluid flow properties of the material (the components of the permeability tensor) are constant, the condensation has to be performed only once at the beginning of the computation and the result can be used in all identical microstructures throughout the computation. The same approach might be followed for the mechanical part of computations, although it should be noted that this only applies to purely elastic deformation under small strain assumption and is not in line with the envisioned multiscale approach in which the choice of constitutive behaviour of the micromechanical components is not restricted by a linearity condition.

5.4 Microscale constitutive relations

For the constitution of the micromechanical REV, the constitutive behaviour of the different components (solid grains, cohesive interfaces and liquid phase) are developed.

5.4.1 Solid constitutive law

As the principle of the microscale model is based on the concept of material degradation (softening, damage,...) and the major part of the deformation to take place in the interfaces between grains, the grains themselves don't need sophisticated constitutive behaviour. Although it is very well possible to introduce any

continuous constitutive relation in the grains, only a simple linear elastic constitutive equation is introduced here. This allows (small) strains in the grains. An isotropic, linear elastic relation is therefore defined for the solid grains as

$$\sigma_{ij} = 2\mu\varepsilon_{ij} + \lambda\varepsilon_{kk}\delta_{ij} \tag{5.101}$$

where ε_{ij} is the small-strain tensor defined as $\varepsilon_{ij} = \frac{1}{2}(\frac{\partial u_i}{\partial x_j} + \frac{\partial u_j}{\partial x_i})$. The Lamé parameters μ and λ are used as model parameters, σ_{ij} is the Cauchy stress, and δ_{ij} the Kronecker delta.

Alternatively, this can be written in matrix form as

$$\begin{bmatrix} 2\mu+\lambda & 0 & 0 & \lambda \\ 0 & 2\mu & 0 & 0 \\ 0 & 0 & 2\mu & 0 \\ \lambda & 0 & 0 & 2\mu+\lambda \end{bmatrix} \begin{Bmatrix} \varepsilon_{11} \\ \varepsilon_{12} \\ \varepsilon_{21} \\ \varepsilon_{22} \end{Bmatrix} = \begin{Bmatrix} \sigma_{11} \\ \sigma_{12} \\ \sigma_{21} \\ \sigma_{22} \end{Bmatrix} \tag{5.102}$$

or taking the variation of the stress state as a linear function of the variation of the deformation gradient tensor;

$$\begin{bmatrix} 2\mu+\lambda & 0 & 0 & \lambda \\ 0 & \mu & \mu & 0 \\ 0 & \mu & \mu & 0 \\ \lambda & 0 & 0 & 2\mu+\lambda \end{bmatrix} \begin{Bmatrix} \delta F_{11} \\ \delta F_{12} \\ \delta F_{21} \\ \delta F_{22} \end{Bmatrix} = \begin{Bmatrix} \delta\sigma_{11} \\ \delta\sigma_{12} \\ \delta\sigma_{21} \\ \delta\sigma_{22} \end{Bmatrix} \tag{5.103}$$

5.4.2 Fluid constitutive law

Fluid compressibility is taken into account using the fluid compressibility modulus k^w;

$$\dot{\rho^w} = \frac{\rho^w}{k^w}\dot{p} \tag{5.104}$$

with $\dot{\rho}^w$ the rate of change of the current fluid density and $\dot{p}$ as a function of the rate of change in pressure p. Integration and the definition of a reference pressure p^0 with corresponding reference density ρ_0^w, gives the formulation of the fluid density as

$$\rho^w(p) = \rho_0^w \exp\left(\frac{p - p_0}{k^w}\right) \tag{5.105}$$

5.4.3 Cohesive interfaces

The cohesive forces are described by a damage law, relating the relative normal and tangential displacement to the normal and tangential cohesive forces respectively. In a first effort, the inter-dependency between the components is reduced as much as possible to facilitate a proper evaluation of the micromechanical response. Therefore a decoupling between normal and tangential components is adopted for the relation between relative displacement and cohesive forces. The damage law is characterized by three parameters;

- T^{max} the maximum cohesion
- $D(t)$ the history of relative displacement between the interface boundaries

- δ^c the critical relative displacement at which complete decohesion is obtained

The history parameter $D(t)$ at time t is defined relative to the critical relative displacement δ^c for the normal and tangential displacement separately:

$$\begin{aligned} D_t^t &= \max\left(\frac{1}{\delta_t^c}\max_{0\le\tau\le t}\left(|\Delta u_t^\tau|\right), D_t^0\right) && \text{if} \quad 0 \le |\Delta u_t^t| \le \delta_t^c \\ &= 1 && \text{if} \quad \delta_t^c < |\Delta u_t^t| \\ D_n^t &= \max\left(\frac{1}{\delta_n^c}\max_{0\le\tau\le t}\left(|\Delta u_n^\tau|\right), D_n^0\right) && \text{if} \quad \Delta u_n^t \le \delta_n^c \\ &= 1 && \text{if} \quad \delta_n^c < |\Delta u_n^t| \end{aligned} \tag{5.106}$$

This defines D^t at time t as a parameter with values between $D^0 > 0$ (initial state) and 1 (complete decohesion). The parameter D^0 serves here as a damage history for the initial configuration (geological history, effects of excavation of the sample, ...), but can also be seen as a control parameter for the stiffness of an 'undamaged' material. D^0 is always larger than 0, since $D^0 = 0$ would introduce infinite stiffness. Although this would be physically correct as it represents a non-active interface, it requires reformulation of the finite element system of equations to avoid infinite stiffness terms and ill-posed systems of equations. Taking a very small (but non-zero) initial state parameter D^0 can serve as an alternative to obtain non-active interfaces, as the very high interface stiffness will serve as a penalization of the relative interface displacement.

Using the state parameter D^t the constitutive laws for the normal and tangential interface cohesion is defined as follows:

$$\begin{aligned} T_n^t &= \tfrac{1}{\delta_n^c}\left(\tfrac{1}{D_n^t} - 1\right) T_n^{max} \Delta u_n^t && \text{if } \Delta u_n^t > 0 \\ &= \tfrac{1}{\delta_n^c}\left(\tfrac{1}{D_n^t} - 1\right) T_n^{max} \Delta u_n^t + \kappa {\Delta_n^t}^2 && \text{if } \Delta u_n^t \le 0 \end{aligned} \tag{5.107}$$

$$T_t^t = T_t^{max}\left(\tfrac{1}{D_t^t} - 1\right)\tfrac{\Delta u_t^t}{\delta_t^c} \tag{5.108}$$

where κ is a penalization term to avoid grain inter-penetration. The penalization is applied as a function of the negative interface opening squared to avoid an incremental non-linearity around $\Delta u_n = 0$. The law describes a classical damage law with a linear softening branch and linear unloading-reloading (Figure 5.10).

The use of the separate interface laws for normal and tangential stress/strain relations implies a decoupling between normal and tangential components, thereby leaving some coupling aspects like interface friction out of consideration. The lack of friction in the interface does however not exclude the mean stress dependency of the response. As a combined effect of the asymmetry introduced by the penalization of the negative normal interface openings and the close contact of all grains, a mean stress dependency in the failure criterion is obtained and relatively high effective internal friction angles can be obtained. Some results of this stress-dependent behaviour is demonstrated in the modelling of the COx mechanical response in Section 14.2.

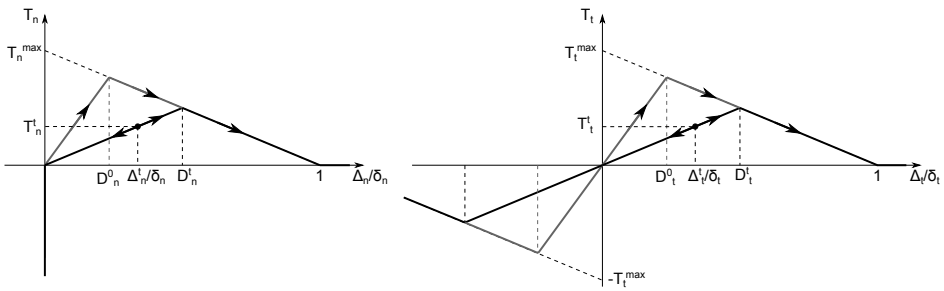

Fig. 5.10: Schematization of the damage laws for the interface cohesive forces T_n and T_t.

5.4.4 The hydraulic constitutive law

The compressibility of the fluid phase is considered to be small with respect to the spatial variation of the fluid pressure, which corresponds to the local assumption of the REV. Given that variation of the fluid phase density is only dependent on local fluid pressure through the fluid compressibility k^w, the fluid density is considered constant throughout the REV.

The change in fluid phase density $\dot{\rho}^w$ is directly related to the change in fluid pressure as:

$$\dot{\rho}^w = \rho^w \frac{\dot{p}}{k^w} \tag{5.109}$$

Given an initial fluid density ρ_w^0 at reference pressure p^0, the closed-form expression of the fluid density is

$$\rho_w(p) = \rho_w^0 \exp\left(\frac{p - p^0}{k_w}\right) \tag{5.110}$$

5.5 Computational homogenized macroscale response

In this section, the homogenization approach for obtaining the macroscale response from the REV under enforced deformation is discussed.

5.5.1 Homogenization of stress

The Hill-Mandel macro homogeneity condition [Hill, 1965, Mandel, 1972] is used as starting point for deriving the micro-to-macro transition of the REV averaged stress and its tangent operator. This condition requires the average microscale work to be equal to the macroscale work. Under small strain assumption the work conjugation of the stress tensor $\boldsymbol{\sigma}$ and strain tensor $\frac{\partial u_i}{\partial x_j}$ are naturally obtained and the macro homogeneity condition can be written in a virtual work formulation

$$W^{M\star} = \sigma_{ij}^M \frac{\partial u_i^{M\star}}{\partial x_j} = \sigma_{ij}^{REV} \frac{\partial u_i^{REV\star}}{\partial x_j} = \frac{1}{V^{REV}} \int\limits_{\Omega^{REV}} W^{m\star} d\Omega \tag{5.111}$$

As the interfaces introduce discontinuities in the microscale displacement field, the microscale virtual work can not directly be related to $\sigma_{ij}^m \frac{\partial u_i^\star}{\partial x_j}$ and an equivalent, continuous microscale displacement field $\hat{u}_i$ needs to be introduced for this

purpose. Around an interface, a zone of arbitrary width l is defined (see Figure 5.11), hereafter referred to as the contact zone.

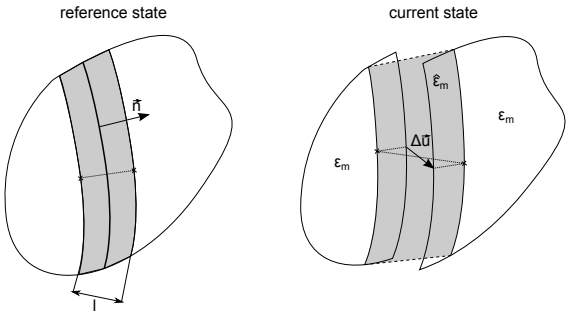

Fig. 5.11: Discontinuous interface with interface contact zone

Given a vector $\vec{l} = l\vec{n}$ (with interface normal vector $\vec{n}$ as its orientation) to characterize the cross section of the cohesive zone, the deformation of the domain by a certain strain field $\frac{\partial u_i^t}{\partial x_j}$ and interface relative displacement Δu_i^t defines the updated length of this vector as:

$$l_i^t = \int_0^l (\delta_{ij} + \frac{\partial u_i^t}{\partial x_j}) dl_j^0 + \Delta u_i^t = l_i^0 + \int_0^l \frac{\partial u_i^t}{\partial x_j} dl_j^0 + \Delta u_i^t \tag{5.112}$$

An equivalent strain of the contact zone can be defined by the introduction of an equivalent displacement field $\hat{u}_i$:

$$\frac{\partial \hat{u}_i}{\partial x_j} = \frac{1}{l} \left(\int_{\vec{l}} \frac{\partial u_i}{\partial x_j} dl + \Delta u_i n_j \right) \tag{5.113}$$

or in terms of a small strain tensor:

$$\hat{\varepsilon}_{ij} = \frac{1}{l} \left(\int_{\vec{l}} \varepsilon_{ij} dl + \frac{1}{2} \left(\Delta u_i n_j + \Delta u_j n_i \right) \right) \tag{5.114}$$

For small enough $\vec{l}$ this is equivalent to

$$\hat{\varepsilon}_{ij} = \varepsilon_{ij} + \frac{1}{2l} \left(\Delta u_i n_j + \Delta u_j n_i \right) \tag{5.115}$$

Outside the contact zone, the strain remains unchanged and $\hat{\varepsilon}_{ij} = \varepsilon_{ij}$. With an integration of the strain over the reference domain, the discontinuities can be taken into account by considering $\hat{u}_i$, which leads to:

$$\frac{\partial u_i^{REV}}{\partial x_j} = \frac{1}{V^0} \int_{\Omega^0} \frac{\partial \hat{u}_i}{\partial x_j} d\Omega \tag{5.116}$$

Note that for $\lim_{l\to 0}$ displacement fields $\hat{u}_i$ and u_i converge, although this means that in the contact zone $\hat{\varepsilon} \to \infty$ with $l \to 0$. Nevertheless, the introduction of the equivalent displacement field allows to apply Gauss theorem to transform the domain integral over deformation into a boundary integral over displacements (5.116), which holds for both displacement fields u_i and $\hat{u}_i$ for any l:

$$\frac{\partial u_i^{REV}}{\partial x_j} = \frac{1}{V^0}\int_{\Omega^0} \frac{\partial \hat{u}_i}{\partial x_j} d\Omega = \frac{1}{V^0}\int_{\Omega} \hat{u}_i dx_j \tag{5.117}$$

Stress continuity is guaranteed over the REV domain under small strain assumption (no interface opening). This means that for small enough l, the stress state σ_{ij} can be assumed constant over the cross section of the contact zone. This means that the Hill-Mandel condition requires

$$\sigma_{ij}^M \frac{\partial u_i^M}{\partial x_j} = \frac{1}{V^0}\int_{\Omega^0} \sigma_{ij}^m \frac{\partial \hat{u}_i}{\partial x_j} d\Omega \tag{5.118}$$

Gauss divergence theorem and equilibrium equation (5.3) (stress and displacement fields $\boldsymbol{\sigma}$ and $\vec{\hat{u}}$ are continuous and the internal boundaries drop out for $\hat{u}_i$) allows to write

$$\frac{1}{V^{REV}}\int_{\Omega} \sigma_{ij}^m \frac{\partial \hat{u}_i^\star}{\partial x_j} d\Omega = \frac{1}{V^{REV}}\int_{\Gamma} \bar{t}_i \hat{u}_i^\star d\Gamma \tag{5.119}$$

Using the periodic boundary conditions (4.8) and (4.11), the virtual displacement of the external boundary is reduced to

$$\frac{1}{V^{REV}}\int_{\Omega} \sigma_{ij}^m \frac{\partial \hat{u}_i^\star}{\partial x_j} d\Omega = \frac{1}{V^{REV}}\int_{\Gamma^F} \bar{t}_i \hat{v}_i^\star d\Gamma \tag{5.120}$$

with $\vec{v}^*$ the virtual "change" of the periodicity vector $\vec{y}$ given by

$$v_i^\star = \frac{\partial u_i^{\star REV}}{\partial x_j} y_j \tag{5.121}$$

Substitution of $\vec{v}^*$ allows to take the virtual part of the displacement outside the integral;

$$\frac{1}{V^{REV}}\int_{\Omega} \sigma_{ij}^m \frac{\partial u_i^\star}{\partial x_j} d\Omega = \frac{1}{V^{REV}} \frac{\partial u_i^{\star REV}}{\partial x_j}\int_{\Gamma^F} \bar{t}_i y_j d\Gamma \tag{5.122}$$

For the Hill-Mandel condition (5.111) to be satisfied, the integral in the right hand side of equation (5.122) needs to hold

$$\sigma_{ij}^{REV} = \frac{1}{V^{REV}}\int_{\Gamma^F} \bar{t}_i y_j d\Gamma \tag{5.123}$$

Gauss theorem and periodic boundary conditions allow rewriting once more into

$$\sigma_{ij}^{REV} = \frac{1}{V^{REV}}\int_{\Omega^0} \sigma_{ij}^m d\Omega \tag{5.124}$$

which provides the definition of the homogenized stress that corresponds to the Hill-Mandel macro-homogeneity condition under small-strain assumptions. In case of finite element discretization of the REV domain for solving the boundary value problem, the macro stress tensor is easily obtained from Equation (5.123) when it is written as the sum of the nodal reaction forces on the follow boundary:

$$\sigma_{ij}^{REV} = \frac{1}{V^{REV}} \sum_{\Gamma^F} f_i^F y_j d\Gamma \tag{5.125}$$

5.5.2 Homogenization of fluid mass flux

For the fluid part of the balance equations given in (3.5), the same approach for establishing the macro-homogeneity can be followed. In other works this method is used by Özdemir [2009] for thermomechanical problems and by Massart and Selvadurai [2012, 2014] for fluid fluxes. The macro-homogeneity condition for the hydraulic balance equations reads:

$$\dot{M}^{REV} p^{\star REV} - m_i^{REV} \frac{\partial p^{\star REV}}{\partial x_i} = \frac{1}{V^{REV}} \int_\Omega \left(\dot{M} - m_i \frac{\partial p^\star}{\partial x_i} \right) d\Omega \tag{5.126}$$

with $\dot{M}$ and m_i on the microscale yet to be defined. As the microscale problem is solved under steady state conditions, validated by the separation of scales, in this case separating the timescales of the hydraulic storage $\dot{M}$ [fluid mass/time] and the flux $\vec{m}$ [fluid mass/time] at the microlevel, this reduces temporarily to

$$m_i^{REV} \frac{\partial p^{\star REV}}{\partial x_i} = \frac{1}{V^{REV}} \int_\Omega m_i \frac{\partial p^\star}{\partial x_i} d\Omega \tag{5.127}$$

with m_i the microscale fluid mass flux. Gauss divergence theorem and the equilibrium of the system allows to write

$$m_i^{REV} \frac{\partial p^{\star REV}}{\partial x_i} = \frac{1}{V^{REV}} \int_\Gamma q p^\star d\Gamma \tag{5.128}$$

where $q = m_i n_i$ is the normal outward mass flux over the REV. The (fluctuation of the) virtual pressures are constrained by the boundary conditions (4.12) and (4.14) which allows rewriting into

$$m_i^{REV} \frac{\partial p^{\star REV}}{\partial x_i} = \frac{1}{V^{REV}} \int_{\Gamma^F} q \left(\frac{\partial p^\star}{\partial x_i} \right)^{REV} y_i d\Gamma \tag{5.129}$$

From this, the definition of m_i^{REV} is found as the integral of the microscale boundary mass flux q^F over the follow boundary:

$$m_i^{REV} = \frac{1}{V^{REV}} \int_{\Gamma^F} q^F y_i d\Gamma \tag{5.130}$$

For the finite element discretization of the REV boundary value problem, this integral can easily be computed as the sum of the fluxes in the nodes on the

follow boundary:

$$m_i^{REV} = \frac{1}{V^{REV}} \sum_{\Gamma^F} q^F y_i \tag{5.131}$$

The microscale outward flux on the follow boundary q^F is the assembly of interface fluxes ϖ and diffusive grain fluxes. This summation is identical to the summation in 5.57 for the total flux over the follow boundaries.

Moreover, applying once more the divergence theorem shows that the macroscale mass flux is the average of the microscale mass flux

$$m_i^{REV} = \frac{1}{V^{REV}} \int_{\Omega} m_i d\Omega \tag{5.132}$$

5.5.3 Homogenization of fluid mass

To obtain the macroscopic fluid content M a direct approach is followed by defining the total amount of fluid in the REV as the amount of fluid in the grain pore space plus the amount of fluid in the interfaces, for which the volume is defined by the integration of the hydraulic opening over the interfaces. The interface volume V^{int} is much smaller than the REV volume $V^{REV} = V^{REV,0}$ and therefore, the amount of fluid is computed as

$$M = \frac{1}{V^{REV}} \left(\int_{\Omega^{REV}} \rho^w \varphi d\Omega + \int_{\Omega^{int}} \rho^w d\Omega \right) \tag{5.133}$$

With ρ^w constant over the REV and the interface volume defined by the integral of the hydraulic interface aperture over the 1D pore network S^{int}, this can be rewritten as

$$M = \frac{\rho^w}{V^{REV}} \left(\int_{\Omega^{REV}} \varphi d\Omega + \int_{S} \Delta u_h ds \right) = \frac{\rho^w}{V^{REV}} \left(\bar{\varphi} V^{REV} + V^{int} \right) \tag{5.134}$$

with $\bar{\varphi}$ the REV average of the grain porosity. To obtain the fluid mass storage term $\dot{M}$, a finite difference approximation is made over the time interval Δt. This time interval is taken to be the same as the macroscale time step. For a time step Δt from $t - \Delta t$ to t, the fluid storage term $\dot{M}^t$ is obtained as follows:

$$\dot{M}^t \approx \frac{M^t - M^{t-\Delta t}}{\Delta t} \tag{5.135}$$

The specific fluid mass M^t depends on the density of the fluid and the relative volume it occupies. As the REV pore volume only changes due to the interface volume, the rate of change in specific fluid mass $\dot{M}$ is found to be dependent on the rate of change of fluid density $\dot{\rho}^w$ and the rate of change of interface volume $\dot{V}^{int}$. This means that the fluid storage has a rheological part as well as a geometrical part. With the assumption of constant grain pore volume (not to be confused with incompressibility of the grains!), the geometrical component of the fluid storage is relatively small. The effect of this definition is investigated in Part III.

6. COMPUTATIONAL HOMOGENIZATION BY STATIC CONDENSATION

The system of equations to be solved for the macroscale boundary value problem (3.4)-(3.5) are, in general, nonlinear. This means that an iterative procedure is needed to solve the system of equations. Different iterative procedures exist, of which the Newton-Raphson method is chosen to be used because

> *"...it is our (not only our) experience that this method is very efficient." ... "More efficient methods are available (quasi Newton method for instance) but they diverge often. Newtons method can be seen as the best compromise."* [Chambon, 2008]

The principle of Newton's method, in which a tangent operator is used to make an estimate of the update of the kinematic fields required to overcome the imbalance of a solution, has a quadratic convergence with the number of iterations, under the condition that a proper linearization around the test solution is possible. A high consistency in the linearization for obtaining the tangent operator is key in the algorithm efficiency, as an inaccurate tangent operator provides inaccurate estimates of the updates in the iterations. When classical constitutive relations are used, an exact solution can often be found as a closed-form analytical solution exists for the partial derivatives of the constitutive equations. More complex constitutive behaviour, for example obtained through the introduction of plasticity or incremental nonlinearities of different degrees, can easily introduce difficulties in the derivability of the constitutive equations. This is certainly the case for the constitutive relation obtained from a microscale finite element relation as presented in this work.

The matrices $[C_{(4\times4)}]$, $[K^{\tau 1}_{hm(3\times4)}]$, $[K^{\tau 1}_{mh(4\times3)}]$ and $[K^{\tau 1}_{hh(3\times3)}]$ introduced in Equation 3.7 as the consistent linearization of the classical constitutive relations are the tangent matrices that are required in the Newton-Raphson scheme. From the integration point objective, this can be recast in the following 7×7 system of equations:

$$\{dU^{\star}\}^T [A_{(7\times7)}] \{dU\} \approx \{dU^{\star}\}^T \{dR\} \tag{6.1}$$

with

$$[A^{\tau 1}_{(7\times7)}] = \begin{bmatrix} [C^{\tau 1}_{(4\times4)}] & [K^{\tau 1}_{mh(4\times3)}] \\ [K^{\tau 1}_{hm(3\times4)}] & [K^{\tau 1}_{hh(3\times3)}] \end{bmatrix} \tag{6.2}$$

as the linearization of the hydromechanical coupled constitutive behaviour and

$$\{dU^{\tau 1}_c\} = \begin{bmatrix} \frac{\partial du_1}{\partial x_1} & \frac{\partial du_1}{\partial x_2} & \frac{\partial du_2}{\partial x_1} & \frac{\partial du_2}{\partial x_2} & \frac{\partial dp}{\partial x_1} & \frac{\partial dp}{\partial x_2} & dp \end{bmatrix}^T . \tag{6.3}$$

The virtual work term $\{dU^\star\}^T\{dR\}$ is related to the out-of-balance of the system to be accounted for in the Newton-Raphson iteration. This defines the residual term as follows:

$$\{dR^{\tau 1}\} = \begin{bmatrix} d\sigma_{11}^{M,\tau 1} & d\sigma_{12}^{M,\tau 1} & d\sigma_{12}^{M,\tau 1} & d\sigma_{22}^{M,\tau 1} & m_1^{M,\tau 1} & m_2^{M,\tau 1} & \dot{M}^{M,\tau 1} \end{bmatrix}^T. \tag{6.4}$$

The residual term is the change in response to the update $\{dU^{\tau 1}\}$ to go from configuration $\Omega^{\tau 1}$ to $\Omega^{\tau 2}$ over an iteration. The challenge is now to find the consistent linearization around configuration $\Omega^{\tau 1}$ that can be used for matrix $[A_{(7\times 7)}]$.

This chapter describes two approaches to obtain the linearization of the homogenized constitutive law for hydromechanical coupling.

6.1 Differentiation by numerical perturbation

In the computation of a time step from $t-\Delta t$ to t, the equilibrated configuration Ω^t is the configuration to be found as an update of configuration $\Omega^{t-\Delta t}$ by the kinematics field $\{\Delta U^t\}$. The solution for the kinematics fields $\{\Delta U^t\}$ satisfying equations (3.4)-(3.5) are found iteratively, by updates $\{dU^{\tau 1}\}$, for which (6.1) is rewritten as

$$[A_{7\times 7}^{\tau 1}]\{dU^{\tau 1}\} \approx -\{R^{\tau 1}\} \tag{6.5}$$

with $\{R^{\tau 1}\}$ the array of local out-of-balance components and $[A^{\tau 1}]$ the linearization around configuration $\Omega^{\tau 1}$ as the incremental relation between the variation of $\{U\}$ and $\{R\}$. The linearization around $\Omega^{\tau 1}$ can be found by a finite difference approximation. The change in response $\{\Delta R\}$ to finite differences ϵ in the deformation $\{U^{\tau 1}\}$, gives an approximation of the consistent linearization. Because the linearization $[A^{\tau 1}]$ has to be consistent with the loading direction of $\{\Delta U^{\tau 1}\}$, the finite differences or perturbations ϵ need to be applied together with the loading step of $\{\Delta U^{\tau 1}\}$. By defining $R_{(i)}^{\tau 1}(\{U^{\tau 1}+\epsilon_j\})$ as the response after loading step to configuration $\Omega^{\tau 1}$ with an additional perturbation of component $U_{(j)}^{\tau 1}$ by a finite perturbation ϵ, the finite difference approximation of the linearization of the macroscale constitutive relation (stemming directly from the microscale equilibrium and flow equations) is found:

$$A_{(ij)}^{\tau 1} \approx \frac{R_{(i)}(\{U^{\tau 1}+\epsilon_j\}) - R_{(i)}^{\tau 1}(\{U^{\tau 1}\})}{\epsilon_j} \tag{6.6}$$

This procedure to obtain the consistent linearization by a finite difference approximation through numerical perturbation of the components of the loading on the REV was used for example by Feyel and Chaboche [2000] for mechanical problems and Marinelli [2013] for hydromechanical coupling.

The consistency of the linearization, or the tangent stiffness matrix will partly determine the efficiency of the Newton-Raphson scheme for finding a solution to the problem to be solved. The consistency is influenced by

- the (non)linearity of the problem to be solved for,
- the precision of the response $\{R^{\tau 1}\}$,

- the size of the numerical perturbation ϵ.

The first two points depend on the specific behaviour of the constitutive law and touch both the fundamental constitutive behaviour and the computational performance and implementation. The size of the numerical perturbation ϵ has to be chosen with respect to these first two points; ϵ has to be small enough to avoid including the nonlinearities of the model in the result and large enough to avoid roundoff errors due to the finite machine precision. A sensitivity analysis of numerical perturbation size ϵ with respect to convergence of hydromechanical coupled FE^2 can be found in Marinelli [2013].

The linearization by numerical perturbation requires the response to a certain load increment to be computed seven additional times, for which a numerical perturbation is added to one of the seven components of $[\Delta U]$. When the constitutive relations are formulated in a classical way, the expense of these additional computations can be neglected relative to the expense of solving the global finite element system of equations. In the case where the response is given by a full computation on the microscale, the computational costs of obtaining the response from the incremental loading of the microstructure quickly exceeds the costs of the global computation at the macroscale. This mean that the additional computations for applying the numerical perturbations have a major impact on the total computational expense.

An alternative to the use of the method of numerical perturbation with higher efficiency and no dependency on the choice of the perturbation is therefore preferred.

6.2 Computational homogenization by static condensation of the mechanical FE system of equations

Computational homogenization by static condensation [Kouznetsova et al., 2001] provides an alternative to the numerical procedure, avoiding the time consuming additional BVPs to be solved. The method is a well-established technique for micro-to-macro scale transition in heterogeneous materials in both the small- and large deformations framework, but has only seen few extensions to multiphysical problems [Geers et al., 2010]. The classical condensation procedure for small strain microscale formulation is repeated here in a slightly modified procedure, generalizing the boundary conditions with respect to geometry and variables for future developments.

The homogenized macro stress $\boldsymbol{\sigma}^{REV}$ is obtained from the REV by a volume average of the micro scale stress by the boundary integral given in Equation (5.123). As the REV boundary value problem is solved using a FE discretization, this integral is approximated by the sum over the nodal forces $\vec{f}^F$ on the follow boundary multiplied by their periodic vectors:

$$\sigma_{ij}^{REV} = \frac{1}{V^{REV}} \sum f_i^F y_j \tag{6.7}$$

The finite element system of equations (5.35) corresponding to a REV in equilibrium is used to solve the REV boundary value problem, with $[K]$ the linearization of the nodal force equilibrium around the updated configuration. This linear system of equations with n degrees of freedom is extended with the variation of the

macroscale variables $\delta\varepsilon^{REV}$ into

$$\begin{bmatrix} 0_{(4\times4)} & 0_{(4\times n)} \\ 0_{(n\times4)} & K_{(n\times n)} \end{bmatrix} \begin{Bmatrix} \delta\varepsilon^{REV}_{(4)} \\ \delta u_{(n)} \end{Bmatrix} \begin{Bmatrix} 0_{(4)} \\ \delta f_{(n)} \end{Bmatrix} \tag{6.8}$$

This system of equations is ill-posed as it does not contain the information of the boundary conditions. For enforcing the periodic boundary conditions and reducing the system of equations to a well-posed system, boundary conditions (4.8) and (4.11), together with the definition of the homogenized stress (6.7) are repeated here for the variation of nodal kinematics and residual forces:

$$\delta u_i^F = \delta u_i^L + \delta\varepsilon_{ij}^{REV} y_j \qquad (4.8) \qquad (6.9)$$

$$\delta f_i^F + \delta f_i^L = 0 \qquad (4.11) \qquad (6.10)$$

$$\delta\sigma_{ij}^{REV} = \frac{1}{V^{REV}} \sum \delta f_i^F y_j \qquad (6.7) \qquad (6.11)$$

The n^d follow degrees of freedom in $\{\delta u^F\}$ can be eliminated together with their nodal force duals in $\{\delta f^F\}$.
From (6.9) it follows that the contribution of each follow DOF δu_i^F can be eliminated by means of their lead degree of freedom and the macroscale kinematics $\delta\varepsilon_{ij}^{REV}$. The elimination of δu_i^F gives a first intermediate equation where the columns corresponding to δu_i^F are redistributed over those of δu_i^L and $\delta\varepsilon_{ij}^{REV}$:

$$\begin{bmatrix} 0^{\star pp}_{(4\times4)} & 0^{\star pi}_{(4\times n^i)} \\ K1^{\star ip}_{(n\times4)} & K1^{\star ii}_{(n\times n^i)} \end{bmatrix} \begin{Bmatrix} \delta\varepsilon^{REV}_{(4)} \\ \delta u_{(n^i)} \end{Bmatrix} = \begin{Bmatrix} 0_{(4)} \\ \delta f_{(n)} \end{Bmatrix} \tag{6.12}$$

n^i is here the number of independent degrees of freedom in th system of equations. The extension of the system of equations with the four degrees of freedom $\delta\varepsilon_{ij}$ requires four additional constraints. These constraints are introduced by the variation of stress response $\delta\sigma_{ij}^{REV}$ through (6.11). The addition of this constraint is obtained by adding the summation of (6.11) in the top 4 equations of the system, leading to the second intermediate equation:

$$\begin{bmatrix} K2^{\star pp}_{(4\times4)} & K2^{\star pi}_{(4\times n^i)} \\ K2^{\star ip}_{(n\times4)} & K2^{\star ii}_{(n\times n^i)} \end{bmatrix} \begin{Bmatrix} \delta\varepsilon^{REV}_{(4)} \\ \delta u_{(n^i)} \end{Bmatrix} = \begin{Bmatrix} \delta\sigma^{REV}_{(4)} \\ \delta f_{(n)} \end{Bmatrix} \tag{6.13}$$

The final step in the reduction of the system of equations is made by taking into account the anti-periodicity of the nodal forces in equation (6.10), which provides a straightforward elimination of δf_i^F by transferring their equations to the equations of their leads δf_i^L. This elimination leads to the reduced system of equations, which naturally satisfies the boundary conditions through the incorporation of $\nabla\delta\vec{u}^{REV} = \delta\varepsilon^{REV}$. Moreover, the anti-periodicity of the boundary traction makes the elimination of the lead nodal reaction forces disappear. The result is the following reduced system of equations:

$$\begin{bmatrix} K^{\star pp}_{(4\times4)} & K^{\star pi}_{(4\times n_i)} \\ K^{\star ip}_{(n_i\times4)} & K^{\star ii}_{(n^i\times n^i)} \end{bmatrix} \begin{Bmatrix} \delta\varepsilon^{REV}_{(4)} \\ \delta u_{(n^i)} \end{Bmatrix} = \begin{Bmatrix} \delta\sigma^{REV}_{(4)} \\ 0_{(n_i)} \end{Bmatrix} \tag{6.14}$$

where n^i in the subscript is the number of remaining independent degrees of freedom, corresponding the degrees of freedom on the internal nodes and the nodes on the lead boundary. Note that the REV periodicity vector $\vec{y}$ is included in the elimination of the follow degrees of freedom, which gives the direct dependency on variation of the macroscale strain tensor $\delta\varepsilon^{REV}$ and results directly in the components of the macroscale stress tensor $\delta\sigma_{ij}^{REV}$. A last step is now to eliminate the remaining independent degrees of freedom by static condensation of the system of equations on the prescribed degrees of freedom in $\{\varepsilon^{REV}\}$. This implies that a four-by-four matrix $[C^{REV}]$ is obtained, relating $\delta\varepsilon^{REV}$ to $\delta\boldsymbol{\sigma}^{REV}$:

$$\left[C_{(4\times4)}^{REV}\right]\{\delta\varepsilon_{(4)}^{REV}\} = \{\delta\sigma_{(4)}^{REV}\} \tag{6.15}$$

with

$$\left[C_{(4\times4)}^{REV}\right] = \left[K_{(4\times4)}^{\star pp}\right] - \left[K_{(4\times n_i)}^{\star pi}\right]\left[K_{(n_i\times n_i)}^{\star ii}\right]^{-1}\left[K_{(n_i\times4)}^{\star ip}\right] \tag{6.16}$$

This tangent stiffness matrix, consistent with respect to the symmetric macroscale strain ε^M as enforced on the REV boundaries, has now to be rotated back into the macroscale frame in consistency with the decomposition of the deformation gradient tensor in 4.3. With the variation (or rate) of the stress tensor is not objective with respect to rotation, this is not straightforward and a somewhat lengthy derivation is required to obtain the correct transformation. The derivation is given in Appendix A.3 to find the transformation from the fourth order tensor ${}^4\boldsymbol{C}^{REV}$ (${}^4\boldsymbol{C}^{REV} : \delta\boldsymbol{U}^M = \delta\boldsymbol{\sigma}^{REV}$) to ${}^4\boldsymbol{C}^M$ (${}^4\boldsymbol{C}^M : \vec{\nabla}\delta\vec{x} = \delta\boldsymbol{\sigma}^M$) as:

$$C_{ijkl}^M = R_{i\alpha}^M R_{j\beta}^M C_{\alpha\beta\gamma\delta}^{REV}\frac{\partial U_{\gamma\delta}}{\partial F_{kl}} - R_{i\beta}^M\frac{\partial R_{\alpha\beta}^M}{\partial F_{kl}}\sigma_{\alpha j} - R_{j\beta}^M\frac{R_{\alpha\beta}^M}{\partial F_{kl}}\sigma_{\alpha i} \tag{6.17}$$

with

$$\frac{\partial U_{\gamma\delta}}{\partial F_{kl}} = \frac{1}{I_1}\frac{\partial R_{kl}^M}{\partial\theta}\left(\left(\delta_{\gamma2}-\delta_{\gamma1}\right)\delta_{\gamma\delta}U_{12} + (1-\delta_{\gamma\delta})(\delta_{l2}U_{11} - \delta_{l1}U_{22})\right) + \delta_{\gamma l}\delta_{\delta l}R_{kl}^M \tag{6.18}$$

and

$$\frac{\partial R_{\alpha\beta}^M}{\partial F_{kl}} = \frac{1}{I_1}\frac{\partial R_{\alpha\beta}}{\partial\theta}\frac{\partial R_{kl}^M}{\partial\theta} \tag{6.19}$$

where I_1 is the first strain invariant $tr(\boldsymbol{U})$, δ_{ij} is the Kronecker delta and θ is the angle of rotation represented by $\boldsymbol{R}^M$.

6.3 Computational homogenization by static condensation of HM coupled FE system of equations

For the macroscale computations, the required tangent stiffness matrix is given by equation

$$\begin{bmatrix} C_{(4\times4)}^{REV} & K_{mh(4\times3)}^{REV} \\ K_{hm(3\times4)}^{REV} & K_{hh(3\times3)}^{REV}\end{bmatrix}\begin{Bmatrix}\delta\varepsilon_{(4)}^{REV} \\ \delta\nabla p_{(2)}^{REV} \\ \delta p^M\end{Bmatrix} = \begin{Bmatrix}\delta\sigma_{(4)}^{REV} \\ \delta m_{(2)}^{REV} \\ \delta M\end{Bmatrix} \tag{6.20}$$

with $\delta[.]$ to indicate an infinitesimal variation of a certain quantity. This system of equations is summarized as

$$[A^{REV}_{(7\times7)}][\delta U_{(7)}] = [\delta\Sigma^{REV}_{(7)}]. \tag{6.21}$$

Following the same procedure as was presented for the mechanical case in Section 6.2, the global system of equations for the fully-coupled hydromechanical finite element computation at the microscale is written in a system of equations extended with 7 terms in each dimension to add the macroscale variables $\{U_{(7)}\}$ and their response duals $\{\Sigma_{(7)}\}$.

There are however, some differences in the approach related to the fluid pressure and fluid mass with respect to the other variables. These differences stem from the variation of pressure δp^M that has not yet been addressed in the developments. The variation of microscale fluid pressure δp^m is split in two parts; those related to the variation in macro pressure and those related to the variation of micromechanical fluctuation and macro pressure pressure gradient in accordance with the definition of the decomposition of microscale pressure obtained in (4.4):

$$\delta p^m = \delta p^M + \delta\hat{p} \qquad \delta p^M >> \delta\hat{p} \tag{6.22}$$

Due to the principle of separation of scales, the variations δp^M are much larger than the variations $\delta\hat{p}$. δp^M is the 7^{th} component of $\{\delta U_{(7)}\}$. The result of introducing the variation of reference pressures $\delta\hat{p}$ is to obtain fluid pressure terms taking into account the macroscale gradient of fluid pressures independent from the p^M. The following (empty) frame for the systems of equations is obtained:

$$\begin{bmatrix} [.]_{(7\times7)} & [.]_{(7\times n)} & [.]_{(7\times m)} \\ [.]_{(n\times7)} & [.]^{mm}_{(n\times n)} & [.]^{mh}_{(n\times m)} \\ [.]_{(m\times7)} & [.]^{hm}_{(m\times n)} & [.]^{hh}_{(m_\times m)} \end{bmatrix} \begin{Bmatrix} \delta U_{(7)} \\ \delta u_{(n)} \\ \delta\hat{p}_{(m)} \end{Bmatrix} = \begin{Bmatrix} [.]_{(7)} \\ [.]_{(n)} \\ [.]_{(m)} \end{Bmatrix} \tag{6.23}$$

For the assembly of this matrix, the equations describing the variation of the response need to be assembled, after which elimination of the dependent degrees of freedom by the equations of the boundary conditions leads to the reduced system of equations which can be condensed on the macroscale variables. The procedure of the assembly is equivalent to those presented for the mechanical problem and the approach to solving the fluid system, although two important differences must be taken care of. The first difference is the variation in specific fluid mass δM, for which a new equation needs to be formulated. The formulation of this equations is straightforward and is given later in this chapter. The second difference is the influence of the variation of macroscale fluid pressure, which used to be constant in microscale computations. The effect of δp^M can be taken into account in the equations of the microscale responses.

The partial derivatives that form the equations to be assembled in the frame above, are derived for the nodal force balance, the fluid mass balance and the macroscale specific fluid mass in the following three sections. The partial derivatives are written in matrix form to represent the relation between variations of the kinematics and its response.

6.3.1 Partial derivatives for the variation of fluid fluxes

For the variation of fluid flux, the influence of δp^M might as well be written on the macroscale by decomposing the variation of macroscale fluid flux

$\delta m_i^{REV} = \delta(v\rho^w)$ into a rheological part $\delta m_i^{REV,R} = v_i^{REV}\delta\rho^w$ and a volumetric part $\delta m_i^{REV,V} = \rho^w \delta v_i^{REV}$. Volumetric flux v_i^{REV} is dependent on the configuration of the REV and the pressure gradient (that is, $\{\delta u_{(n)}\}$ and $\{\delta\hat{p}_{(m)}\}$), whereas the fluid density ρ^w only depends on the macroscale fluid pressure p^M. From its definition, it is already clear that $\delta m_i^{REV,R}$ can be computed completely on the macroscale level, and it is easily verified that

$$\delta m_i^{REV,R} = \frac{m_i^{REV}}{\rho^w}\delta\rho^w = \frac{m_i^{REV}}{k^w}\delta p^M \tag{6.24}$$

which can be written in matrix form as

$$\left[M1_{(2\times1)}\right]\delta p^M = \left[\delta m_{(2)}^{REV,R}\right] \qquad \left[M1_{(2\times1)}\right] = \frac{1}{k^w}\begin{bmatrix} m_1 \\ m_2 \end{bmatrix} \tag{6.25}$$

The variation of the volumetric part $\delta m_i^{REV,V}$ is dependent on the microscale kinematics δu and $\delta\hat{p}$, which have couplings with the mechanical parts of the microscale model. On the microscale, the volumetric part of the variation of the nodal fluid mass balance δq^V with respect to δu and $\delta\hat{p}$ is defined as

$$\{\delta q_{(m)}^V\} = [K_{(m\times n)}^{hm}]\{\delta u_{(n)}\} + [K_{(m\times m)}^{hh}]\{\delta\hat{p}_{(m)}\} \tag{6.26}$$

The last matrix has been defined for solving the fluid system for the given REV configuration:

$$\left[K_{(m\times m)}^{hh}\right] = [G] \qquad \text{(Equation (5.53))} \tag{6.27}$$

The first matrix has not yet been defined, as the fluid problem has been solved decoupled from the mechanical microscale problem. It contains the assembly of the partial derivatives of the interface mass fluxes ϖ with respect to the nodal displacements $\vec{u}$. To obtain the element matrices $[K^{hm}]^e$ for the assembly of $[K_{(m\times n)}^{hm}]$, the partial derivatives with respect to the displacements of the nodal coordinates $U_{(i)}^{Node}$ as components of $\{U_{Node}\{$ are derived:

$$\frac{\partial\varpi}{\partial U_{(i)}^{Node}} = \rho^w(p^{n_2}) - p^{n_1})\frac{\partial\phi}{\partial U_{(i)}^{Node}} \tag{6.28}$$

To be able to solve the non-linearities in the interface element integration, the definition of the hydraulic conductivity term ϕ is rewritten as the integral in the parent element:

$$\begin{aligned} \phi^l &= \rho^w \left(\int_{s^i}^{s^j} \frac{1}{\kappa(s)} ds \right)^{-1} \\ &= \rho^w \left(\int_{\xi_1=-1}^{+1} \frac{1}{\kappa(\xi_1)} \frac{\partial s}{\partial \xi_1} d\xi_1 \right)^{-1} = \rho^w \left(\int_{\xi_1=-1}^{+1} \frac{1}{\kappa(\xi_1)} J^{\Gamma\gamma} d\xi_1 \right)^{-1} \end{aligned} \tag{6.29}$$

The partial derivatives with respect to $U_{(i)}$ can then be developed:

$$\frac{\partial \phi}{\partial U_{(i)}^{Node}} = -\frac{\phi^2}{\rho^w}\frac{\partial}{\partial U_{(i)}^{Node}}\left(\int_{\xi_1=-1}^{+1}\frac{1}{\kappa(\xi_1)}J^{\Gamma\gamma}d\xi_1\right) \tag{6.30}$$

$$= -\frac{12\mu\phi^2}{\rho^w}\frac{\partial}{\partial U_{(i)}^{Node}}\left(\int_{\xi_1=-1}^{+1}\Delta u_h(\xi_1)^{-3}J^{\Gamma\gamma}d\xi_1\right) \tag{6.31}$$

Rather than further developing the derivation of the partial derivative for the full integral and changing to numerical integration afterwards, the integral is first replaced by a numerical integration as the weighted sum over the integration point after which the derivation is continued for the sum of the individual components:

$$\begin{aligned}
\frac{\partial \phi}{\partial U_{(i)}^{Node}} &= -\frac{12\mu\phi^2}{\rho^w}\frac{\partial}{\partial U_{(i)}^{Node}}\left(\sum_{i=1}^{npi}\Delta u_h(\xi_1)^{-3}J^{\Gamma\gamma}W^i\right) \\
&= -\frac{12\mu\phi^2}{\rho^w}\sum_{i=1}^{npi}\frac{\partial\left(\Delta u_h(\xi_1)^{-3}\right)}{\partial U_{(i)}^{Node}}J^{\Gamma\gamma}(\xi_1)W^i \\
&= -\frac{12\mu\phi^2}{\rho^w}\sum_{i=1}^{npi}\frac{\partial\left(\Delta u_h(\xi_1)^{-3}\right)}{\partial \Delta u_h(\xi_1)}\frac{\partial \Delta u_h(\xi_1)}{\partial U_{(i)}^{Node}}J^{\Gamma\gamma}(\xi_1)W^i \\
&= \frac{36\mu\phi^2}{\rho^w}\sum_{i=1}^{npi}\Delta u_h(\xi_1)^{-4}J^{\Gamma\gamma}(\xi_1)W^i\frac{\partial \Delta u_h(\xi_1)}{\partial U_{(i)}^{Node}} \\
&= \sum_{i=1}^{npi}\left(\frac{36\mu\phi^2}{\rho^w}\Delta u_h(\xi_1)^{-4}\right)J^{\Gamma\gamma}(\xi_1)W^i\frac{\partial \Delta u_h(\xi_1)}{\partial U_{(i)}^{Node}} \qquad (6.32)
\end{aligned}$$

(6.33)

These partial derivatives can be cast in a $[1\times 8]$ matrix as:

$$\left[\frac{\partial \phi}{\partial U^{Node}}{}_{(1\times 8)}\right] = \sum_{i=1}^{npi}\left(\frac{36\mu\phi^2}{\rho^w}\Delta u_h(\xi_1)^{-4}\right)J^{\Gamma\gamma}(\xi_1)W^i\left[\frac{\partial \Delta u_h(\xi_1)}{\partial U^{Node}}{}_{(1\times 8)}\right] \tag{6.34}$$

The variation of Δu_h at any point ξ in the parent element is given by (5.25). Substitution of the different equations leads to the definition of the element matrix:

$$[K^{hm}]^e = \rho^w(p(n_2)-p(n_1))\begin{bmatrix}-1\\1\end{bmatrix}\left[\frac{\partial \phi}{\partial U^{Node}}{}_{(1\times 8)}\right] \tag{6.35}$$

where the matrix $[-1;1]$ comes from the relation between interface fluid mass flux ϖ and the residual mass balance at the interface hydraulic nodes $\{q^e\}$:

$$\{q^e\} = \begin{bmatrix}-1\\1\end{bmatrix}\varpi \tag{6.36}$$

The element coupling matrix therefore holds the relation

$$\{\delta q^e\} = [K^{hm}]^e \{\delta U_{Node}\} \tag{6.37}$$

The element matrices $[K^{hm}]^e$ can be assembled to find the matrix $[K^{hm}_{(m\times n)}]$ after which all matrices for the variation of the fluid flow are defined.

6.3.2 Partial derivatives for the variation of specific fluid mass M

In the same way as presented for the fluid flux, the variation of the specific fluid mass δM can be divided in a rheological part $\delta M^R = V\delta\rho^M$ and a volumetric part $\delta M^V = \delta V \rho^M$. For the rheological part, it is straightforward to obtain the incremental relation, which in matrix form can be written as

$$[M2_{(1\times 1)}]\delta p^M = \delta M^R \qquad\qquad [M2_{(1\times 1)}] = \frac{M}{k^w} \tag{6.38}$$

with k^w the fluid compressibility.

The volumetric contribution requires the relation between variations of hydraulic interface openings and nodal displacements. This is obtained from the integration of the variation of hydraulic interface opening over the interface elements. The variation of the normal and tangential opening of an interface element is given by (5.25) from which the equation for the variation of the hydraulic interface opening can be obtained:

$$\delta\Delta u_h = \begin{bmatrix} 0 & \frac{\partial \Delta u_h}{\partial \Delta u_n} \end{bmatrix} [T^I][B^I]\{\delta U_{Node}\} \tag{6.39}$$

The partial derivative $\partial\Delta u_h/\partial\Delta u_h$ depends on the state of opening of the interface (see Section 5.2):

$$\begin{aligned} \frac{\partial \Delta u_h}{\partial \Delta u_n} &= a^h \qquad \text{if} \quad \Delta u_n \geq \Delta u_n^{lin} \\ &= 0 \qquad \text{if} \quad \Delta u_n < \Delta u_n^{lin} \end{aligned} \tag{6.40}$$

Numerical integration will define an element matrix $[V1^e]$ as

$$[V1^e] = \frac{1}{V^{REV}} \sum_{i=1}^{npi} \rho^w \begin{bmatrix} 0 & \frac{\partial \Delta u_h}{\partial \Delta u_n} \end{bmatrix} [T^I][B^I] J^{\Gamma\gamma} W^i \tag{6.41}$$

which holds the incremental relation

$$\delta M^{Ve} = [V2^e]\{\delta U_{Node}\} \tag{6.42}$$

with δM^{Ve} the volumetric part of the contribution of the interface element to the variation of the specific fluid mass. Assembly of these element matrices leads to the last required global matrix for the variation of the specific fluid mass:

$$[V1_{(1\times n)}]\{\delta u_{(n)}\} = \delta M^V \tag{6.43}$$

6.3.3 Partial derivatives for the variation of nodal forces

The third set of responses in the coupled frame is that of the variations of stresses $\{\delta\sigma_{(4)}\}$ which depend on variations of macroscale pressure δp^M and nodal displacements δu. Both are involved in the microscale equilibrium of nodal forces f and the relation of the variation of nodal residual forces can be written as

$$\{\delta f_{(n)}\} = [K^{mm}_{(n\times n)}]\{\delta u_{(n)}\} + [K^{mP}_{(n\times 1)}]\delta p^M \tag{6.44}$$

The matrix $[K^{mm}_{(n\times n)}]$ has been used to solve the system of equations of the mechanical problem for constant p^M and needs no development The matrix $[K^{mP}_{(n\times 1)}]$ takes into account the variation of fluid pressure acting normally on the grain boundaries. The variation of the hydraulic pressure $\delta\vec{f}^p_{loc}$ acting normally on the grains is directly dependent on the variation of the macroscale fluid pressure δp^M. Writing this as a vector for straightforward incorporation in the interface element integration gives a normal fluid pressure contribution vector:

$$\delta\vec{f}^p_{loc} = \begin{bmatrix} 0 \\ -\delta p^M \end{bmatrix} \tag{6.45}$$

Following an equivalent development of numerical integration as outlined in Section 5.1.2 for the stiffness matrix related to the interface cohesion , the variation of the nodal contribution of the fluid pressure on the residual forces of the interface elements as a function of the variation of macroscale fluid pressure can be found:

$$[N^{Ie}] = \sum_{i=1}^{npi} J^{\Gamma\gamma}(\xi^i_1)[B^{Ip}(\xi^i_1)]^T[T^{Ip}(\xi^i_1)]^T \begin{bmatrix} 0 \\ -1 \end{bmatrix} W^i \tag{6.46}$$

with $[0;-1]$ representing the partial derivatives $\partial f^p_t/\partial p^M$ and $\partial f^p_n/\partial p^M$. The matrices $[T^{Ip}]$ and $[B^Ip]$ are define as follows:

$$[B^{Ip}] = \begin{bmatrix} -N^{(1)} & -N^{(2)} & N^{(3)} & N^{(4)} \\ -N^{(1)} & -N^{(2)} & N^{(3)} & N^{(4)} \end{bmatrix} \tag{6.47}$$

$$[T^I] = \begin{bmatrix} \frac{\partial x_t}{\partial \xi_1} & 0 \\ 0 & \frac{\partial x_n}{\partial \xi_2} \end{bmatrix} \begin{bmatrix} \frac{\partial \xi_1}{\partial x_1} & \frac{\partial \xi_1}{\partial x_2} \\ \frac{\partial \xi_2}{\partial x_1} & \frac{\partial \xi_2}{\partial x_2} \end{bmatrix} = \begin{bmatrix} \cos(\theta) & \sin(\theta) \\ -\sin(\theta) & \cos(\theta) \end{bmatrix} \tag{5.24}\ (6.48)$$

This interface element matrix holds the following relation;

$$\{\delta f^p\}^e = [N^{Ie}]\delta p^M \tag{6.49}$$

The assembly of the the interface element matrices $[N^{ie}]$ provides global matrix $[N_{(n\times 1)}]$.

6.3.4 Assembly, reduction and condensation of the coupled matrix

The matrices containing the equations for the variations of forces, fluid fluxes and fluid mass derived in the previous sections can be assembled into the frame of

6.23, which leads to the following system of equations:

$$\begin{bmatrix} \begin{bmatrix} 0_{(4\times4)} & 0_{(4\times2)} & 0_{(4\times1)} \\ 0_{(2\times4)} & 0_{(1\times2)} & M1_{(2\times1)} \\ 0_{(1\times4)} & 0_{(1\times2)} & M2_{(1\times1)} \end{bmatrix} & \begin{bmatrix} 0_{(4\times n)} \\ 0_{(2\times n)} \\ V1_{(1\times n)} \end{bmatrix} & \begin{bmatrix} 0_{(4\times m)} \\ 0_{(2\times m)} \\ 0_{(1\times m)} \end{bmatrix} \\ \begin{bmatrix} 0_{(n\times4)} & 0_{(n\times2)} & K^{mP}_{(n\times1)} \end{bmatrix} & \begin{bmatrix} K^{mm}_{(n\times n)} \end{bmatrix} & \begin{bmatrix} 0_{(n\times m)} \end{bmatrix} \\ \begin{bmatrix} 0_{(m\times4)} & 0_{(m\times2)} & 0_{(m\times1)} \end{bmatrix} & \begin{bmatrix} K^{hm}_{(m\times n)} \end{bmatrix} & \begin{bmatrix} K^{hh}_{(m_\times m)} \end{bmatrix} \end{bmatrix} \begin{Bmatrix} \delta\varepsilon^{REV}_{(4)} \\ \delta\nabla p^{REV}_{(2)} \\ \delta p^{M} \\ \\ \delta u_{(n)} \\ \delta p_{(m)} \end{Bmatrix} = \begin{Bmatrix} \delta 0_{(4)} \\ \delta m^{R}_{(2)} \\ \delta M \\ \\ \delta f_{(n)} \\ \delta q_{(m)} \end{Bmatrix} \tag{6.50}$$

The system of equations (6.50) is reduced by eliminating the dependent degrees of freedom located on the follow boundary. This is done by means of the following boundary conditions:

$$\delta u^F_i = \delta u^L_i + \varepsilon^M_{ij} y_j \qquad \text{(Equation (4.8))} \tag{6.51}$$

$$\delta \hat{p}^F = \delta \hat{p}^L + \frac{\partial p^M}{\partial x_j} y_j \qquad \text{(Equation (4.12))} \tag{6.52}$$

$$\delta f^F_i = -\delta f^L_i \qquad \text{(Equation (4.11))} \tag{6.53}$$

$$\delta {q^V}^F = -\delta {q^V}^L \qquad \text{(Equation (4.14))} \tag{6.54}$$

In addition, the following averaging summations are used for row-operations towards the upper 6 rows of the system of equations:

$$\delta\sigma^{REV}_{ij} = \sum_{\Gamma^F} \delta f^F_i y_j \tag{6.55}$$

$$\delta m^{V,REV}_i = \sum_{\Gamma^F} \delta {q^V}^F_i y_j \tag{6.56}$$

The total variation of macroscale fluid flux δm_i is the sum of its rheological and volumetric parts

$$\delta m^{REV}_i = \delta m^{REV,R}_i + \delta m^{REV,V}_i \tag{6.57}$$

The resulting reduced system of equations is given the following:

$$\begin{bmatrix} \begin{bmatrix} T^1_{(4\times4)} & 0_{(4\times2)} & T^2_{(4\times1)} \\ T^4_{(2\times4)} & T^5_{(1\times2)} & M1_{(2\times1)} \\ T^8_{(1\times4)} & 0_{(1\times2)} & M2_{(1\times1)} \end{bmatrix} & \begin{bmatrix} T^3_{(4\times n_i)} \\ T^6_{(2\times n_i)} \\ V1^\star_{(1\times n_i)} \end{bmatrix} & \begin{bmatrix} 0_{(4\times m_i)} \\ T^7_{(2\times m_i)} \\ 0_{(1\times m_i)} \end{bmatrix} \\ \begin{bmatrix} T^9_{(n\times4)} & 0_{(n_i\times2)} & K^{\star mP}_{(n_i\times1)} \end{bmatrix} & \begin{bmatrix} K^{\star mm}_{(n_i\times n_i)} \end{bmatrix} & \begin{bmatrix} 0_{(n_i\times m_i)} \end{bmatrix} \\ \begin{bmatrix} T^{10}_{(m_i\times4)} & T^{11}_{(m_i\times2)} & 0_{(m_i\times1)} \end{bmatrix} & \begin{bmatrix} K^{\star hm}_{(m_i\times n_i)} \end{bmatrix} & \begin{bmatrix} K^{\star hh}_{(m_i\times m_i)} \end{bmatrix} \end{bmatrix} \begin{Bmatrix} \delta\varepsilon^{REV}_{(4)} \\ \delta\nabla p^{REV}_{(2)} \\ \delta p^{M} \\ \\ \delta u_{(n_i)} \\ \delta p_{(m_i)} \end{Bmatrix} = \begin{Bmatrix} \delta\sigma_{(4)} \\ \delta m^{REV}_{(2)} \\ \delta M \\ \\ 0_{(n_i)} \\ 0_{(m_i)} \end{Bmatrix}$$

(6.58)

with $[T^{1-11}]$ some temporary matrices, the superscript * indicating the reduced form of the original matrix and n_i and m_i the number of independent mechanical and hydraulic degrees of freedom respectively. A shorter notation is introduced for this reduced system of equations:

$$\begin{bmatrix} [T_A] & [T_B] \\ [T_C] & [T_D] \end{bmatrix} \begin{Bmatrix} \delta U^{REV}_{(7)} \\ \delta U_{(n_i+m_i)} \end{Bmatrix} = \begin{Bmatrix} \delta \Sigma^{REV}_{(7)} \\ 0_{(n_i+m_i)} \end{Bmatrix} \tag{6.59}$$

with $[T_{A-D}]$ the reduced matrix and $\{\delta U^m_{(m_i+n_i)}\}$ the independent microscale degrees of freedom.

From this system of equations, the independent degrees of freedom are reduced by static condensation on the seven macro variables. This results in the following condensed system of equations:

$$[A^{REV}_{(7\times7)}][\delta U_{(7)}] = [\delta \Sigma^{REV}_{(7)}] \tag{6.60}$$

with

$$[A^{REV}_{(7\times7)}] = [T_A] - [T_B]\,[T_D]^{-1}\,[T_C] \tag{6.61}$$

A last transformation is needed to change from fluid mass M to the rate of change of the fluid mass $\dot{M}$. For the incremental time step Δt, the rate of change of fluid mass density is computed as

$$\dot{M}^t = \frac{M^t - M^{t-\Delta t}}{\Delta t} \tag{6.62}$$

this means that the variation of the rate of change of the fluid mass density $\delta \dot{M}^t$ can be found as

$$\delta \dot{M} = \frac{\delta M^t}{\Delta t} \tag{6.63}$$

this transformation requires the seventh row of matrix [A] to be divided by Δt. Splitting matrix $[A_{(7\times7)}]$ into the matrices $[C^{REV}_{(4\times4)}]$,$[K^{REV}_{hm(3\times4)}]$,$[K^{REV}_{hh(3\times3)}]$ and $[K^{REV}_{mh(4\times3)}]$, gives the linearization of the constitutive relations relative to the REV symmetric orientations. A consistent rotation of these tangent stiffness matrices by $\boldsymbol{R}^M$ (Equation (4.16)) gives the consistent tangent stiffness matrices of the classical part required in Equation (3.7). The rotation of matrix $[C^{REV}]$ to $[C^M]$ is given above in section 6.2, for which the full derivation is given in appendix A.3. For the rotation of the other coupled terms, the rotation back to the macroscale reference follow the same objective rotation of the stiffness matrix. Their results can be found in Appendix A.3.

6.4 Computational homogenization by static condensation of HM coupled FE systems of equations with the diffusive flow

The procedure for computational homogenization by static condensation for HM-coupled macroscale behaviour introduced in the previous section is a general

procedure, but the example of the assembly of the extended system of equations for the combination of micro and macro variables was given for the pore channel flow model only. The incorporation of the diffusive flow model in the computational homogenization is straightforward and only requires the contribution of the diffusive flow to be added to the assembled system of Equations 6.50.

The contributions of the diffusive flow model, which is completely independent of the deformation, are at play in the rheological terms of the the specific fluid mass (grain pore volume is assumed constant, which means that the volumetric part of the variation remains unchanged) and the total fluid mass flux (both rheological and volumetric contributions). The contribution to the rheological part of the variation of specific fluid mass is the introduced pore volume in the grains, which means that specific fluid mass M in (6.38) has to be computed as the sum over the fluid mass in the interfaces and the grain pore volume.

The rheological part of the fluid flux is taken into account at the macroscale by the macroscale mass flux m_i^{REV} in matrix $[M1_{(2\times1)}]$. The volumetric contribution is taken into account in the equations for solving the microscale hydraulic problem by condensed matrix $[H^\star]$ in equation (5.100), which is repeated here as:

$$\begin{bmatrix} G + H^{\star hh} & H^{\star hp} \\ H^{\star ph} & H^{\star pp} \end{bmatrix} \begin{Bmatrix} \delta p^h \\ \delta \nabla p^M \end{Bmatrix} = \begin{Bmatrix} \delta q^V \\ \delta m^{\star diff} \end{Bmatrix} \qquad (5.100) \qquad (6.64)$$

The assembly of matrix $[H^\star]$ in (6.50) leads to:

$$\begin{bmatrix} \begin{bmatrix} 0_{(4\times4)} & 0_{(4\times2)} & 0_{(4\times1)} \\ 0_{(2\times4)} & H^{\star pp}_{(2\times2)} & M1_{(2\times1)} \\ 0_{(1\times4)} & 0_{(1\times2)} & M2_{(1\times1)} \end{bmatrix} & \begin{bmatrix} 0_{(4\times n)} \\ 0_{(2\times n)} \\ V1_{(1\times n)} \end{bmatrix} & \begin{bmatrix} 0_{(4\times m)} \\ H^{\star ph}_{(2\times m)} \\ 0_{(1\times m)} \end{bmatrix} \\ \begin{bmatrix} 0_{(n\times4)} & 0_{(n\times2)} & K^{mP}_{(n\times1)} \end{bmatrix} & \begin{bmatrix} K^{mm}_{(n\times n)} \end{bmatrix} & \begin{bmatrix} 0_{(n\times m)} \end{bmatrix} \\ \begin{bmatrix} 0_{(m\times4)} & H^{\star hp}_{(m\times2)} & 0_{(m\times1)} \end{bmatrix} & \begin{bmatrix} K^{hm}_{(m\times n)} \end{bmatrix} & \begin{bmatrix} K^{hh}_{(m\times m)} \end{bmatrix} \end{bmatrix} \begin{Bmatrix} \delta \varepsilon^{REV}_{(4)} \\ \delta \nabla p^{REV}_{(2)} \\ \delta p^M \\ \delta u_{(n)} \\ \delta \hat{p}_{(m)} \end{Bmatrix} = \begin{Bmatrix} \delta 0_{(4)} \\ \delta m^R_{(2)} + \delta m^{\star diff}_{(2)} \\ \delta M \\ \delta f_{(n)} \\ \delta q^V_{(m)} \end{Bmatrix} \qquad (6.65)$$

where $[K^{hh}_{(m\times m)}]$ is now defined as:

$$[K^{hh}_{(m\times m)}] = [G] + [H^{\star hh}] \qquad (6.66)$$

The reduction of this system of equations and its condensation into the 7×7 consistent tangent operator $[A^{REV}_{(7\times7}]$ is exactly identical to the procedure described in the previous chapter.

CONCLUSIONS PART II

In this part, a modified version of the Frey model for hydromechanical coupling was presented. The main modifications have been the adoption of the small strain assumption and the introduction of the separation of scales in the description of the fluid pressures. This has allowed the decomposition of the coupled problem at the microscale in a mechanical and a hydraulic problem that can be solved subsequently and has introduced a consistent description of the hydromechanical boundary conditions on the REV with respect to the principle of separation of scales. Secondly, the modifications allowed the consistent application of computational homogenization for the micro-to-macro transition. The procedure of first order computational homogenization was extended for the case of hydromechanical coupling and can now be used for obtaining the homogenized response to deformation loading and the associated consistent tangent operators. In this way, the modelling of the response of a micromechanical REV provides a numerically homogenized first order constitutive relation for hydromechanical coupled behaviour. This constitutive relation can be used in a macroscale computation. When implemented in a finite element code, this gives the finite element squared (FE^2) method. The numerical implementation of the model, its combination with computational homogenization and the implementation as a constitutive relation in an existing finite element code are the subject of the next Part.

Part III

IMPLEMENTATION AND APPLICATION EXAMPLES OF THE DOUBLESCALE MODEL

7. NUMERICAL IMPLEMENTATION

In order to solve the macroscale REV boundary value problem introduced in the sections above, the microscale model is implemented in the finite element code Lagamine [Charlier, 1987] as an independent constitutive law to provide the constitutive relations to be used in the macroscale iterative loading step $\Omega^{t-\Delta t} \rightarrow \Omega^{\tau 2}$ with $\Omega^{\tau 2}$ the next test solution for configuration Ω^{t}. The corresponding microscale BVP of enforcing the deformation loading step $F^{t-\Delta t} \rightarrow F^{\tau 2}$ on the periodic REV is again solved using the finite element method. In this chapter, some aspects of the implementation of the microscale model in a finite element code are discussed.

7.1 Numerical scheme for solving the microscale system of equations

The microscale finite element code is used for the computation of the behaviour of the REV in the loading path from initial configuration $\Omega^{t-\Delta t}$ to $\Omega^{\tau 2}$. A global scheme of the microscale computations is given in Figure 7.1, starting with the transition of the local macroscale variables to the microlevel. From the previous loading steps, the REV configuration $\Omega^{t-\Delta t}$ is known. This initial configuration is fully characterized by the microscale nodal positions $\{x^{t-\Delta t}\}$ and the interface state parameters $\{D^{t-\Delta t}\}$. Starting from this initial configuration, the mechanical problem is solved following a full Newton-Raphson scheme, using the symmetric part of the macroscale deformation gradient tensor $U^{\tau 2}$ for the periodic boundary conditions and the macroscale pressure $p^{\tau 2}$ for the normal fluid forces acting on the interface boundaries.

7.1.1 Enforcing the periodic boundary conditions

The periodic displacements of the REV boundaries are enforced through penalization of the periodic couples δu_i^L and δu_i^F by adding the following penalization equations to the global stiffness matrix during the first iteration:

$$\pm G^p \delta u_i^F \mp G^p \delta u_i^L = \pm G^p \Delta U_{ij}^{\tau 2} y_j \tag{7.1}$$

with $\Delta U_{ij}^{\tau 2} = U_{ij}^{\tau 2} - U_{ij}^{t-\Delta t}$ the required update of the symmetric part of the macroscale deformation gradient tensor (the macro stretch) related to the macroscale iteration to configuration $\Omega^{\tau 2}$. For all subsequent microscale iterations, the penalization of periodic boundary conditions reduces to

$$\pm G^p \delta u_i^F \mp G^p \delta u_i^L = 0 \tag{7.2}$$

Penalization term G^p has no physical meaning and penalization is only used for solving the boundary value problem. The size of the penalization term has to be

chosen carefully; a too large penalization term introduces numerical inaccuracies in the result as larger penalization numbers will increase the relative difference in the eigenvalues of the system of equations and the underlying equations will be lost in the numerical precision of the terms. A too small penalization can lead to boundary conditions which are not met accurately.

This method of penalization of the boundary conditions is not a unique method and other ways of enforcing the periodic constraints can be envisioned. However, the penalization method provides a straightforward way of introducing a deformation update without a-priori defined assumptions about the field of deformation. This means that the deformation loading can be applied during the first iteration. It should be noted that the penalization terms for the periodic boundary conditions are not required in the condensation for obtaining the consistent tangent stiffness matrix and a separate global system of equations needs to be assembled for this purpose without taking into account the periodic boundary conditions. The periodic boundary conditions are taken into account by means of reduction of the global system of equations instead.

7.1.2 Microscale convergence criterion

The Newton-Raphson iterative procedure to solve the mechanical problem follows the classical procedure, which is repeated in Table 7.1. Its convergence is evaluated by means of an evaluation of the residual forces, which are the components of array vector $\{f\}$ containing the nodal reaction and out-of-balance forces. To define a dimensionless number for the convergence criterion, reaction (or external) force and out-of-balance (or internal) force summations are defined as;

$$R^{ext} = \{(f^{ext})\}_{(i)}\{(f^{ext})\}_{(i)} \tag{7.3}$$

$$R^{int} = \{(f^{int})\}_{(i)}\{(f^{int})\}_{(i)} \tag{7.4}$$

The normalized norm of the residual forces is then defined as the square root of the ratio of R^{int} and R^{ext}:

$$R^{norm} = \sqrt{\frac{R^{int}}{R^{ext}}} \tag{7.5}$$

The microscale computation is supposed to be in equilibrium as soon as $R^{norm} < \epsilon^c$, with ϵ^c a small value of choice. The choice of this value determines not only the precision of the results, but will also influence the consistency of the tangent operators. This means that the convergence criterion ϵ^c has to be chosen as small as possible to obtain the best possible macroscale results. The practical limit of precision for ϵ^c is around 1×10^{-8}. Whenever the residual term of external forces becomes zero, an alternative formulation is required to obtain convergence and a replacement value has to be used for R^{ext}. There is some arbitrariness in the choice of a replacement value, as it has to correspond to the order of magnitude of element residual forces under consideration, which can vary depending on the application of the model.

7.1.3 Microscale non-convergence mitigation

The deformation loading step enforced on the REV by the macroscale deformation is applied in a single step, corresponding to the macroscale loading step related to the configuration update $\Omega^{t-\Delta t} \rightarrow \Omega^{\tau 2}$

In general, a solution for the boundary value problem can be found using a single deformation loading step on the REV, which corresponds to the macroscale loading step. For high linearity of the micromechanical constitutive relations and due to the lack of geometrical non-linearities, microscale convergence is usually very efficient.

In case of non-convergence (determined by means of number of iterations) of the microscale Newton-Raphson scheme, some additional successive techniques are used to solve microscale BVP:

- Taking substeps: whenever the maximum number of iterations is reached for a microscale loading step, the loading step at the microscale is reduced by a factor 2. This procedure is repeated up to a minimum loading step, for which non-convergence is considered to indicate the impossibility of finding a solution for this configuration of the REV.

- Microlevel numerical damping. In order to mitigate numerical oscillations between or around possible solutions, numerical damping is applied on the nodal displacement update as soon as the number of iterations reaches half of the maximum number of iterations.

- Weakening the microscale convergence condition. Whenever the microscale time step is reduced, the convergence criterion is temporarily weakened: $\epsilon_c := \sqrt{\epsilon_c}$. The final substep to obtain the total deformation loading step uses the original convergence criterion to guarantee a good convergence, which is required for obtaining a sufficiently consistent tangent operator and homogenized stress tensor.

With a combination of these three techniques, most of the non-convergence problems at the microscale can be mitigated. However, taking substeps can significantly increase the number of iterations for a deformation loading step on a single REV, and the computation time for a single macroscale iteration can easily increase from several minutes to several hours. If, eventually, no solution can be found on the micro level, the macroscale NR scheme is restarted for a smaller loading step.

7.1.4 The routine for the microscale loading steps

The computations on the microscale can be divided into three main parts of computations:

- The Newton-Raphson iterative routine for solving the mechanical problem

- The direct routine for solving the fluid flow problem

- The condensation routine for the computational homogenization by static condensation of the consistent tangent operators.

This is schematically presented in Figure 7.1.

The mechanical system is solved for by enforcing the macroscale deformation gradient tensor $\boldsymbol{F}^{REV,\tau 2}$ and fluid pressure $p^{M,\tau 2}$ on the REV boundary value problem starting from the configuration of the last converged step $\Omega^{t-\Delta t}$, characterized completely by its nodal coordinates $\{x^{t-\Delta t}\}$ and interface state parameters $\{D^{t-\Delta t}\}$.

Once microscale equilibrium is obtained for configuration $\Omega^{\tau 2}$, the updated microscale nodal coordinates and interface state parameters are stored as a candidate for the final configuration Ω^{t}. Based on the mechanical interface openings, the hydraulic interface openings Δu_h are defined and the specific fluid mass $M^{\tau 2}$ is obtained from an integral of the (spatially constant) fluid density $\rho^{w\,\tau 2}$ over the REV. Both interface channel pore space V^{int} and grain porosity φ are taken into account in this integral.

With the information on the hydraulic opening of the interfaces, the fluid system can be solved for fluid mass fluxes $\vec{m}^{\tau 2}$. The fluid system is solved twice; once to obtain the microscale fluid pressure difference over the interface elements $\Delta^e \hat{p}$ in Equation (6.22) and once by condensing directly on the macroscale pressure gradient to find the fluid flux of Equation (5.63) or (5.64). The element pressure difference is needed for the derivations of the equations for the additional couplings that need to be taken into account in the computational homogenization. These derivations are given in Sections 6.3.1, 6.3.2 and 6.3.3. These additional coupling terms are obtained in loop over the (interface) elements, using the updated configuration $\Omega^{\tau 2}$ with the interface pressure differences $\Delta^e \hat{p}^{\tau 2}$.

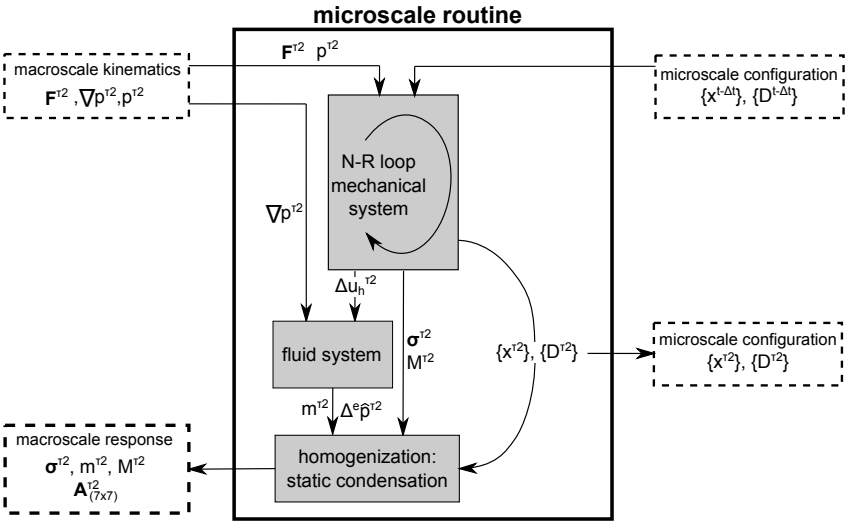

Fig. 7.1: Global scheme for solving the coupled microscale problem. The transition of auxiliary information (stiffness matrices, local information) is not shown.

Using the information that is available from the decoupled solving of the mechanical and hydraulic systems, the routine for the condensation into the tangent stiffness matrix is launched. This routine contains the aforementioned element routine for the missing coupling terms, after which the coupled extended global system of equations is assembled. The system is then reduced and condensed into

the tangent stiffness matrix $[A_{7\times7}]$ as presented before.

For solving the numerical systems of equations related to the condensation of (6.61) (that is, finding a temporary term $[T^{temp}] = [T_D]^{-1}[T_C]$, the auxiliary problem $[T_D][T^{temp}] = [T_C]$ is solved by Gaussian-elimination of the augmented matrix $[T_D|T_C]$. Efficiency of the procedure of the Gaussian elimination is obtained by taking into account the bandwidth, which is optimized by means of the renumbering of the mechanical system of equations following the Cuthill-McKee algorithm [Cuthill and McKee, 1969], which is a standardized approach for bandwidth reduction. The profile of such a reduced system of equations is given in Figure 12.3. In case of purely mechanical problems, the auxiliary problem to obtain the temporary matrix is solved for the static condensation in (6.16).

7.2 A routine for material point BVPs

The microscale model gives, together with the computational homogenization for scale transition, the possibility to define a macroscale constitutive relation based on the microstructure REV. The behaviour of this law represents the material behaviour as an average response to deformation loading on the microstructure. To study the local behaviour of this macroscale law under a certain loading path, the loading has to be applied incrementally (due to the (incremental) nonlinearity of the model) and the solution for each increment has to be solved iteratively based on the loading path conditions. A stand-alone routine is designed for applying mixed-mode (as a combination of stress and strain components) loading paths, thereby replacing the macroscale finite element computation. This routine is developed completely outside the macroscale finite element code.

Two column vectors $\{\dot{U}\}$ and $\{\dot{\Sigma}\}$ are defined as the time derivatives of the vectors $\{U\}$ and $\{\Sigma\}$, containing the deformation gradient tensor $\boldsymbol{F}$, fluid pressure gradient $\nabla_0 p^M$ and mean fluid pressure p^M and its response duals σ^M, $\vec{m}$ and M respectively. The time derivatives are defined with respect to the dimensionless time α. The material point boundary value problem is fully defined when for each of the seven components, one of the two duals is prescribed. For this purpose, the vectors are split in a prescribed part $^{(P)}$ and a reaction part $^{(R)}$ such that for each prescribed component $\dot{U}^{(P)}_{(i)}$ there are reaction components $\dot{\Sigma}^{(R)}_{(i)}$. In the same way, the prescribed components of the reaction vector $\dot{\Sigma}^{(P)}_{(i)}$ have corresponding kinematical components $\dot{\Sigma}^{(R)}_{(i)}$ as a reaction. The distribution in prescribed and reaction components

$$\{\dot{U}\} = \begin{Bmatrix} \dot{U}^{(P)} \\ \dot{U}^{(R)} \end{Bmatrix} \qquad \{\dot{\Sigma}\} = \begin{Bmatrix} \dot{\Sigma}^{(R)} \\ \dot{\Sigma}^{(P)} \end{Bmatrix} \tag{7.6}$$

The number of prescribed or reaction components depends on the boundary conditions of the unit cell boundary value problem and different steps in the loading conditions can require different subdivisions into prescribed and reaction components during a single simulation. Incremental loading by time steps $\Delta\alpha$ can be applied to follow the specified loading path. The loading increments related to $\{\dot{U}^{(P)}\}$ can be directly enforced as increments $\dot{U}^{(P)}_{(i)}\Delta\alpha$. The loading increments related to $\{\dot{\Sigma}^{(P)}\}$ are enforced through their responses $\{\dot{U}^{(R)}\}$. As the relation between $\{\dot{\Sigma}^{(P)}\}$ and $\{\dot{U}^{(R)}\}$ is unknown, the loading increments $\{\Delta U^{(R)}\}$ corresponding to $\{\dot{\Sigma}^{(P)}\Delta\alpha\}$ need to be solved for iteratively. A Newton-Raphson

iterative scheme is followed for this purpose. Using this scheme the iterative corrections are found by solving the linearized system of equations

$$[A^{\alpha}_{(7\times7)}]\{dU\} = -\{d\Sigma\}^{\alpha} \tag{7.7}$$

with $[A^{\alpha}_{(7\times7)}]$ the auxiliary matrix to find an update $\{dU^{(R)}\}$ that mitigates the out-of-balance stress $\{d\Sigma^{(P)}\}$. Convergence is obtained when the norm of the out-of-balance response in the stress rate-controlled components of the loading path are sufficiently small. In this way, the iterative Newton-Raphson solution scheme of the macroscale finite element problem described in Section 3.1 is simulated by the material point BVP. Combined with the possibility of the rotation of the REV with respect to the reference frame in which the loading is defined, it provides a versatile tool for studying the material behaviour under different loading paths. Moreover, the use of the tangent operator $[A]$ for solving the incremental displacements loading steps for the stress rate-controlled loading allow to assess the quality of the computationally homogenized constitutive relation by means of the convergence of the numerical scheme. To evaluate the convergence of the material point BVP, a criterion has to be defined based on the out-of-balance terms in $\{U\}$ and/or $\{\Sigma\}$. Considering the iterative updated $\{d\Sigma\}$ that is required to obtain the stress-controlled loading state, the residual term for the material point BVP R^{mp} is defined with three terms corresponding to the components of stress, fluid mass flux and fluid mass respectively.

$$R^{mp} = \frac{|\{d\Sigma^{(P)}_{(1-4)}\}|}{|\{\Sigma^{\alpha}_{(1-4)}\}|} + \frac{|d\Sigma^{(P)}_{(5-6)}|}{|\Sigma^{\alpha}_{(5-6)}|} + \frac{|d\Sigma^{(P)}_{(7)}|}{|\Sigma^{\alpha}_{(7)}|} \tag{7.8}$$

with $|.|$ the norm and $d[.]$ the out-of-balance or error with respect to the prescribed components in $\{\Sigma\}$. Note that the residual combines the relative out-of-balance norms for stresses (1-4), fluid mass flux (5-6) and fluid mass (7). In the case of deformation-controlled loading, the out-of-balance components are zero as no update is required. In case of a zero denominator, a minimum value is defined to avoid numerical infinity.

As an example, for the biaxial compression of a material point at 2 MPa confinement with constant pore pressure $p^M = 1\ MPa$ and vertical pressure gradient of 100 kPa/m, the following loading rates are applied in the material point BVP;

for $\alpha = -1 \rightarrow 0$		for $\alpha = 0 \rightarrow 10$	
$\dot{U}^{(P)} =$	$\dot{\Sigma}^{(P)} =$	$\dot{U}^{(P)} =$	$\dot{\Sigma}^{(P)} =$
$-$	$-2MPa$	$-$	0
$-$	0	$-$	0
0	$-$	0	$-$
$-$	$-2MPa$	$-.01$	$-$
$0MPa/m$	$-$	0	$-$
$0.1MPa/m$	$-$	0	$-$
$1MPa$	$-$	0	$-$

The time steps $\Delta\alpha$ used for the application of the mixed-mode loading are controlled by an algorithm increasing and decreasing $\Delta\alpha$ as a function of the

number of iterations required to obtain convergence of the macroscale material point BVP for stress-controlled loading.

The use of this routine is twofold; on one side it allows studying the behaviour of the material that was defined by the microstructure in the REV, on the other hand it can be used to test the computational homogenization, since the tangent stiffness matrices obtained through the computational homogenization are used to iteratively apply the correct loading path on the material point. The routine will therefore be used in the following chapters to study the material behaviour obtained from the microscale computations at the material point level. In addition, the quality of the obtained tangent operators is assessed by studying the rate of numerical convergence of the Newton-Raphson scheme of this routine.

1. initiate global stiffness matrix $[G]$ and reaction array $\{R\}$
2. compute boundary conditions update $\Delta y_i^{\tau 2} = U_{ij}^{\tau 2} y_j^0 - y_i^{t-\Delta t}$
3. Assemble penalization equations for boundary condition updates in $\{R\}$
4. i = 1
5. start iteration i
   (a) assemble penalization terms in $[G]$
   (b) element loop: build element system of equations and nodal forces
   (c) assemble equations in $[G]$ and nodal forces in $\{R\}$
   (d) check convergence: if $R^{norm} < \epsilon^c$ go to 6
   (e) solve for nodal updates $[G]\{dx\} = -\{R\}$
   (f) i = i+1, reset $[G]$ and $\{R\}$
   (g) go to 5
6. end of Newton-Raphson scheme

Tab. 7.1: microscale Newton-Raphson scheme

8. VERIFICATION OF THE MICROSCALE MODEL

In a first verification assessment, simplified microstructures are used, for which analytical solutions can be easily obtained. The first of these microstructures is given in Figure 8.1, together with the microscale constitutive parameters.

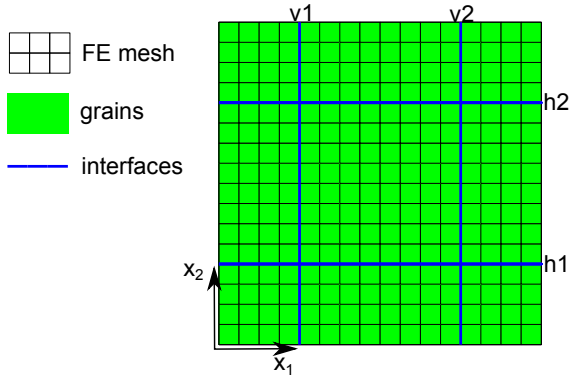

solids:	
E [GPa]	4.0
ν	0.300
k_{11} [10^{-15}m^2]	0.1
k_{22} [10^{-15}m^2]	1.0

interfaces:	
E_0 [GPa]	8.0
T^{max} [MPa]	10.0
δ^c	0.005
Δ_h^{min}	0.050 μm

Fig. 8.1: Microstructure used for the verification of the micromechanical model with the microscale constitutive parameters. Horizontal and vertical interface channels are labeled as $h1, h2$ and $v1, v2$ respectively.

8.1 Response to extension

For applying uniaxial extension of microstructure 8.1, the following macroscale kinematical loading paths are enforced on the REV;

$$\dot{\boldsymbol{F}} = \begin{bmatrix} 0 & 0 \\ 0 & 0.02 \end{bmatrix}, \qquad \dot{\vec{\nabla}} p^M = \vec{0}, \qquad \dot{p}^M = 0 \tag{8.1}$$

or:

$$\{\dot{U}\}^{(P)} = \begin{Bmatrix} 0 \\ 0 \\ 0 \\ 0.02 \\ 0 \\ 0 \\ 0 \end{Bmatrix} \tag{8.2}$$

The macroscale boundary conditions correspond to a macroscale axial strain ε_a^M that is enforced on a material point. For REV dimensions 1×1, the axial strain can be decomposed into the vertical component of the strain of the grains ε_{22} and

the normal interface openings of the horizontal interfaces Δu_n^{h1} and Δu_n^{h2}:

$$\varepsilon_a^M = \varepsilon_{22} + \Delta u_n^{h1} + \Delta u_n^{h2} \tag{8.3}$$

In addition to the parameters given in Figure 8.1, the permeability tensor for the solid parts is defined as:

$$\boldsymbol{k}^g = \begin{bmatrix} 10^{-16} & 0 \\ 0 & 10^{-15} \end{bmatrix} m^2 \tag{8.4}$$

Computations are performed both with and without taking into account the grain permeability. To assess the hydraulic properties the macroscale permeability is studied, for which a full hydromechanically coupled computation is not required.

As a function of the stiffness of the vertical interfaces $E_0^{v1} = E_0^{v2}$ (resulting from the interface cohesion parameters δ^c, D^0 and T^{max}) and the elasticity of the grains described by Lamé parameters λ and μ the vertical stress in the REV σ_{22} for a given vertical strain in the grain ε_{22} can be found analytically by taking into account the symmetry of the microstructure. This is done by considering the extension of a single grain as a system of a block of width 1/2 and a vertical interface (the interface spacing is 1/2), which is schematically presented in figure 8.2.

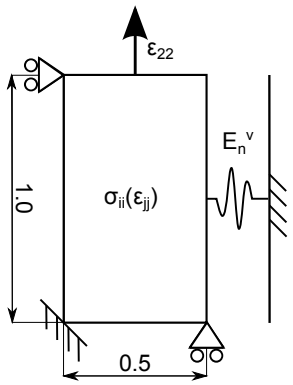

Fig. 8.2: Analytical model of the extension of a block, taking into account the interface stiffness

From the constitutive relation of the grains (5.103) and the stiffness of the vertical interface $E_n^v = T_n^v / \Delta u_n^v$ it follows that

$$\sigma_{11} = (2\mu + \lambda)\varepsilon_{11} + \lambda\varepsilon_{22} \tag{8.5}$$

$$\sigma_{22} = \lambda\varepsilon_{11} + (2\mu + \lambda)\varepsilon_{22} \tag{8.6}$$

$$T_n^v = E_n^v / \Delta u_n^v \tag{8.7}$$

Equilibrium on the vertical grain boundary requires $\sigma_{11} = T_n^v$ and the (vertical) interface spacing of 1/2 leads to $\Delta u_n^v + 0.5\varepsilon_{11} = 0$. This allows expressing ε_{11} as a function of ε_{22} by combining (8.5) and (8.7):

$$\varepsilon_{11} = -\frac{\lambda}{2\mu + \lambda + \frac{1}{2}E_n^v}\varepsilon_{22} \tag{8.8}$$

It follows from (8.6) that

$$\sigma_{22} = \left(2\mu + \lambda - \frac{\lambda^2}{\frac{1}{2}E_n^{v1} + 2\mu + \lambda}\right)\varepsilon_{22} = K^s \varepsilon_{22} \tag{8.9}$$

with ε_{22} the strain component in the grains and K^s a bulk stiffness term taking into account the stiffness of the vertical interfaces. Defining the interface normal stiffness of horizontal interfaces as E_n^{h1} and E_n^{h2}, the global response to extension according to (8.1) can be found by solving the system of equations for the opening of both interfaces and the strain in the grains.

$$\sigma_{22} = -E_n^{h1}\Delta u_n^{h1} \tag{8.10}$$
$$\sigma_{22} = -E_n^{h2}\Delta u_n^{h2} \tag{8.11}$$

The stiffness moduli E_n^{h1} and E_n^{h2} are used to characterize the interface cohesive tractions T_n^{h1} and T_n^{h2}, with the same relation for both interfaces. This gives a unique solution for the loading until softening takes place. In the softening regime, the uniqueness of the solution is lost, as either one of the two interfaces can soften while the other unloads, or both can follow the same softening path. In this example, two possible loading paths are followed: In case A the upper interface enters the softening regime, while the lower interface follows the unloading path until it closes (see Figure 8.3). In case B both interfaces are set to follow the unloading branch, leading to a symmetric solution for the deformation of the REV.

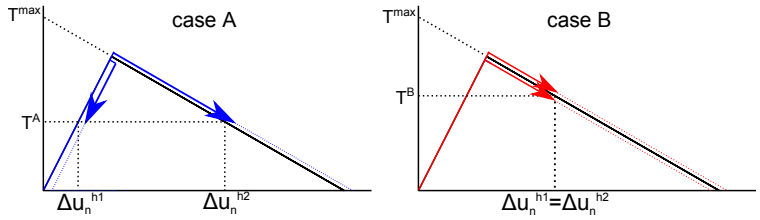

Fig. 8.3: Loading path of the normal component of the interfaces

Solving equations (8.9)-(8.11) for the interface openings Δu_n^1 and Δu_n^2 as a function of macro deformation ε_{22}^M provides an analytical solution for the homogenized permeability of cases A and B when the interface openings are translated into equivalent permeability terms. These cases give an upper and a lower bound solution for the general case in which no constraint on the interface softening is introduced. They form the reference solutions for the numerical response in Figure 8.4.

Mechanical response

The mechanical response to extension of the microstructure is given in Figure 8.4. The response of the both cases A and B is identical up to the point at which the softening limit of the interface damage law is reached (point a). The stress at this point corresponds well to the initial softening state parameter $D_n^0 = 0.2$ and a reference maximum cohesion $T_n^{max} = 10\ MPa$:

$$\sigma_{22} = T_n = T_n^{max}(1 - D_n^t)\frac{\Delta u_n^t}{\delta_n^c} = E^t \Delta u_n^t \tag{8.12}$$

Solving Equation (8.9) for an initial interface stiffness $E^0 = 8.0\ GPa$ results in the macroscale extension of $\varepsilon_{22}^M = 1/300$ as the point at which the first softening is induced (point a in the upper graph). After this point, cases A and B show a different loading path. The macroscale extensions of point b corresponds to the critical opening $\delta^c = 0.005$ of the interface channel following the softening branch in case A. Point c corresponds to twice this critical opening, as both upper and lower interfaces are forced to follow the softening branch.

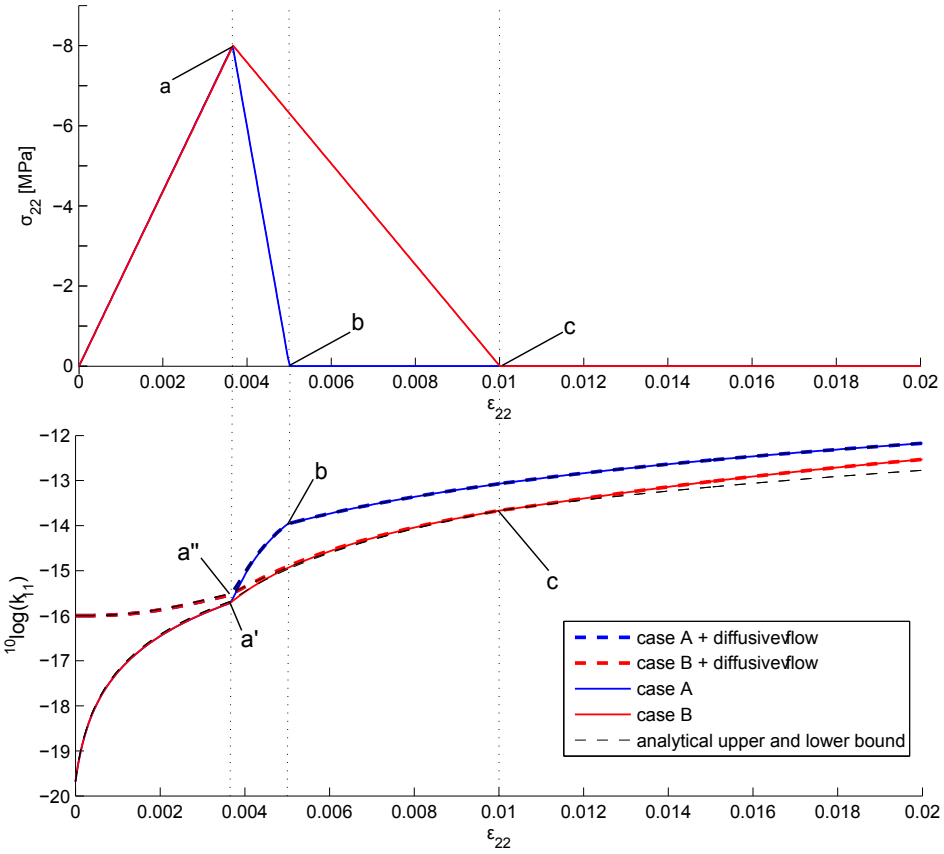

Fig. 8.4: Top: stress response to mechanical response to oedometric extension. Bottom: Evolution of horizontal permeability as a response to oedometric extension.

Hydraulic response

To study the effect of the deformation loading on the hydraulic behaviour, the macroscale equivalent permeability is evaluated. This permeability can be obtained analytically to compare with the numerical results. The macroscale axial strain $\varepsilon_a = \varepsilon_{22}^M$ can easily be related to the microscale strain and interface openings due to the geometry of the REV. For homogeneous strain ε in the grains, the macroscale axial strain can be related to the strain in the grains and the interface openings for a 1×1 REV:

$$\varepsilon_a = \varepsilon_{22} + \Delta u_n^{h1} + \Delta u_n^{h2} \tag{8.13}$$

With the analytical solutions for stress as a function of the microscopic strain ε_{22} and interface opening given above, the analytical solution for the interface opening as a function of ε_a^M can be found for cases A and B:

- $0 < \varepsilon_a < 1/300$

$$\begin{aligned} \Delta u_n^{h1,h2} &= \frac{K^s \delta^c D_n^0}{2K^s \delta^c D_n^0 + T_n^{max}(1 - D_n^0)} \, \varepsilon_a \qquad (8.14) \\ &\approx 0.298 \, \varepsilon_a \qquad (8.15) \end{aligned}$$

- Case A: $1/300 < \varepsilon_a < 0.005$

$$\begin{aligned} \Delta u_n^1 &= \frac{K^s \delta^c (1 - D_n^0)}{K^s (1 - 2D_n^0)\delta^c - T_n^{max}(1 - D_n^0)} \, \varepsilon_a \\ &\quad - \frac{K^s D_n^0 \delta^{c2} + T_n^{max}(1 - D_0^n)\delta^c}{K^s (1 - 2D_n^0)\delta^c - T_n^{max}(1 - D_n^0)} \qquad (8.15) \\ &\approx 2.426 \, \varepsilon_a - 0.00713 \end{aligned}$$

$$\begin{aligned} \Delta u_n^2 &= \frac{K^s D_n^0 \delta^c}{T_n^{max}(1 - D_n^0) - \delta^c K^s (1 - 2D_n^0)} \, \varepsilon_a \\ &\quad - \frac{K^s D_n^0 \delta^{c2}}{T_n^{max}(1 - D_n^0) - \delta^c K^s (1 - 2D_n^0)} \qquad (8.13) \\ &\approx -0.606 \, \varepsilon_a + 0.00303 \end{aligned}$$

- Case B: $1/300 < \varepsilon_a < 0.01$

$$\begin{aligned} \Delta u_n^{1,2} &= -\frac{\delta^c K^s}{T_n^{max} - 2K^s \delta^c} \, \varepsilon_a + \frac{T_n^{max} \delta^c}{T_n^{max} - 2K^s \delta^c} \\ &\approx 0.6016 \, \varepsilon_a - 0.00102 \qquad (8.10) \end{aligned}$$

It is stressed here again that the interface opening is dimensionless, or relative to the REV size. The hydraulic opening Δu_h can be computed from the normal mechanical openings Δu_n^{h1}, Δu_n^{h2}, Δu_n^{v1} and Δu_n^{v2} using (5.66). Translation parameters $\Delta u_h^0 = 0.02 \mu m$, $\Delta u_h^{min} = 0.01 \mu m$ and $a^h = 1 \; mm$ are used, resulting in an initial permeability in the order of $10^{-20} \; m^2$ related to the pore channel flow. In this chapter, these parameters are used for both the computations with only pore channel flow ($k_{ij}^g = 0$) and computations with combination of pore channel flow and diffusive flow in the grains:

$$k_{11}^M = \frac{1}{12L} \left({\Delta u_h^{h1}}^3 + {\Delta u_h^{h2}}^3 \right) + k_{11}^g \qquad (8.11)$$

$$k_{22}^{M} = \frac{1}{12L}\left(\Delta u_h^{v1\,3} + \Delta u_h^{v2\,3}\right) + k_{22}^{g} \tag{8.12}$$

with L the unit length in the out-of-plane direction, which is most conveniently chosen to be 1. The term k_{ii}^{g} is the (averaged) grain permeability, which in this case can be added in superposition with the interface conductivity. Diagonal term k_{12}^{g} is kept zero to avoid the analytical solution to become too complex and to be able to apply the superposition of contributions of the interfaces and the grains to the permeability. Moreover, superposition can be used only in this example with homogeneous hydraulic properties. In the general case with hydraulic heterogeneity (when either one of the interface elements transmissivity or grain permeability is not homogeneously distributed over the REV), the superposition of the separately computed hydraulic conductivity of interface flow and diffusive flow does not apply.

The numerical results are given in Figure 8.4 together with the results obtained from the numerical computations. The solutions for case A and B are, in line with the mechanical behaviour, identical up to the point of initiation of softening. The localization of the softening in a single interface in case A induces a higher rate of opening of this interface. This leads to a stronger increase in permeability for case A starting in points a' and a''. This effect comes to a hold at the complete unloading of the microstructure in point b, after which the increase in interface opening is identical to the increase in strain and the REV is stress-free.
For case B, in which the interfaces are enforced to open identically, point a' identifies the point of entering the softening branch, where the increase of the rate of change in permeability can be related to the unloading of the grains. This effect disappears at the point of unloading in point c. The requirement of equal interface openings has reproduced the lower bound solution that was found analytically. After point c, no constraint on the interface opening was enforced, leading to unequal opening of the upper and lower interface. The effect of this unequal interface opening is the increase of the permeability with respect to the lower bound solution after point c for equally-opened interfaces.

With the minimum hydraulic interface opening being very low, the definition of the grain permeability makes the diffusive flow the most prominent fluid mass flow mechanism under initial deformation state. With increasing opening of the interfaces, the interface flow will take over as the leading fluid transportation mechanism.

8.2 Pressure-induced permeability

For further verification of the evolution of the permeability as an effect of deformation, the following loading path is applied on the REV of Figure 8.1:

$$\dot{\boldsymbol{F}} = \begin{bmatrix} 0 & 0 \\ 0 & 0 \end{bmatrix}, \quad \dot{\vec{\nabla}} p^{M} = \begin{Bmatrix} 0 \\ 0 \end{Bmatrix}, \quad \dot{p}^{M} = 100 MPa/\alpha \tag{8.13}$$

The mechanical behaviour of the grains is characterized by their Young's modulus $E = 4GPa$ and Poisson's ratio $\nu = 0.3$. For isotropic loading under plane strain conditions, this corresponds to a bulk modulus $K^{*} = 6.5GPa$. An initial opening of the hydraulic interfaces is defined as $\Delta u_h^0 = 0.05\mu m$, corresponding to an

initial equivalent permeability of $2.083 \times 10^{-20} m^2$ for two interfaces per REV. Loading is applied in the form of an increasing fluid pressure p^M, while enforcing the macroscopic strain to be zero. In a first case, no normal cohesive forces are introduced. The opening of the interfaces is therefore completely controlled by the compressibility of the grains. Given the symmetry of the microstructure and the homogeneous distribution of the interfaces, it is easily verified that there is an analytical solution for the normal mechanical opening of the interfaces under the constraint that both interfaces are equally opened (as one of the possible solutions when cohesive softening takes place). The relation between normal interface opening and the fluid pressure is:

$$\Delta u_n = \frac{1}{2} \frac{p^m}{K^\star} 10^{-3} m \tag{8.14}$$

Making the transformation to hydraulic opening allows computing the macroscale effective permeability by Equation (8.11), including a possible grain permeability $\boldsymbol{k}^g$. This provides the analytical solution that is to be compared with the numerical result.

For the numerical results, two case are considered; case A with a normal interface cohesion $T_n^{max} = 40 MPa$, case B with a negligible interface cohesion $T_n^{max} = 1.0\ kPa$ (zero cohesion is avoided to guarantee a proper solution in the initial part of loading). Case B is compared with the analytical results in figure 8.6, which shows that the numerical results are in good agreement with the analytical solution.

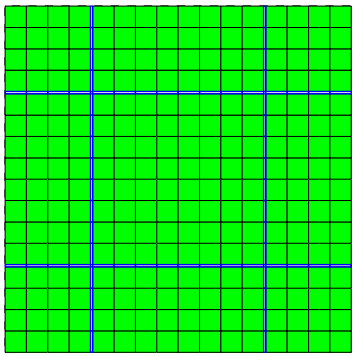

Fig. 8.5: Deformed microstructure at pressure $p^M = 10 MPa$. The normal interface opening is $\Delta u_n = 0.0065$, corresponding to a hydraulic opening of $\Delta u_h = 6.55\ \mu m$

Figure 8.6 has been obtained by artificially constraining the interface openings to be equal, in order to avoid the possible 'drifting' of the solutions such as observed after complete decohesion of the interfaces in Figure 8.4. Moreover, the difference between cases A and B demonstrates the different stages in the evolution of permeability with increasing pore pressure.

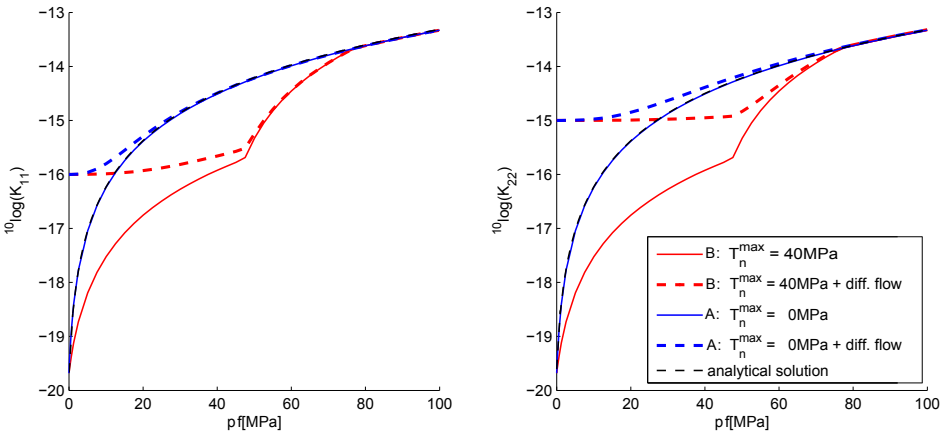

Fig. 8.6: pressure-induced permeability evolution. Dotted lines take into account the grain permeability (8.4). For the red lines, normal cohesive forces are active

8.3 Undrained isotropic loading

In this third example, microstructure 1 is loaded from the initial configuration up to an isotropic stress state of 100 MPa (extension) and $-100MPa$ (compression) under undrained conditions. This is done for different values of grain porosities φ and the pore fluid pressure as a response to this loading is studied. The influence of the porosity on the global response is through the rheological part of the fluid storage: The constant pore volume in the grains allows local storage of fluid mass with increasing fluid pressure through the compressibility of the fluid. The relation between the interface normal opening and corresponding interface hydraulic opening is presented graphically in Figure 5.7. With a minimum hydraulic opening of $\Delta u_h^{min} = 0.025\mu m$ and an initial hydraulic opening of $\Delta u_h^0 = 0.025\mu m$, there is a local variation in pore volume even for slightly negative (penalized) mechanical openings, which contributes to a geometric component of the local fluid storage.

Since the applied isotropic stress state is obtained through the application of a macroscale deformation, it is possible to distinguish the two tests by a compressive loading (negative stresses) and extensive loading (positive stresses). The hydraulic responses to compressive loading are given in Figure 8.7 for compression (left) and extension (right) for different grain porosities φ. For this example, the cohesive forces at the interfaces are taken to be negligible with respect to the normal interface contact forces and the hydraulic forces on the interface boundaries. In the case of extensional loading, the pore pressure p directly follows the enforced stress and $\partial p/\partial \sigma_{ii} \approx -1$. As the interface cohesion plays an inferior role, and in extension no interface normal forces are active, practically all forces are taken by the water. In Biot's consolidation theory, such a response corresponds to a Skempton coefficient $\beta_p \approx 1$, independent of the grain porosity. In case of compressive loading, the mechanical forces at the interfaces can take a more significant role in the micromechanical equilibrium. It is important to realize that the REV is considered globally undrained, but locally a redistribution of fluid mass is possible. This redistribution allows the fluid mass in the interface elements to enter the pore space in the grains (which is considered to be constant

and therefore independent of the grain deformation) depending on the pore pressure required for the compression of the fluid mass. The larger the ratio between the grain pore volume and the initial interface volume, the lower the pore fluid pressure drives the fluid out of the interfaces and the easier the normal interface contact forces can take over the isotropic stress σ_{ii}. The result is a series of pore pressure response curves starting with a one-to-one correspondence in case of zero grain porosity where the compressive loading remains fully taken by the (nearly incompressible) fluid. With increasing grain porosity, the change of pore pressure with confining stress decreases towards a $-\mathrm{d}p/\mathrm{d}\sigma_{ii}$ in the order of 0.01 for $\varphi = 0.1$.

The non-linearities are an effect of the non-linear nature of the normal part of the contact forces, where the non-linearities come mainly from the penalization of negative normal opening. The cohesive forces for positive interface openings are negligible with respect to the measured pore pressures in the experiment as can be observed from the quasilinear relation in case of extension. The non-linear response in case of compression shows the transition from a (quasi-)linear relation between stress and fluid pressure at relatively low pressure and a (quasi-) quadratic relation at higher pressures. This transition is a transition from a hydraulics-controlled response to a mechanics-controlled response. In the hydraulics-controlled response, the compressive load in the interfaces is mainly taken by the fluid pressure, which requires a compression of the fluid mass equal to the change in interface hydraulic volume. The (constant) grain porosity introduces an additional amount of water to be compressed and the total change in fluid volume (equal to the total change in interface volume) will therefore be larger in case of higher porosity φ. As an effect, the change in normal interface openings will be larger for higher grain porosity and a transition to a mechanics-controlled response is obtained at lower compressive stress states.

In the mechanics-controlled response, the interface contacts are penalized and the quadratic penalization leads to a change in hydraulic interface opening with the square root of the applied compressive load. The result is the 2:1 inclination in the logarithmic plot between loading and hydraulic response.

The point at which the transition from hydraulic-controlled to mechanics-controlled response takes place is determined by the relative change in fluid mass volume per change in fluid pressure. In other words, the position of the different graphs along the diagonal in Figure 8.7 is a function of the fluid bulk modulus k^w and the ratio between (initial) interface hydraulic volume and the grain pore volume.

With a relatively high fluid bulk modulus of the fluid ($k^w \sim 1 \times 10^9 Pa$), the nonlinearities due to the fluid compressibility is small in the applied range of stresses ($|p^M| < 1 \times 10^8\ Pa$)

Note that the smallest loading step applied here is $\Delta\sigma_{11} = 1.0 \times 10^{-4}\ MPa$, which explains the choice for range of the horizontal axis. For smaller compressive loading, the $\varphi = 0.1$ curve will coincide with the $\varphi = 0$ curve to qualitatively show the same behaviour as the other curves.

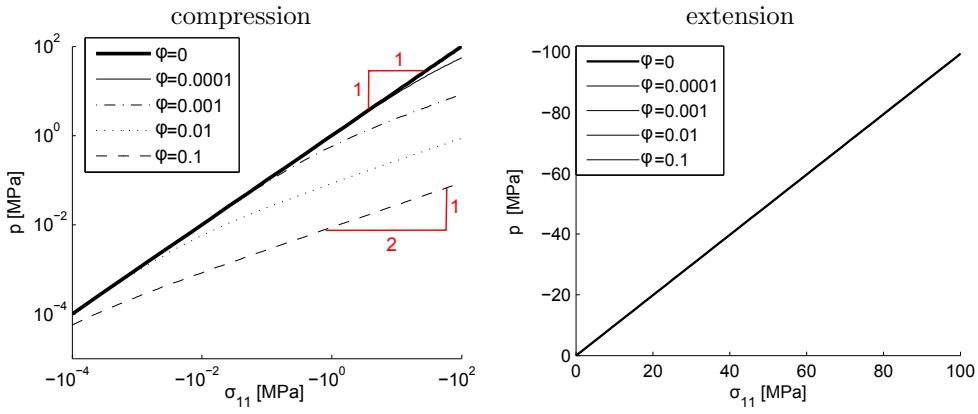

Fig. 8.7: Pore fluid pressure as a reaction to undrained loading

The numerical experiments above demonstrate that even for simplified microstructures a constant relation between macroscale stress and fluid pressure is not easily obtained. It is therefore not straightforward to compare the macroscale behaviour with for example Biot's theory without a strong restriction in the domain of stress/strain states to linearize different aspects of the microscale behaviour. For example, to take away the non-linear effects in Figure 8.7, the penalization of the normal interface opening should be omitted or the hydraulic interface opening should be independent from the mechanical normal opening. Another option for linearization could be to consider fluid incompressibility.

9. VERIFICATION OF THE CONSISTENCY OF HOMOGENIZATION: TANGENT OPERATORS

Matrix $[A_{(7\times7)}]$ containing the linearization of the constitutive relation obtained from the microscale computation is used in the macroscale finite element as the consistent tangent stiffness matrix $[A_{(7\times7)}]$ for solving the hydromechanical coupled field equations. The consistency of the linearization of the constitutive relation needs to be high for a proper convergence at the macroscale. It is therefore necessary to evaluate the quality of $[A_{(7\times7)}]$ with respect to consistency.

The microstructure introduced in Figure 8.1 is subjected to a strain-controlled loading path to obtain the following deformation:

$$\boldsymbol{F} = \begin{bmatrix} 0.995 & -0.01 \\ 0 & 1.01 \end{bmatrix}, \qquad \vec{\nabla} p = \begin{Bmatrix} 1.0 \\ 10 \end{Bmatrix} \; MPa/m, \qquad p^M = 1.0 \; MPa \tag{9.1}$$

This loading path can be applied directly and no tangent operators are required to solve for the time steps. Over the next loading step to obtain the configuration, the material constitutive linearization $[A_{(7\times7)}]$ is determined using computational homogenization by static condensation (CHSC) and numerical perturbation (NP). Different values of perturbations ϵ^m and ϵ^h are used for perturbations of mechanical and hydraulic variables respectively. To assess the quality of the tangent stiffness matrix, the relative difference of the individual components are compared. The relative difference is defined as follows:

$$\Delta A_{(ij)} = \| \frac{A^{\epsilon}_{(ij)}}{A^{ch}_{(ij)}} - 1 \| \tag{9.2}$$

with $A^{\epsilon}_{(ij)}$ the components obtained by numerical perturbation and $A^{ch}_{(ij)}$ the components obtained by computational homogenization through static condensation. Figure 9.1 shows the results for the components $[\Delta A]$, in which the mechanical components $\Delta C_{(ij)}$, the hydraulic components $K^{hh}_{(ij)}$ and the coupling components $K^{hm}_{(ij)}$ and $K^{mh}_{(ij)}$ are identified according to (6.2).

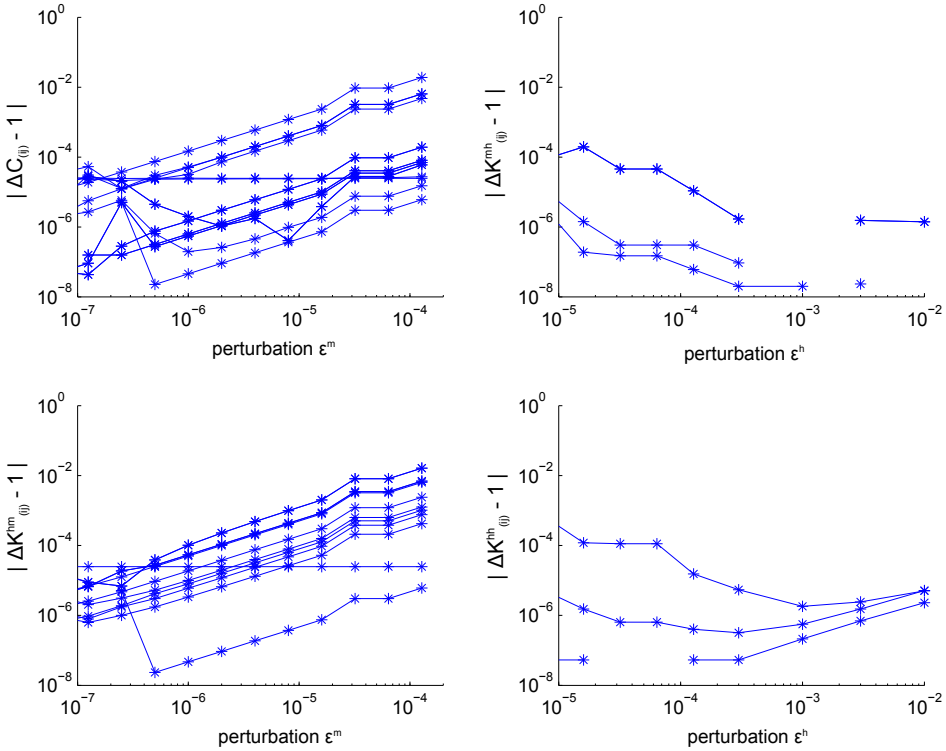

Fig. 9.1: Relative difference between the components of the tangent operator obtained by computational homogenization with static condensation and numerical perturbation as a function of the size of the numerical perturbation ϵ. Missing data indicates equal components ($\log(0) = NaN$).

The relative error in the tangent operators obtained by numerical perturbation suffer from influences of the model non-linearities for larger perturbations and numerical imprecision for smaller perturbations.

For the components related to a variation of the macro strain ($C_{(ij)}$ and $K^{hm}_{(ij)}$) the relative difference in the components of the tangent operators as a function of the numerical perturbation shows a smaller inconsistency between the two approaches for smaller perturbations, which is in line with the expectations considering material non-linearities. The components related to the variation of hydraulic kinematics terms show less variation with changing size of the numerical perturbation and the relative difference is smaller than observed for the components related to variation of strain. Moreover, only 7 components are shown. These 7 components correspond to the variation of macroscale fluid pressures. The components related to the pressure gradient for numerical perturbation and condensation are identical.

To test the efficiency of the obtained tangent operators in a computation, a kinematics-controlled loading path $\{\dot{U}^{(P)}\}$ is followed until dimensionless time $\alpha = 1$ to reach the state of deformation given in (9.1). From this configuration, the corresponding response rate $\{\dot{\Sigma}^{(R)\alpha}\}$ is used to define the response-controlled loading rate $\{\dot{\Sigma}^{(P)}\}$ to be applied during a subsequent time increment $\Delta\alpha = 0.01$. The convergence of the error R^{mp} of the Newton-Raphson scheme for iteratively solving for the correct $\{\Delta U^{(R),1+\Delta\alpha}\}$ corresponding to the enforced $\{\Delta\Sigma^{(P)}\}$ is

given in Figure 9.2. Convergence graphs are given for computations using condensation (CHSC) and numerical perturbation (NP). The size of the numerical perturbation is chosen based on the minimum relative difference between condensation and numerical perturbation according to Figure 9.1 ($\epsilon^m = 1 \times 10^{-6}$ for perturbations of the mechanical components and $\epsilon^h = 1 \times 10^{-3}$ for the perturbations of the hydraulic components) and an arbitrary perturbation size $\epsilon^m = \epsilon^h = 3 \times 10^{-5}$ for comparison. The convergence graphs show that the computation with condensation shows the best convergence in this example.

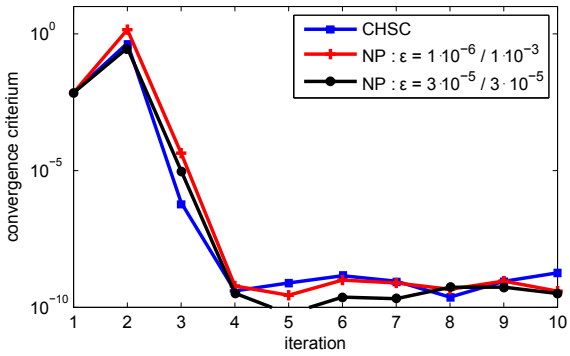

Fig. 9.2: Convergence of a stress-controlled loading step using tangent stiffness matrices obtained by computational homogenization through static condensation (blue), numerical perturbation with 'optimized' perturbation sizes (red) and averaged perturbation sizes (black)

The same procedure of assessing the consistency of the tangent operators is repeated with a more complex microstructure (Figure 9.3-left), in which the deformation loading path has induced microscale damage (9.3-right). This microstructure is one of the realizations of the calibrated microscale model against experimental data of the Callovo-Oxfordian claystone, for which details can be found in Section 14. The following deformation is enforced before evaluating the tangent stiffness matrix:

$$\boldsymbol{F} = \begin{bmatrix} 0.99 & -0.02 \\ 0 & 1.03 \end{bmatrix}, \qquad \vec{\nabla} p = \begin{Bmatrix} 1.0 \\ 10 \end{Bmatrix} \; MPa/m, \qquad p^M = 10 \; MPa \quad (9.3)$$

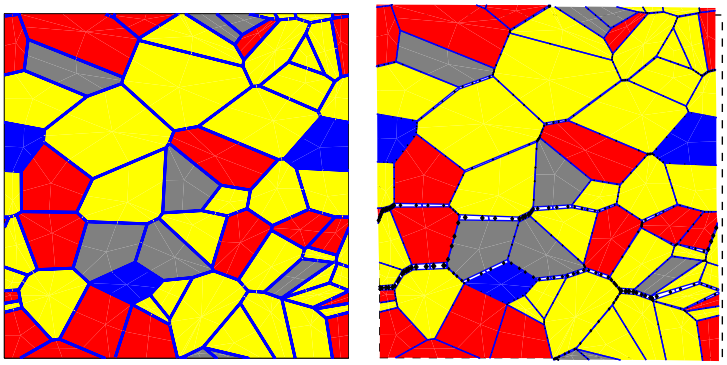

Fig. 9.3: Left: undeformed microstructure with heterogeneous grain stiffness. Yellow grains represent the clay matrix with $E \approx 2GPa$. Right the deformed state corresponding to a linear strain-controlled loading path given in (9.3). Black symbols represent the state of softening. See Section 14 for microscale model parameters.

The relative error in the stiffness components between numerical perturbation and condensation are shown in Figure 9.4. Again, a good agreement is found between the components of $[C_{(4\times4)}]$ for small perturbations. This proves that even for complex microstructures with softening phenomena, the condensation provides consistent tangent operators for the mechanical system. Matrix $[K^{mh}]$ shows the highest consistency between condensation and perturbation at a perturbation of $\varepsilon^h = 100Pa$. The increasing inconsistency away from this perturbation size can be related to a loss of numerical precision for smaller perturbations and nonlinear effects incorporated in the linearization by the finite difference approximation for larger perturbations. For matrices $[K^{hm}]$ the terms related to the variation of fluid fluxes (shown in red) show a strong inconsistency. This inconsistency is found both with respect to the condensation and between different values of perturbation. The same inconsistency is found in the terms related to the variation of fluid flux as a reaction to the variation of fluid pressure $K^{hh}_{(1,1)}$ and $K^{hh}_{(2,1)}$, represented by the red lines in the lower right graph. The origin of these inconsistencies is the high sensitivity to to mechanical alterations of the microstructure (in other words, the strong coupling from mechanics to hydraulics), which causes a precision problem in the determination of the hydraulic flux. This can be demonstrated by applying several small deformation loading steps $\Delta F_{11} = -0.00001$ to the deformed microstructure and measuring the subsequent increments of hydraulic fluxes Δm_i related to these increments. Figure 9.5 shows a strong variation of the incremental changes in fluid flux as response to the incremental deformation for different convergence criteria use in the microscale computation. These strong variations can only be related to the imprecision of the computed fluid flux and therefore a correct linearization of these terms is impossible to obtain. The results for these coupling terms in the stiffness matrix obtained by computational homogenization are therefore just as useful as any other stiffness matrix, since consistency can not be obtained due to a too strong variation in the response of the model itself. The other terms in the two lower stiffness matrices $[K^{hm}]$ and $[K^{hh}]$, related to the variation of fluid mass and the variation of pressure gradient show good consistency. As for the

purely mechanical components, those related to a variation of deformation show the highest consistency for the smallest variations. The terms relating variation of pressure gradient to variation of fluid flux show little influence of variation of numerical perturbation, as their results are both obtained computationally. The remaining difference of a factor 10^{-5} can be found in the precision of the numerical algorithms that were used to solve the systems of equations in both methods.

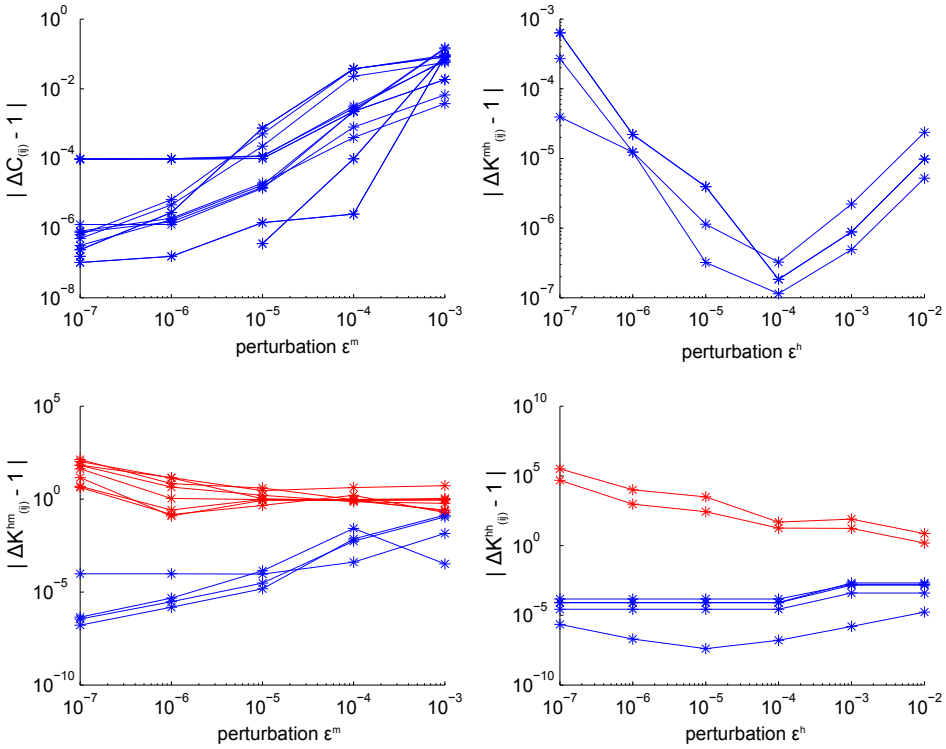

Fig. 9.4: Relative difference in the components of the tangent stiffness matrix $[A_{(7\times7)}]$ for different perturbations ε

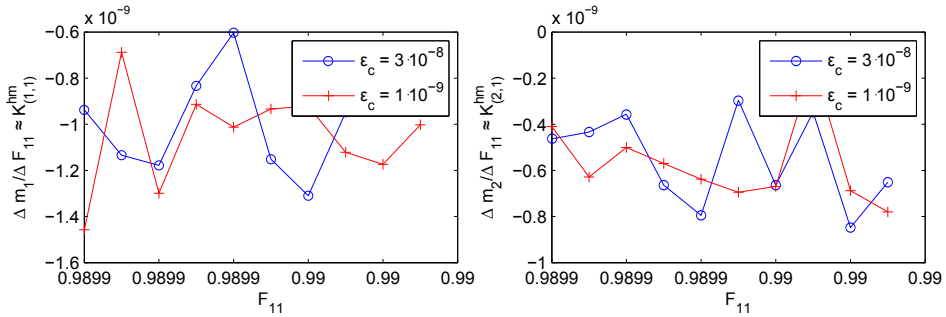

Fig. 9.5: Variation in the increment of flux as a response to an increment of deformation for two computations with different convergence criteria ϵ_c.

To evaluate the quality of convergence obtained by the tangent operators, a

stress-controlled continuation of the example above is performed. Starting from the deformed state of the REV in Figure 9.3-right, the following stress-controlled loading rates are enforced:

$$\dot{\boldsymbol{\sigma}} = \begin{bmatrix} -6.08 & -0.11 \\ -0.11 & -2.33 \end{bmatrix} MPa, \qquad \dot{\vec{m}} = \begin{bmatrix} -6.05 \\ -4.75 \end{bmatrix} 10^{-12}\ kg/s, \qquad \dot{M} = 23.07\ kg \tag{9.4}$$

The convergence graphs in Figure 9.6 show the convergence for different time steps $\Delta\alpha$, with the convergence norm R^{mp} computed according (7.5).

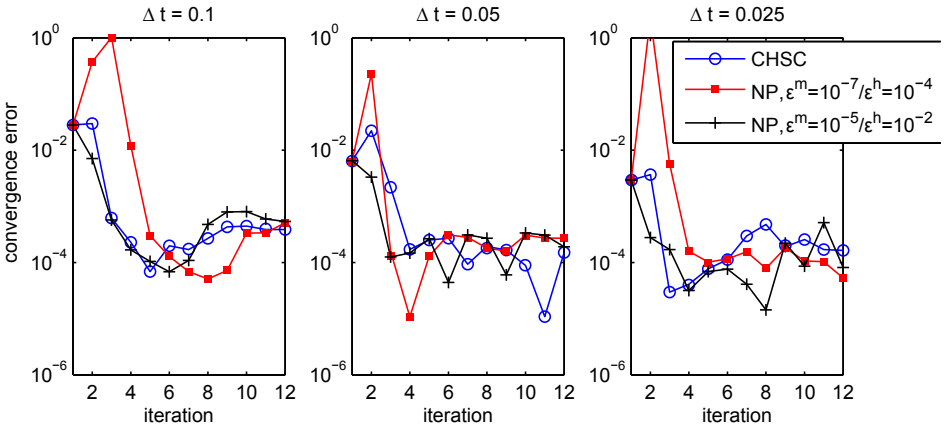

Fig. 9.6: Convergence obtained while enforcing the stress rate-controlled loading on REV 9.3-right by stress rate (9.4) for different time steps.

From the convergence graphs in Figure 9.6 it can be concluded that a consistent tangent stiffness matrix for the full hydromechanical coupled problem can be found using computational homogenization by static condensation. Its consistency is demonstrated to be of the same order as the best results obtained by numerical perturbation and convergence of the material point systems of equations is demonstrated to be of comparable quality. The term 'consistent' is demonstrated to be of doubtful meaning to some coupling terms in complex REVs. Nevertheless, the linearization $[A_{(7\times7)}]$ obtained through computational homogenization by static condensation can be used as a tangent stiffness matrix for solving the material point boundary value problem of stress rate controlled loading.

The displacement loading condition on the REV boundaries are enforced by means of the penalization of the displacement updates. This means that no initial estimate has to be made on the deformation in order to start the microscale Newton Raphson iteration. In this way, non-objective results with respect to the triggering of irreversible deformation through a biased initial test solution of the microscale configuration of the first iteration are avoided. On this point, the numerical methods of solving the microscale BVP on one hand and static condensation of the global stiffness matrix into the tangent operators on the other show a fundamental difference in the way of enforcing the periodic boundary conditions. For well-posed systems of equations, this difference should not introduce additional problems. In case the problem becomes ill-posed, for example in the vicinity of bifurcation points, the penalization might introduce numerical inaccuracies (a higher numerical noise level). This means that both the converged

solution of the microscale problem and the tangent operator loose their quality, since the behaviour becomes less differentiable or non-differentiable. An example of this was given in Figure 9.5.

Nevertheless, it can be concluded that on the material point level, the presented micromechanical model can provide a macroscale HM-coupled model by applying the principle of computational homogenization on the micromechanical REV, for which the boundary value problem is dictated by the macroscale deformation. Both macroscale stress response and tangent operators can be found by computational homogenization, in order to be used in a material point boundary value problem, simulating the local material behaviour under arbitrary loading paths. Following the same approach, the micromechanical model is suitable for the use in doublescale computations, as will presented in the following chapter.

10. MACROSCALE CODE: DOUBLESCALE COMPUTATIONS

In this chapter, several examples of doublescale computations for hydromechanical coupling are given, thereby demonstrating the possibilities and restrictions of the (HM-coupled) FE^2 method.

10.1 Oedometric extension

An oedometric test with a simplistic microstructure is modelled (Figure 10.1). This test was modelled by Marinelli [2013] with the original Frey model in a large strain formulation using a column of 20 1×1 mm elements applying very small instantaneous loads to maintain the close-to-linear conditions near the initial configuration. Here, the modified version of the model is used. The modifications allow taking into account larger pressure gradients as the local material behaviour can be obtained independently from the pressure gradient. A refined mesh at the point of drainage allows the accurate modelling of higher pressure gradient, with less oscillations as commonly observed in coarse meshes for transient problems. Note that oedometric extension is modelled here rather than the (conventional) oedometric compression: The rectangular grains prevent a progressive evolution of hydraulic properties under compressive loading as the normal compression of the interfaces will hardly influence the hydraulic properties of the interfaces.

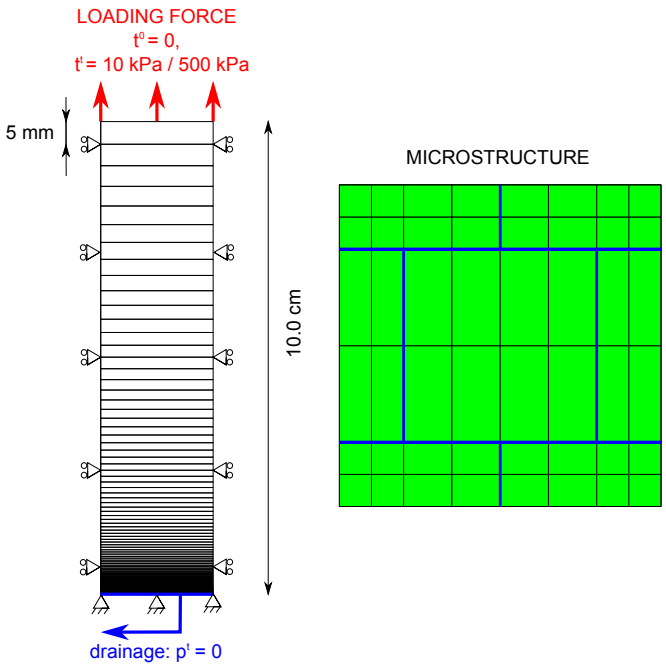

Fig. 10.1: Macroscale mesh for oedometric extension (left) and micromechanical REV (right).

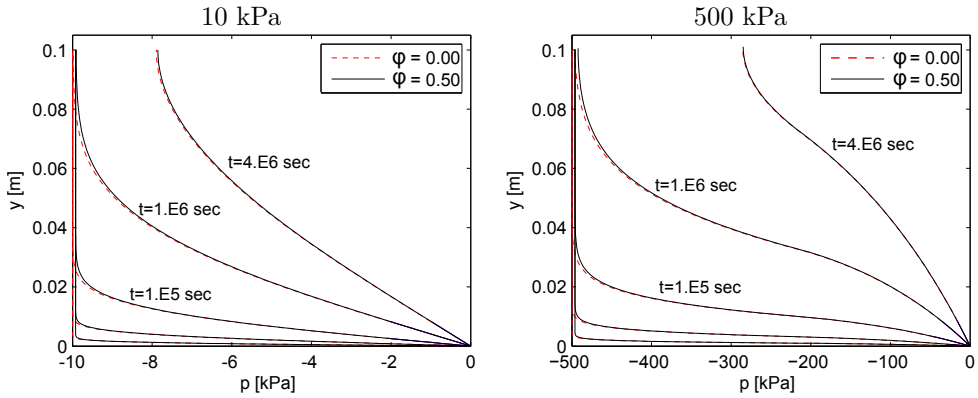

Fig. 10.2: Fluid pressure curves to oedometric loading, curves shown correspond to $t = 1.0 \times 10^3,\ 1.0 \times 10^4,\ 1.0 \times 10^5,\ 1.0 \times 10^6,\ 4.0 \times 10^6$ sec. for grain porosity $\varphi = 0$ and $\varphi = 0.5$

The fluid pressure profiles shown in Figure 10.2 for the oedometric extension at 10 kPa show good resemblance with the profiles that are usually obtained for computations of consolidation problems [Biot, 1941, Terzaghi, 1943]; as an effect of the relatively low loading forces with respect to the interface cohesion, the interface openings remain close to their original state and hydraulic properties (total pore volume, permeability and fluid density) remain practically unchanged.

The 500 kPa test shows a significantly different pressure profile, as the higher fluid pressures induce variations in the hydraulic properties. This effect has been

demonstrated in the material point computations above and now manifests in a change in macroscopic behaviour; the resulting profile shows a combination of the classical solution to the consolidation problem and the effects of a fluid mass slowly intruding the material from the bottom of the sample. This increase in fluid content through the opening of interfaces causes an increase of permeability, facilitating the progressive invasion of the material by the fluid mass. From this example, it is clear that it is no longer possible to compare the results of the doublescale model with those obtained by 'simple' classical models with constant permeability, since the hydraulic properties show a too strong differentiation throughout the test. The effect of a fluid mass and fluid pressure progressively moving through the material will be further explored in the next section, where this effect will manifest more as a moving front.

For both tests, a small influence of grain porosity (tests were performed with $\varphi = 0$ and $\varphi = 0.5$ respectively) can be observed as an effect of the redistribution of the fluid mass between interfaces and grain pore space. This redistribution provides the fluid mass required for the interface opening, thereby activating some of the cohesive forces and lowering the fluid pressure plateau. In this way a Biot coefficient $\alpha \approx 1$ is obtained for macroscopic undrained loading.

10.2 Pressure dissipation

A second doublescale test consists of the hydraulic loading of a 10 cm sample, for which displacement of the top and bottom are constrained together with horizontal displacement for the entire sample. Three series of test are performed with pressure increments of 10kPa, 1MPa and 10MPa enforced on the bottom of the sample, while no fluid flux is allowed on the other boundaries (see Figure 10.3). In the first two series (10 kPa and 1 MPa), the fluid pressure is applied in a single step, in the last series (10 MPa) the fluid pressure is applied in ten steps of 1 second each. Each series contains two tests with grain porosities of $\varphi = 0.00$ and $\varphi = 0.50$.

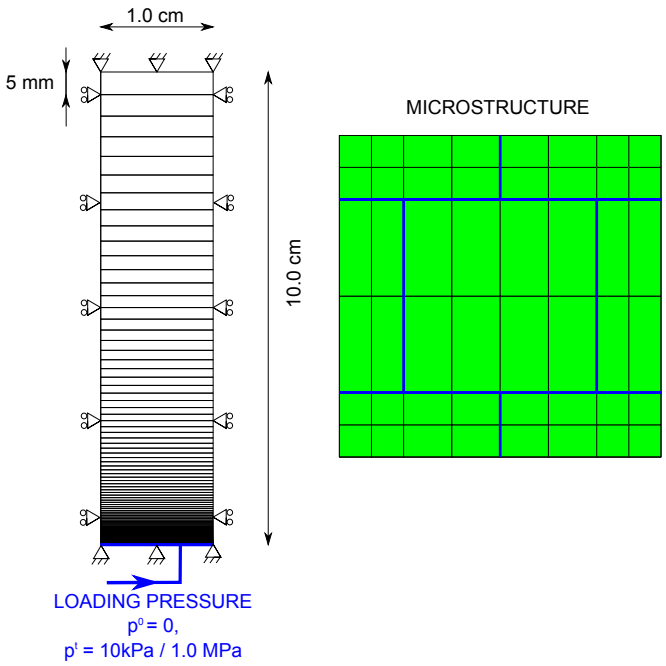

Fig. 10.3: Macroscale mesh for pressure dissipation test at $p = 10\ kPa$ and $p = 1\ MPa$(left) and micromechanical REV (right).

The pressure response profiles to hydraulic loading of the sample in Figure 10.4 demonstrate again the influence of the grain porosity on the macroscale behaviour, as the water storage is influenced by the change in total pore volume. This influence comes only from the fluid rheological part through the compressibility of the fluid; the model does not consider grain pore volume change and total pore volume change remains fully related to the change in interface opening. Nevertheless, the fluid compressibility allows fluid mass redistribution at high grain porosity, such that the applied loading is almost completely taken by the mechanical system in case of higher grain porosity. As an effect, fluid pressure remains close to zero for the points that have not been reached by the macroscale fluid flow (the increase of fluid mass). This means that for high grain porosities, the increase of fluid pressure is only possible through the macroscopic displacement of fluid mass, driven by a fluid pressure gradient. For low or no grain porosity, the pressure increase is directly linked to the macroscopic strain due to the hydraulic loading, for which a negative volumetric strain induces a direct rise in pore pressure. This can be observed as the fluid pressure increases homogeneously in the upper part of the sample in the case of grain porosity $\varphi^g = 0.0$.

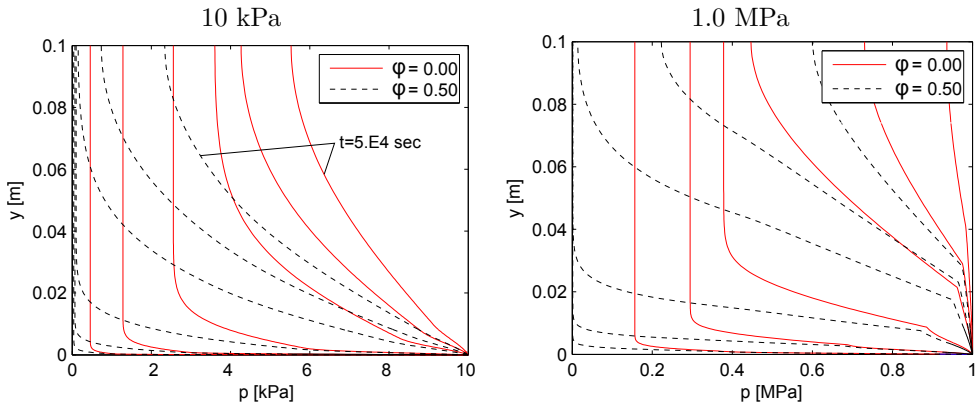

Fig. 10.4: Fluid pressure curves as a response to fluid pressure loading (Figure 10.3) at t=10, 100, 1000, 10.000, 25.000 and 50.000 seconds.

Similar to the observed behaviour in the oedometric loading tests, higher hydraulic loading shows a stronger effect of the increasing permeability and the effects of a pressure front that advances from the bottom upwards can be noticed in the pressure profiles for 1 MPa hydraulic pressure. Figure 10.5 shows the evolution of the permeability profile for the dissipation of the 1 MPa fluid pressure load. The increase in permeability of more than one order of magnitude can be observed (Figure 10.5). The advancing front of increased permeability corresponds well with the advancing pressure front in Figure 10.4.

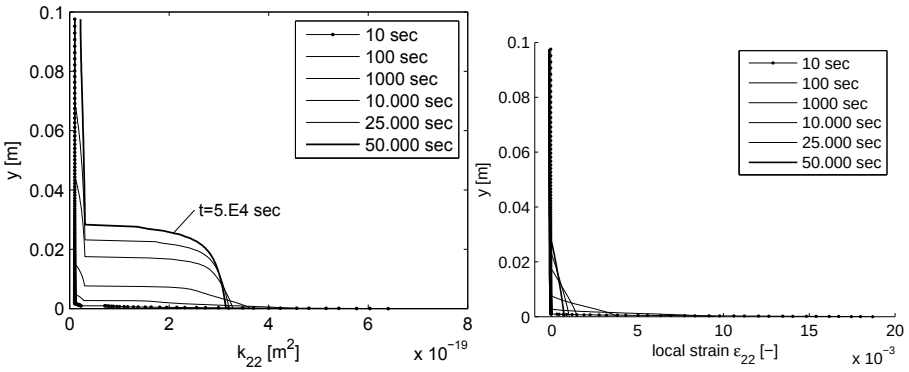

Fig. 10.5: Permeability at different states of pressure dissipation for $p = 1\ MPa$ $n = 0.50$. Initial permeability is $k_{22} = 1.04\text{E}^{-20}\ m^2$

In the third series of simulations, a pressure increment of 10 MPa is applied in 10 subsequent time steps of 1 second each. The dissipation of the imposed pressure is then followed over a period of 100 seconds. Incremental time steps of 1 second are used for the integration. The dissipation response to this higher loading is quite different from the behaviour of the pressure loading above, in the sense that the fluid pressure profiles of consolidation are no longer found. Instead, the effect of the advancing pressure front is the main mechanism of pressure dissipation as can be found in Figure 10.6left. As an effect of a clearly defined pressure front, the position of this front as a function of time can be followed (10.6right)

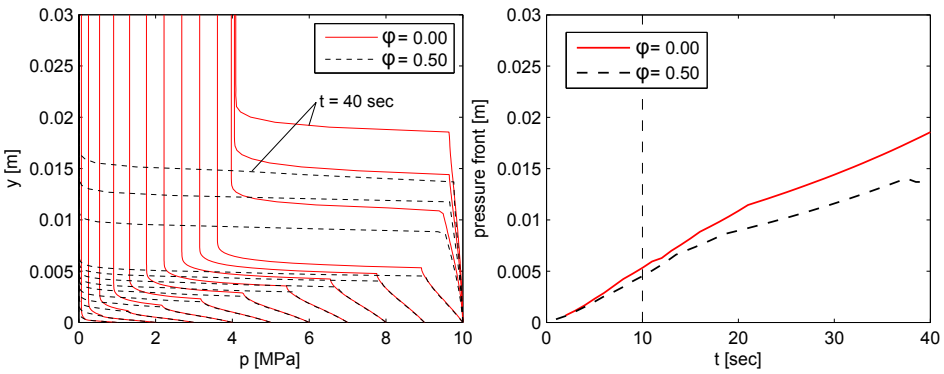

Fig. 10.6: Pressure response to pressure loading for $p(y = 0) = 10\ MPa$. Left: pressure profiles for $t = 1, 2, 3, 4, 5, 6, 7, 8, 9, 10, 20, 30, 40$ seconds. Right: advance of pore pressure front as a function of time.

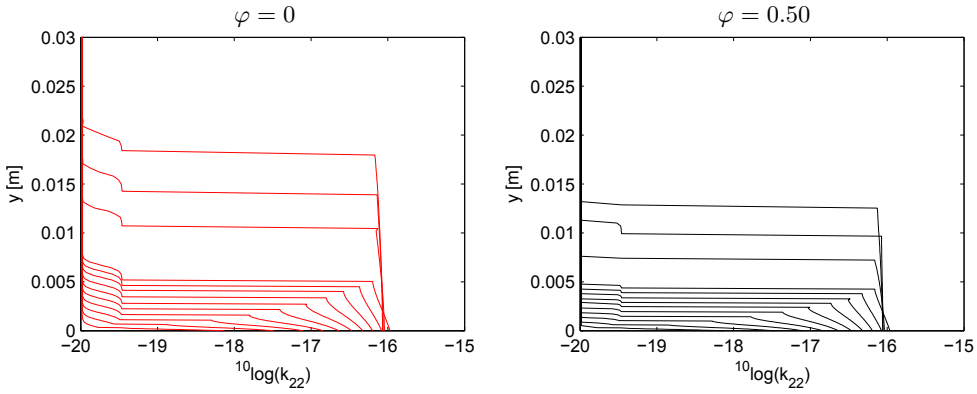

Fig. 10.7: Permeability evolution as a response to pressure loading $p(y = 0) = 10\ MPa$ for grain porosity $\varphi = 0$ (left) and $\varphi = 0.50$ (right) for time $t = 1, 2, 3, 4, 5, 6, 7, 8, 9, , 20, 30, 40$

The pressure front represents some very high gradients of pressure to be accounted for in the finite elements. As the pressure front translates upwards with time, the size of the elements in the mesh that have to capture this gradient increases. This eventually introduces mesh-dependent results when the element size becomes too large with respect to the zone of the pressure front. In the simulations above, these effects start to develop when the pressure front has advanced 1 cm into the sample and the advance per time step becomes smaller than a single element. This makes the advance of the pressure front erratic and introduces errors in the pressure fields. The start of this effect can be seen in the advancement of the pressure front for the $\varphi = 0.50$ computations in Figure 10.6 starting from $t = 37$ sec. This effect clearly marks the limitation of the macroscale finite element method when it comes to high pressure gradients with this mesh size, as it fails to deal with the strong pressure gradients present in the sample.

Figure 10.7 shows the evolution of the pressure front from a permeability point of view. With increasing fluid pressure, the grains are compressed and the interfaces are opened. For $p = 10\ MPa$ this results in an increase of permeability

of 4 orders of magnitude.

It should be noted that, due to the oedometric conditions of the sample and relatively low stiffness of the interface cohesion(1), no interface softening has taken place in the simulations above. The effect of interface softening would increase the evolution of the permeability. Moreover, localization of deformation might mitigate the quasi-1D approach that is followed here and can introduce localized effects even in a column of 1 element wide.

10.3 Localization in biaxial compression test - mechanical model

In this section, a 2D doublescale biaxial compression test is modelled, using the mechanical model in combination with the local second gradient model. A simple microstructure of four hexagonal grains is used in the REV (Figure 10.8). As the purpose of this computation is to demonstrate the doublescale approach with second gradient model, the representativeness of the microstructure is of no importance, but it should be noted that the low number of interfaces strongly influences the macroscale behaviour and a strong anisotropic response can be expected.

Figure 10.8 shows the macroscale domain with boundary conditions and the micromechanical REV. The domain is discretized using 4800 square elements. Displacement-controlled axial deformation is enforced on the top of the sample, for which a perfectly smooth boundary is assumed, allowing horizontal displacement of the top of the sample. No confining pressure is applied.

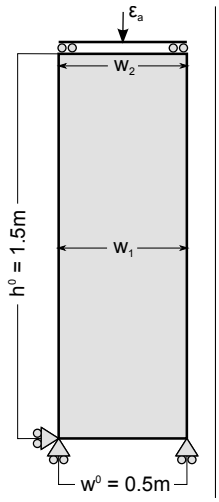

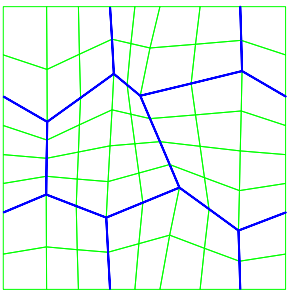

solids:	
E [GPa]	3.46
ν	0.200
interfaces:	
E_0 [GPa]	1.96
T^{max} [MPa]	5.0
δ^c	0.125
SG model:	
D [kN]	20.0

Fig. 10.8: The boundary conditions on the macro level (left) and the mesh for the REV with microstructure on the micro level (right). In green the elements for the solids, in blue the interface elements.

Figure 10.9 A) shows the nominal stress response to biaxial compression, including a softening response initiated at approximately 1.25% shortening of the

(1) the term stiffness is used here with respect to the slope of the cohesion-displacement graph, or the ratio $\partial T/\partial \Delta u$

sample. The volumetric strain response is given in Figure 10.9 B), with the average volumetric strain of the sample $(V_{sample}/V^0_{sample} - 1)$.

The ratio between initial lateral and axial strain rate $-\dot{\varepsilon}_{lat}/\dot{\varepsilon}_a = 0.835$ that is observed in the plane-strain simulation corresponds to an effective Poisson's ratio $\nu = 0.455$, which is much higher than the Poisson's ratio of the individual grains. This difference is the effect of the dilatancy introduced by the interfaces as soon as deviatoric strain takes place; the transduction of shear stress over the interfaces between the grains requires a relative displacement and relative displacement of the interfaces requires some interfaces to be opened, leading to a dilatant global response. The lack of interface static friction will contribute to this effective dilatant behaviour.

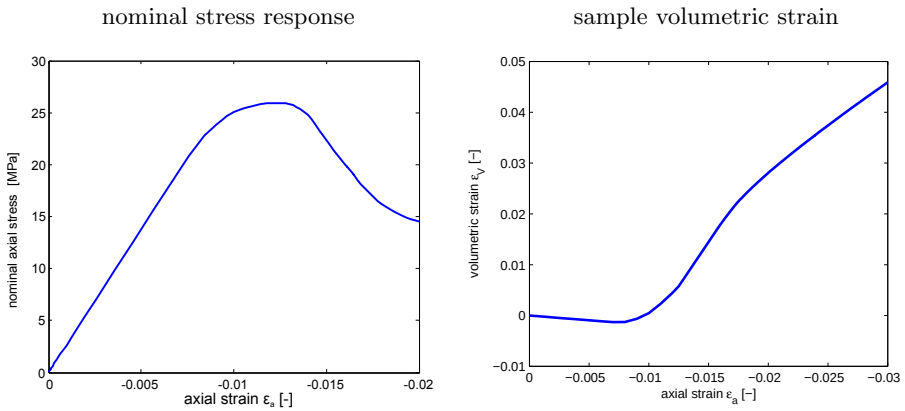

Fig. 10.9: A) nominal stress response to biaxial compression. B) volumetric strain response, computed based on w_1, w_2 and a total volume integral.

Figure 10.10 shows the deformed microstructure at nominal axial compression $\varepsilon_a = -1.9\%$ with Von Mises (VM) equivalent strain ε_{VM} defined as

$$\varepsilon_{VM} = \sqrt{\frac{2}{3}\left({\varepsilon_{11}}^2 + {\varepsilon_{22}}^2 + 2{\varepsilon_{12}}^2\right)} \tag{10.1}$$

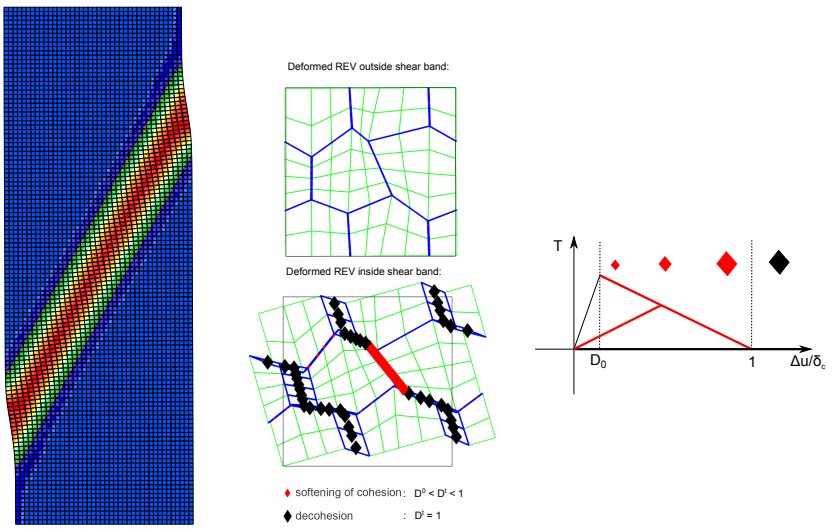

A) ($\varepsilon_a = -1.9\%$) *B*) deformed REVs *C*) damage state

Fig. 10.10: *A*) Deformed meshes at $\varepsilon_a = 1.9\%$ with ε_{VM} colorscale. No magnification of displacements. *B*) Deformed REVs with damage states according to the stageds in the cohesive damage law in *C*).

Figure 10.10B) shows the deformed microstructures at $\varepsilon_a = -1.9\%$ outside the shear band (taken close to the center of the bottom boundary) and at the center of the localization band. For each interface integration point, the damage state of the interfaces is given. The red symbols indicate a state of softening, the black symbold indicate a decohesion of one of the components of the interface chesion. The size of the red symbolds indicates the amount of softening. An almost continuous path of interfaces with complete decohesion of at least one component (normal or tangential) is observed in the localization band near the end of the test; only one channel of this path has a remaining cohesive force, which is close to decohesion. It is important to observe that the orientation of the paths of softening at the microscale are conjugated with respect to the shear band that is present at the macroscale and that the orientation of microscale localizations of damage do not necessarily have to align with the macroscale shear band.

As mentioned before, the anisotropy in the model that is introduced by the low number of grains is strong. This anisotropy plays an important role in the initiation of the strain localization, as it introduces preferential directions for localization bands. As the macroscale behaviour does not have an axial symmetry, conjugate shear bands are less favorable. In addition, localization in a shear band involves a local rotation. Because rotations are restricted at the top and bottom boundaries, the initiation of a band that does not interfere with these restrictions is preferential. The constraints of the local second gradient model on the gradient of deformation will then provide for a (weak) condition to 'push' the shear band to the center of the sample to obtain symmetry with respect to the top and bottom boundaries.

For this reason, the same solution is found for different computations with this microstructure.

10.4 Localization in biaxial compression - hydromechanical coupling

In this section, a biaxial compression test on a fluid-saturated sample under transient conditions is modelled. The initial state of the sample is homogeneous with (total) stress $\sigma_{ii}^M = 0\ MPa$ and pore water pressure $p = 0\ MPa$. Drainage is applied on the top and the bottom of the sample (see Figure 10.11).

Microscale interface cohesion parameters $\delta_{n/t}^c$ and macroscale second gradient parameter D are chosen such that for a perfectly drained analysis (i.e., a purely mechanical analysis), snapback of the macroscale response is just avoided and the resulting shear band is approximately 4 elements wide.

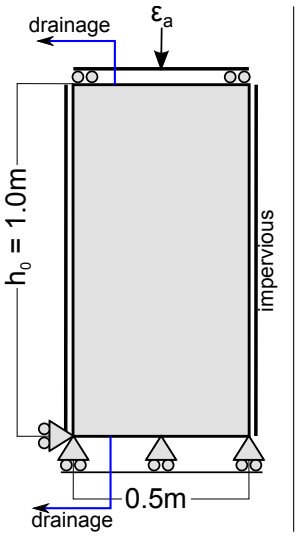

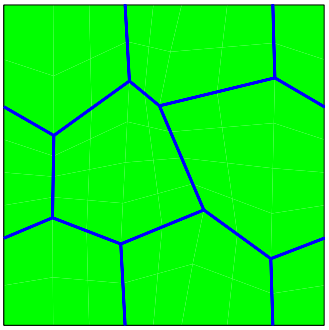

solids:	
E [GPa]	3.60
ν	0.20
k_{ii} [10^{-20}m^2]	1.00
φ^g	0.18
interfaces:	
E_0 [GPa]	9.8
T^{max} [MPa]	4.9
δ^c	0.040
SG model:	
D [kN]	100.0

Fig. 10.11: Boundary conditions for biaxial compression of a fluid-saturated sample under zero confinement (left) and the micromechanical REV with constitutive parameters (right).

The biaxial compression test is performed four times; once without taking into account the pore pressures (perfectly drained or purely mechanical) and three times with different deformation loading rates:

- Test A : mechanical ($p^t(\vec{x}) = 0$)
- Test B : $\dot{\varepsilon}_a = 1E^{-11}/s$
- Test C : $\dot{\varepsilon}_a = 1E^{-10}/s$
- Test D : $\dot{\varepsilon}_a = 1E^{-09}/s$

Initial permeability is set to $k_{ii} = 1.0 \times 10^{-20}\ m^2$ through the grain permeability, which is constant over the REV.

Figure 10.12 shows the nominal axial stress response and the pore pressure response at the center of the sample. These responses show a dependency of the developing reaction forces on the rate of loading as higher loading rates induce

higher negative over-pressures. These negative over-pressures lead to higher and delayed peak stresses for higher loading rates.

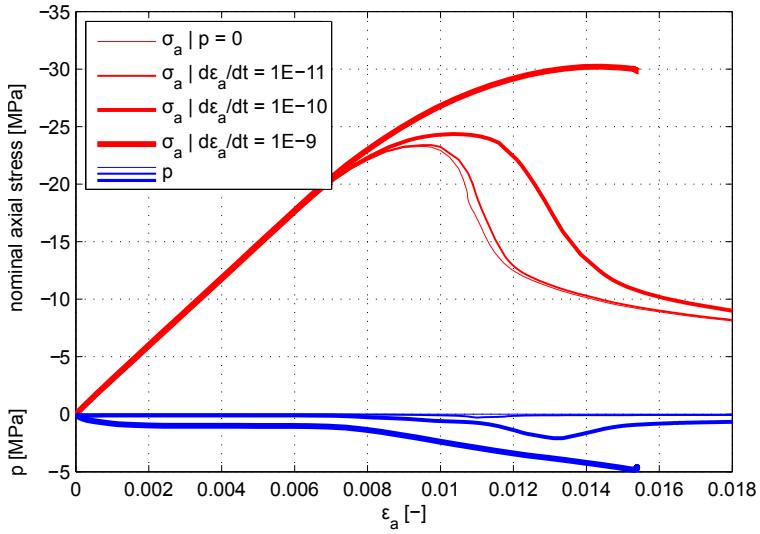

Fig. 10.12: Nominal stress response to biaxial compression at 0 confinement (red) and the fluid pressure response at the sample center (blue).

Comparing the VM strain and fluid pressure fields (Figure 10.13) for different loading rates demonstrates that at the lower loading rates, the mechanism of deformation is not changed and the shear band develops in the same way as for the mechanical computation. The fluid pressure follows the deformation, with negative pressure gradients towards the localizations. The dilatancy of the material is the main reason for this behaviour and the fluid flux is towards the zones of strongest deformation rate, which corresponds with a pore volume increase due to interfaces that are being opened.

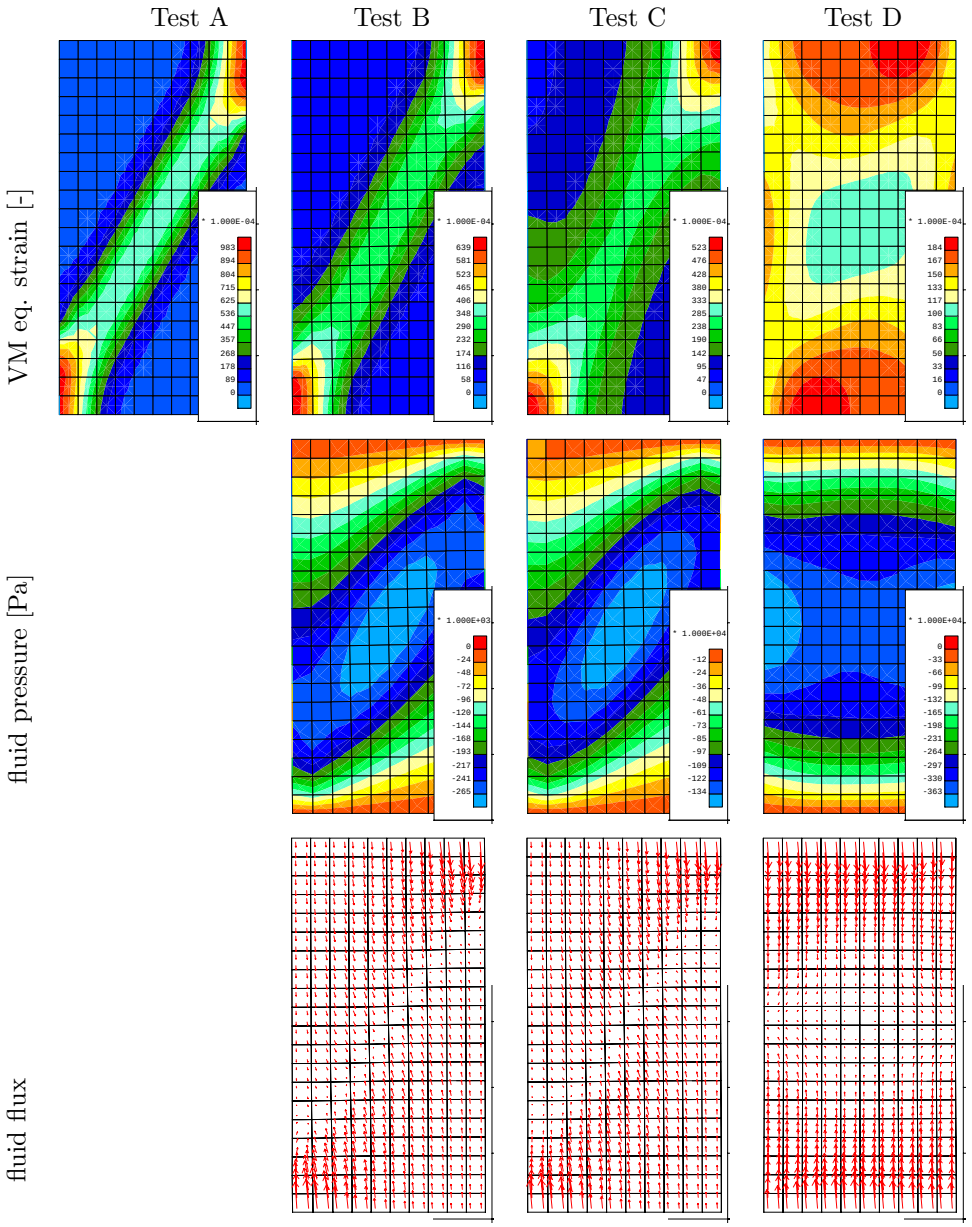

Fig. 10.13: Deformed meshes with VM equivalent strain (top), fluid pressure (center) and relative fluid flux (bottom) at $\varepsilon_a = 1.20$ %

Test A, B and C have localizations developing through the center of the sample. This means that the anisotropic preference for this orientation is stronger than the negative fluid pressure favoring localizations close to the top of the sample. For the highest loading rates, the negative fluid pressure buildup is stronger and the influence of the fluid pressure becomes dominant in the localization, preventing the development of strain localization through the center of the sample. This can be observed in Figure 10.13 Test D, where the highest deviatoric

strains are concentrated in the zones of least fluid negative overpressure.

At the end of Test D (that is, at $\varepsilon_a = 1.54\%$ when a converged solution can no longer be found due to (local) snapback effects) two localization bands are developing, reflecting at the top and bottom boundary, as can be seen in Figure 10.14 left.

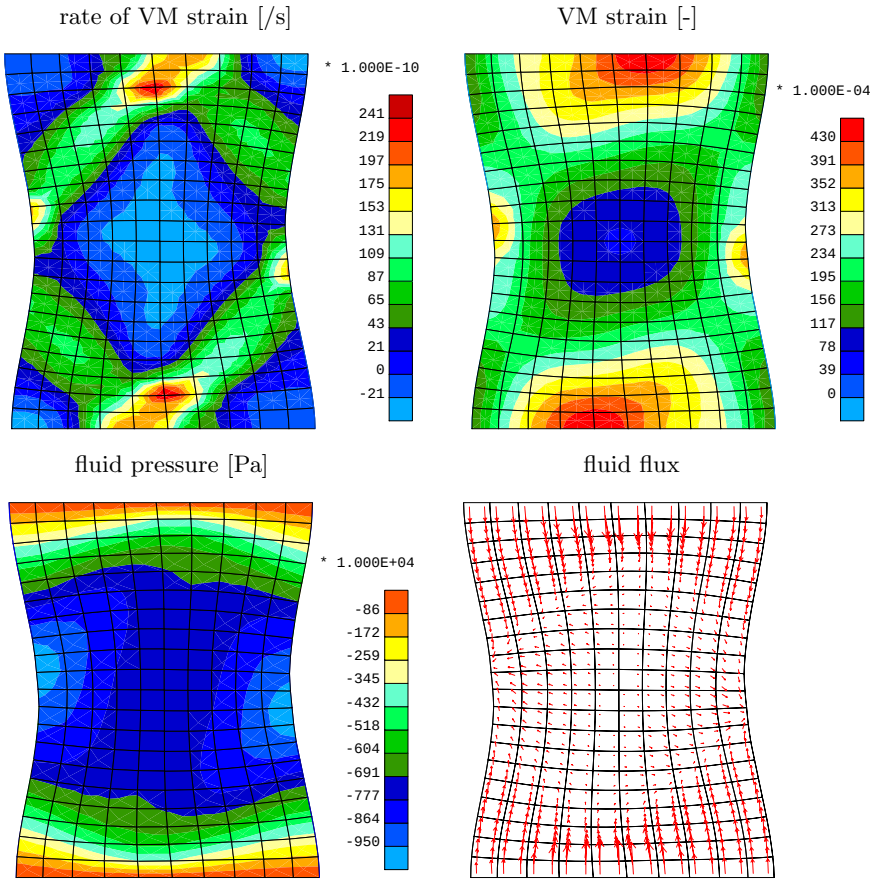

Fig. 10.14: Deformed mesh (displacements multiplied 10×) at the end of Test D.

11. THE MICROSTRUCTURAL REV

Many results on heterogeneous microstructures in literature are based on a variation in constitutive parameters, used to characterize the heterogeneity (see for example [Barbe et al., 2001a,b, Gitman et al., 2007] to name a few). These results can be obtained for simulations of inclusions in a matrix as well as heterogeneity in the form of polycrystalline microstructures. Two major differences between these results and the model presented in this work are the following;

- localization takes only place in the interfaces, and the interface orientation and connectivity plays an important role in the possible percolation of localization paths. A low number of grains and the periodic boundary conditions can strongly constrain the possibility of the full percolation of a localization path.
- the application to geomechanical problems introduces a compressive loading path to reach the softening response of the material. The mechanisms of localization under compressive loading associated to the material softening are more complex than those of the tensional loading which is the common approach in the afore-mentioned references.

In the previous sections, only theoretical microstructures were demonstrated to clarify the principles of the microscale model. Although these simplified microstructures can very well be used in doublescale computations and are of great value in the validation of the developed models, their global response can not be considered to properly represent the behaviour of geomaterials. Especially their behaviour under compressive loading will show a strong orientation dependency through the preferential orientation of the grains and the interfaces.

The generation of more complex microstructures requires a certain randomness in order to prevent user-dependent bias in microstructure realizations and a general algorithm to be able to produce large and multiple realizations of these microstructures is required.

From an application point of view, the definition of the microstructure has to resemble the microstructure of the material that is to be simulated and therefore the geometry of the microstructure might be derived directly from actual microstructural observations. The discretization of microstructure images is in this case the most straightforward approach in defining the microstructure for a REV. This requires the selection of representative images of the microstructure, for which the representativeness has to be tested based on a certain set of geometrical parameters.

A different approach is to start from these geometrical parameters (which by themselves characterize the (main) features of the microstructure) and reproduce microstructures that statistically match these characteristics. This allows realizations of an unlimited number of microstructures and in addition provides a way of

investigating the effect of variations in the microstructure characteristics. A more practical consequence of this approach is that a reduction in complexity of the microstructure is easily obtained by only taking into account a limited number of parameters for the characterization of the microstructure.

In this context a routine for generating simple microstructures with a limited number of parameters is developed. Although it is possible to generate advanced microstructures (see for example Sonon et al. [2012]) a straightforward and efficient way of obtaining microstructures is followed here.

11.1 The microstructural REV generator

A microstructure generator based on random initialization of grains is designed, based on the well-known Voronoï tessellation. The use of Voronoï tessellation for generating microstructures is often used in numerical methods to produce microstructures [Lee and Ghosh, 1995, Alonso-Marroquín et al., 2005, Verhoosel and Gutiérrez, 2009, Benedetti and Aliabadi, 2013]. A detailed description of the generation of Voronoï-based periodic REVs with finite element meshing is given by Fritzen et al. [2009]. Several variations in the generation of the initial Voronoï tessellation can be used for modifying the connectivity of the resulting Voronoï diagrams through the variation of the initial random sites. In addition, anisotropy in the grain geometry is easily introduced by a modification of the distance function [Barbe et al., 2001a]. In addition to these variations in Voronoï generation, the microstructure grain shape can be modified in a post-processing step, as will be introduced in the following part. This modification was initially introduced to avoid grain shapes that introduce difficulties with finite element mesh generation, but has proved to play an important part in the global response through the specific imbrication of the grains. This grain-shape dependency will be addressed in 11.2. The algorithm for generating the microstructure consists of the following operational sequence, corresponding to Figure 11.1;

(a) A 1×1 periodic domain is defined, in which n sites are generated randomly. To obtain periodicity, the sites are copied to each periodic quadrant. Each site will initiate a grain, eventually resulting in n unique grains in the periodic domain.

(b) Inverse mapping by the grain shape tensor $\boldsymbol{T}^{-1}$ is applied for introducing the required grain stretching and rotation (Section 11.1.2).

(c) Voronoï tessellation based on the periodic sites in the inverse mapped configuration produces the grain interfaces.

(d) Grain circularity optimization (Section 11.1.1) is performed to obtain more regular shapes.

(e) Mapping by grain shape tensor $\boldsymbol{T}$ is applied to transform the deformed periodic boundaries back to the initial configuration, thereby applying the grain shape tensor $\boldsymbol{T}$ on the grains.

(f) The center periodic domain is isolated by cutting the grains at the periodic boundaries, after which the finite element mesh is generated for the grains and the grain interfaces and material properties are assigned to the different micromechanical constituents.

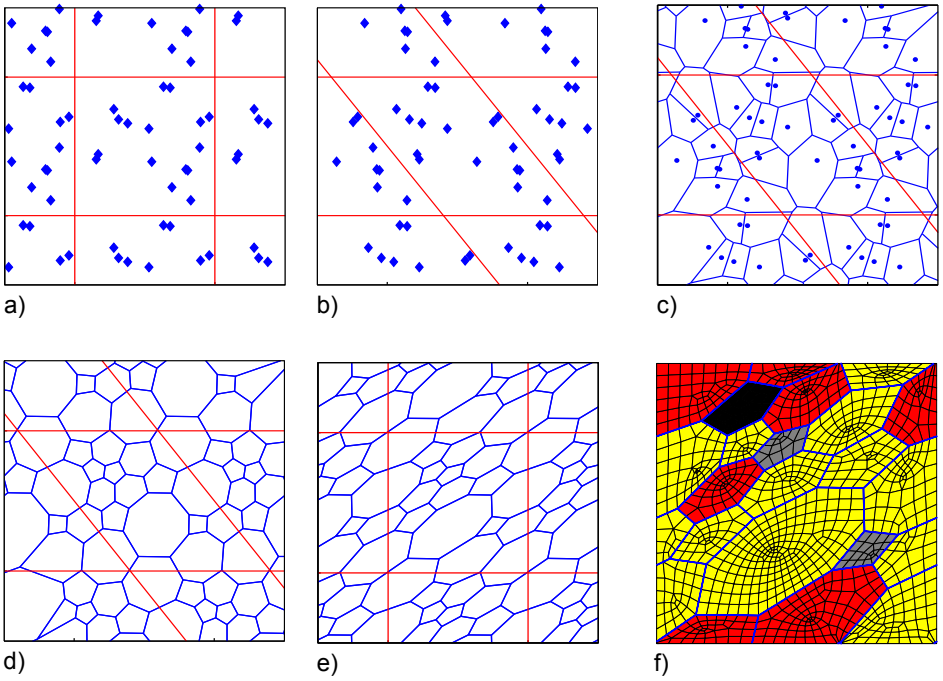

Fig. 11.1: Illustration of the algorithm for anisotropic REV generation with grain shape tensor $T = [1 \;\; 0.8 \;;\; 0 \;\; 1]$.

11.1.1 Grain circularity optimization

The grain shapes obtained through Voronoï tessellation can be very unfavourable for creating the finite element mesh of the grains, for example through very short interface lengths. Moreover, the irregular grain shape might introduce undesired microstructural properties in the material behaviour. In order to have a control on the grain shape, a circularity correction is introduced to have control over the grain shape. For this reason, the grain shape is optimized with respect to interface length l and a configuration of the intersection points of the Voronoï diagram is sought for which the sum of the squared length of the interfaces is minimal. With l^i the length of interfaces i out of a total of I interfaces and x_i^j the coordinates of one of the J intersection points, the minimum of the sum of the squares interface channel lengths has to hold:

$$\frac{\partial \sum_{i=1}^{I} l^i l^i}{\partial x_i^j} = 0 \tag{11.1}$$

The only interface channels l^i that need to be considered in this condition are those connected to intersection point $\vec{x}^j$ and it is straightforward to verify that this condition implies that the components of $\vec{x}^j$ are the average of the directly connected intersection points:

$$x_i^j = \frac{1}{K} \sum_{k=1}^{K} x_i^{j_k} \tag{11.2}$$

with $\vec{x}^{j_k}$ the coordinates of the K intersection points directly connected to $\vec{x}^j$ by an interface channel. The most convenient way of solving the coordinates of all intersection for the given constraints is iteratively updating of individual intersection points following a Gauss-Seidel iteration scheme until convergence of the iterative updates to approximately zero. This scheme of subsequently updating the coordinates of individual intersection points avoids dealing with boundary conditions, which would have been necessary in case of a direct solution.

The result is a Voronoï-based microstructure with optimal circular grains as given in Figure 11.1d. The only possible influence on preferential orientation (apart from the anisotropy introduced by the stretch and rotation of the Voronoï diagram by tensor $\boldsymbol{T}$) comes from the periodicity in the microstructures, all other features are randomly initialized. A circularity optimization parameter η is introduced to control the amount of optimization to be taken into account, ranging linearly from $\eta = 0$ (the original Voronoï diagram) to $\eta = 1$ (full optimization). With $\{x^0\}$ the coordinates of the intersection points of the original Voronoï diagram and $\{x^1\}$ the configuration after full optimization, the parameter η is taken into account by a linear interpolation between the two configurations:

$$\{x^\eta\} = (1-\eta)\{x^0\} - \eta\{x^1\} \tag{11.3}$$

Figure 11.2 gives an example of different optimization factors applied on a fixed set of Voronoï sites.

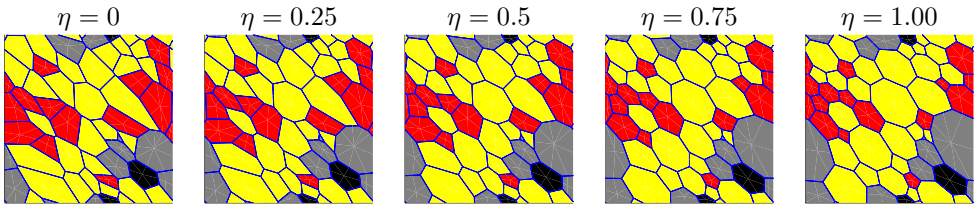

Fig. 11.2: An example of 5 REVs with $\xi = 0.5$, $\theta^{bed} = -45°$ and different circular optimizations η

11.1.2 Material anisotropy - grain shape tensor T

The random initialization for the generation of periodic REVs by Voronoï tesselation provides a distribution of grain shapes in which only the periodic boundary conditions influence the orientation of the grains and thereby anisotropy in the macroscale response. For REVs with increasing number of grains, this anisotropy will decrease and the expected response of the microstructural REV will therefore be less anisotropic. In order to obtain microstructures with grains with a certain preferential orientation, the grain shape tensor $\boldsymbol{T}$ is introduced for stretching and rotating the microstructure with respect to the periodic frame.

Although four components can be defined in $\boldsymbol{T}$, only two independent variables will be present in the final grain shape. These variables are here defined as the grain stretch ratio ξ and the bedding θ^{bed}, which can be related defining tensor $\boldsymbol{T}$ as follows;

$$\boldsymbol{T} = \begin{bmatrix} \xi\cos\theta^{bed} & \sin\theta^{bed} \\ -\xi\sin\theta^{bed} & \cos\theta^{bed} \end{bmatrix} \tag{11.4}$$

For an arbitrary grain shape tensor, the grain stretch ratio ξ corresponds to the ration of major principle stretch λ_1/λ_2, or the ratio of the eigenvalues of the symmetric stretch tensor $\boldsymbol{U} = (\boldsymbol{T}^T \cdot \boldsymbol{T})^{1/2}$. The bedding orientation θ^{bed} is the orientation of the major stretch with respect to $\vec{e}_1$, or the orientation of the eigenvector of stretch tensor $\boldsymbol{U}$ corresponding to the largest eigenvalue.

Figure 11.3 shows a microstructure with partial circular optimization ($\eta = 0.5$) and grain anisotropy $\xi = 1.5$ for a bedding plane $\theta^{bed} = 0°$.

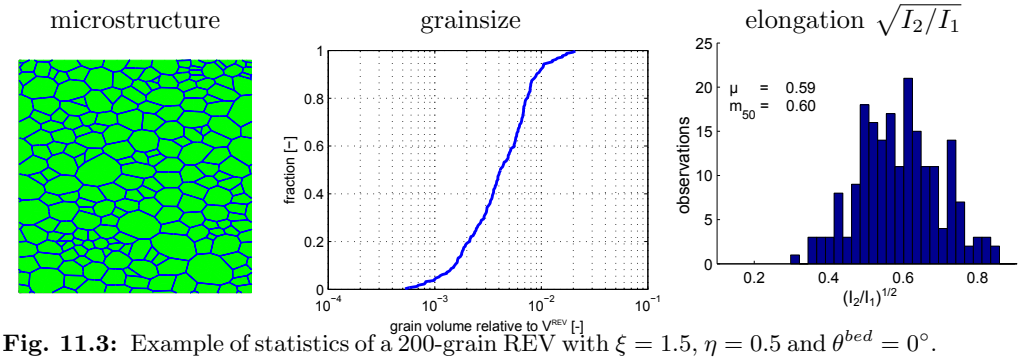

Fig. 11.3: Example of statistics of a 200-grain REV with $\xi = 1.5$, $\eta = 0.5$ and $\theta^{bed} = 0°$.

11.2 REV size and shape

The size and shape of the REV has an influence on the macroscale response. Three types of influence are distinguished here:

- The first type of influence is the representativeness of the REV with respect to the microstructure: In line with its classical definition, the REV needs to be large enough to contain a representative number of microstructural features to provide a proper macroscale average. Larger REVs will lead to better statistical representation of the microstructure.

- The second type is here the choice of the REV dimensions and the length scale it introduces in case of a softening response. This effect is present as soon as the material response looses its periodicity (generally around the peak response) and the REV size defines the relative spacing between possible localizations at the microscale (see Bilbie et al. [2008]).

- The last type of influence considered here is the choice of the shape (orientation) of the periodic frame in which the locally periodic microstructure is captured. This influence is present in the softening response and introduces orientation-dependent post-peak response. This effect will be referred to as the periodic frame effect.

In the following chapters, the three effects are demonstrated by several (statistical) characterizations.

11.2.1 Representativeness of the elementary volume

The first type of influence is not directly related to the boundary value problem of the REV. However, to REV-obtain objective results, the representativeness of the

microstructural geometry must be guaranteed and the reduction of the influence of the periodic frame on the grain geometry should be sufficient.

As an example, the convergence of the expected grain elongation $e = \sqrt{I_2/I_1}$ (to be compared with the experimentally observed distribution of elongation index $e = l_2/l_1$ (1.1)) towards a constant distribution with increasing number of grains per REV is shown in Figure 11.4. The expected distribution is obtained from a minimum number of 10.000 grains or 100 REV realizations each per REV size. The results for $\eta = 0$ and $\eta = 1$ show that the circularity optimization is influenced by the size of the REV and convergence of the expected grain elongation is obtained only for very large REVs. REVs with smaller numbers of grains suffer from a bias towards elongated grains. This effect is due to the periodicity in the Voronoï diagrams that prevents a proper optimization and stretches the grains due to the connectivity of the Voronoï diagram.

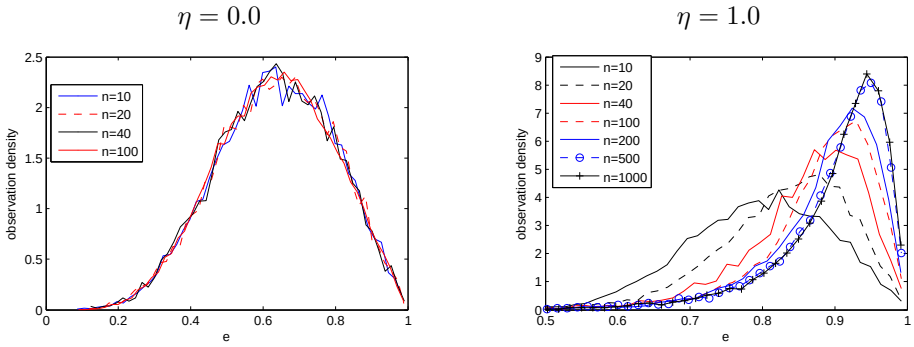

Fig. 11.4: Statistical distribution of grain elongation e as a function the number of grains per REV n.

As discussed in above, a low number of grains in a single REV can introduce a strong anisotropic response as the grains form a too small sample size for averaging and an increasing number of grains will lead to representativeness. In case the low number of grains would be the only effect playing on the response of the REV, the expected value for a randomly generated REV with low number of grains should be the same as the response found with a large number of grains. In a similar way, an REV with a limited number of grains provides only a limited number of localization paths between the grains and a low number of grain interfaces constraints the development of interface damage for certain orientations of applied deformation. Again, a larger number of grains lead to a better representation as the constraints on possible patterns of damaged interfaces is reduced.

To study these effects for REVs with relatively lower numbers of grains, a statistical averaging approach is followed to avoid the time-consuming computations on REVs with too many degrees of freedom. The averaged result of several randomly generated microstructures is studied to smoothen out the non-representativeness of the low number of grains and to obtain the peak response expectation. Microstructures with 10, 20, 40 100 and 200 grains are studies for circularity optimization of $\eta = 0$ (original Voronoï diagram) and $\eta = 1.0$ (optimal circularity). The peak response to biaxial vertical compression under 2 MPa lateral confinement pressure is studied to make a statistical characterization of the effect of the size and orientation of the REV on the global response. Figures 11.5

and 11.6 show the peak response to loading as a function of the orientation of the REV. A normal and log-normal distribution are then fitted to provide the 95% probability interval and the median, ploted together with the individual results.

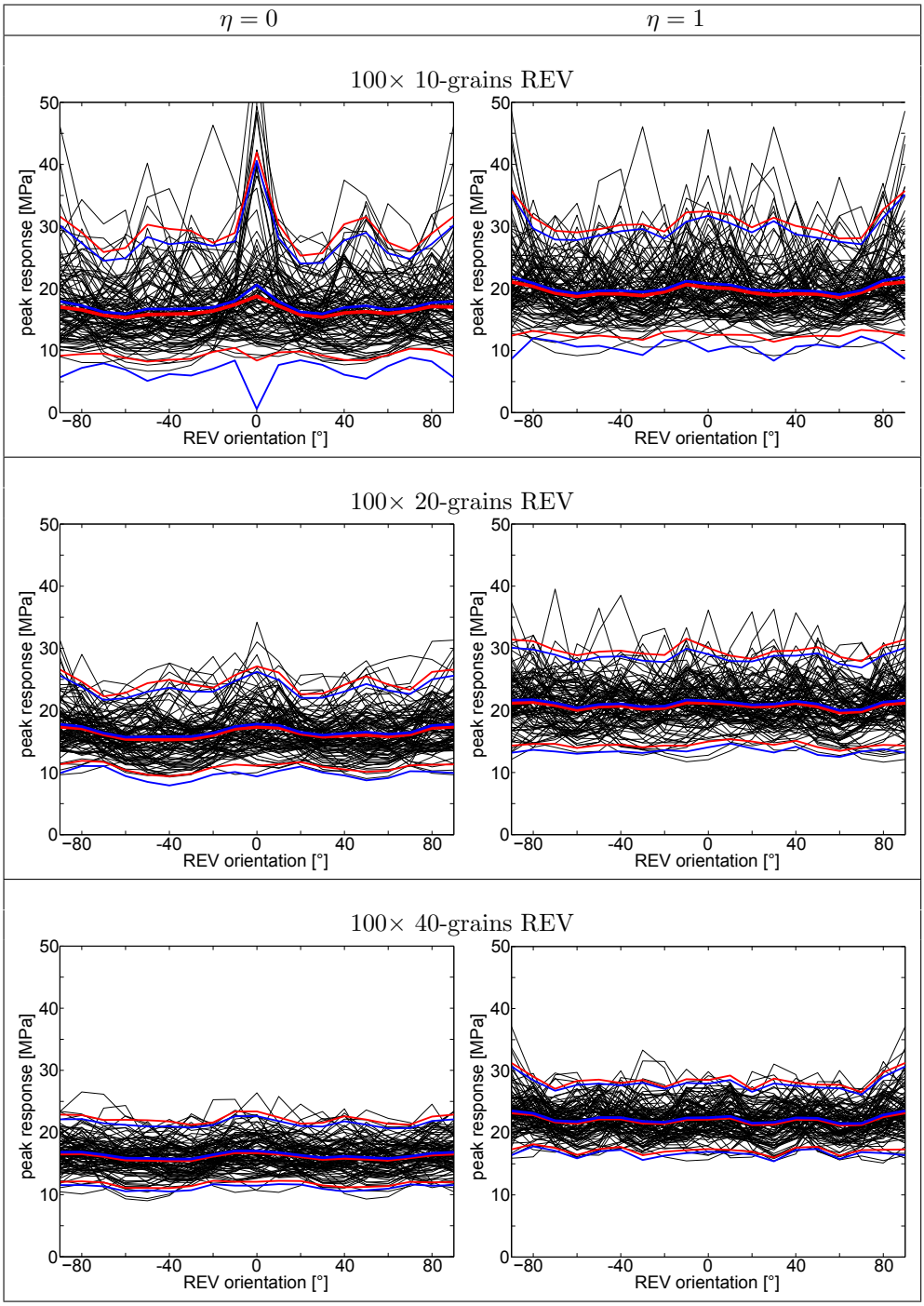

Fig. 11.5: Comparison of series of REVs of 10, 20 and 40 grains with the expectation and 2.5% probability upper and lower bound based on fitted norma (blue) and lognormal (red) distribution functions as a function of REV orientation θ^I

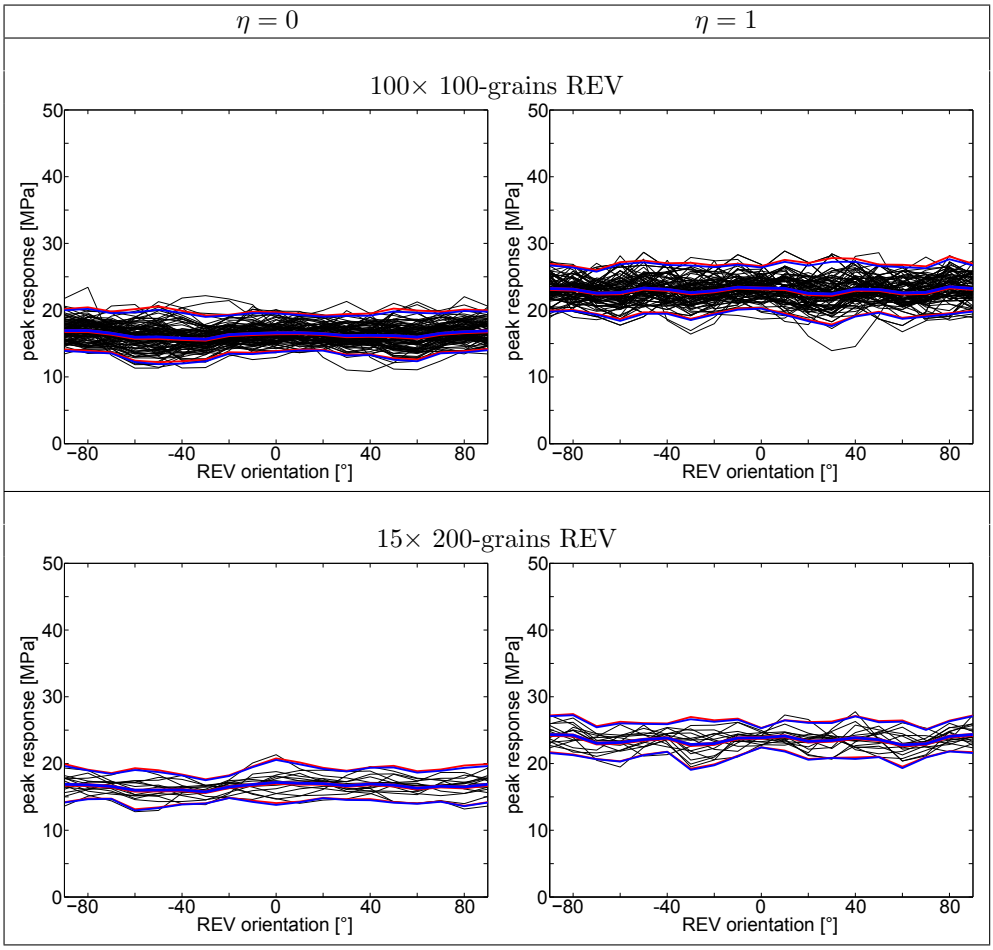

Fig. 11.6: Comparison of series of REVs of 100 and 200 grains with the expectation and 2.5% probability upper and lower bound based on fitted normal (blue) and lognormal (red) distribution functions as a function of REV orientation θ^I

From Figures 11.5-11.6 it can be concluded that for both types of REVs (0% and 100 % sphericity optimization), an increasing number of grains corresponds to a decreasing variability in response and therefore a better representativeness as is expected from the general concept of the REV. More specific convergence can be observed when the averaged curves for the different numbers of grains per REV are compared. For this purpose, the average over the expectation as a function of REV orientation (mean), the average over the standard deviation as a function of the REV (std) and a measure of the variation in the expected response as a function of REV orientation θ^I (computed as the maximum difference in response expectation divided by the average response expectation) are computed and presented in Figure 11.7.

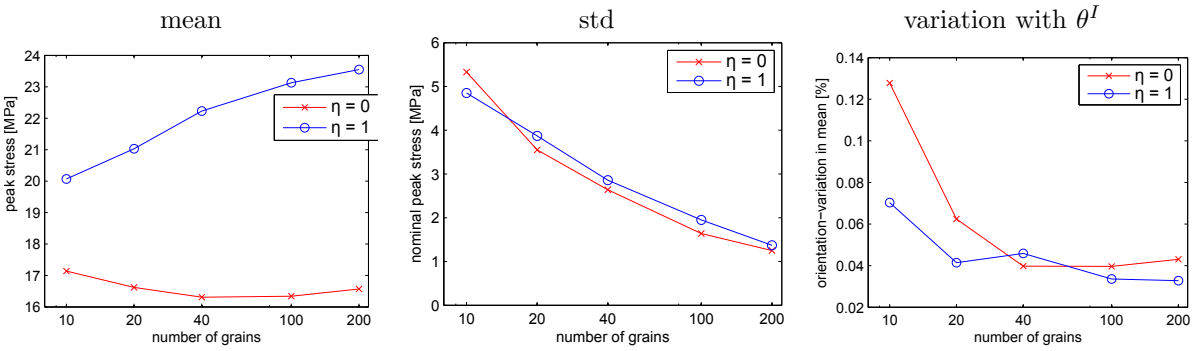

Fig. 11.7: Statistics of the peak nominal stress as a function of the number of grains per REV.

From Figure 11.7 the following can be concluded:

- The mean of nominal stress peaks appears to be constant for $\eta = 0$ for REVs with more than 40 grains. In the case of $\eta = 1$ a strong dependency can be observed in the mean of the expected peak stress, which can be related to the change in elongation as observed in Figure 11.4. The circularity of the grains appears to have a strong effect on the expected peak stress.
- The standard deviation in the peak response decreases with increasing number of grains per REV both for $\eta = 0$ and $\eta = 1$, which is perfectly in line with the concept of the representative elementary volume.
- The variation in the expected peak response as a function of REV orientation decreases with increasing number of grains per REV. This can be explained by the increase in possible patterns of damaged interfaces with the increase of grains in the REV. This convergence with increasing number of grains comes to a hold at 40 grains, where the relative variation becomes independent of the number of grains. This means that with more than 40 grains per REV, other effects (the periodic frame effect) become dominant in the orientation-dependency of the response.

It can be concluded that the REVs with an increasing number of grains in the REV, a (statistically) more isotropic peak stress response is obtained:. This indicates that a REV exists in the sense that it gives a reasonably objective description of the material behaviour and the influence of the boundary conditions vanishes asymptotically. In the post-peak regime, this is not the case, as the material periodicity is lost and localizations of interface deformation govern the behaviour. The influence of the localization manifests itself both through the length scale that is introduced by the (relative) size of the REV and the periodic shape effect.

11.2.2 The periodic frame effect

For the series of 100-grain REVs, the orientation-dependent stress response to biaxial loading is averaged over the 100 unique realizations. This gives statistically representative stress-strain curves for REVs with 100 grains at different orientations θ^I. Figure 11.8-left shows these curves for the REVs with 100% sphericity

optimization. Two types of curves can be destinguished based on their softening rate. These two types of softening response correspond to the two types of damage patterns in the interfaces; the stronger softening corresponds to a single localization path in the REV and the weaker softening to a double localization path. To demonstrate the relation between the REV orientation θ^I and the post-peak response, a crosssection of the stress-strain curves is taken at $\varepsilon_a = -0.025$. Figure 11.8-right shows the crosssections for the averaged stress-strain curves of 0% and 100% optimization. It is clear that there is a strong influence of the orientation of the REV and more precicely the orientation of the periodic boundary conditions in the response, with peaks in a 45° interval. Consequence is that the REV boundary orientations remain influencing the post-peak behaviour and presents preferential orientation of localization through the softening response.

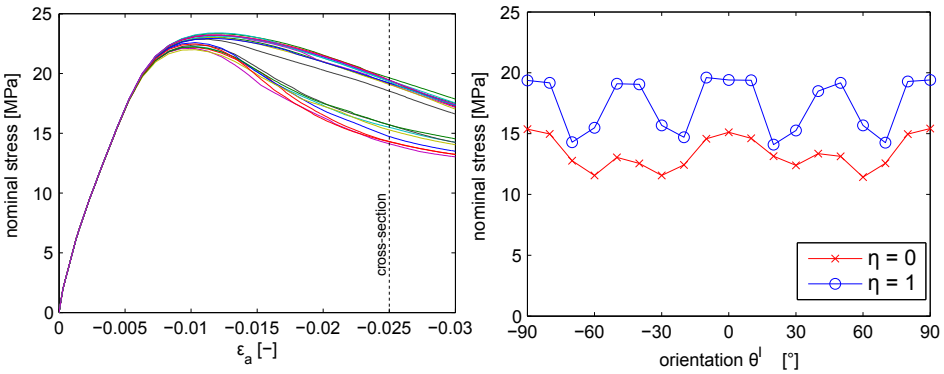

Fig. 11.8: Left: 100-test averaged stress-strain response for different loading orientations of 100-grains REVs with grain sphericity optimization $\eta = 1$. Right: orientation-dependent 100-test averaged response at -2.5% axial strain for $\eta = 1$ and $\eta = 0$.

12. PERFORMANCE AND COMPUTATIONAL EFFICIENCY

Compared to the classical FE methods with macroscale phenomenological constitutive laws, the FE^2 method is computationally expensive. Although the relative cost of the microscale computations goes down significantly with increasing numbers of degrees of freedom at the macro scale, the major part of the computation time is spent on the micro scale computations.

The possible gain in computational efficiency is therefore an important argument in the choice for computational homogenization by condensation, as it makes the additional four computations needed for the finite difference approximation of the consistent tangent stiffness matrix by numerical perturbation obsolete. Without these four additional computations, the theoretical reduction in computation time through the introduction of the condensation is a factor five (for mechanical problems) or eight (for hydromechanical coupling). However, the routine for homogenization by condensation requires some matrix operations as well and a certain overhead of initialization of the problem is required. This will reduce the factor 5 (or 8) to a theoretical upper limit of efficiency which, especially for relatively small microstructures, is difficult to obtain.

For the computational homogenization by static condensation (CHSC) to be effective, both its overall and its absolute efficiency has to be competitive with the method of numerical perturbation (NP). This requires in the first place a convergence of the macroscale Newton-Raphson scheme to be of the same quality as obtained by NP. Secondly, the computational effort required for the condensation needs to be much smaller than the computations it is replacing. In this chapter the performance of the developed methods are discussed with respect to computational effort and quality of convergence in doublescale computations.

12.1 Doublescale convergence studies

To assess the convergence of doublescale computations with hydromechanical coupling, several loading steps of the computation of Test B in Section 10.4 are repeated. Starting from the same state of deformation, identical loading steps are applied using either NP or CHSC for obtaining the consistent tangent stiffness matrices. Three loading steps are evaluated; a loading step in the elastic domain ($\varepsilon_a = -0.25$ %), a loading step just after the peak ($\varepsilon_a = -1.00$ %) and one at the end of the snap-through ($\varepsilon_a = -1.20$ %). Figure 12.1 shows the graphs for force convergence (left) and displacement convergence (right) as evaluated by the macroscale finite element program Lagamine, with;

FNORM	the norm of the out-of-balance forces (on the DOFs to be solved for),
RNORM	the norm of the reaction forces (the prescribed DOFs),
UNORM	the norm of the iterative updates of the DOFs to be solved for,
DNORM	the norm of the loading step updates of the DOFs to be solved for.

The ratios FNORM/RNORM and UNORM/DNORM can be compared with convergence criteria for the forces (combining nodal (double) forces and nodal fluid mass balance) and displacements (DOFs u_i ν_{ij} and p). Details of the normalization of the different terms are not discussed here, as only a comparison between NP and CHSC is made.

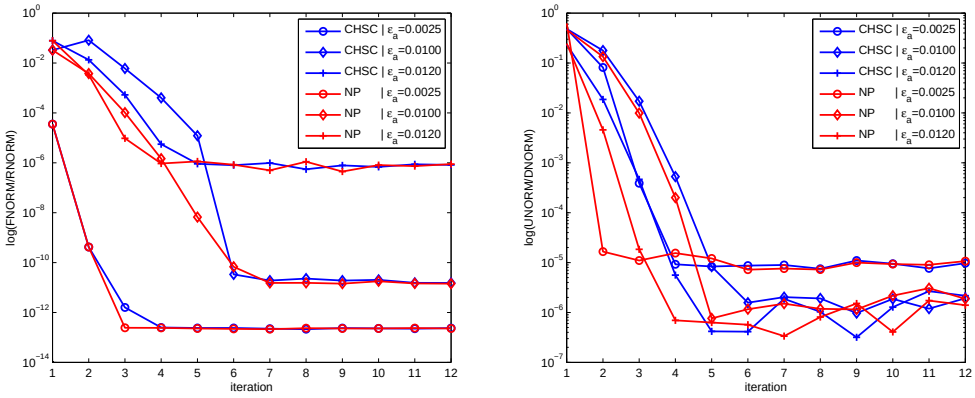

Fig. 12.1: Convergence graphs for computational homogenization by static condensation (CHSC) and numerical perturbation (NP) for the HM-coupled biaxial compression test $D = 1 \times 10^{-11}$ in Section 10.4

The convergence graphs in Figure 12.1 demonstrate that the convergence of the macroscale Newton-Raphson scheme obtained when using CHSC is of the same quality as when NP is used. This holds for the elastic domain as well as the softening domain. However, it is not guaranteed that this result always holds and the Newton-Raphson algorithm does not necessarily leads to convergence and stiffness matrix obtained by a numerical approximation such as the numerical perturbation might sometimes better deal with the material non-linearities to be taken into account around the test configuration.

For the simulation of the biaxial compression with fluid in Section 10.3, the convergence profiles for forces and displacements are generated using numerical perturbation and condensation for obtaining the tangent operators. The comparison at different states of deformation (linear domain, at peak response and after snapthrough) are given in Figure 12.2. The convergence criteria present the combined normalized errors for nodal forces and double forces.

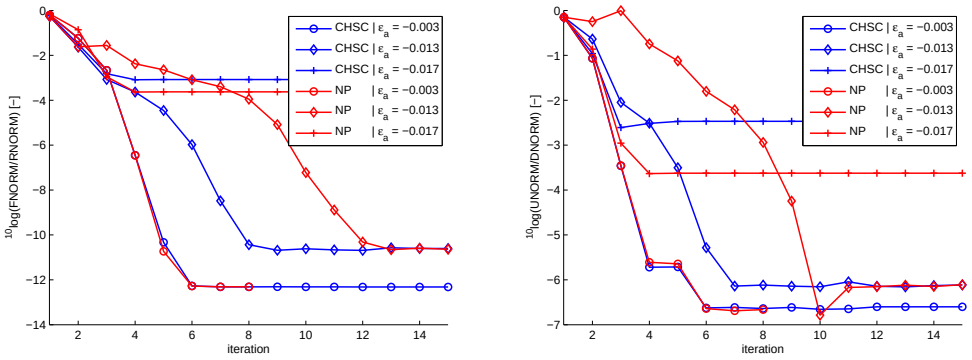

Fig. 12.2: Convergence at $\varepsilon_a = -0.30\%$, $\varepsilon_a = -1.3\%$ and $\varepsilon_a = -1.90\%$ for the mechanical biaxial test in Section 10.3

12.2 Computational efficiency: NP vs. CHSC

The finite element method is based on the linearization and discretization of the nonlinear field equations into a system of linear auxiliary equations to obtain a solution in an iterative way. From a computational expense point of view, solving these linear systems of equations is the core business of the finite element method. With increasing number of degrees of freedom, practically all computation time is spent in solving the auxiliary systems of equations. In the optimization of the efficiency of the finite element code, it is key to solve these kind of systems as efficient and as few times as possible. The reduction of the number of times the system of equations has to be solved is closely related with the consistency of the finite element formulation, which was discussed above. The efficiency of the numerical solvers and routines is discussed in this section.

12.2.1 Condensation vs. numerical perturbation

One of the arguments of the introduction of the computational homogenization by static condensation is the possible gain in computational efficiency of the code. This gain is obtained through the reduction of the number of times the microscale systems of equations have to be executed, as no solutions for the 4 or seven perturbations are required. The condensation routine, in which no microscale decoupling of the hydraulic and mechanical systems is possible, also involves solving linear systems of equations and the gain in efficiency will depend on the complexity and size of these systems of equations with respect to the computations usually needed for the perturbations. An objective characteristic time for the computational cost of the perturbations is the time taken by the microscale model to complete a single iteration of its N-R algorithm. Therefore, the following two routines are distinguished in the comparison of computational efficiency:

One microscale iteration This iteration concerns only the mechanical system of equations. The main computational work in this routine consists of;

- a loop over the elements, building the element stiffness matrices,
- the global assembly of the system of equations,

- evaluation of convergence of the NR algorithm
- solving the system of equations to find a correction of the nodal positions
- updating the nodal positions

The number of operations with respect to the number of degrees of freedom is of a first order $O(n^1)$ for all these points except for solving the system of equations: Triangular decomposition and back-substitution of the system of equations in skyline storage [Bonet and Wood, 2000, Zienkiewicz and Taylor, 2000, Press et al., 1993] is used for solving this. With a constant maximum number of degrees of freedom per equation (a node has only so many nodal connections in the finite element mesh), this leads to a complexity $O(n^2)$ for solving the linear system of auxiliary equations.

The mechanical condensation routine

Only the purely mechanical condensation routine is considered, because the routine for hydromechanical coupling is not optimized with respect to the bandwidth of the coupled system of equations (see Figure 12.3). The main computational work in this routine concerns;

- building the dense system of equations from the sparce system of equations (last micromechanical iteration)
- reducing the dependent degrees of freedom and reactions from the system of equations $[K] \rightarrow [K^*]$
- solving the condensation system of equations $[K^{*ff}][X] = [K^{*fp}]$
- matrix multiplication $[S] = [K^{*pp}] - [K^{*pf}][X]$

Again, the most computationally expensive part of the routine is solving the system of equations, which is done by a Gauss-Jordan algorithm and is of order $O(n^2)$ with respect to the number of degrees of freedom n. The complexity of order two is provided by the relatively low number of degrees of freedom per equation and the band width that can be taken into account.

Renumbering of the equations following the Cuthill-McKee algorithm [Cuthill and McKee, 1969, Bonet and Wood, 2000] is used to provides a system of equations with optimally reduced bandwidth. This is advantageous to both routines, as the band width can be used for the reduction of the number of operations to be performed in solving the system of equations. Moreover, a smaller bandwidth leads to a more efficient skyline storage, as fewer zero terms are taken into account. This renumbering is only taken into account for the mechanical part of the system of equations; the combination of hydraulic (p) and mechanical (u_i) degrees of freedom, defined on different nodes with a more complicated level of dependency has not been implemented. This means that no optimal band width renumbering is available for the HM-coupled systems of equations in the condensation of the coupled tangent operators.

An example of a (reduced) HM-coupled system of equations profile is given in Figure 12.3. It clearly shows the band in the mechanical part of the system of equations, whereas the hydraulic part and the coupled part show an irregular pattern, which is unfavourable for both storage and numerical performance.

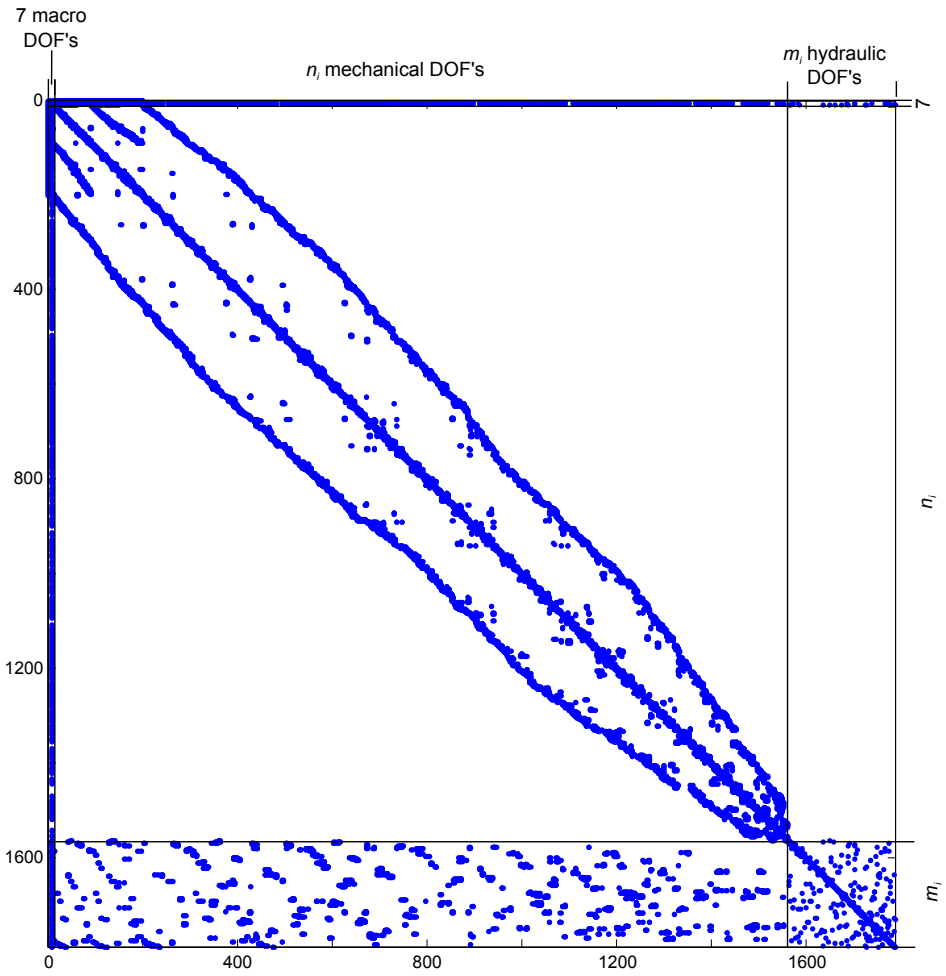

Fig. 12.3: Matrix profile of the reduced global system of equations (6.58) for a typical REV with hydromechanical coupling and 822 mechanical nodes. The number of nonzero terms in this matrix is 32022

The performance tests in this section, as well as most of the computations presented in this work, are all performed on a machine with the following processor specifications:

Processor	: Intel(R) Core(TM) i7-2670QM CPU @ 2.20→3.10 GHz
RAM	: 8 GB
cache memory	: L1 = 4 × 32 kB
	L2 = 4 × 256 kB
	L3 = 6 MB

Figure 12.4 shows the average computation time required for the different routines, obtained from computations on REVs with different numbers of degrees of freedom. It shows that for smaller REVs, the computational time is indeed quadratic with the number of equations ($O(n^2)$) for both routines and the condensation routine takes 2 to 3 times as much time as a single microscale iteration.

grains	DOFs	profile size	profile memory
10	440	42.780	342 kB
14	580	67.208	538 kB
20	772	101.730	814 kB
28	998	145.952	1.17 MB
40	1346	233.752	1.87 MB
50	1570	262.054	2.10 MB
60	1974	497.604	3.98 MB
80	2458	565.496	4.52 MB
100	**3086**	**792.144**	**6.33 MB**
120	3696	1.335.474	10.7 MB
150	4530	2.377.810	19.0 MB
200	5884	5.369.486	43.0 MB
240	6960	9.041.958	72.3 MB
300	8520	16.364.914	131 MB
340	9758	24.198.572	194 MB

Tab. 12.1: Size of upper/lower triangle profile of the global mechanical system of equations for different REV size.

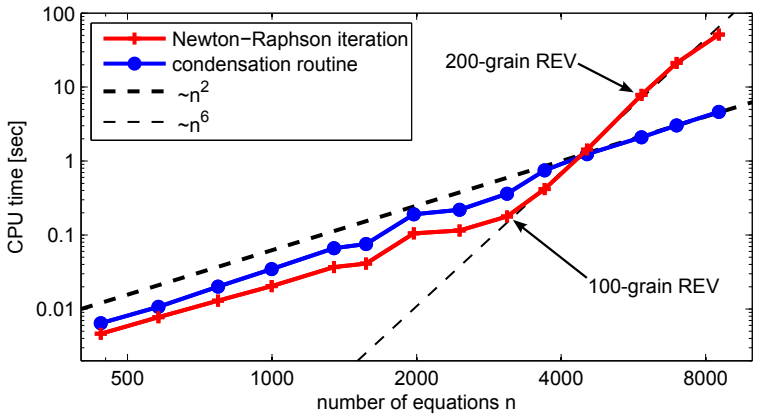

Fig. 12.4: Computation time of the condensation routine, compared to the computation time of the FE iteration.

The sudden strong increase in CPU time of the Newton-Raphson scheme starting at approximately 3000 equations can be traced back to the CPU cache size of 6.144 MB. As the routine for triangular decomposition of the mechanical system of equations does not take into account the memory access, significant loss in computational efficiency takes place when the workable set of data no longer fits the size of the cache memory and RAM memory needs to be accessed. Table 12.1 contains the size of the skyline storage, required for the upper and lower part of the stiffness matrices. The maximum cache size of 6.144 MB corresponds well with the start of the rapid increase of computation time for REVs with more than 100 grains.

The effective gain in total computation time between NP and CHSC does not only depend on the ratio between the two routines discussed above because the total time is strongly influenced by the number of iterations at the micro-

scale. In addition, there is a certain amount of time required for the initiation and preprocessing of the microscale finite element computations, which can be seen as an overhead cost on the REV computations. It is therefore unlikely that the upper bound limit of gain in efficiency (5 times for mechanical computations and 8 times for hydromechanical coupling) will be obtained, especially in case of small increments, for which the microscale computation requires a small number of iterations (typically less then 10) to converge. The efficiency is therefore computation-dependent; both with respect to REV size (relative overhead cost and numerical efficiency) and model complexity (number of microscale iterations). In the following paragraphs, results for the assessment of the gain in computational efficiency are given for the doublescale computations presented earlier.

12.2.2 Gain in efficiency for mechanical computations

CPU time required for the mechanical simulation presented in Section 10.3 using numerical perturbation and static condensation respectively are measured. An automatic strategy is used for defining the loading time steps, based on their (non)convergence. Due to a good agreement in the rate of convergence between the two methods, the same loading steps could be applied and the total number of iterations required for obtaining the converged loading steps is equal between the two methods.

Results are presented in Table 12.2 for the entire computation. The most important result is the overall speed-up by a factor 3.20. This ratio contains the overhead cost of the FE computations and the costs of the computational homogenization itself, which reduces the efficiency from the an optimal ration of 5 to a ration 3.20. In computations with larger microscale problems, the efficiency ratio can increase.

computations $\varepsilon_a = 0 \rightarrow -2.0\%$	NP	CHSC	ratio
total computation time	6.25×10^4	1.95×10^4	3.20
- on micro level	6.04×10^4	1.74×10^4	**3.47**
- on macro level	2.10×10^4	2.10×10^3	-
number of converged loading steps	36	36	-
number of iterations leading to convergence	189	189	-
average microscale comp. time (per IP)	12.10 ms	3.49 ms	3.47

Tab. 12.2: Computation time for biaxial compression test up to $\varepsilon_a = 2.0\%$

Computations have been performed without parallelization of the computation. As indicated in Table 12.2, the computations related to the micro level take most of the time. As these computations are highly suitable for parallelization, an important gain in efficiency can be obtained by parallelization of the micro level routine and evaluating multiple REV boundary value problems in parallel.

12.2.3 Gain in efficiency for HM coupled computations

For the three loading steps for the evaluation of the convergence graphs in a HM-coupled test in Section 10.4, the time per iteration for NP and CHSC is compared. Compared to the theoretical ratio of 8, the ratio in computation

time of 4.7 obtained for these computations seems very reasonable, and allows a very significant speedup. This includes all overhead such as memory allocation, preprocessing and the additional time for the condensation of the coupled system of equations, for which no band width optimization is implemented.

step	time/iter CHSC [*sec*]	time/iter NP [*sec*]	ratio NP:CHSC
$\varepsilon_a = 0.25$ %	4.50	21.42	4.76
$\varepsilon_a = 1.00$ %	4.25	19.83	4.66
$\varepsilon_a = 1.20$ %	4.36	21.18	4.85

Tab. 12.3: Effective efficiency double scale computation macroscale loading step for the HM-coupled biaxial compression test in Section 10.4

CONCLUSIONS PART III

It can be concluded that on the material point level, the presented micromechanical model can provide a macroscale HM-coupled constitutive relation by applying the principle of computational homogenization on the micromechanical REV dictated by the macroscale kinematics. Both macroscale stress response and tangent operators can be found by computational homogenization, in order to be used in a material point BVP, simulating the local material behaviour under arbitrary loading paths. Following the same approach, the micromechanical model is used in doublescale computations, providing a complete framework for the modelling of hydromechanical macroscale poromechanical behaviour based on micromechanical constituents.

With the purpose of easily producing microstructures with statistically consistent grain shapes and a certain randomness, an algorithm was presented generating REVs based on Voronoï diagrams. The peak response to biaxial compression was used to demonstrate the influence of the periodic frame on the macroscale response. Statistical analysis has shown that a systematic variation in peak strength as a function of REV orientation is present. The same goes for the influence of the periodic frame with respect to the post-peak response to biaxial compression: the definition of the periodic frame has an influence on the post-peak behaviour that appears as an orientation-dependency in the post-peak stiffness.

Part IV

APPLICATION TO DOUBLESCALE MODELLING OF HYDROMECHANICAL BEHAVIOUR OF CLAYSTONE

13. MODELLING ANISOTROPIC BEHAVIOUR

In this section the anisotropic behaviour of the macroscale response is investigated using a microstructure with a less prominent preferential direction than in the example computation given above. The anisotropy, which is deliberately introduced through the grain shape, is investigated by evaluating the response to biaxial compression of the REV under different orientations θ^I. Microscale constitutive parameters are chosen such that the initial stiffness of the interfaces is high with respect to the stiffness of the grains. This results in a nearly isotropic initial effective stiffness, as the influence of the interfaces will be small.

A REV with grain shape parameters $\xi = 1.5$, $\eta = 0.2$ and $\theta^{bed} = 0$ (see Section 11) containing 40 grains with identical stiffness properties is defined (see Figure 13.1). The effect of the introduction of the anisotropy due to the elongation of the grains is studied.

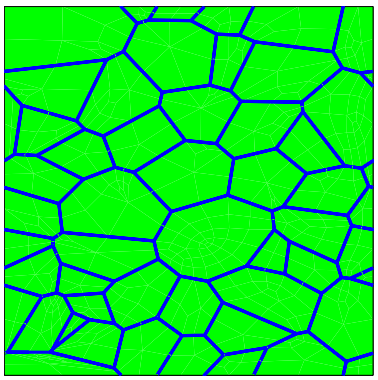

grains:	40
χ	1.5
η	0.2
θ^g [°]	0
solids:	
E [GPa]	6
ν [-]	0.2
interfaces:	
$\delta^c_{t/n}$	0.05
$D^0_{t/n}$	0.002
$T^{max}_{t/n}$ [MPa]	5.0

Fig. 13.1: Microstructure with uniform grain properties for anisotropic macroscale response.

13.1 Materialpoint biaxial compression

Biaxial compression under 12MPa confinement stress is applied on a single material point. The orientation of the REV with respect to the direction of compression is changed and the difference in peak stress response to biaxial compression is studied for characterizing the anisotropy in the material behaviour.

Figure 13.2 shows the stress-responses of seven different orientations. The initial stiffness of the material is consistent between the different orientations and is equal to the stiffness of the grains. As an effect of the high initial stiffness of the interfaces, the macroscale stiffness is governed by the stiffness of the grains

and no initial anisotropy is present.

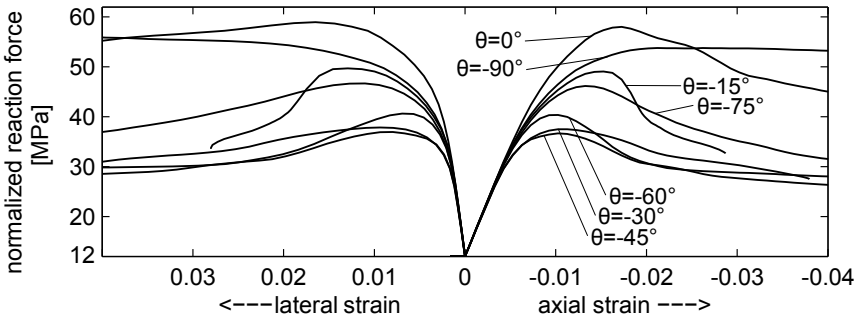

Fig. 13.2: Response to the biaxial compression for different REV orientations.

The peak response shows a strong variation with REV orientation. Figure 13.3 shows the peak response as a function of REV orientation, visualizing the anisotropic nature of the material strength. This strength can be related to the bedding: loading perpendicular and parallel to the bedding gives approximately equal responses, intermediate orientations give lower strengths and a smooth graph with peaks at -90 and 0 degrees and a minimum close to 45 degrees can be drawn as a function of the loading orientation. Such anisotropy in material strength correspond well to strongly-isotropic shales, see for example the experimental work of Niandou et al. [1997].

Fig. 13.3: Anisotropy in material strength. The continuous line is obtained from material point biaxial compression tests, the points are the nominal peak stress responses of doublescale biaxial compresison simulations.

The deformed microstructures for REV orientations (and thereby also bedding planes) at an interval of 15 degrees is given in figure 13.4. From the microscale point of view, the softening phenomena seem to align with the bedding orientation, except for the case of parallel ($-90°$) and perpendicular ($0°$) loading.

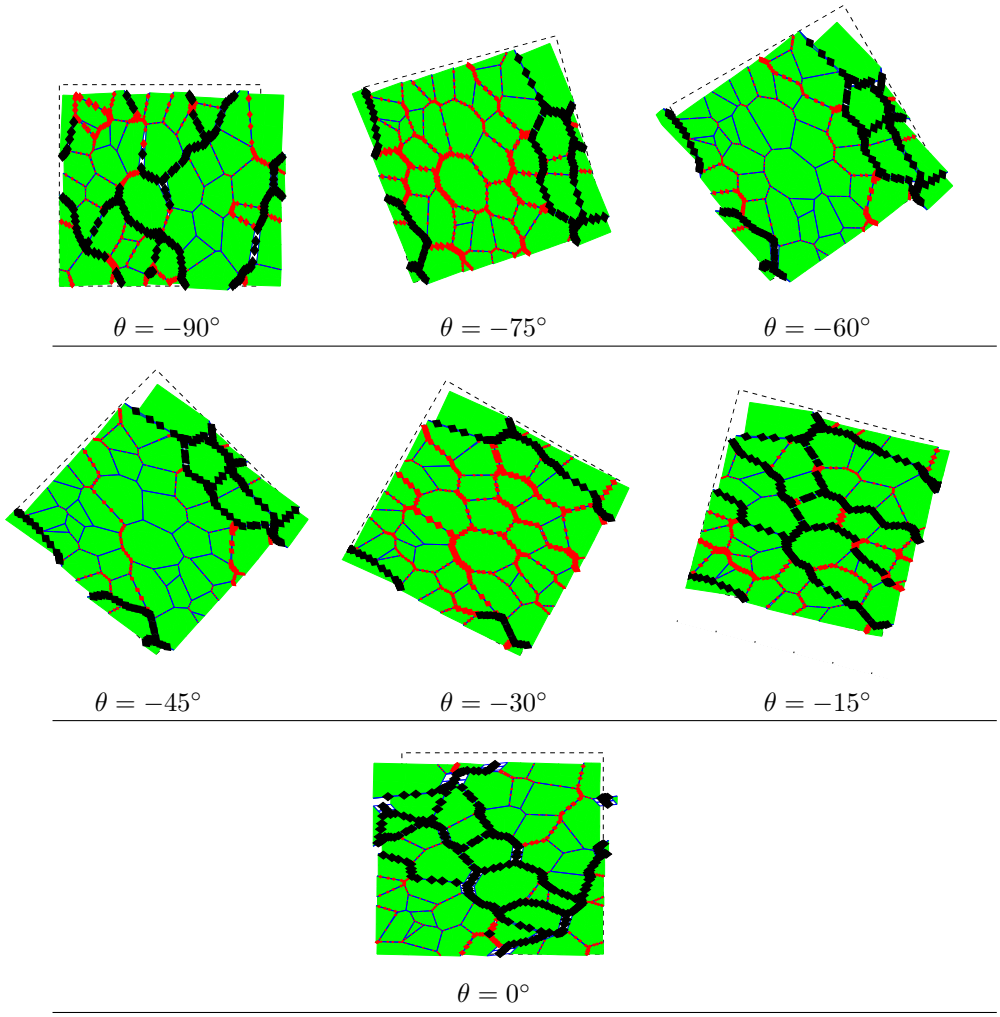

Fig. 13.4: Deformed microstructures for different REV orientations; microscale localizations.

13.2 Doublescale simulation of biaxial compression

The REV presented in the analysis above is used in the doublescale modelling of biaxial compression of a 38×76 mm sample under 12 MPa confinement. The local second gradient model is used to obtain mesh-objective results for strain localization. The second gradient parameter D is calibrated at 1.25 kN to obtain a shear band of approximately 5 elements (≈ 20 mm) wide. REV orientations on an interval of 15° between $\theta^I = -90°$ and $\theta^I = 0°$ is used. The peak response of the different doublescale biaxial compression tests is included in Figure 13.3 and coincide perfectly with the local peak response, which suggests a homogeneous deformation at least up to the peak response. The local stress-strain curves for two tests are given in Figure 13.5, including the local response obtained by the material point BVP. Good agreement between the global and local responses is found until the curves separate at the peak response as an effect of localized deformation in the doublescale computations. The same pre-peak agreement can

be found for the other orientations.

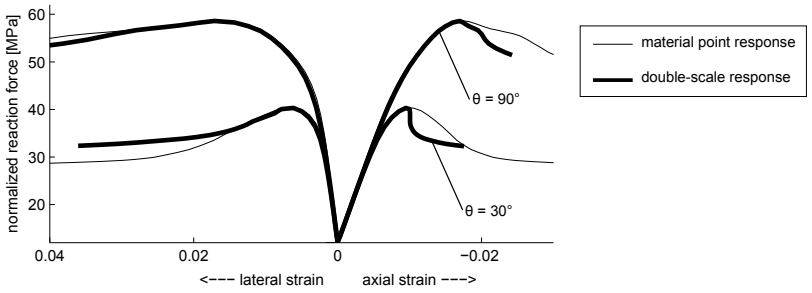

Fig. 13.5: Material point response and macroscale nominal stress response to biaxial compressive deformation.

Figure 13.6 shows the deformed meshes at macro and micro level for $\theta^I = 0$ and $\theta^I = -60$. Strain localization in a shear band can be observed in the both macroscale meshes

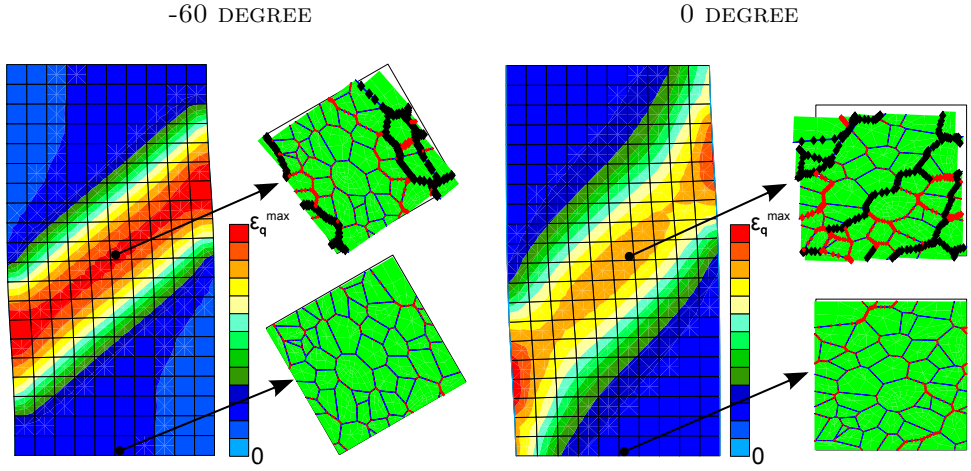

Fig. 13.6: Deformed mesh with total Von Mises equivalent strain at maximum compression. The microstructures show the micromechanical damage (red) and decohesion (black) related to the macroscale material softening.

Comparing the orientation of the macroscale localization with the micromechanical pattern of damage and decohesion, it is important to notice that no correlation between micro and macro localization orientation exists. This has important implications for possible enhancements of the doublescale approach, such as the continuous/discontinuous frameworks, for which criteria are required for the initialization of the discontinuous enhancements of the macroscale domain.

The $\theta^I = -60°$ test has demonstrated that the orientation of the macroscale localization is independent of the bedding orientation, and here appears approximately conjugate to the macroscale localization band.

14. CALIBRATION OF THE MICROSCALE MODEL TO COX

14.1 Grain shape modelling

For obtaining the correct shape of inclusions in the REV several approaches can be envisioned. One of them would be to construct the REV from images of the microstructure itself by discretization into matrix material and different types of inclusions. In this way, the observed inclusion geometry and their spatial relation can very accurately be captured in the REV simulation. However, some modifications are then required to obtain locally periodic REVs and meshing might be difficult. Moreover, the potential interfaces in the matrix domain will have to be defined, which requires some assumptions on the potential of micro cracks forming between the inclusions.

An alternative approach is used here by generating REVs with the routine introduced in Chapter 11. The characterization of the geometry and orientation of the inclusions (tectosilicates and carbonates) is available from imaging analysis [Robinet, 2008, Robinet et al., 2012], as summarized in Chapter 1. The objective is to capture these characteristics using the Voronoï-based REVs. This is done by calibrating the grain shape variables (ξ, η and θ^I) against the grain shape characteristics derived from experimental observations as presented in Chapter 1.

Although a more consistent approach would include the evaluation of the different types of inclusions individually, the shape of the assembly of grains generated by the REV generator will be used here. As the REV generator is not designed to distinguish between different groups of grains, considering their properties individually is not a valid approach and the characterization of the grain shapes of the simulations will therefore be done on the assembly of numerical grains (both inclusions and matrix material) as a whole.

Fitting the numerical simulations of the grain shapes to the experimental results in Figure 1.3 is based on statistical averaging. For a range of parameters ξ and η, a series of 100 REVs with 200 grains is generated. A fixed bedding plane $\theta^{bed} = 10°$ is used to meet the orientation of the grains (Figure 14.1), rather than to match the in-situ inclination of the bedding plane which is between 1° and 1.5° [Andra, 2005a]. The histograms of the individual grain orientation β and grain elongation $e = \sqrt{(I_2/1_1)}$ are compared with the equivalent experimental histograms. The application of the circularity optimization η is found to have a strong influence on the distribution of the orientations, as it tends to align the grains in the principal direction of θ^{bed}.

From the characterization of the COx microstructure, histograms of the statistical distribution of the elongation and orientation of carbonate and textosilicate inclusions are available. The spatial distribution of the inclusions (clustering of inclusions, contacts, spatial correlation in orientation, ...) is not characterized. With the current method of simulation of the microstructure only a single inde-

		⊥ to bedding plane	∥ to bedding plane
H	ξ	1.3	1.0
	η	0.1	0.1

Tab. 14.1: Results of the numerical calibration of the grain geometry parameters to be used in the REV generator against image analysis data on COx.

pendent distribution of respectively grain elongation, grain orientation and grain size is provided. Assigning different properties to distinguish between different inclusions can therefore not result in multiple independent statistical distributions for each type of inclusion without risking a very biased distribution for the remaining grains that make up the clay matrix. For this reason, the choice of the individual grains to assign the inclusion material properties to is made randomly and the resulting distributions of simulated inclusion shapes is identical to the initial grain shape distributions. This means that only a single distribution is available from the simulation and comparison between experimental observations and simulations is therefore a comparison between the distributions of the specific inclusions (experimental) with the overall grain shape (simulations).

Two sets of histograms of the experimental characterization of the inclusion shapes are available; one for the carbonate inclusions (Figure 14.1) and one for the tectosilicates (Figure 14.2). Each set contains histograms perpendicular and parallel to the bedding plane for the inclusion elongation e and orientation. The best fit of the numerical simulations for ξ and η to both histograms leads to the calibration results given in Table 14.1 The numerical and experimental results in 14.1 show that the preferential orientation at 10° is correctly reproduced and the variation in orientation frequency is accurately simulated. The histogram for elongation index shows a less good agreement, which can be explained by the effect of elongated carbonate inclusions of organic origin that can not be simulated by Voronoï-based grain structures.

The histograms for the elongation index of tectosilicates shows a better agreement between numerical and experimental results. The histogram the distribution of the grain orientation could be improved by reducing anisotropy ξ, but in that case the good agreement with the distribution of the carbonates is lost.

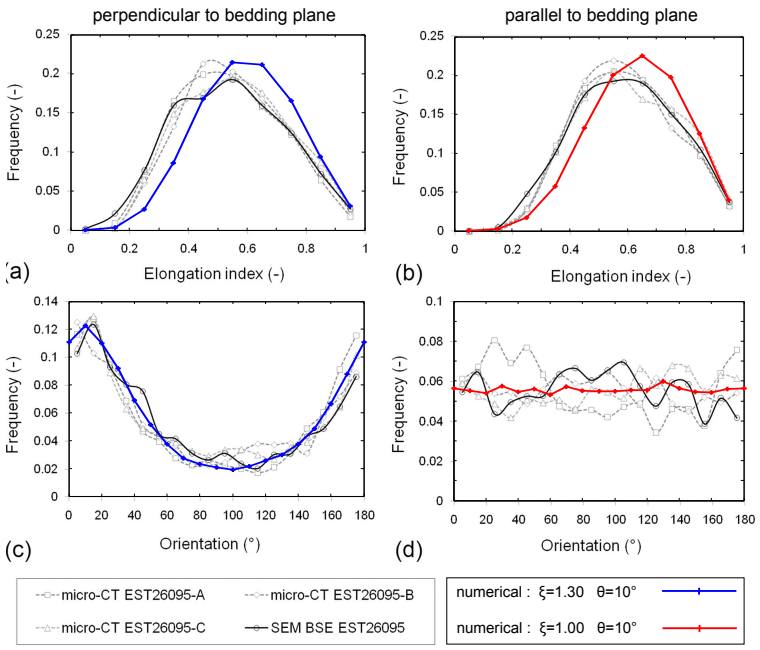

Fig. 14.1: Shape statistics of carbonate inclusions from 2D images perpendicular (left) and parallel (right) to the bedding plane [Robinet et al., 2012] in comparison with simulated grain shapes.

	volume %	E [GPa]	ν [-]
tectosilicates (quartz)	15%	95	.074
carbonates (calcite)	25%	84	.317
heavy minerals (pyrite)	3 %	305	.154
clay matrix material	57%	-	-

Tab. 14.2: Elastic properties assigned to the inclusions

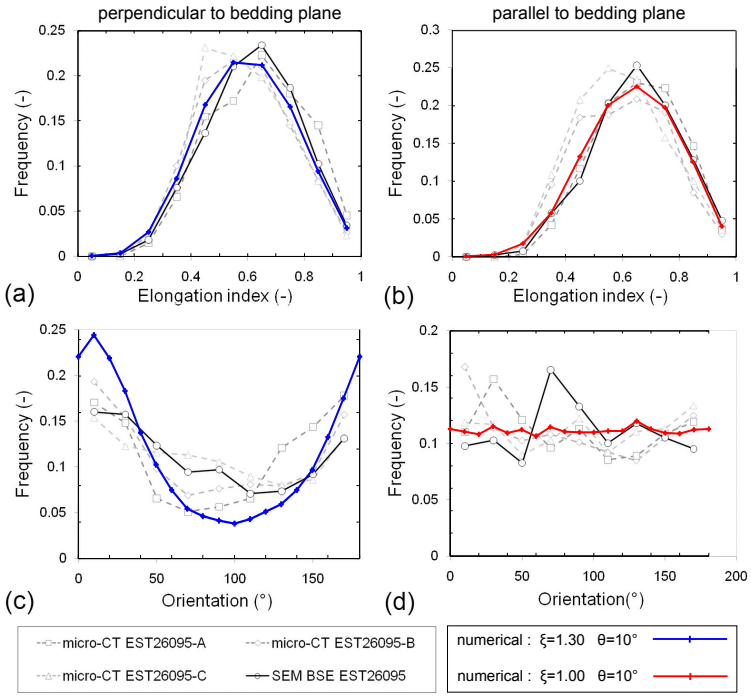

Fig. 14.2: Shape statistics of tectosilicate inclusions from 2D images perpendicular (left) and parallel (right) to the bedding plane [Robinet et al., 2012] in comparison with simulated grain shapes.

From the histograms of elongation and orientation it can be concluded that the Voronoï-based REV generation can, from a statistical point of view, reproduce well the available characteristics of the inclusion geometry.

With the calibrated grain characteristics, 40-grain REVs can be generated for further calibration against the mechanical characteristics of the claystone. One realization of these REVs is given in Figure 14.3. As no geometrical differentiation is made between the shape or size of the inclusions, inclusion properties can be assigned randomly based on their volume fraction obtained from image analysis. The volume fractions given in Table 14.2 are used for the distribution of the in the REV by calculating the relative number of grains related to each volume fraction (rounded upward).

14.2 Fitting the macroscopic material response

With the grain geometry fitted and the inclusions assigned to several grains, the macroscale response to biaxial compression needs to be fitted against results obtained from drained triaxial compression tests. Therefore the elastic properties of carbonates (calcite), tectosilicates (quartz) and heavy minerals (pyrite) are assigned to the corresponding grains according to Table 14.2. The mechanical characteristics for the calibration of the remaining grains representing the clay matrix and the interfaces are obtained from triaxial tests [Andra, 2013, Armand et al., 2013]. For the numerical modelling under plane strain conditions to be comparable with the results of triaxial data, the different appearance of stiffness and Poisson's ratio need to be taken into account. An apparent plane-strain modulus E^{ps} can be defined to compare with the Young's modulus derived from the triaxial tests;

$$E^{ps} = \frac{\delta\sigma_a}{\delta\varepsilon_a} = \frac{E}{1-\nu^2} \tag{14.1}$$

The same can be done for the Poisson's ratio:

$$\nu^{ps} = -\frac{\delta\varepsilon_{lat}}{\delta\varepsilon_a} = \frac{\nu}{1-\nu} \tag{14.2}$$

The plane strain modulus E^{ps} is the ratio between variations of axial stress σ_a and axial strain ε_a, the plane strain Poisson's ratio ν^{ps} is the ratio between variations of axial strain and lateral strain ε_{lat} . When applied to the reference parameters for the COx claystone ($E \approx 4.0\ GPa$ and $\nu \approx 0.3$, [Armand et al., 2013]), the plane strain equivalent parameters become:

$$E^{ps} = 4.4\ GPa, \qquad \nu^{ps} = 0.428 \tag{14.3}$$

This difference in elastic properties has to be taken into account when comparing the numerical biaxial and experimental triaxial results. The material strength (nominal peak stress) derived from triaxial tests can not be translated directly to plane strain conditions as it requires information on the dependency of the the peak strength (the 'failure') on the Lode angle (defined by the dependency on the intermediate principal stress). This information can generally be obtained from the failure criterion, which is unknown. Moreover, in the doublescale modelling approach, out-of-plane stress is not defined, which means that the Lode angle can not be obtained for making the comparison. Only a qualitative prediction can be made, based on the stress paths of biaxial- and triaxial tests and the properties of general failure criteria. This would predict a lower (or at least an equal) peak response in case of triaxial compression compared to the biaxial compression test (plane strain conditions) when constant confinement stress is applied.

To avoid the quantification of the difference in peak response, the peak response of the biaxial compression test is fitted to be equal to the triaxial compression test.

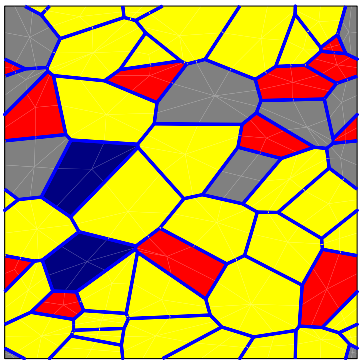

solids:	Si_mO_n	$-CO_3$	FeS_2	clay
E [GPa]	95	84	305	2.3
ν [-]	0.074	0.317	0.154	0.11

interfaces:	
$\delta^c_{t/n}$	0.05
$D^0_{t/n}$	0.002
T^{max}_n [MPa]	1.0
T^{max}_t [MPa]	5.5

Fig. 14.3: Microstructure '8' with carbonate (gray), tectosilicate (red) and pyrite (deep blue) inclusions in a matrix of clay (yellow). Grain selection for material allocation has been performed randomly.

The remaining micromechanical parameters (the clay matrix elasticity and the interface cohesion parameters) are adjusted in order to fit the numerical material point response to the biaxial compression to the post-peak part of the experimental results. This is done following the following procedure:

- The initial state of softening for normal and tangential components of cohesion D^0_n and D^0_t are chosen high, such that the initial stiffness of the interfaces is high with respect to the stiffness of the grains. The initial response of the REV is therefore mainly controlled by the stiffness of the grains.
- The stiffness parameters E and μ to be used for the grains that make up the clay matrix are fitted such that the initial response to compressive loading represents the correct macroscale Young's modulus and Poisson's ratio (see (14.1) and (14.2).
- The normal and tangential components of the maximum cohesive forces T^{max}_n and T^{max}_t are used for fitting the macroscale peak response. The ratio between T^{max}_t and T^{max}_n is increased in order to reduce the pressure-dependency of the response.
- The critical opening is chosen such that the macroscale deformation at macroscale peak strength corresponds well with the experimental observations.

With this procedure in mind, the parameters are fitted in a manually-iterative (trial-and error) procedure until a reasonable fit with the experimental results is obtained.

Four triaxial tests (1 at 2 MPa confinement, 3 at 12 MPa confinement [Andra, 2013]) are used for the calibration. Their stress-strain curves are given in Figure 14.4 together with the results of the calibrated numerical response to biaxial compression for different REV orientations. They show a good agreement in initial stiffness, peak stress and axial strain at peak stress. Lateral strain shows good agreement at low stress levels, but the numerical results show a stronger dilatancy at higher stress levels and when softening takes place. This high degree of dilatancy is strongly linked to the fact that relative displacement between grains (which is needed for interface softening) can only be obtained by the opening of

adjacent interfaces. As the rearrangement of grains is not taken into account in the finite element formulation, this relative opening of the interfaces continues regardless the state of deformation.

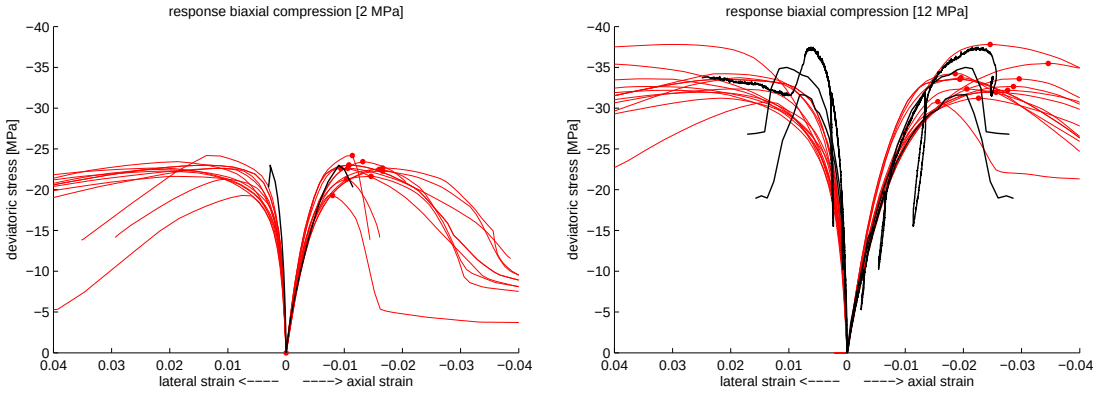

Fig. 14.4: Deviatoric stress response to biaxial material point compression for orientations at an interval of 15°. In black the experimental results, obtained by triaxial compression.

In Figure 14.5 the derivatives of axial stress with respect to axial strain are given, again showing good agreement with respect to the experimental results up to the point at which the peak stress is reached. It is important to note that strong fluctuations in the stiffness can be observed in the post-peak domain for several 2 MPa confinement tests, some of which indicate a snapback at the end of the numerical simulation. This effect can not be observed under 12 MPa confinement, where the response is much smoother.

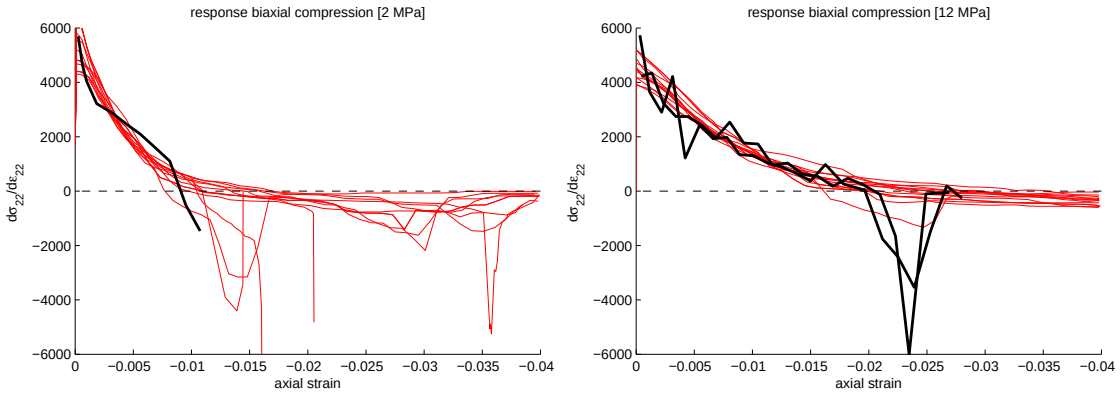

Fig. 14.5: Structural stiffness. In red the responses of numerical simulations for θ^{REV} at an interval of 15°. In black the experimental results.

A small variation in initial stiffness can be observed in the numerical results. This variation in initial stiffness is the combined effect of the heterogeneity of the grain stiffness, the grain elongation with respect to grain shape and distribution of interface orientations. Figure 14.6 shows the initial stiffness of the material

under confining pressure as a function of the orientation of deformation.

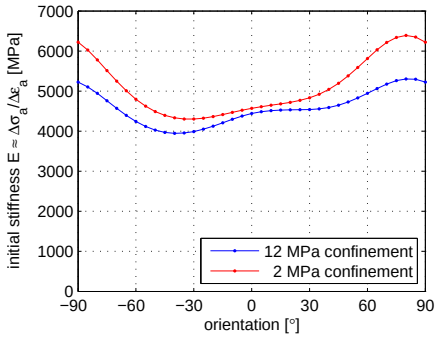

Fig. 14.6: Anisotropy of the initial stiffness under different confining pressures. Orientation $\theta^{REV} = -10°$ corresponds to loading perpendicular to the bedding plane, which was introduced as $\theta^{bed} = 10°$.

The anisotropy in the peak response is shown in Figure 14.7. Its profile is much more irregular than that of the initial stiffness, as the peak strength is mainly determined by the interfaces. Nevertheless, the numerical results show a very good agreement with the experimental results in general.

By determining the peak stress at different confining stresses, the apparent friction angle and cohesion is defined by adopting a Mohr-Coulomb failure criterion (Figure 14.7).

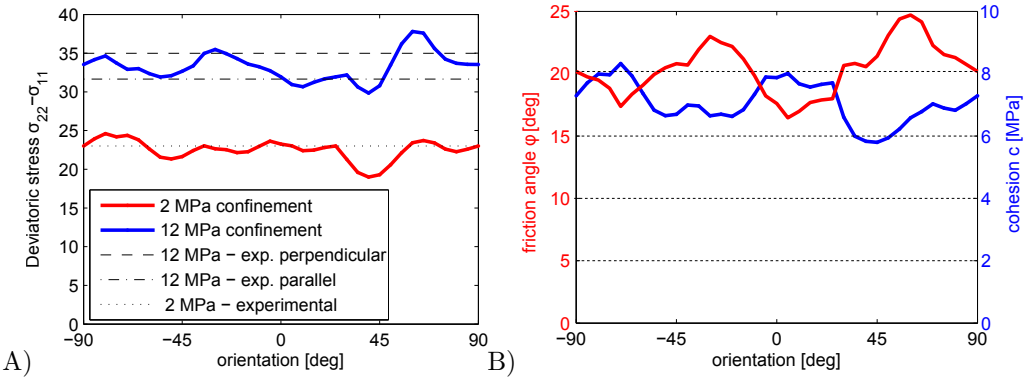

Fig. 14.7: A) Evolution of the deviatoric stress peak with respect to the REV orientation for the 2 MPa and 12 MPa lateral stress simulations. B) Friction angle ϕ and cohesion c interpreted from the Mohr-Coulomb failure criterion derived from the biaxial compression simulations at 2 MPa and 12 MPa.

Unloading and reloading during biaxial compression tests can be performed to study the residual stiffness of the material as an effect of the interface damage. Two examples are given for the material response with REV orientations of 0° and 50° respectively, for which unloading to the initial state is applied from several stages of compression. The results are shown in Figure 14.8. The unloading-reloading branches are perfectly elastic (no hysteresis is taken into account). The

higher stiffness observed at lower axial strain is due to the regained contact of the interfaces.

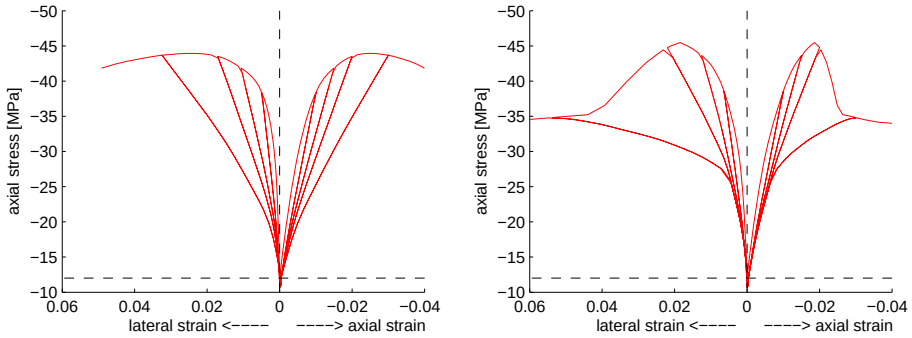

Fig. 14.8: Stress response to displacement-controlled axial loading, unloading and reloading under constant confining stress for $\theta^{REV} = 0°$ (left) and $\theta^{REV} = 50°$ (right).

For unloading response that better represents the experimentally observed behaviour, the interface cohesive laws will have to be modified in order to take into account plastic deformation. A possible modification is to introduce plastic behaviour in the interfaces by modifying the unloading branch of the interface constitutive relation (Figure 14.9). This conceptually simple modification could provide a proper unloading/reloading branch in the macroscale behaviour.

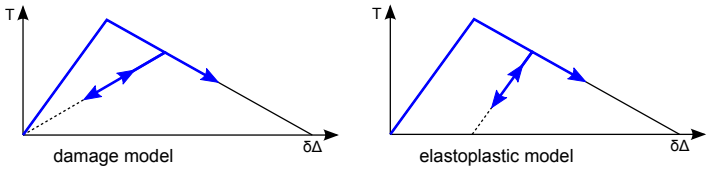

Fig. 14.9: Original damage model for interface cohesion (left) and alternative plastic damage model (right).

14.3 Strain localization in an unconfined compression test

A doublescale unconfined compression test is modelled with the calibrated microstructure . A 38×76 *mm* sample is modelled by means of a 10×20 element mesh and strain-controlled loading is applied. Several computations are performed with a range of second gradient parameters $D = 0.5,\ 1,\ 2,\ 4,\ 8\ kN$, for a calibration of this parameter against the mesh-size. No confinement stress is taken into account, which means that (under the assumption of a Mohr-Coulomb failure criterion for the comparison between biaxial and triaxial results) the peak stress corresponds to the unconfined compressive strength of the material.

Figure 14.10 gives the nominal stress-strain curves for all tests (left), together with the envelope of the nominal stress-strain curves (right). Good agreement is found between the different test up to $\varepsilon_a = -1.1\%$, at which heterogeneous deformation starts and the second gradient model induces different solutions for different second gradient parameter D. A shear band with the same orientation is

triggered in all computations and the slope of the stress response curve is relative to the width of the developing band. Convergence problems are encountered shortly after the initiation of the shear band, forcing the computations to be performed using smaller loading steps.

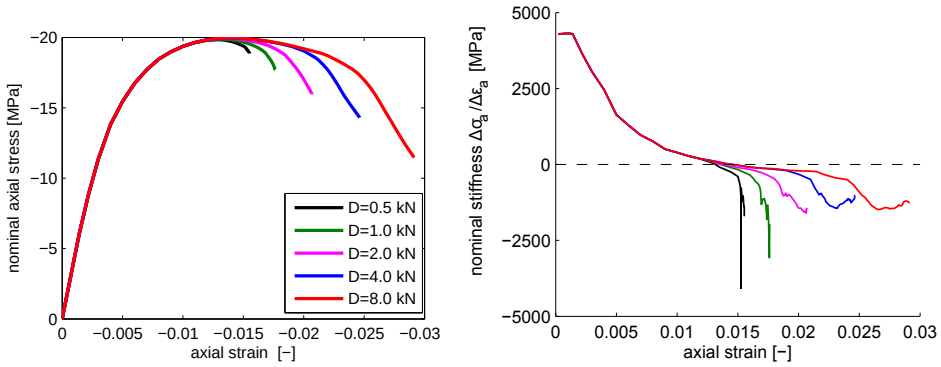

Fig. 14.10: Nominal response to uniaxial compression with different second gradient parameters. The stiffness indicates that the computations with $D = 0.5\ kN$ and $D = 1.0\ kN$ tend towards snapback.

Figure 14.11 and 14.12 show the deformed microstructures for the two computations with smallest second gradient parameters at the last converged loading step. The state of deformation is best described by the VM equivalent stress (middle). The nodal velocities (left) and VM equivalent strain rate (right) indicate the current activities with respect to deformations. The incipient shear band seems to develop in the center of the sample, touching the top and bottom boundary due to its high inclination. With continuing compression, the active part of the band shifts to one side, thereby introducing an asymmetry in the deformation pattern and a reflection of the band at the top boundary. Strong spatial variations in strain rate and nodal velocities can be observed in this reflection (the upper left corner of the sample), suggesting a loss of the mesh independence or numerical instabilities as the dimensions of the strain localization approaches the element size. This causes rather erratic nodal displacements, both in space and time. For larger parameters D the shear band remains at its initial position.

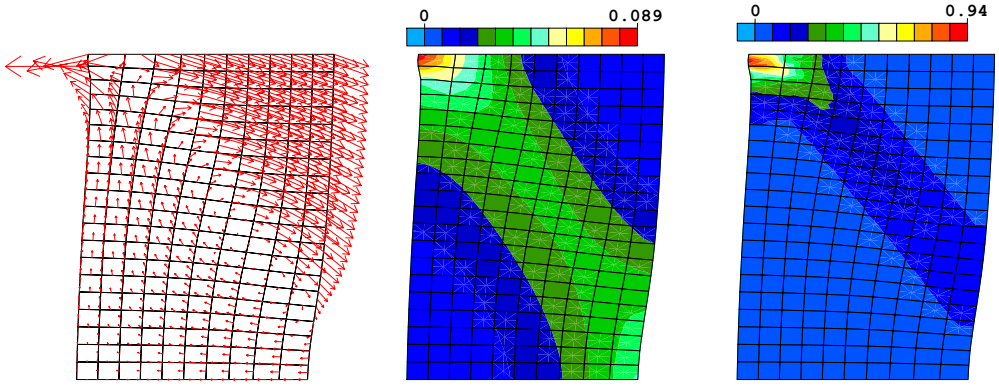

Fig. 14.11: Deformed meshes for $D = 0.5kN$ (displacements multiplied 10×).

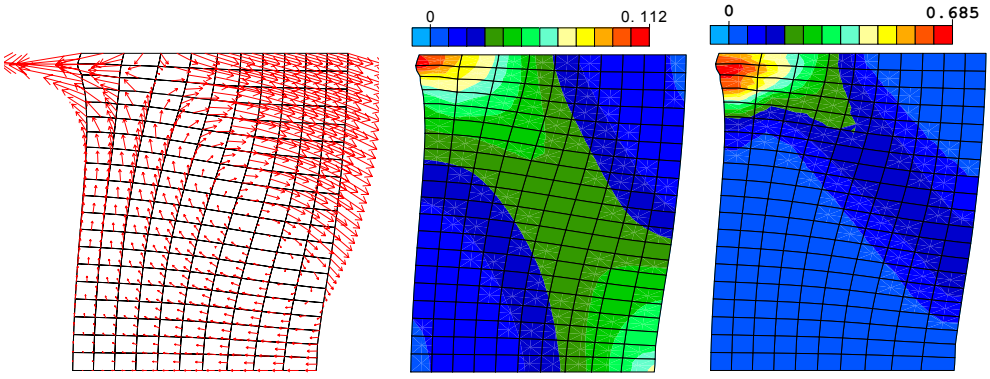

Fig. 14.12: Deformed meshes for $D = 1.0kN$ (displacements multiplied 10×).

15. STUDY ON THE LOCAL BEHAVIOUR OF THE DOUBLESCALE BIAXIAL COMPRESSION

The biaxial compression test for a dry sample presented in Section 14.3 suffers from computational difficulties that start somewhere after the peak. The computational difficulties express themselves in convergence problems of the macroscale Newton-Raphson scheme in the post-peak domain, where small increments are required to obtain a proper convergence of the macroscale problem. Figure 15.1 shows the details of the nominal stress-strain curve near the end of the $D = 1.0\ kN$ test.

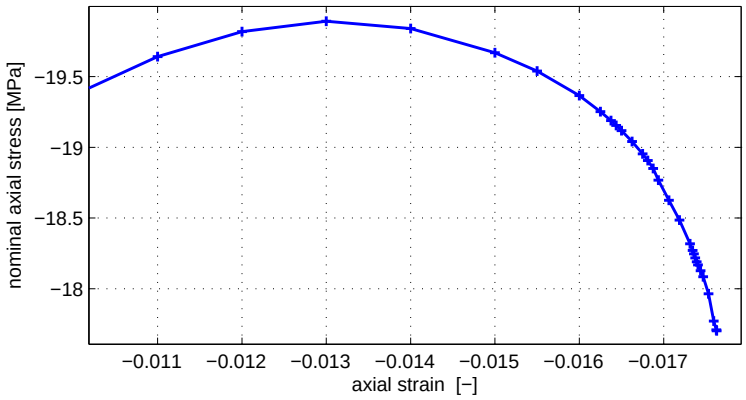

Fig. 15.1: Zoom on the nominal stress-strain response curve for the unconfined compression with $D = 1\ kN$. The markers indicate the individual loading steps.

To get a better understanding of the processes at play in the macroscale behaviour obtained in the doublescale computations, several indicators are investigated for the description of the macroscale behaviour. These indicators are based on existing theories such as bifurcation analysis, which can not always be applied directly to any type of model. It must therefore be stressed that these techniques only serve as indicators of the true behaviour and therefore provide a heuristic approach to the assessment of the phenomena and serve as an indicator of computational problems.

In addition to the notion that a heuristic approach is followed, a differentiation must be made between the analysis of local material behaviour (on the material point level) and the global behaviour (that of the boundary value problem); the local second gradient model in large strain formulation and the boundary value problem are not considered in this analysis and the focus will be on the local macroscale behaviour of individual material points.

The next sections describe some tools to assess the macroscopic material point

behaviour and their application on the local material state of the biaxial compression tests.

15.1 Deformed microstructures and interface damage states

The top left corner of the test for $D = 1000N$ shows the strongest spatial variation in strain rates and can be expected to cause the computational difficulties. Figure 15.2 shows a zoom of the upper left corner of the sample with elements 171, 181 and 191 containing the peak in $\dot{\varepsilon}_{VM}$. The microstructures of the integration points in these elements at the last converged loading step are given in Figure 15.3. Although significant differences can be observed in the distribution of softening and decohesion even within the same elements, it is difficult to point at processes that could cause the computational difficulties.

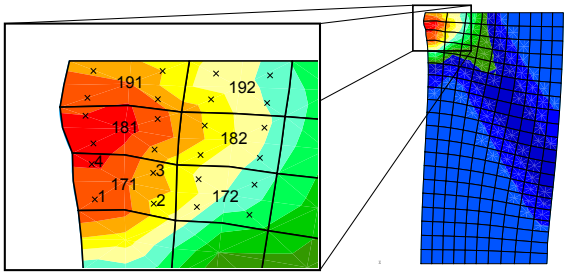

Fig. 15.2: Zoom of the deformed mesh for element and integration point numbering. Displacements multiplied 10×.

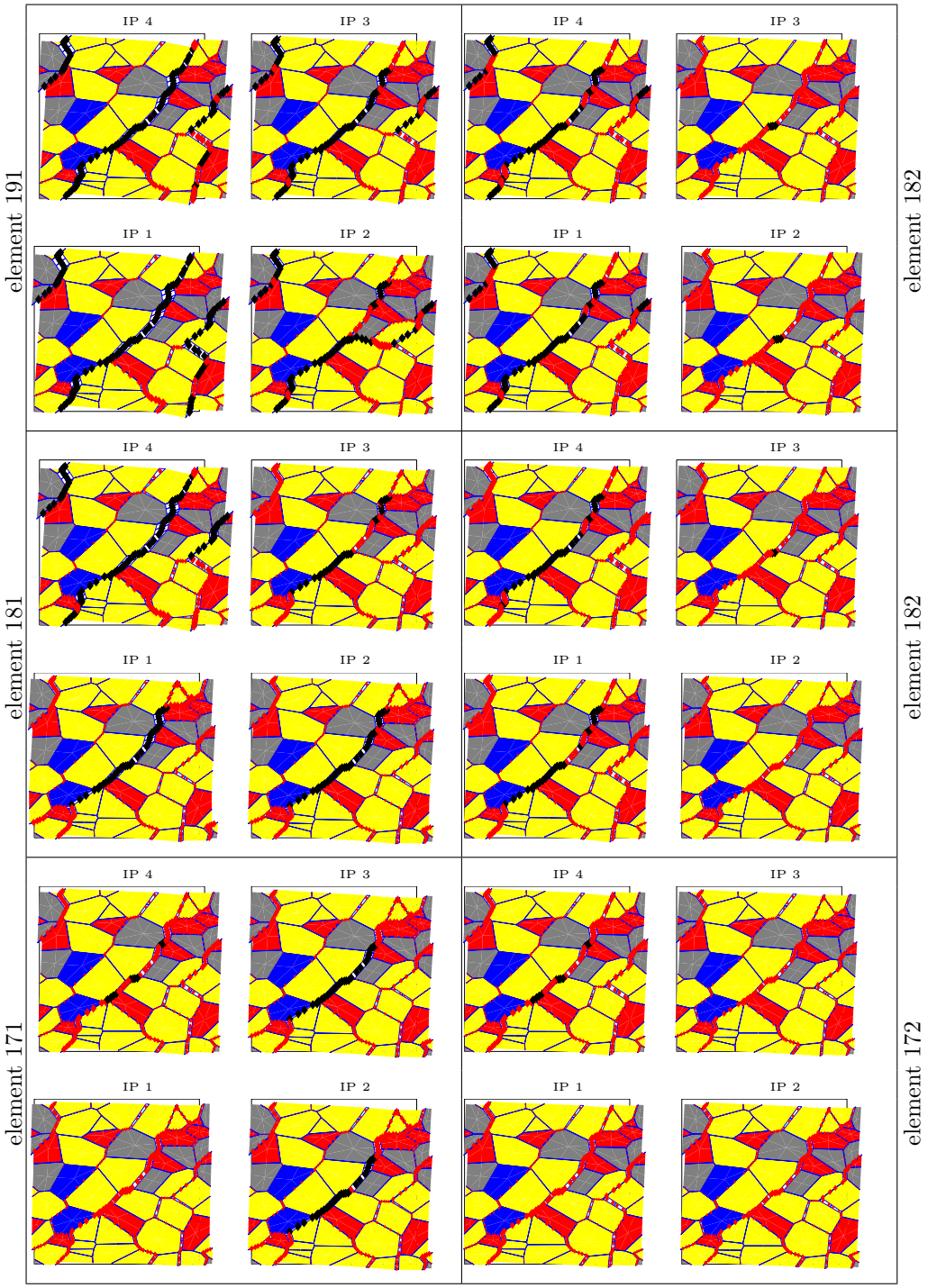

Fig. 15.3: Deformed microstructures for elements 191 & 192 (top), 181 & 182 (center) and 171 & 172 (bottom). Red diamonds indicate interface cohesive softening, black diamonds indicate decohesion, either in normal or in tangential mode.

15.2 Gudehus diagrams

A general tool for the evaluation of the local constitutive relations is the representation of the stress (or strain) response to small strain (or stress) increments applied on a material point in a certain configuration. This method was proposed by Gudehus [1979] applying strain increments with constant amplitude in all orientations in ε_{ii} space. The graphical representation of the constitutive relation between strain increment and stress increment is the diagram of stress responses $\Delta\sigma_{ii}$ to the applied strain increments. The constitutive behaviour of the material point can be interpreted by means of the shape of the stress response diagram.

Although the application of equal stress increments to study the behaviour of its strain response is often applied (see for example Royis and Doanh [1998]), this approach is not followed here for the simple reason that it is not guaranteed that all stress increments can be applied. The application of strain increments does not suffer from this effect and therefore allows the evaluation of the material response to loading at any given state of the material.

In general, shear strain is not considered in the application of strain increments and the shear stress response $\Delta\sigma_{12}$, which is non-zero, is not taken into account in the diagram. This results in a diagram as a projection of the Cauchy stress tensor on the $\sigma_{12} = 0$ plane in $\sigma_{11} - \sigma_{22} - \sigma_{12}$ space.

The strain increments are chosen such that

$$|\Delta\varepsilon| = \sqrt{\Delta\varepsilon_{11}^2 + \Delta\varepsilon_{22}^2} \tag{15.1}$$

and

$$\tan\alpha = \frac{\Delta\varepsilon_{22}}{\Delta\varepsilon_{11}}. \tag{15.2}$$

With strain increment $|\Delta\varepsilon|$ constant and the orientation α covering the range between 0° and 360°, a radially symmetric (un-)loading is applied. The stress response to this loading visualizes the direction-dependent material behaviour. For small increments $|\Delta\varepsilon|$, the response approximates the incremental relation consistent to the variation of loading directions. Larger strain probes will include possible non-linear effects in the stress response and in this case the Gudehus diagram represents a secant approximation of material response to the different deformation loading paths. Figure 15.4 (left) shows the Gudehus diagram for the REV in Figure 14.3 around the initial configuration $\boldsymbol{F}^t = \boldsymbol{F}^0 = \boldsymbol{I}$ for a range of different strains. This figure clearly shows the nonlinear response effects with respect to $|\Delta\varepsilon|$, as the stress does no longer increases in some orientations for $|\Delta\varepsilon| > 0.1\%$. This can be related to the failure of the material. It is clear that these responses do not represent a linearization of the local material behaviour but capture an entire loading path.

To compare the diagrams related to the smallest strain increments, the diagrams are normalized by $|\Delta\varepsilon|$. The normalized diagrams are shown in 15.4(right). The difference between the diagrams for smallest strain increments can be related to the nonlinearities introduced by the penalization of closed interfaces, as the material becomes stiffer for larger compressive strain increments. The differences between the diagrams at largest strain increments are the effect of softening and

eventually decohesion of the interfaces at the microscale, which leads to a decrease in secant stiffness, especially in the case of large ($> 0.1\%$) extensional strain increments.

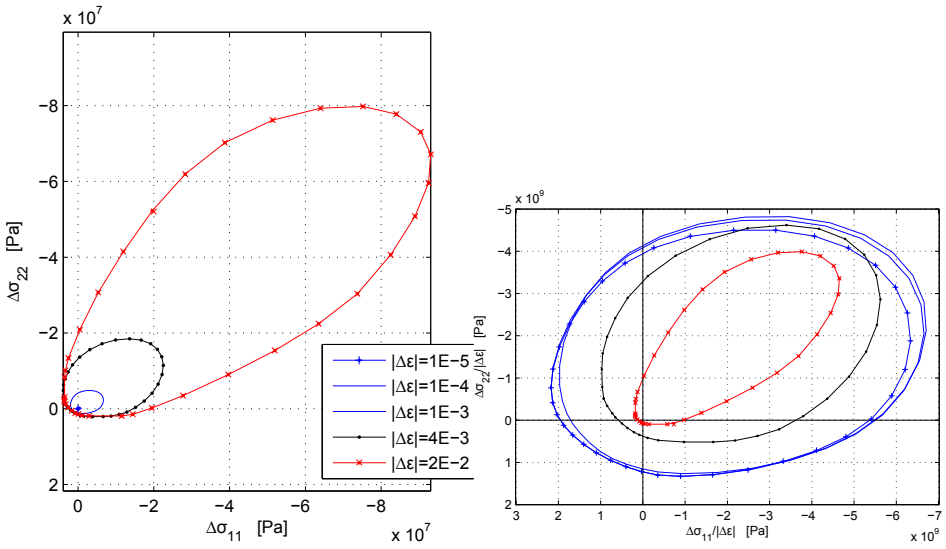

Fig. 15.4: Gudehus diagrams for strain probes from the non-deformed state for stress response (left) and relative stress response (right)

15.2.1 Extended Gudehus diagrams

In general, the Gudehus diagram is a projection of a contour in $\sigma 11 - \sigma 22 - \sigma 12$ space on the $\sigma_{12} = 0$ plane and this projection can have different shapes, which is an ellipse in case of incremental linearity. From the Gudehus diagrams above it is clear that the behaviour of our model is not incrementally linear at the presented state and the representation of the incremental relation between stress and strain cannot be given by a deformation direction-independent stiffness matrix. The individual evaluation of the response to all strain increment directions is therefore required for a more detailed evaluation and an evaluation of only the diagonal components of the strain increments and stress responses is not sufficient and the shear components need to be taken into account as well. This implies an evaluation of the incremental response in the spirit of the Gudehus diagrams by applying a set of strain increments $d\varepsilon$ describing the spherical relation

$$|d\epsilon| = \sqrt{d\varepsilon_{11}^2 + d\varepsilon_{22}^2 + d\gamma^2} \tag{15.3}$$

with

$$\begin{aligned} d\varepsilon_{11} &= dF_{11} \\ d\varepsilon_{22} &= dF_{22} \\ d\gamma &= dF_{12} + dF_{21}, \qquad \text{with } dF_{12} = dF_{21} \end{aligned}$$

The strain increment can be characterized by its amplitude $|d\epsilon|$ and the polar

coordinates α and β defined in Equation (15.4) and illustrated in Figure 15.5

$$\tan\alpha = \frac{d\varepsilon_{11}}{d\varepsilon_{22}}, \qquad \sin\beta = \frac{d\gamma}{|d\varepsilon|} \tag{15.4}$$

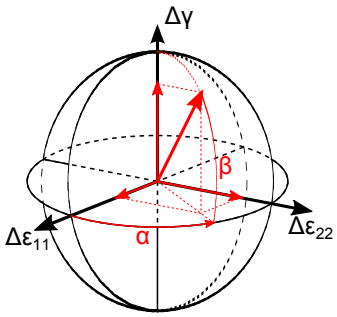

Fig. 15.5: Coordinate system for the extended Gudehus diagrams with (symmetric) shear stain component $d\gamma = dF_{12} + dF_{21}$ where $dF_{12} = dF_{21}$ is used to avoid the influence of stress rotation.

This type of extension of the Gudehus diagrams introduces two difficulties. First the choice of the ratio between $d\varepsilon_{ii}$ and $d\gamma$ is somewhat arbitrary. Second difficulty is the representation of the results, as the stress increment response gives a surface in 3-dimensional stress space. Two examples of these surfaces are given in Figure 15.6, corresponding to the same elements as analyzed in Figure 15.8 at $\lambda = 1.76$. The stress response for element 1 shows a perfect ellipsoid, indicating incremental linearity of the material behaviour corresponding to the elastic state of a material point outside the zone of localized strain. The ellipse in the corresponding Gudehus diagram is a projection on the $\sigma_{12} = 0$ plane of the cross section of the ellipsoid related to the $\delta\gamma = 0$ strain increments.
The stress response in element 181, as part of the strain localization band, gives a more complex response. The stress response surface has two distinct parts; one part forming an almost perfectly collapsed surface, the other part is a part of an ellipsoid that is turned inside-out (the response has changed direction with respect to the stress response in the initial configuration).

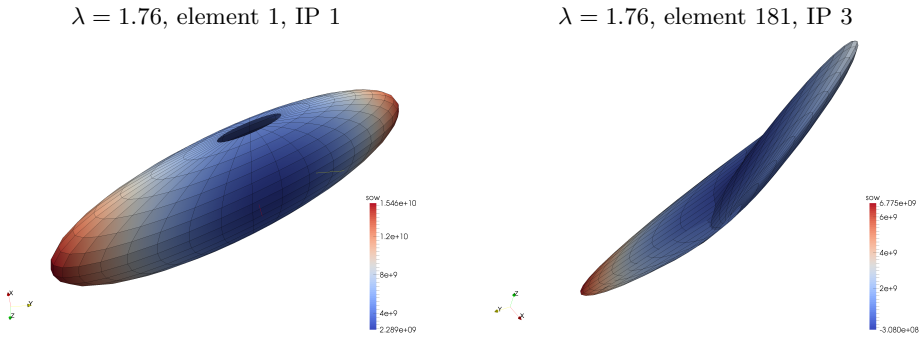

Fig. 15.6: 3D stress response surfaces with color scale corresponding to the second order work ($\dot{\sigma}_{ij}\dot{\varepsilon}_{ij}$). For element 181 the origin lies outside volume enclosed by the stress response surface. Relative scales between the diagrams are not equal, axes (x, y, z) correspond to $(d\sigma_{11}, d\sigma_{22}, d\sigma_{12})$

15.2.2 Test incremental non-linearity of current configuration

For studying the macroscale behaviour of the material in the vicinity of bifurcation points, several approaches can be followed. A possible approach is studying the existence and uniqueness of possible solutions of the problem [Chambon and Caillerie, 1999] or a bifurcation analysis based on the evaluation of the acoustic tensor [Rudnicki and Rice, 1975, Desrues and Chambon, 1989]. The later makes use of the tangent operator L_{ijkl} under the assumption that it is only dependent on current stress, deformation and material state parameters and not on the direction of the rate of deformation. In other words, the macroscale material behaviour has to be incrementally linear or at least piecewise linear.

It is easily verified from the extended Gudehus diagram that the model presented here is not always incrementally linear, as the stress response to incremental loading is different for loading and unloading increments.

Nevertheless, it is possible to investigate incremental non-linearity of the current configuration of the microstructure by comparing the difference in stress response ($d\sigma^+_{ij} + d\sigma^-_{ij}$) for strain increments in opposite directions ($d\varepsilon^+_{ij}$ and $d\varepsilon^-_{ij}$, $d\varepsilon^+_{ij} := -d\varepsilon^-_{ij}$). This allows adding a second curve to the Gudehus diagram, representing the non-linearity in the model. In the presented model, incremental non-linearities can be found numerically as an effect of two micromechanical effects:

- The transition from opened to closed interfaces. Although the transition is incrementally linear from a mathematical point of view due to the penalization by the squared negative opening, a small numerical variation can induce strong nonlinear effects, which in practice manifests as incrementally nonlinear behaviour. This effect can be observed in the Gudehus diagrams for the initial state of the REV, where compression and extension show significant differences for a strain increments of $|\Delta\varepsilon| = 2 \times 10^{-6}$. A less strong penalization can provide a better linearity for the behaviour of closed interfaces, but compromises the physical representation of the interfaces.

- The softening of the interface cohesive forces. The use of the simplified damage model introduces incrementally nonlinear effects when changing

between increasing and decreasing relative displacement Δu, either in normal or in tangential direction.

A combination of these two micromechanical effects leads to the non-linearity diagram, as presented in Figure 15.7.

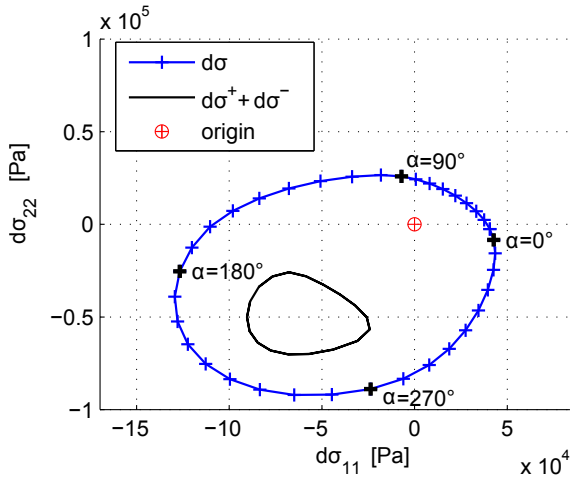

Fig. 15.7: Gudehus graph for Micro 8 initial state, with incremental nonlinear difference diagram for $|d\varepsilon| = -1 \times 10^{-6}$

When the non-linearity diagram reduces to the origin, the behaviour is incrementally linear and $d\sigma_{ii}^{+} = -d\sigma_{ii}^{-}$. For a complete evaluation of the incremental nonlinearity, the third component of the deformation, $d\gamma$ needs to be taken into account and the criterion for numerical incrmental linearity is given by

$$\frac{|d\sigma^{+} + d\sigma^{-}|}{|d\sigma^{+}| + |d\sigma^{-}|} < \epsilon \tag{15.5}$$

with

$$|d\sigma| = \sqrt{{d\sigma_{11}}^2 + {d\sigma_{22}}^2 + {d\sigma_{12}}^2} \tag{15.6}$$

If this is true for all strain increments $|d\varepsilon|$ then the material behaviour incrementally linear from a numerical point of view.

This numerical approach for the evaluation of linearity should be handled with care, as the small strain increments can comprise material nonlinearities that are interpreted as incremental nonlinearities. An example of such an effect is the polynomial penalization of the interfaces, which easily introduces a direction-dependent response for small but nevertheless finite strain increments. The effect of such material nonlinearities captured by the finite strain increments can be observed in the example above; from a numerical point of view the model is incrementally nonlinear, although from a mathematical point of view all the global material behaviour should be incrementally linear. The apparent incremental non-linearity is thus an effect of the choice of the strain increment, which can not be taken small enough to numerically linearize the effect of the polynomial penalization of closed interfaces.

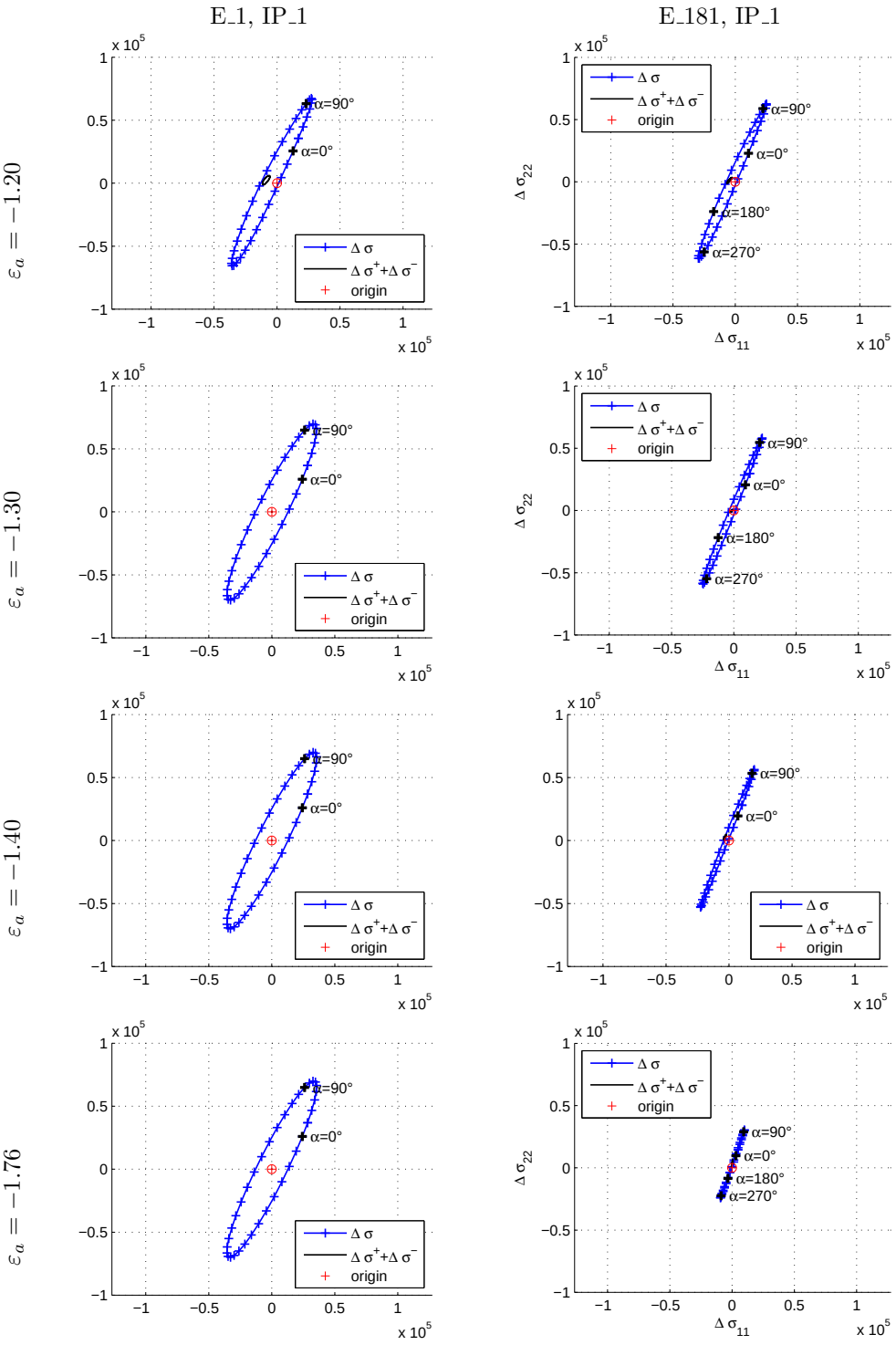

Fig. 15.8: Gudehus diagram for IP1 in elements 1 (left) and 181 (right) around the peak and at the end of the computation.

From the Gudehus diagrams in Figures 15.6 and 15.8, several conclusions can be drawn:

- The loss of homogeneity starts before the peak response is reached, as the Gudehus diagrams are different between elements 1 and 181. Looking at the deviatoric strain rate reveals that significantly non-homogeneous deformation can be found at stresses as low as $80 - 85\%$ of the peak stress.
- Both integration points show a slight non-linearity before the peak response.
- The stress response surface in the 3D extension of the Gudehus diagram collapsing into a disk can serve as an indication of numerical difficulties in the finite element computation. It is straightforward to observe that in case of a (partly) collapsed surface, only a restricted part of the orientations in stress space is accessible by strain increments. Moreover, identical stress increments of the remaining accessible stress space can be reached by different strain increments. At the local scale, this can indicate both problems of existence of a solution (due to an inaccessible stress space) and uniqueness of a solutions (different strain increments for the same stress increments). Whether or not these local problems lead to numerical problems in the Newton-Raphson iteration of the macroscale finite element loading step will depend on the complete macroscale boundary value problems. Nevertheless, the collapse of part of the Gudegus stress response surface can be seen as an indication of difficulties arising from the constitutive law.

15.2.3 Elasticity condition

A more theoretical approach to assess the incremental non-linearity of the material would therefore be the analysis of the state of all individual micromechanical components that might introduce incremental nonlinearities. In the presented model with damage interface laws and polynomial penalization of closed interfaces, the only possible direction-dependent response at the microscale comes from interface softening ($\dot{\Delta u}_i > 0 \ \wedge \ \Delta u_i/\delta_i^c = D_i$). This implies that if $\Delta u_i/\delta_i^c < D_i$ for all interfaces, incremental linearity is guaranteed from a mathematical point of view and we can say that the material is in an elastic state. This elasticity criterion is easily verified at the end of the computations and can serve as an indicator for the local state of the material. Although easily implemented at the level of the element loop of the microscale finite element program, this method has a strong model-dependence.

15.3 Uniqueness and the second order work criterion

Simplifying Equation (3.1) to a small-strain, classical framework and considering stress rate $\dot{\sigma}$ as a generalization of all σ, the balance equation can be rewritten as [Chambon and Caillerie, 1999]

$$\int_\Omega \dot{\sigma}_{ij}\dot{\varepsilon}^\star_{ij} d\Omega - \int_\Gamma \dot{t}_i \dot{u}^\star_i = 0 \tag{15.7}$$

with

$$\varepsilon = \frac{1}{2}\left(\boldsymbol{F} + \boldsymbol{F}^T\right) - \boldsymbol{I} \tag{15.8}$$

and $\dot{u}_i^\star$ a kinematically admissible virtual velocity obeying the boundary conditions. By doing so, the second gradient model and the finite strain formulation at the macroscale are no longer taken into account and the value of the theoretical results obtained hereafter reduce to an indicative quantity.

It can be verified [Hill, 1958] that a unique solution exists when

$$\int_\Omega \Delta\dot{\sigma}_{ij}\Delta\dot{\varepsilon}_{ij}d\Omega > 0 \tag{15.9}$$

with $\Delta\dot{\varepsilon} = \dot{\varepsilon}^2 - \dot{\varepsilon}^1$ the difference between any two kinematically admissible fields of strain rate $\dot{\varepsilon}^1$ and $\dot{\varepsilon}^2$ that comply with equation 15.7. Equation 15.9 is met when $\Delta\dot{\sigma}_{ij}\Delta\dot{\varepsilon}_{ij} > 0$ for the entire domain, which allows the local evaluation to provide a guaranteed uniqueness of the global BVP. This expression resembles the second order work defined as

$${}^2W(\dot{\varepsilon}) = \dot{\sigma}_{ij}\dot{\varepsilon}_{ij} \tag{15.10}$$

For several constitutive models in the framework of small strains it can be proved that ${}^2W(\dot{\varepsilon})$ and ${}^2W(\Delta\dot{\varepsilon}) = \Delta\dot{\sigma}_{ij}\Delta\dot{\varepsilon}_{ij}$ can be interchanged in the assessment of uniqueness of solutions but for a general model only $\Delta\dot{\varepsilon}$ can guarantee uniqueness according to (15.9) and the second order work ${}^2W = \dot{\varepsilon}_{ij}\dot{\sigma}_{ij}$ is only a specific case of ${}^2W(\Delta\dot{\varepsilon})$ that does not suffice to prove uniqueness [Chambon and Caillerie, 1999].

For closed-form analytical constitutive relations it can be straightforward to derive these criteria for second order work for all possible combinations of strain rates. In computationally more challenging models, such as our doublescale model, this is not possible and a numerical approach is needed, computing the stress rate $\dot{\sigma}_{ij}$ corresponding to a range of possible strain rates $\dot{\varepsilon}_{ij}$. In case of rate-independent behaviour of computational models, the strain rate $\dot{\varepsilon}$ and corresponding stress rate $\dot{\boldsymbol{\sigma}}$ can be replaced by a strain increment $d\varepsilon$ and its stress response $d\boldsymbol{\sigma}$.

The execution of the extended Gudehus analysis provides a set of stress responses to strain increments in all directions in 3D strain space. Although this set of strain increments only contain those related to $|d\varepsilon| = cst$, combinations of any two strain increments $d\varepsilon^1$ and $d\varepsilon^2$ can be obtained. In this way the following three quantities of second order work ${}^2W$ are defined;

- ${}^2W^1 = \dot{\varepsilon}^1_{ij}\dot{\sigma}^1_{ij}$
- ${}^2W^2 = \dot{\varepsilon}^2_{ij}\dot{\sigma}^2_{ij}$
- ${}^2W^\Delta = \Delta\dot{\varepsilon}_{ij}\Delta\dot{\sigma}_{ij} = (\dot{\varepsilon}^2_{ij} - \dot{\varepsilon}^1_{ij})(\dot{\sigma}^2_{ij} - \dot{\sigma}^1_{ij})$

In case one of the three is negative, uniqueness can (locally) no longer be guaranteed. If all three values are positive, the second order work of any linear combination of $\dot{\varepsilon}^1$ and $\dot{\varepsilon}^2$ needs to be evaluated to complete the analysis. This can be done by defining a fourth term W^a as

$$\begin{aligned} {}^2W^a &= (\dot{\varepsilon}^2_{ij} - a\dot{\varepsilon}^1_{ij})(\dot{\sigma}^2_{ij} - a\dot{\sigma}^1_{ij}) \\ &= a\Delta\dot{\varepsilon}_{ij}\Delta\dot{\sigma}_{ij} + (1-a)\,\dot{\varepsilon}^2_{ij}\dot{\sigma}^2_{ij} + (a^2-a)\dot{\varepsilon}^1_{ij}\dot{\sigma}^1_{ij} \\ &= a^2W^1 - a({}^2W^1 + {}^2W^2 + {}^2W^\Delta) + {}^2W^2 \end{aligned} \tag{15.11}$$

with $a \in \Re^+$. Given that ${}^2W^1 > 0$, ${}^2W^2 > 0$ and ${}^2W^\Delta > 0$ the minimum value of ${}^2W^a(a)$ is found to be

$$min\left({}^2W^a(a)\right) = {}^2W^2 - \frac{1}{4}\frac{\left({}^2W^1 + {}^2W^2 + {}^2W^\Delta\right)^2}{{}^2W^1} \tag{15.12}$$

Following this approach allows a full evaluation of the uniqueness of the solution using only the numerical pair stress responses to strain increments $|d\varepsilon^1| = |d\varepsilon^2| = cst$. The complexity of the number of strain increments to be applied (and thereby the number of finite element computations to be executed) is hereby reduced from $\Re^3$ to $\Re^2$. Moreover, the results obtained from the extended Gudehus diagrams can be used in this evaluation. Nevertheless, it must be noted that;

- The evaluation remains a numerical approximation and only a finite number of orientations of strain increments can be tested. It can not be guaranteed that possible orientations leading to negative second order work are neglected.
- the developments as an extension of the Gudehus diagrams is done in the framework of small strains, thereby omitting the effect of material rotation in the behaviour.
- Only local information is obtained and the kinematical admissibility with respect to the macroscale boundary conditions and equilibrium equation is not yet taken into account. This implies that certain results of negative second order work do not lead to any instabilities, simply because their orientation(s) of strain rate do not correspond to the actual loading direction.

With the developments above and using the stress response data obtained from the extended Gudehus analysis, the terms ${}^2W^1$, ${}^2W^2$, ${}^2W^\Delta$ and ${}^2W^a$ can be computed for all available (combinations of) strain increments as approximations of the strain rate. Figure 15.9 gives a stereographic plot of the orientations $d\varepsilon^1$ for $W^1 < 0$ (red dot) together with $d\varepsilon^1$ (blue circle) and $\Delta\varepsilon$ (red cross) for $W^\Delta < 0 | W^i > 0$ as a function of α and β. The current macroscale loading is indicated with a blue cross. The results shown are those of integration point 3 in element 181 at different states of deformation (see Figures 15.2 and 15.1). Well before the peak ($\varepsilon_a = -1.1\%$), negative second order work ${}^2W^1$ and negative ${}^2W^\Delta$ can be observed, although their corresponding orientations $d\varepsilon^1$ and $\Delta\varepsilon$ do not agree with the current loading. Right after the peak ($\varepsilon_a = -1.4\%$), the orientations with negative second order work appear around the orientation of current deformation rate, developing into a well-defined zone of orientations towards the end of the loading path visible as a red cloud in the projection at $\varepsilon_a = -1.76\%$.

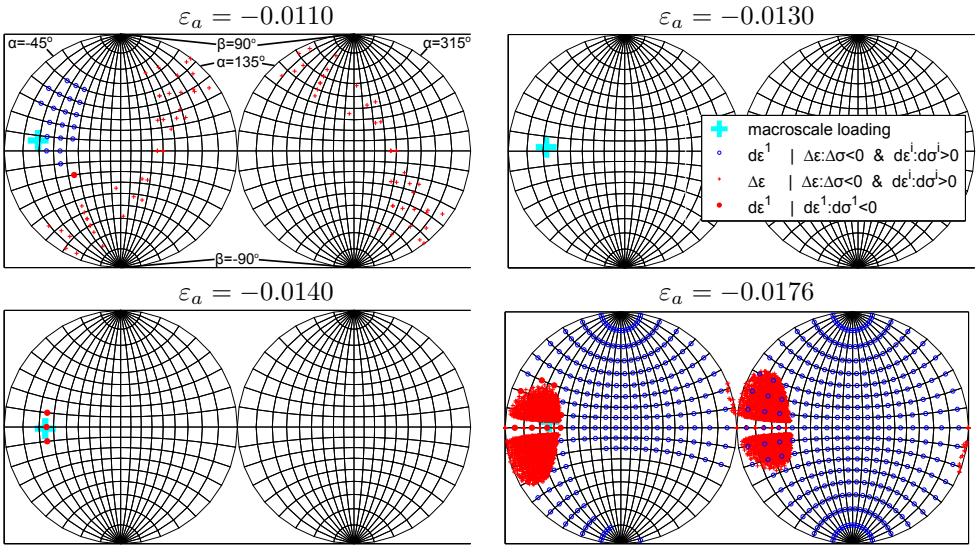

Fig. 15.9: Negative second order work $\dot{\sigma}_{ij}\dot{\varepsilon}_{ij}$ (red) and $\Delta\dot{\sigma}_{ij}\Delta\dot{\varepsilon}_{ij}$ (blue) in element 181 around the peak and at the end of the computation.

From the figure above it can be concluded that, locally, uniqueness can not be guaranteed for states of deformations well before the peak, although it is likely that the orientations corresponding to the negative second order work are not admitted by the kinematically constraints of macroscale balance- and boundary conditions. After the peak, local uniqueness of the solution is definitely lost as the orientations of negative second order work and current loading direction coincide. This is a first indication of numerical instability, leading to computational difficulties at the macroscale.

Appendix B contains some more examples of stereographical representations of the different definitions of negative second order work.

15.4 RICE bifurcation criterion

The mechanical tangent stiffness matrix ${}^{\mathbf{4}}\boldsymbol{C}^{M}$ provided by the computational homogenization of the REV response to deformation $\boldsymbol{F}$ describes the variational relation

$$\delta\sigma_{ij}^{t} = C_{ijkl}^{M,t}\delta F_{kl}^{t} \tag{15.13}$$

This relation is consistent with respect to the direction of deformation at time t. As the model is incrementally non-linear, each other increment of deformation δF_{ij} entails a different tangent operator ${}^{\mathbf{4}}\boldsymbol{C}$. Under the strong assumption that C_{ijkl}^{M} can be used for any strain increment (incremental linearity) the derivation of Rice's criterion for bifurcation [Rudnicki and Rice, 1975], this derivation is usually rewritten as

$$\dot{\sigma}_{ij} = L_{ijkl}\dot{\varepsilon}_{kl} \tag{15.14}$$

where the constitutive tensor ${}^{\mathbf{4}}\boldsymbol{L}$ is roughly approximated by ${}^{\mathbf{4}}\boldsymbol{C}$ under the assumption that the geometrical nonlinearities can be ignored (see Bésuelle and

Rudnicki [2003] for a review). The theory then defines an orientation for a possible localization band with a normal tensor $\vec{n}$, such that the rate of deformation inside the shear band can be written as

$$\dot{\varepsilon}_{kl} = \dot{\varepsilon}^0_{kl} + g_k n_l \tag{15.15}$$

where $\dot{\varepsilon}^0$ is the rate of deformation outside the band and $\vec{g}$ characterizes the direction of relative displacement of the opposite sides of the band. From the stress continuity equilibrium $\nabla \cdot \boldsymbol{\sigma} = \vec{0}$ it follows that

$$n_i \sigma_{ij} = n_i \sigma^0_{ij} \tag{15.16}$$

It is important to repeat here that the influence of the global boundary value problem and the local second gradient model on the continuity are ignored in this analysis. Combination of (15.15) and (15.16) leads to the condition

$$n_j L_{ijkl} g_k n_l = 0 \tag{15.17}$$

This naturally holds for the trivial solution $g_k = 0$, which corresponds to the homogeneous deformation as one of the solutions. Rice's criterion for bifurcation is met when a second, non-trivial ($\vec{g} \neq \vec{0}$), solution to (15.17) exists. Such a solutions exist if

$$det(\boldsymbol{A}) \leq 0 \tag{15.18}$$

with $\boldsymbol{A}$ the so-called acoustic tensor corresponding to $n_j L_{ijkl} n_l$. The existence of a non-trivial solution indicates a local bifurcation point. In case of a homogeneous problem, this point is instantaneously reached over the full domain. In case of a (initially) heterogeneous deformation, the bifurcation criterion can be met locally. As mentioned earlier, our model is an incrementally non-linear model and the bifurcation analysis cannot be extended any further than (multi)linear models as ${}^4\boldsymbol{L}$ will depend on both $\vec{n}$ and $\vec{g}$. A more consistent approach might comprise the comparison of the current loading rate $\dot{\varepsilon}_{ij}$ with the vector product $g_i n_j$ corresponding to possible orientations of the strain tensor that meet the bifurcation criterion.

Given the constitutive tensor ${}^4\boldsymbol{L}$ (or in its place the orientation-dependent consistent tangent ${}^4\boldsymbol{C}$) analytical solutions to Equation (15.17) can be found [Vardoulakis, 1980]. Finding a solution contains solving a fourth-order equation. In case the orientation of $\vec{g}$ is of little interest, a more pragmatic way of evaluating Rice's criterion it to perform a numerical analysis of (15.18) for a series of $\vec{n}$ with different orientations. This way of evaluation only requires a computation loop over the different orientations performing the matrix multiplications of computing the determinant of the acoustic tensor. Once a deformation has been applied on the REV and a solution is found for the stress response and the corresponding linearization of the constitutive relation, the evaluation of the Rice criterion is a straightforward routine which takes negligible computational effort. The Rice criterion can therefore easily be used in an evaluation of the doublescale computation without additional computational effort. In addition, the orientation of $\vec{n}$ corresponding to the minimum if $\det(\boldsymbol{A})$ can serve as an indicator of possible localization orientations.

Figure 15.10 shows the zones where the Rice criterion is satisfied for several states of deformation of the biaxial compression test under evaluation.

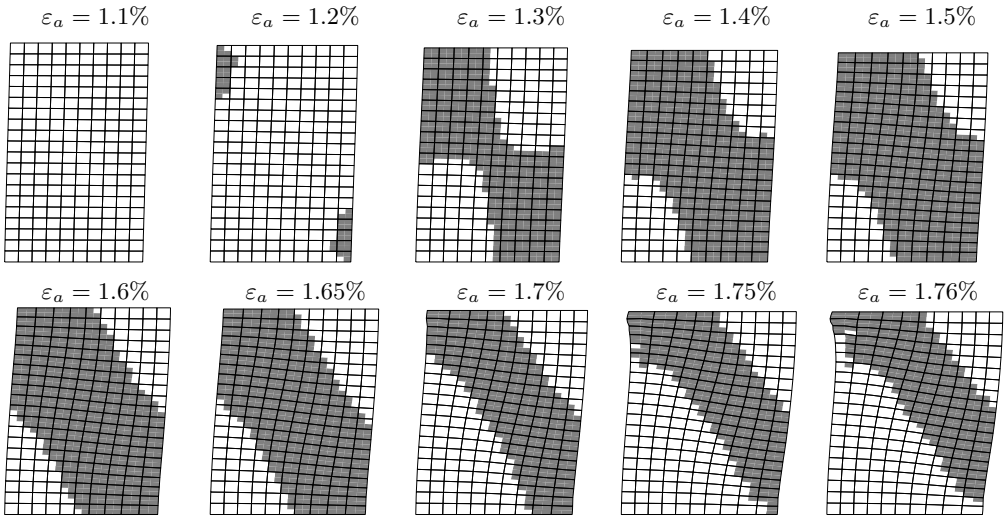

Fig. 15.10: Rice's criterion for different stages of the biaxial compression test; shaded element quadrants indicate ($\exists det(\boldsymbol{A}) < 0$) in the corresponding integration point. Displacements multiplied $10\times$.

15.5 Different local indicators in a global setting

Through the adoption of several simplifications and assumptions, a number of indicators has been defined for the local material behaviour. These indicators are here used to give some insight into the (global)state of the boundary value problem. Figure 15.11 contains the indicators of the sections above with Rice criterion (using the approximation of the direction-independent stiffness matrix) with $\vec{n}$ for the minimum determinant of the acoustic tensor, the numerical elasticity condition and the different conditions of negative second order work ${}^2W^1$ and ${}^2W^\Delta$. Starting at the first state of deformation corresponding to $\varepsilon_a = -1.1\%$ which lies well before the peak, the criteria of second order work indicates local loss of uniqueness in a zone which is later to be the zone of strain localization. From the stereographical plots in 15.9 and Appendix B it was concluded that at this stage the current loading rate and the loading increments related to negative second order work do not agree and the possible fields of velocities that satisfy $\Delta\varepsilon_{ij}\Delta\sigma_{ij} < 0$ do most likely not obey the boundary conditions of the macroscale BVP. The Rice criterion at this stage is not met and the orientation of minimum determinant of the acoustic tensor is conjugate to the final shear band orientation.

It is interesting to note that heterogeneous deformation is encountered far before the peak, which indicates that the local second gradient model plays a role in the pre-peak part of the computations and the results of computations for different second gradient parameters will diverge from a point well before the peak. This can be observed from the fields of of VM equivalent strain in Figure 15.11, where the incipient shear band can be observed well before the peak response and a variation in the order of 10% in the total VM strain can be observed as soon as $\varepsilon_a = -0.011$.

For the states of deformation around the peak, the following observations are made;

- Negative second order work criteria seem to behave chaotically, changing rapidly between the different states of deformation. Whether or not this is a numerical effect of the large loading steps or inaccurate convergence criteria is not clear.

- The low number of points for which local uniqueness can not be proved at the peak, suggests that the solution found at the peak ($\varepsilon_a = -1.3\%$) is most likely a unique solution. This can explain the good convergence at the peak and the possibility of taking (relatively) large deformation loading steps in the computations.

- The Rice criterion is met for a small part of the domain before the peak response is reached. The first continuous 'band' of points that meet Rice's criterion is found at the peak and corresponds well with the developing band.

- Vector $\vec{n}$ corresponds well with the orientation of the incipient shear band for all points for which Rice criterion is met.

At the final state ($\varepsilon_a = -1.76\%$) the Rice criterion and negative second order work criteria show very good agreement and both criteria seem to accurately follow the shear band activity (see the VM strain rate in Figure 14.12). The alignment of orientations related to negative second order work and current loading direction shown by the stereographical plots for this state of deformation, suggest that uniqueness is lost. This might explain the computational problems of finding a well-converged solution.

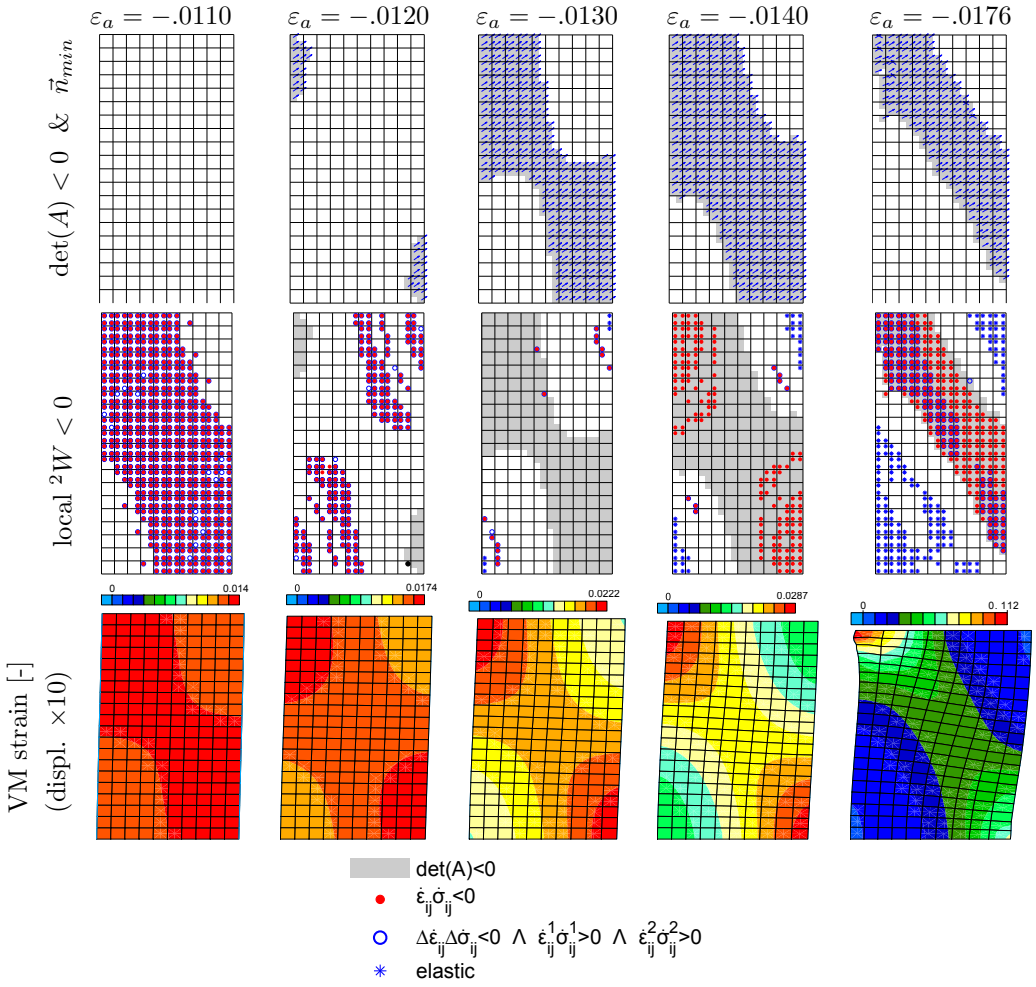

Fig. 15.11: Different indicators of localized deformation rate with Rice criterion and orientation of vector $\vec{n}$ (top), the different indicators based on second order work and interface softening rate (middel) and Von Mises equivalent strain in current configuration with displacements magnified 10× (bottom)

As a final remark, it can be stated that the evaluation of ${}^2W^1 < 0$ seems to be sufficient for most points; only very few points exists for which ${}^2W^1 > 0$ and ${}^2W^\Delta < 0$ (or ${}^2W^a < 0$). However, the kinematical admissibility of deformation increments $d\varepsilon^1$ and $d\varepsilon^2$ has to be considered in this type of analysis.

16. MODELLING OF A GALLERY EXCAVATION

The setting of the underground research laboratory (URL) described in Section 1 is taken as the starting point of the modelling of a gallery excavation problem with the doublescale model, first for purely mechanical behaviour and later with taking into account hydromechanical coupling. The focus will be on the development of strain localizations around the gallery excavation as a response to the unloading of the future gallery wall to simulate of the excavation of a gallery drift.

For a reasonably low constraint on the development of shear bands around the gallery, the element size must be small with respect to gallery dimensions: The width of possible shear bands must be small enough with respect to the dimensions of the gallery and the mesh size must be small enough to allow a proper integration over the strain gradients on the element level (to guarantee mesh-objective results). In case the chevron cracks of Figure 1.4 are modelled by a single shear band, the shear band in the numerical modelling is supposed to be in the order of 10 cm wide. To have a shear band of at least 3 elements wide, this band width requires an element size of 3 cm, which is too fine to apply in a doublescale computation of a gallery with a diameter of 5.4 m. Therefore, concessions have to be made with respect to the correct band width and the computational expense. The same goes for the choice of the domain (a quarter gallery against a full gallery) and the detail of the microstructure in the REV. Nevertheless, the use of realistic boundary conditions with a model of restricted detail can be used to study general tendency in the response and can serve as a proof of concept for future computations with higher details and computational cost.

16.1 Macroscale geometry for mechanic analysis

Figure 16.1 shows the mesh for the spatial discretization at the macroscale. The quarter of the domain around the gallery is divided into two zones. A first inner zone from the gallery wall up to a distance of 3 times the gallery radius. This is the zone in which the EDZ is expected to develop. A second zone is defined up to a distance of 50 m. At this distance, influences of the excavation on the stress state is expected to be negligible, thereby defining the computational domain. A fine mesh is used for the first zone, dividing the quarter circle of the gallery wall by 40 equally-sized elements. The length-width ratio of the elements in the first zone is set to one to optimize element integration. In the second zone, where only small elastic strains are expected, the elements are stretched to reduce the total number of microscale REV boundary value problems to solve. This gives a total number of 1640 elements.

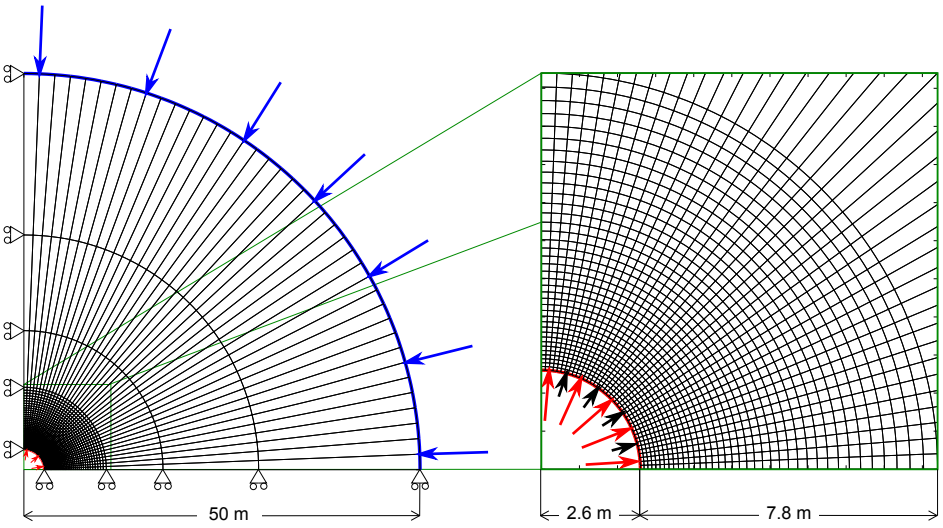

Fig. 16.1: Macroscale mesh for the modelling of gallery excavation.

The choice for a quarter of a gallery is one based on the computational expense of the problem. Although for the modelling of a gallery excavation often only a quarter of the gallery is considered assuming symmetry to be maintained throughout the computation, the validity of this assumption is not maintained when localization phenomena take place and non-symmetric solutions can be encountered. This was demonstrated for initially symmetric problems in several studies, such as Sieffert et al. [2009] and Marinelli et al. [2015]. In case of anisotropic behaviour that does not coincide with the horizontal and vertical axes, the boundary conditions will certainly influence the response, as will be demonstrated later on. Zero displacement perpendicular to the radial boundaries is used to enforce the quarter of the gallery domain. Boundary conditions with respect to the gradient of displacement, which can be used for enhancing the symmetry [Zervos et al., 2001, François et al., 2014] with respect to the local second gradient model is not used here. These conditions are only applicable in models with axes of symmetry on the domain boundaries which does not apply to the general model derived from the microscale computations. As a consequence, the double stresses perpendicular to the radial boundaries are considered zero. This is once more not consistent with the modelling of a full gallery.

An initial stress state at zero deformation is used to simulate the in-situ stress state given in Section 1.4:

$$\boldsymbol{\sigma}^{is} = \begin{bmatrix} 16.12 & 0 \\ 0 & 12.4 \end{bmatrix} \; MPa \tag{16.1}$$

The boundary traction related to the far-field boundary (blue) and gallery wall boundary (red) have both a normal and a tangential component as an effect of the anisotropic stress state. These components can be computed as the product of the stress tensor $\boldsymbol{\sigma}$ and the normal outward vector $\vec{n}$. The farfield boundary traction (in blue) is thereby given by

$$\tau_i^{field} = \sigma_{ij}^{is} n_j \tag{16.2}$$

On the gallery wall, the boundary traction is gradually reduced until a support of $\tau_n^{sup} = 0.3\ MPa$ is reached that acts normal on the gallery wall.

$$\tau_i^{wall} = (\sigma_{ij}^{is} - \delta_{ij}\tau_n^{sup})(1-\lambda)n_j + \delta_{ij}\tau_n^{sup}n_j \tag{16.3}$$

The dimensionless time or loading parameter λ is used to define the state of unloading of the gallery wall, simulating the excavation. In-situ stress conditions are maintained for $\lambda = 0$ and the final gallery wall support σ^{sup} is obtained at $\lambda = 1$.

For the modelling of possible strain localization phenomena, the element size has to be small enough to guarantee mesh independent results. Referring to the observations made around the galleries of the URL (Section 1.4), the distinct localizations that can be taken into account individually are those of the chevron cracks as a homogeneous zone in the order of a decimeter wide. The extension and shear fractures close to the gallery wall can only be modelled in a homogenized way in a continuous zone of deformation.

With a minimum element size of $10cm$ (corresponding to 40 elements at the gallery wall), the localization bands will be at least 30 cm wide. This can be a reasonable first approximation of the width of the chevron cracks. A detailed mesh is generated in a zone around the gallery up to 4 times the gallery radius (10.4 m) as no strong deformations are expected outside this zone. In order to apply a consistent farfield pressure, the total domain of computations was extended to 50 m from the gallery center. Only a few elements were used to model this zone, as the deformation and stress fields in this zone are expected to be nearly homogeneous.

16.2 Mechanical simulation of quarter gallery I

The gallery excavation computation is performed using the calibrated REV 8 (Figure 14.3). For the calibration of the second gradient parameter, the computations of the biaxial compression are used, calibrating the local second gradient model parameter D at a relatively low value of 40 kN, which in the setting of unconfined compression would correspond to a final shear band of approximately 10 cm wide.

The unloading of the reaction forces on the gallery wall according (16.3) is applied with convergence criterion on forces $\epsilon_f = 1 \times 10^{-4}$ and displacements $\epsilon_u = 1 \times 10^{-4}$, providing well-converged solutions. The resulting fields of deviatoric stress and strain are shown in Figure 16.2. The deviatoric strain field shows no strain localization in shear bands. Only the initiation of localization of deformation is visible close to the upper part of the gallery wall. This zone shows the highest deviatoric stress of the domain. When looking at the evolution of the deviatoric strain with unloading, the integration points for the element at the top of the gallery wall appear to have past the peak deviatoric stress just before complete unloading (Figure 16.3).

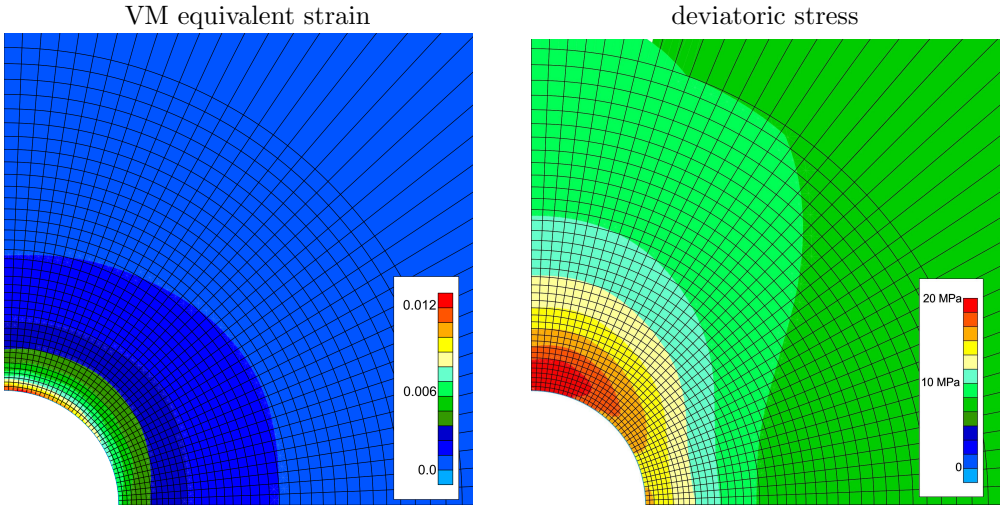

Fig. 16.2: Micro '8': VM equivalent strain and deviatoric stress after gallery excavation at $\lambda = 1$.

This deviatoric stress peak corresponds with the maximum of deviatoric stress of biaxial compression under low confinements, as for example observed for biaxial compression at 2MPa confinement (Figure 14.4) and the doublescale unconfined compression (Figure 14.10). The microstructure in this element shows only a slight initiation of softening, with the early development of continuous paths of interfaces in a state of softening.

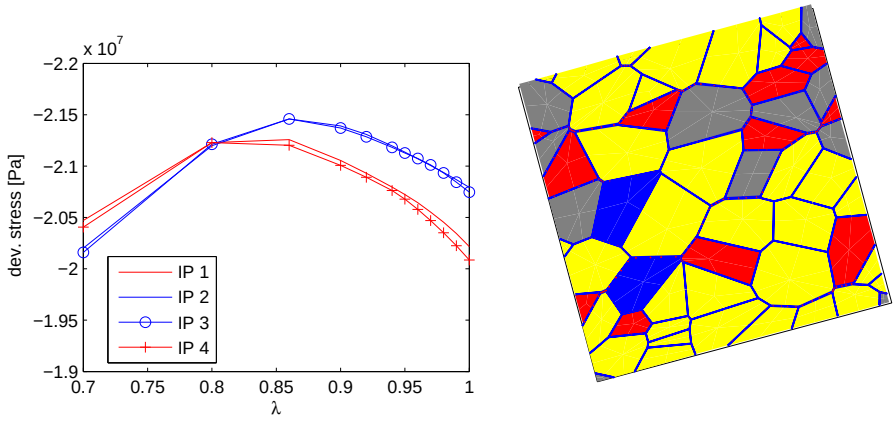

Fig. 16.3: Left: Deviatoric stress in the integration points in element 1600 (on top gallery wall). Integration point 1 and 4 are closest to the gallery wall. Right: Deformed microstructure of IP4 at $\lambda = 1$

The absence of strain localization in shear bands in the numerical simulation after calibration of the mechanical behaviour is not in good agreement with the observations of localized deformation in the field. An explanation for this absence is not easily found and can be sought in different directions. A possible reason is the incorrect representation of mechanical properties of the constitutive law which

were not considered in the model calibration. The constant dilatant behaviour with continued loading for example might not be representative for the claystone. In combination with a relatively large internal length scale, this could lead to an arching effect around the gallery, leading to a too resistant response of the material.

16.3 Mechanical simulation of quarter gallery II

For further studies on the localization around the gallery excavation, an alternative REV is calibrated against the experimental data. As a trade-off between computational efficiency on one hand and accuracy in representing a material with enough detail on the other, the number of grains in the REV is reduced by a factor two with respect to the example given above. To avoid a too strong effect of the heterogeneity of the grain stiffness with the reduced number of grains, homogeneous grain stiffness is adopted equal to the initial material stiffness mentioned in literature (Andra [2005a] and the references therein).

From a series of 100 REVs with 20 grains each, the REV with the lowest anisotropy in the peak strength was chosen. This REV (REV 28, shown in Figure 16.4) was then calibrated against the experimental results from triaxial compression tests under 12 MPa confining stress. The results of the calibration are given in the accompanying table:

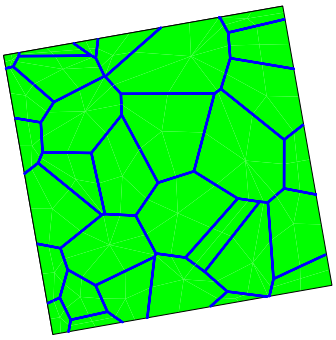

θ^{REV} [°]	-80.0
solids:	20
E [GPa]	4.0
ν	0.3
k_{ii} [$\times 10^{-20} m^2$]	1.0
φ[−]	0.18
interfaces:	
$\delta^c_{t/n}$	0.125
$D^0_{t/n}$	0.01
$T^{max}_{t/n}$ [MPa]	1.00

Fig. 16.4: Microstructure '28' for the modelling of

Only a partial calibration with respect to experimental results was performed for this microstructure. As for a given microstructural geometry the effective friction angle (as the pressure-dependency of the peak response) and the dilatancy are difficult to control, not all parameters available from the experimental data can be calibrated. The approach followed here is therefore to only calibrate against the 12 MPa experimental results. It has to be stressed again that the comparison is done between numerical results obtained under plain strain conditions and experimental results obtained from triaxial compression tests. As the influence of the Lode angle (or the intermediate principal stress) on the behaviour of the Callovo Oxfordian claystone is not well known, an assumption of the failure criterion is required to make a comparison. Although it was pointed out in Section 14.2 that the biaxial compression can be expected to lead to higher peak responses than

triaxial compression tests, the peak stress is here calibrated conservatively in order to correct for the possible influence that the strong dilatancy might have on the localization. For this reason, the peak stress response to biaxial compressive loading is calibrated to significantly underestimate the failure load and thereby to favor the localizations. The peak stress response as a function of REV orientation is calibrated not to exceed the maximum of the experimental results (Figure 16.5). With an effective friction angle that is higher than observed by experiments, this leads to a material that is weaker than the COx under low confinement.

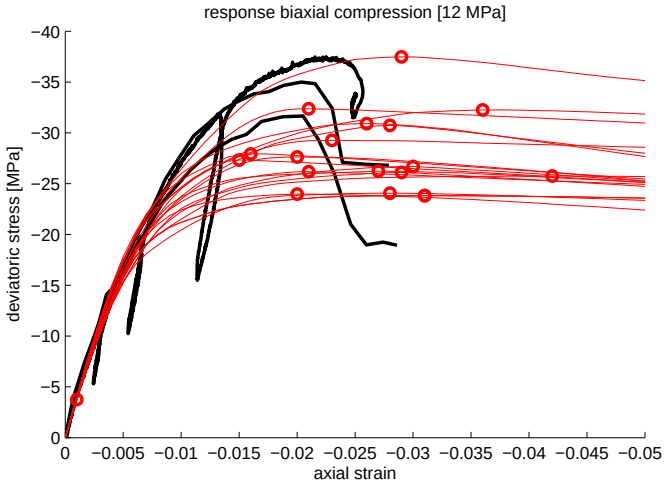

Fig. 16.5: Deviatoric stress response to material point biaxial compression at 12 MPa confining stress for different orientations θ^I compared to the experimental results obtained by triaxial compression tests.

Figure 16.6 shows the anisotropy in the peak response to biaxial compression at 2 MPa and 12 MPa confining stress. The initial orientation of the REV has been rotated $-80°$ such that the maximum peak stress coincides with loading in $0°$ orientation. It is clear that for all orientations, the peak strength of the material is lower than the strength observed in the experiments.

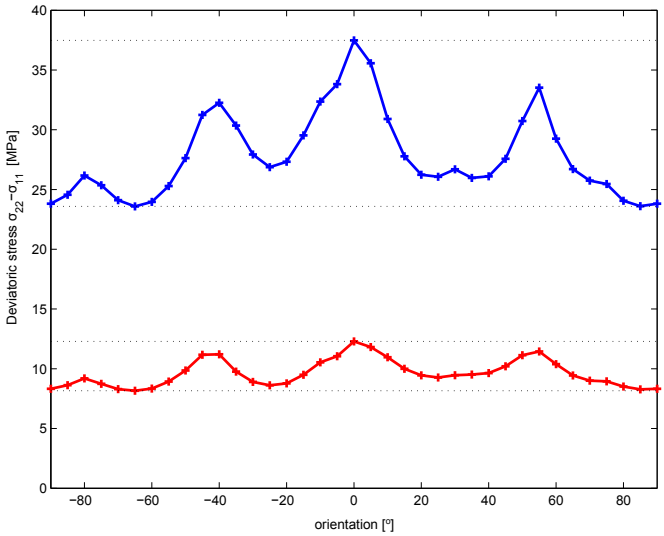

Fig. 16.6: Peak response to biaxial compression as a function of REV orientation for confining stress of 2 MPa (red) and 12 MPa (blue).

Figure 16.7 shows the evolution of the deviatoric strain. For four stages, the total deviatoric strain and the strain rate is plotted. As most of the unloading at the gallery wall results in homogeneous deformation around the gallery, most focus goes to the final 10% of the unloading, during which strain localization takes place. From the plots of deviatoric strain, the following can be observed:

- Strain localization is triggered along the gallery wall, but the initial location of localization of strain (visible at the top of the gallery, the point of highest deviatoric stress in the early stage of unloading) does not necessarily lead to the first localization bands.
- Bands are activated and deactivated during the evolution of deformation. This is not related to instabilities of different solutions, but rather to the evolving anisotropy of the material through the geometry of the microstructure.
- The localization bands appear to have preferential directions, instead of the curved bands that are observed in the field or reproduced using classical constitutive relations [Varas et al., 2005, Marinelli et al., 2015] or constitutive relations from REV numerical simulations leading to a more isotropic material response [Nguyen, 2013].
- The localization bands appear mesh independent and reasonably constant, demonstrating the ability of the local second gradient model to properly regularize the continuum for this complexity of constitutive behaviour. A more complex behaviour with stronger fluctuations of material stiffness as observed in the biaxial compression test with the REV in FIgure 14.3 will lead to more variation in the dimensions of strain localizations.

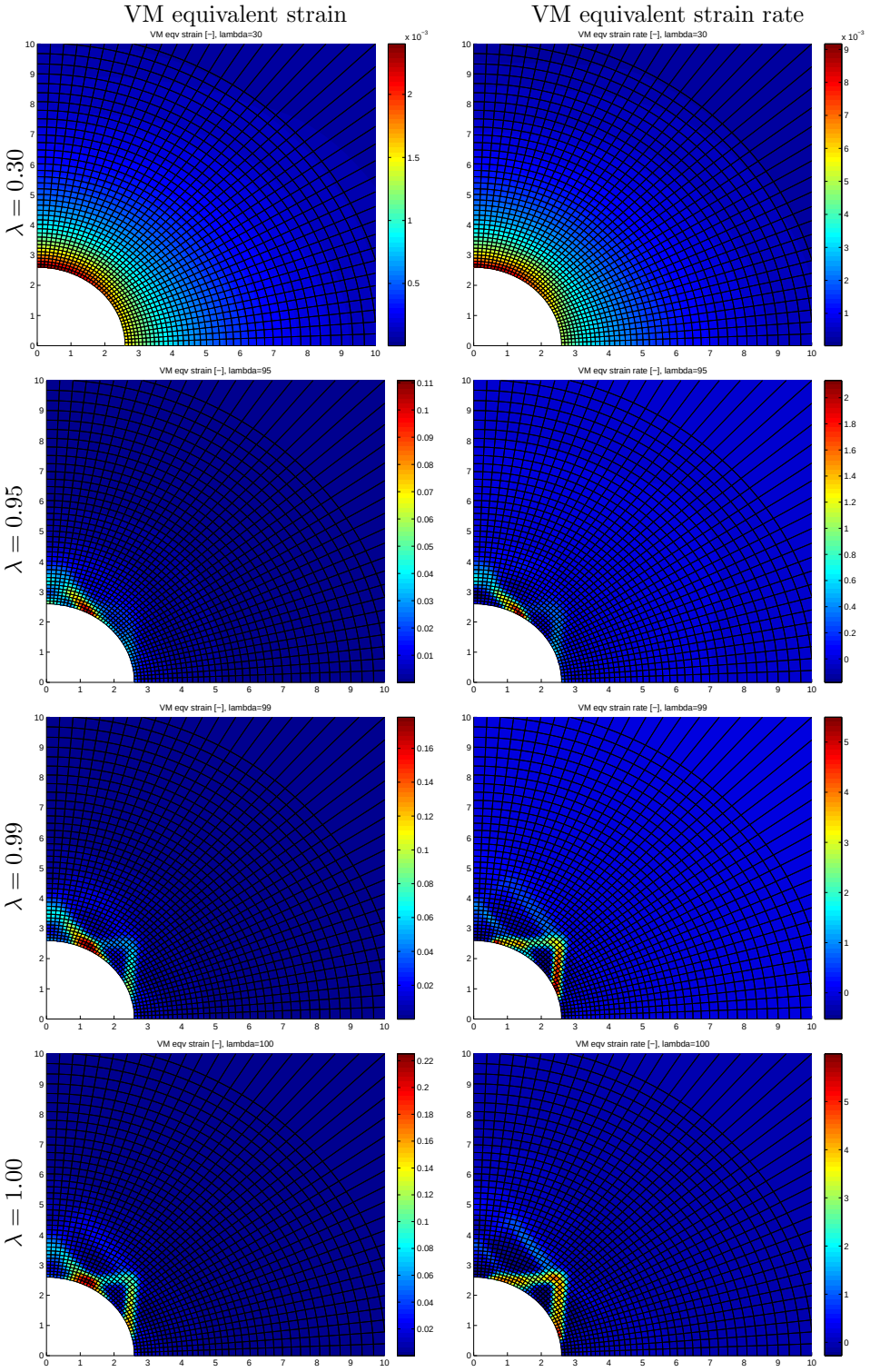

Fig. 16.7: Deviatoric (Von Mises equivalent) strain and strain rate for different stages of excavation, simulated by the unloading parameter λ.

To further study the preferential orientation of the localization bands, deformed microstructures are plotted for different points in different bands. These microstructures are given in Figure 16.8.

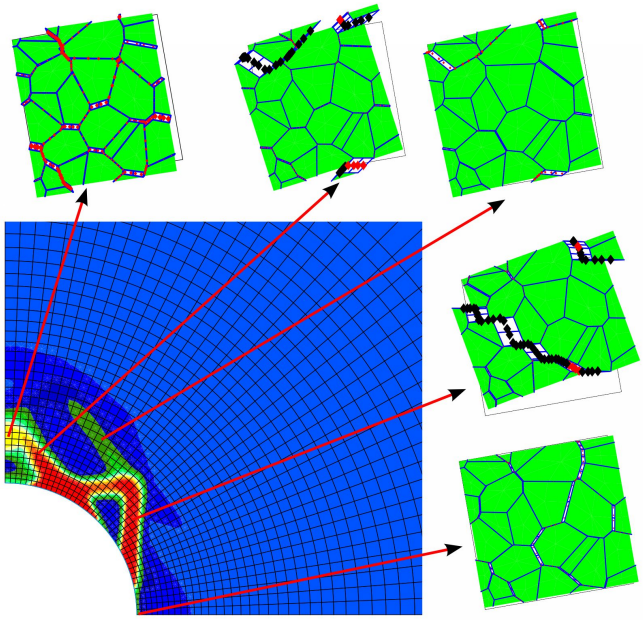

Fig. 16.8: Macroscale mesh with VM equivalent strain after unloading ($\lambda = 1$) and deformed microstructures for different integration points.

The pattern of interface softening and decohesion at the microscale is strongly related to the mode of localization at the macroscale; each orientation of localization at the macroscale corresponds to a specific pattern of the interface degradation. This can be traced back to the anisotropy in the post-peak response. Each of the preferential orientations of macroscale localizations corresponds to one of the valleys in the post-peak response domain.

For REVs with relatively low number of grains, the pattern of anisotropy is already present in the peak stress and will for the better part correspond to the post-peak anisotropy. This anisotropy (a material property) can be linked to the initiations of the different localization bands.

16.4 Quarter gallery with hydromechanical coupling

In this section, the modelling of the gallery excavation is repeated for the case of hydromechanical coupling, which introduces a time-dependency into the modelling framework. Even if the modelling of the excavation itself can be considered as an undrained exercise, the dissipation of the (induced variation of) pore water pressure after the excavation is a transient process.

The in-situ conditions are simulated for a gallery orientated in the direction of the minor principal in-situ stress. This corresponds to the following initial stress state for the modelling of the cross section of the gallery excavation problem in

plane strain conditions :

$$\begin{aligned} \sigma_{11}^0 &= 16.12\ MPa \\ \sigma_{22}^0 &= 12.70\ MPa \\ \sigma_{12}^0 &= 0.00\ MPa \\ p^0 &= 4.70\ MPa \end{aligned}$$

The modelling of the hydromechanical coupling requires the (loading) time steps to be controlled carefully to guarantee a proper time integration and application of the different loads. This leads to a strong increase in computation time. To be able to perform these kind of computations, a coarser mesh is used to reduce the computational cost of the total number of microscale computations. To be able to properly capture the hydraulic pressure gradient of the dissipating fluid pressure, the zone of square elements is extended to 50 m from the center of the gallery and the full domain is extended to 200 m. Figure 16.9 shows the mesh with the applied boundary conditions, where the number of elements along the quarter circle of the gallery is reduced from 40 to 20.

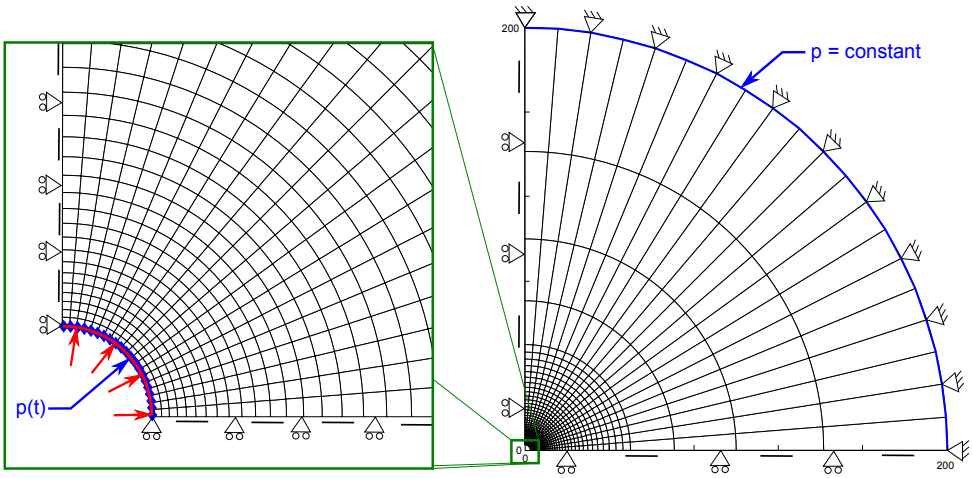

Fig. 16.9: Mesh for HM-coupled computation of gallery excavation.

For the boundary conditions applied on the mesh in Figure 16.9, three groups of boundaries are considered;

1) the gallery wall

$$\begin{aligned} p^t &= p^{is}(1-\lambda_p^t) \\ \tau_i^t &= \sigma_{ij}^{is}(1-\lambda_{mech}^t)n_j \end{aligned} \tag{16.4}$$

2) the farfield boundary

$$\begin{aligned} p^t &= p^{is} \\ u_i^t &= 0 \end{aligned} \tag{16.5}$$

3) the radial boundaries

$$\begin{aligned} m_i^t n_i &= 0 \\ u_i n_i &= 0 \end{aligned} \tag{16.6}$$

n_i are the components of the normal vectors to the boundaries and λ_{mech}^t and λ_p^t the loading multipliers for forces and fluid pressure as a function of time. Figure 16.10 presents the applied loading on the gallery wall, simulating a passing excavation front at the plane of interest at $t = 14$ days [Andra, 2013]

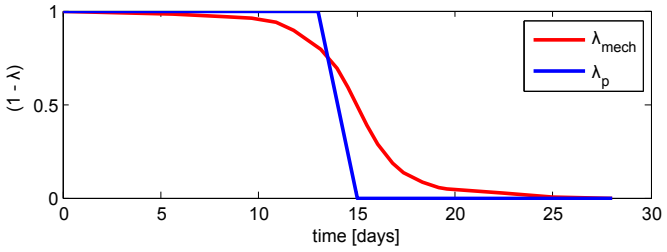

Fig. 16.10: Multipliers λ for the gallery wall boundary conditions as a function of time, simulating the excavation front passing at $t = 14$ days.

For the regularization, the second gradient model with parameter $D = 40kN$ is used, identical to the mechanical simulation of the gallery excavation presented in 16.3.

REV 28 with the constitutive parameters given in Figure 16.4 is used at the microscale. For the coupling between the mechanical hydraulic opening of the interfaces with the fluid problem, the minimum opening of the interfaces is defined at 0.02 μm and the relation $a^h = \partial \Delta u_h / \partial \delta u_n = 1\ mm$ (Equation (5.66)) is used to introduce a physical length in the hydraulic opening. With these values and an isotropic grain permeability $k_{11/22} = 1.0 \times 10^{-20}\ m^2$, the initial permeability of the REV is:

$$\boldsymbol{k}^0 = \begin{bmatrix} 1.26 & 0.00 \\ 0.00 & 1.28 \end{bmatrix} \times 10^{-20} m^2 \tag{16.7}$$

The (average) porosity of the grains is set at $\varphi = 0.18$. This results in an initial fluid content of 180.56 kg/m^3, including the effect of fluid compressibility and interface hydraulic volume. A REV orientation of $\theta^{REV} = 0°$ is used. For this reason, the specific modes of localized deformation can not be compared with those presented in Section 16.3.

A first impression of the response to unloading is given by the physical convergence of the gallery wall with time of the ground response curves [Brown et al., 1983, Alonso et al., 2003, Lee and Pietruszczak, 2008]. This response is given in Figure 16.11 for three points along the wall; the intersection with the horizontal axis (0°), the vertical axis (90°) and the intersection of the gallery wall with the diagonal (45°). The convergence during the first 28 days $\approx$ (0.08 year) shows strong resemblance with the mechanical loading parameter λ_{mech} (Figure 16.10) and indicates a predominantly elastic response to unloading of the gallery wall. This elastic response is due to the close-to-undrained conditions of the material

around the gallery. This can be verified by the pore pressure field after unloading ($t = 30\ days$), which is given in Figure 16.12 together with the Von-Mises equivalent strain. With the exception of the gallery wall on which fluid pressure is enforced to be zero, the fluid pressure is negative in the zones of higher deformation and reaches negative pressures as low as $-4\ MPa$. This negative pore pressure as a direct reaction to the mechanical unloading of the gallery wall is explained by the dilatancy due to the deformation of the material. This dilatancy is a direct result of the opening of interfaces that is required for any macroscale deformation other than that due to elastic deformation of the grains. The pressure drop of around $8MPa$ is in the range of the drop in mean total stress due to the unloading of the gallery wall.

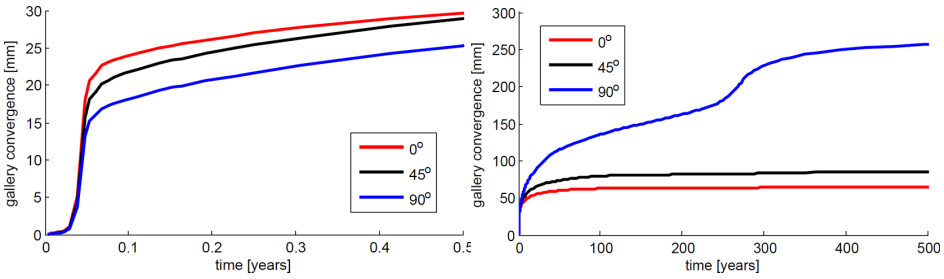

Fig. 16.11: Gallery convergence with time: gallery wall displacement relative to gallery center

The longterm response (1-500 years) corresponds more to transient behaviour, with asymptotic convergence of points $\beta = 0°$ and $\beta = 45°$, which can be related to the dissipation of the fluid underpressure that allows further gallery wall convergence through deviatoric (and therefore volumetric) deformation. The point at $\beta = 90°$ initially shows the same response, after which an acceleration with time can be observed. This stronger convergence can be related to the (initiation of) localized deformation close to this point. The activity of these localizations can be observed at different locations, depending on the state of dissipation of the negative pore pressures. Examples of this effect are given by the strain rate fields in Figure 16.12 at times $t = 5$ years and $t = 50$ years. This time-dependent response due to the pressure dissipation is strongly influenced by the dilatant nature of the material. A consequence of formulating the microscale model such that the dilatancy is high and pore volume can only increase with deformation is that the development of negative pore pressures can not be avoided.

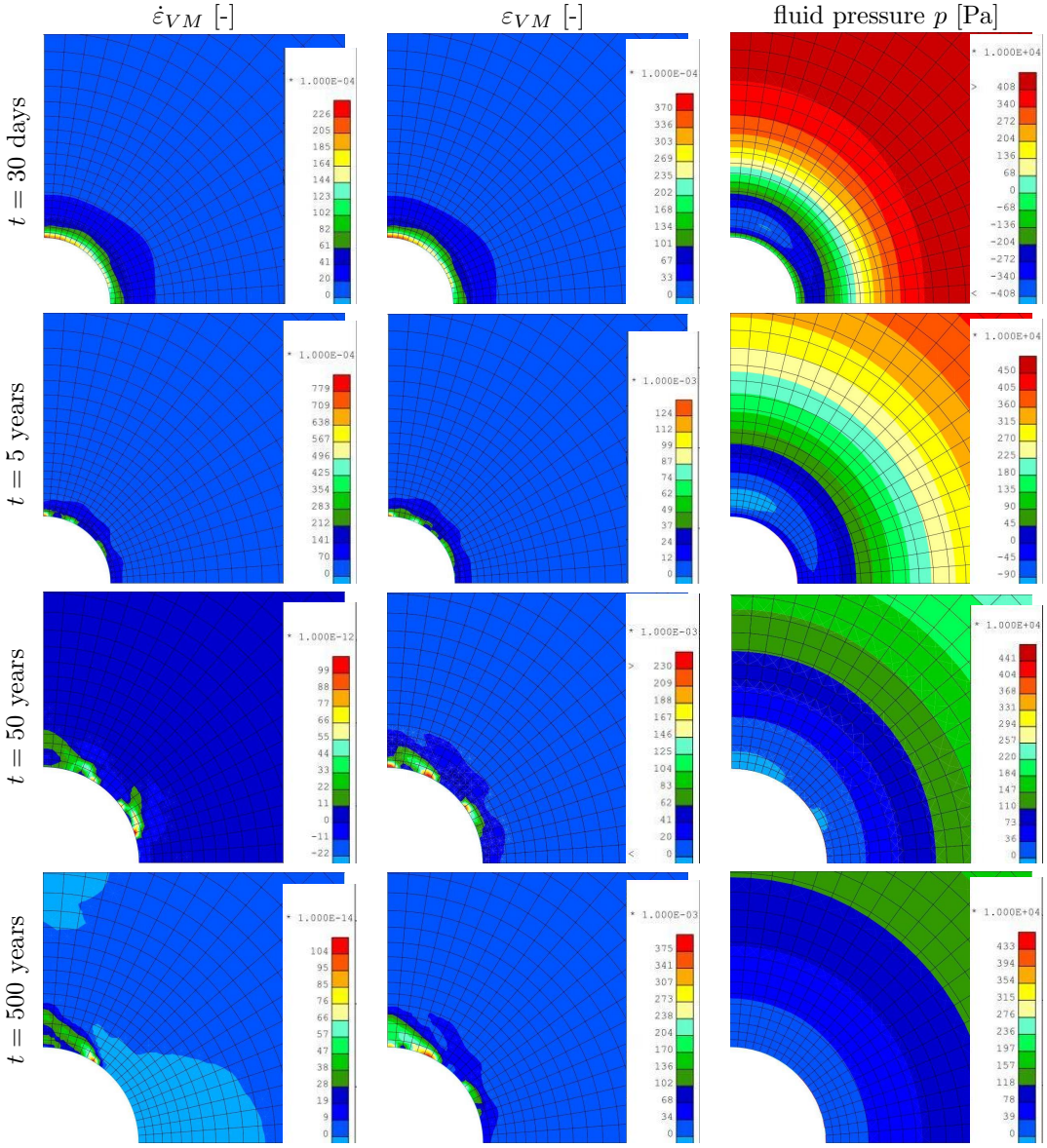

Fig. 16.12: Response to unloading at $t = 30$ days, $t = 5$ years, $t = 50$ years and $t = 500$ years.

16.5 Evolution of permeability

The evolution of the permeability with macroscale degradation is investigated in this section. For this purpose, Figure 16.13 shows the distribution of the individual components of permeability tensor $\boldsymbol{k}$ at the end of the simulation.

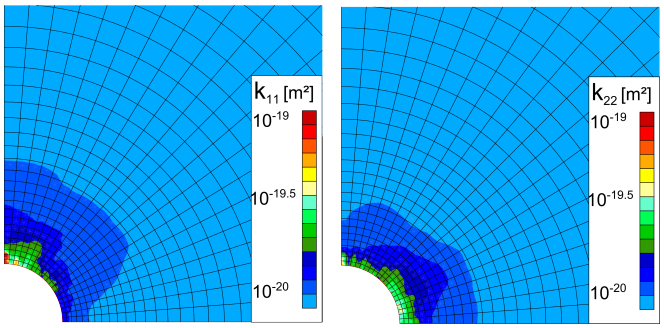

Fig. 16.13: Permeability distribution at the end of the simulation for hydromechanical coupling. Color scales are truncated.

The permeability increases in the zones of stronger deformation (close to the gallery wall) as an effect of the opening of individual interfaces. The orientation of the individual interfaces influence the orientation of the increase in permeability, which introduces a strong anisotropy of permeability. The increase in permeability as reported in literature (see Section 1 and Armand et al. [2014]) is not found in the simulations. This can be explained by the two-dimensionality of the microstructure and the need for grain contacts in case of a compressive state of the material. This prevents the development of continuous paths of opened interfaces for the fluid to percolate from one side of the REV to the other and therefore keeps the permeability low. An extension of the microscale model to 3D or the introduction of an interface dilatancy effect to simulate the effect sliding interfaces with rough surfaces could introduced the effect of the three-dimensionality of the pore network (see for example Massart and Selvadurai [2012]).

An exception to this restricted evolution of permeability can be found in some REVs in the upper corner, for which excessive strains lead to complete decohesion of the interfaces and a continuous opening of interface channels. This leads locally to an increase of the permeability of several orders of magnitude, but the mode of deformation in these elements is far from mesh-objective and the modes of deformation ae not necessarily representative for the correct structural response.

17. MESOSCALE HETEROGENEITY; RANDOM REV ORIENTATION

The effect of the orientation of the microstructure and the periodic frame of the REV has been discussed in different sections above. Section 11.2 has demonstrated that the orientation of the REV with respect to the macroscale introduces anisotropy in the material behaviour, either as a desired effect, or as an effect of the non-representativeness of the microstructure in the REV. In addition, the influence of the periodic frame in the post-peak regime was demonstrated to play an important role. In section 16.3 it was demonstrated that the combined effect of microstructure and periodic frame leads to preferential orientations of shear bands due to the anisotropy of the macroscale material behaviour.

The representativeness of the REV in the non-softening regime is easily obtained by taking more and more grains into consideration and complies with the classical definition of the REV. However, the increasing number of degrees of freedom in the microscale finite element computations leads to an excessive computational cost of the evaluation of the microscale boundary value problem.

In this section an alternative approach is followed to mask the effects of both the low number of grains in the REVs and the periodic frame by introducing a spatial variability of the configuration of the microstructure and orientation of periodic frame. The configuration of the REV can be changed by means of a variation of:

- realizations of the microstructure
- microscale constitutive parameters
- orientation of the microstructure
- orientation of the periodic frame
- a combination of these points

Furthermore, different approaches can be envisioned for the introduction of the spatial variability, based on the spatial correlation between the parameters on which the variation is applied. The introduction of this spatial correlation is required to obtain mesh-independent spatial variation of material properties and therefore a mesh-independent computation.

In a first attempt the only variation that is introduced is the REV orientation, which is the most straightforward variation from an implementation point of view. The variation of the orientation of the REV implies that the variation of the orientation of the microstructure and the orientation of the periodic frame are identical and only θ^{REV} is changed. No spatial correlation is introduced, which implies a certain mesh-sensitivity to be expected in the results as an additional length scale is introduced by the size of the macroscale mesh. Nevertheless, the

application of the local second gradient model will regularize an important part of this mesh sensitivity and the internal length of strain localizations is maintained.

The REV orientation is defined randomly and independently in each integration point, as schematically presented in Figure 17.1. The values for θ^{REV} are uniformly distributed between 0° and 180°.

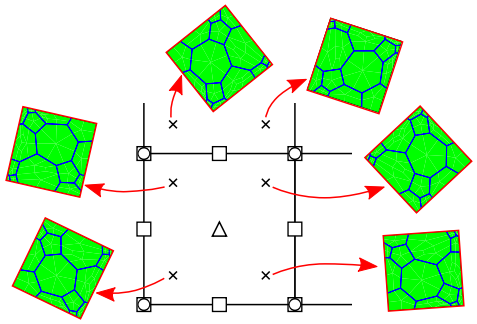

Fig. 17.1: Macroscale enhanced finite elements with REV orientation θ^{REV} assigned randomly to the integration points.

17.1 Microstructure REV

The microstructure for this test is given in Figure 17.2 together with the constitutive parameters. The low number of grains leads to a concise finite element problem to be solved at the microscale, which allows a detailed macroscale computation with a fine mesh as well as small loading steps.

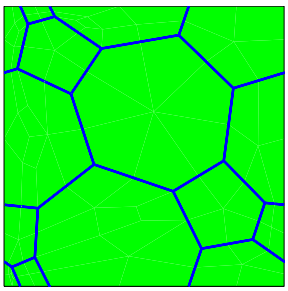

grains:	8
ξ	1.0
η	1.0
solids:	
E [GPa]	7.2
ν	0.200
interfaces:	
E_0 [GPa]	3.3
T^{max} [MPa]	5.0
δ^c	0.125

Fig. 17.2: Microstructure REV 184 with microscale constitutive parameters.

Figure 17.3 shows the material-point response to unconfined biaxial compression for different REV orientations θ^{REV}. A small variation in the initial stiffness can be observed, as an effect of the interface distribution. The orientation-dependency in peak response to biaxial compression shows a combination of low number of grains, periodic frame orientation and material anisotropy with a peak of increased strength every 30°. The slopes of the softening branches of the nominal stress response show relatively few variations between the different REV

orientations, with 2 or 3 notable exceptions, related to microscale damage in a single path through the REV.

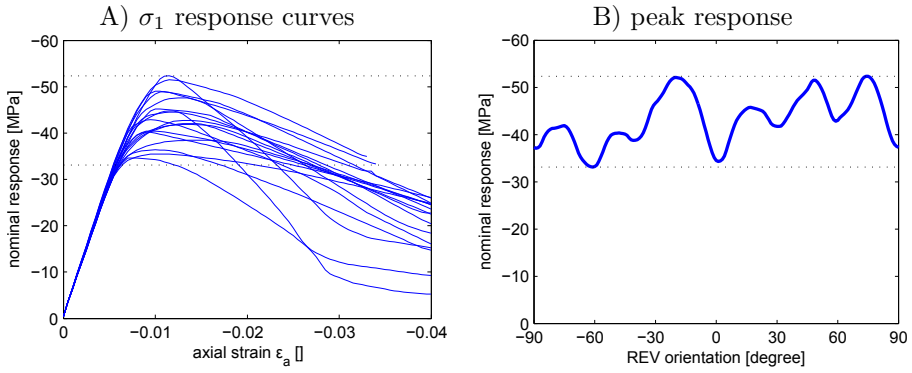

Fig. 17.3: A) material point response to unconfined compression for REV orientations on a 10° interval. B) peak response as a function of REV orientation θ.

Two doublescale unconfined biaxial compression tests on a $38\times76\ mm^2$ sample is are simulated by means of a regular mesh of 40×80 finite elements. Local second gradient model parameters $D = 100\ N$ and $D = 25\ N$ are used for the two simulations.

Figures 17.4 and 17.5 show ε_{VM} and $\dot{\varepsilon}_{VM}$ for different stages of the simulation with D. As an effect of the spatial variation at the intermediate length scale, slightly heterogeneous strain fields are obtained from the first loading step on (in the order of 10% in step A). Multiple incipient shear bands can be observed from the point where the global response becomes non-linear in step B and C (the first non-linear effects appear around 50% of the peak strength). The bands develop at different rates until the peak of the global stress-strain curve is reached (step D), where some bands stop being active and localized deformation takes place in a few bands only. In the post-peak regime (Figure 17.5) only two active bands remain and the demain outside these bands is unloading (hence the rate of ε_{VM} is negative). These bands develop from the peak onwards, becoming narrower and more distinct untill they reach a final width. Eventually, one of the bands becomes inactive (between step F and G) and further deformation takes place in a single remaining active band. It should be noted that no special measures were taken to either trigger or stop the development of strain localization. This is fully controlled by the material behaviour and its intermediate scale of heterogeneity that was introduced through the random distribution of the initial orientation of the REV.

In Figures 17.6 and 17.7 the results of the simulation for $D = 25\ N$ are presented. The fields of deviatoric strain and rate of deviatoric strain in the initially linear part (step A) shows no difference with the simulation with $D = 100\ N$ and has a spatial scale of fluctuation directly prescribed by the element size. Heterogeneity of deformation at a spatially larger scale occurs as soon as nonlinear responses are obtained (step B). The length scale of these heterogeneities is difficult to compare quantitatively between the simulations for $D = 25\ N$ and $D = 100\ N$, but it can be observed that the heterogeneities for a smaller parameter D tend to have a smaller length scale. Again, the incipient localization bands fade out

during the continuous pre-peak loading (step C and D) after which a single shear band develops from the point of peak response onwards (steps E-H). Due to the smaller parameter D the band width is less wide. Moreover, only a single shear band develops after the peak. As a result of the reduction of both the width and the number of shear bands, snap-back is more likely to take place. Step H is the last converged point before snapback and no solutions can be found without the use of more advanced loading control algorithms.

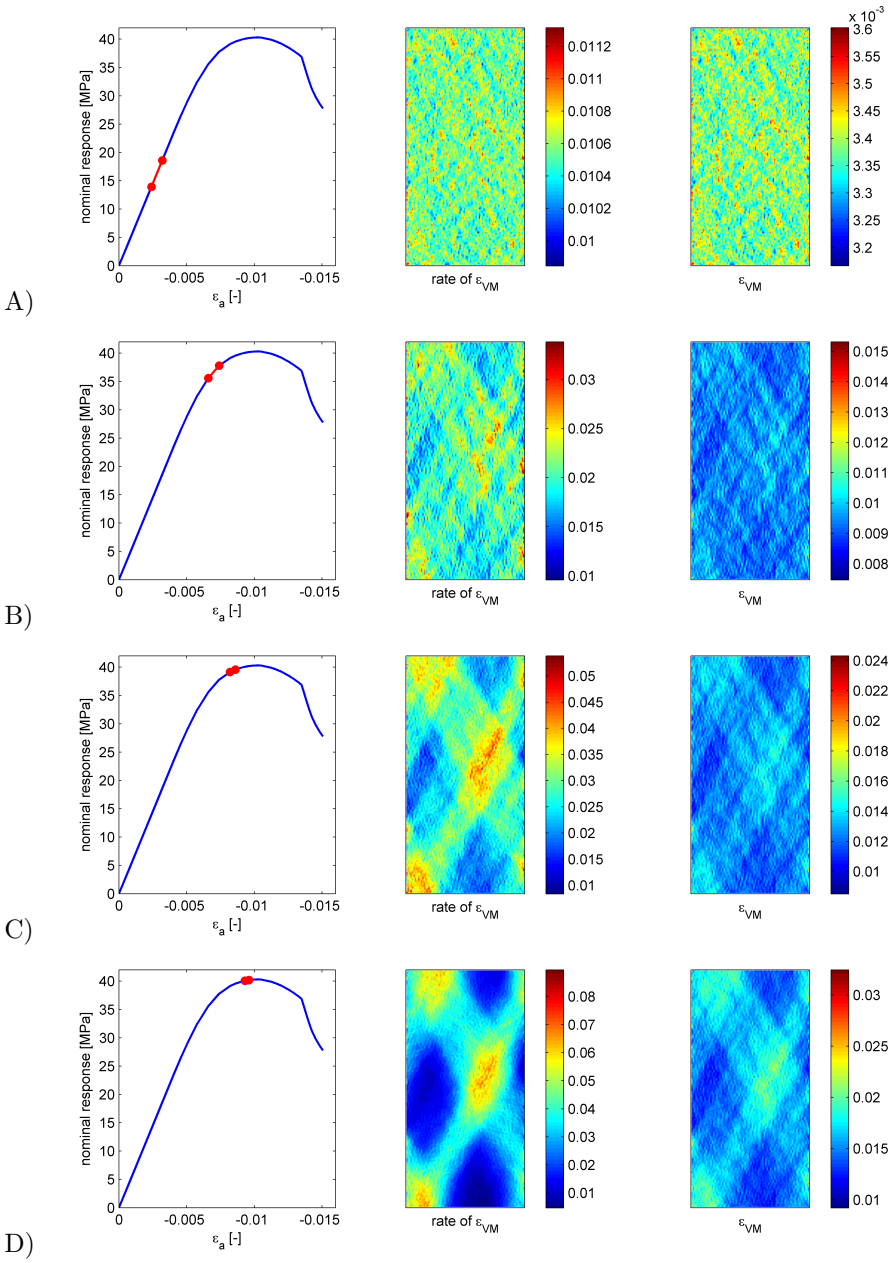

Fig. 17.4: Pre-peak (rate of) Von Mises equivalent strain (ε_{VM}) for $D = 100\ N$.

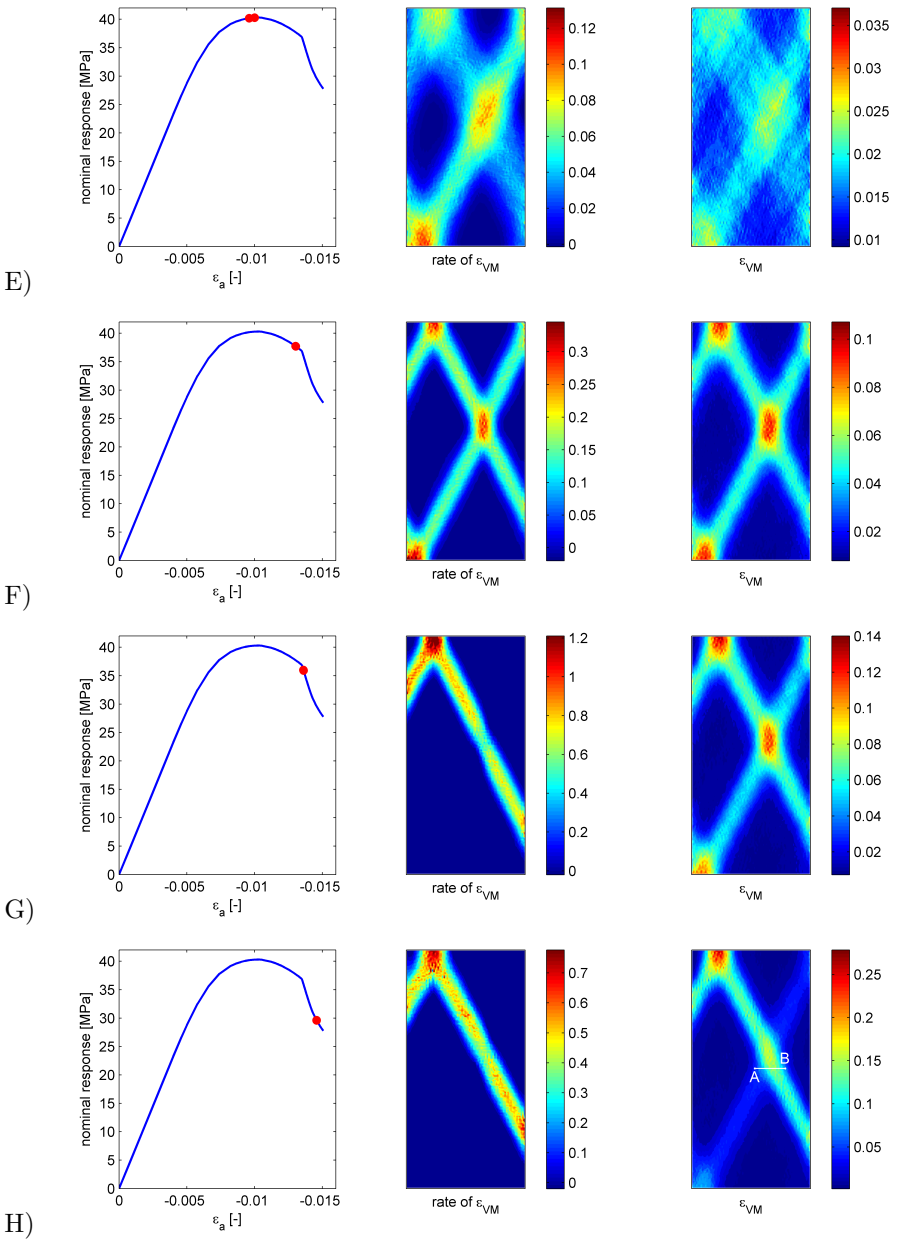

Fig. 17.5: Post-peak (rate of) Von Mises equivalent strain (ε_{VM}) for $D = 100\ N$.

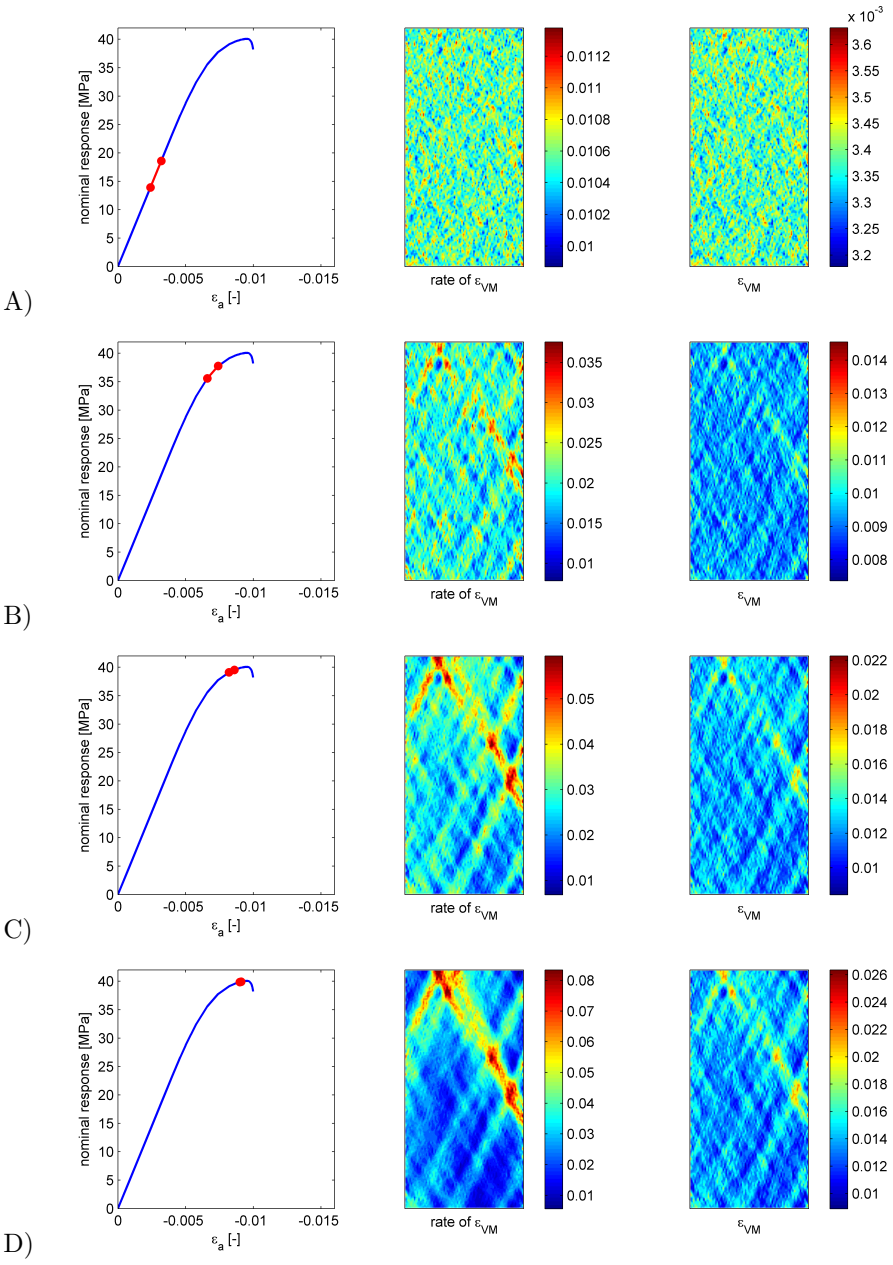

Fig. 17.6: Pre-peak (rate of) Von Mises equivalent strain (ε_{VM}) for $D = 25\ N$.

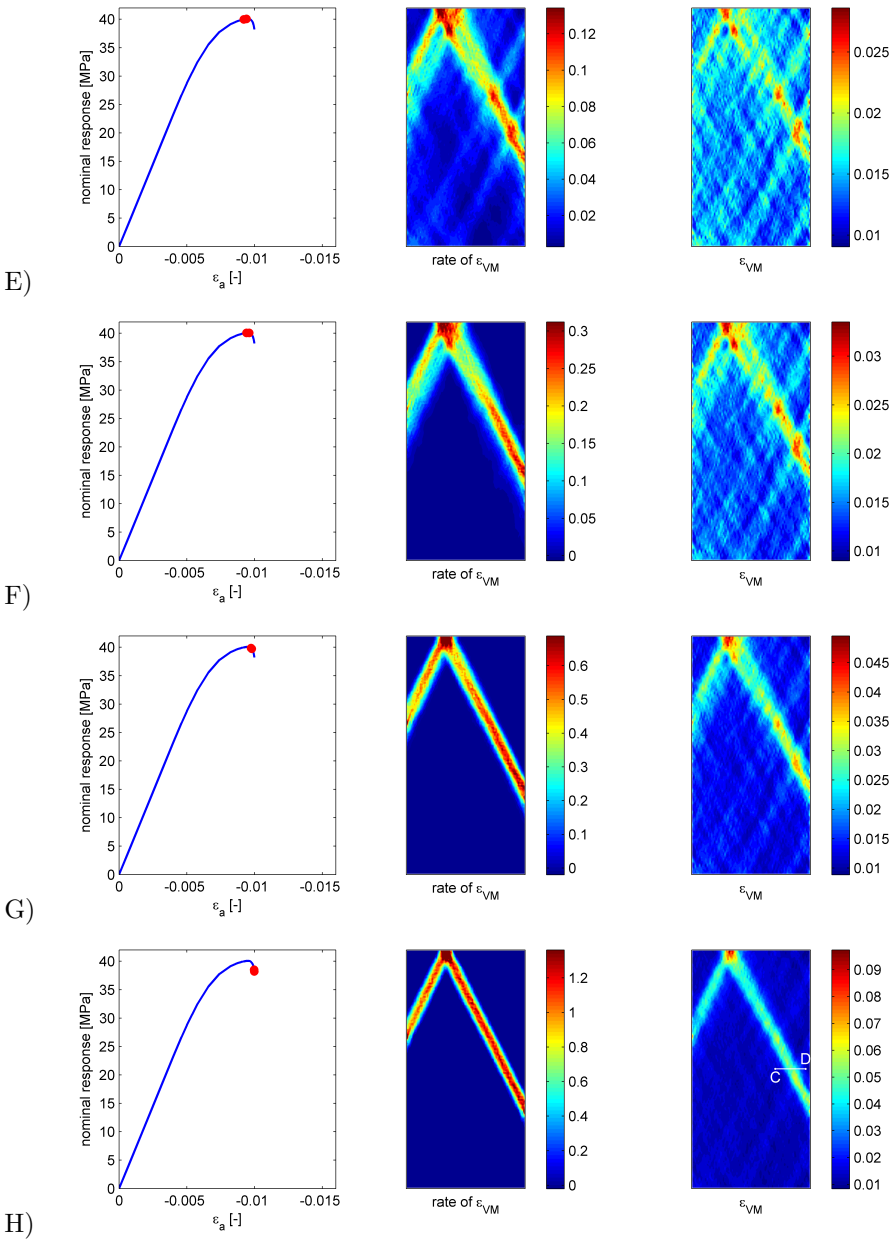

Fig. 17.7: Post-peak (rate of) Von Mises equivalent strain (ε_{VM}) for $D = 25\ N$.

Figure 17.8 gives a magnification of the deformation of the shear band of the simulation with $D = 25\ N$. With a $\times 10$ magnification of the displacements, the deformed mesh shows clearly that the width of the shear band is mesh-objective with a width of about 6 elements. Nevertheless, smaller fluctuations in the displacement fields can be observed at the level of the element, both as irregularities in the mesh and as small local variations in the deviatoric strain field. These fluctuations are the effect of the random variation of the REV at the integration points and can be seen as an intermediate scale of heterogeneity with a length scale that is directly related to the element size. The amplitude of these fluctuations are determined by the anisotropy in the REV response, influenced by both the microstructure anisotropy and the periodic frame effect in the post-peak regime.

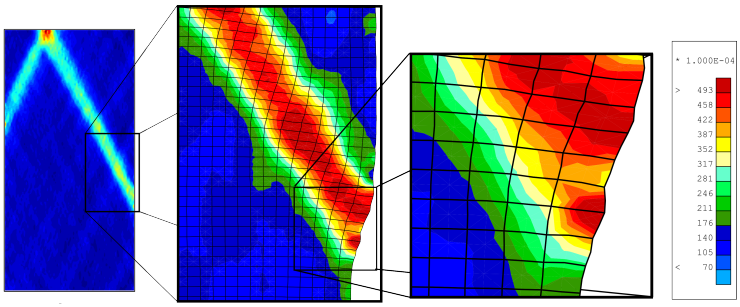

Fig. 17.8: Magnification of Figure 17.7H) at the point where the shear band touches the domain boundary (displacements multiplied $\times 10$) with truncated ε_{VM} colorscale.

The variation of the REV orientation has restored the isotropy of the material at the macroscale, which has allowed the conjugated shear bands to develop, as well as the reflection on the top and bottom of the sample. This does not necessarily mean that the periodic frame effect has been resolved; the effect has been masked by spreading out the response in all loading direction, but locally still constrains the modes of deformation. In addition, the size-dependency of the REV has not been resolved and the number of grains per REV still plays a role in the (post-peak) response.

Nevertheless, the application demonstrates the capabilities of the doublescale modelling approach in case the periodic frame effect and problems of microstructure representativity are resolved.

17.2 Microscale mode of deformation

The macroscale shear band can now be compared with the deformation of the microstructure and the damage of the interface decohesion. For this purpose, the deformed REVs along a cross-section through the shear band in the final stage of both simulations is made (see Figures 17.5H) and 17.7H)). Along the cross sections $A - B$ and $C - D$, ten deformed microstructures are presented in respectively Figure 17.9 and 17.10. As an effect of the variation in REV orientation, the modes of deformation at the microscale are no longer unique to the macroscale mode of deformation as it was observed in for example Figure 16.8. Due to the

different states of deformation at the end of the simulations (steps H), the results in Figures 17.9 and 17.10 can not be compared in detail.

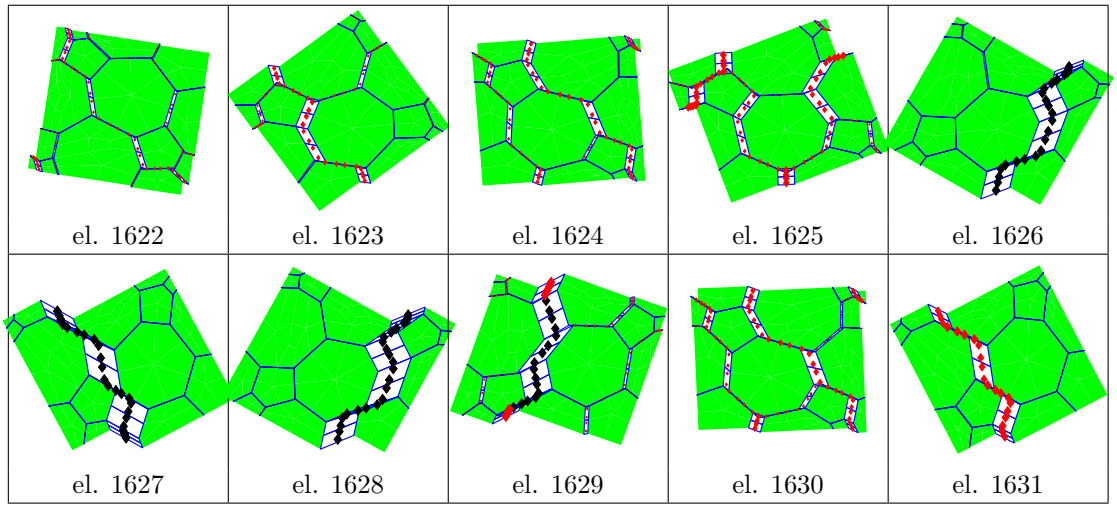

Fig. 17.9: Deformed microstructures of integration point 2 for the elements 1629 to 1638 along cross section $A - B$ (Figure 17.5H))

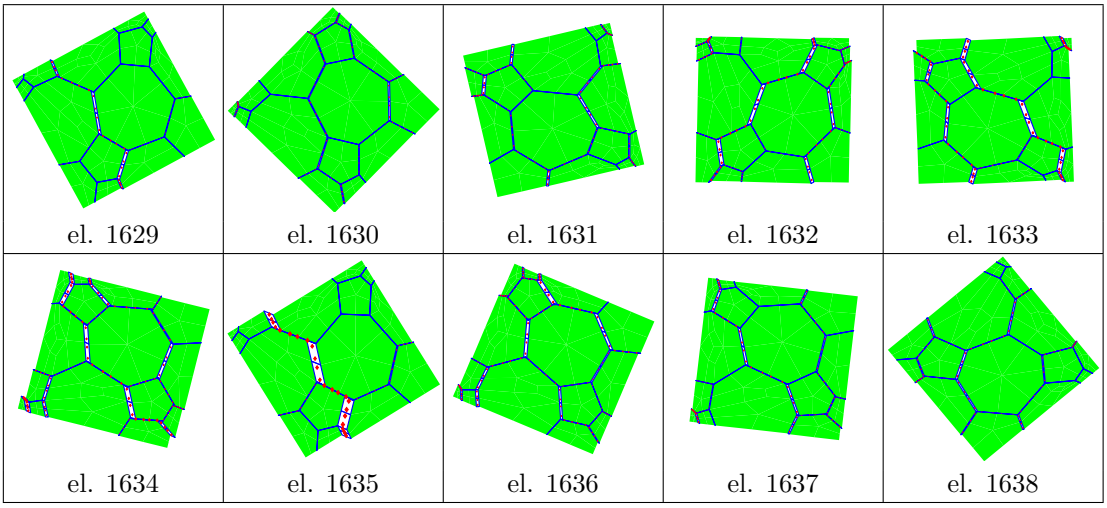

Fig. 17.10: Deformed microstructures of integration point 2 for the elements 1629 to 1638 along cross section $C - D$ (Figure 17.7H))

17.2.1 Comparison with experimental observations

Several aspects of the incremental strain fields show good resemblance with experimental observations. Figure 17.11 shows incremental deviatoric strain fields (second invariant of strain increments) obtained from an experimental biaxial compression test on a sample of Callovo-Oxfordian claystone under a lateral confinement of 12 MPa [Bésuelle, 2015]. The fields of deviatoric strain increments

for different loading steps are obtained from digital image correlation between photographs taken before and after the loading step [Lanatà, 2015].

Comparing the experimental results with the numerical results presented in the section above, the following observations can be made in both numerical and experimental fields of deviatoric strain increments:

- The deviatoric strain field in the initial (approximately linear) stage of deformation shows no spatial correlation, although a certain heterogeneity is observed as small as the resolution of observation.
- With continuing axial loading, heterogeneity in the form of conjugated bands start to develop well before reaching the peak stress response. This heterogeneity starts to appear at the moment the stress-strain relation becomes non-linear. In the numerical simulations, this non-linearity is the direct effect of interface cohesion softening.
- Towards the peak, some of these bands become inactive while others show increased activity. The most active bands tend to prevail after the stress response peak.
- Just after the peak only a few bands remain active, of which a single band prevails.

The numerical results obtained with the random distribution of the REV orientation indicates that for the accurate modelling of pre-peak heterogeneous deformation with incipient shear bands, the introduction of an additional scale of heterogeneity can be of great importance.

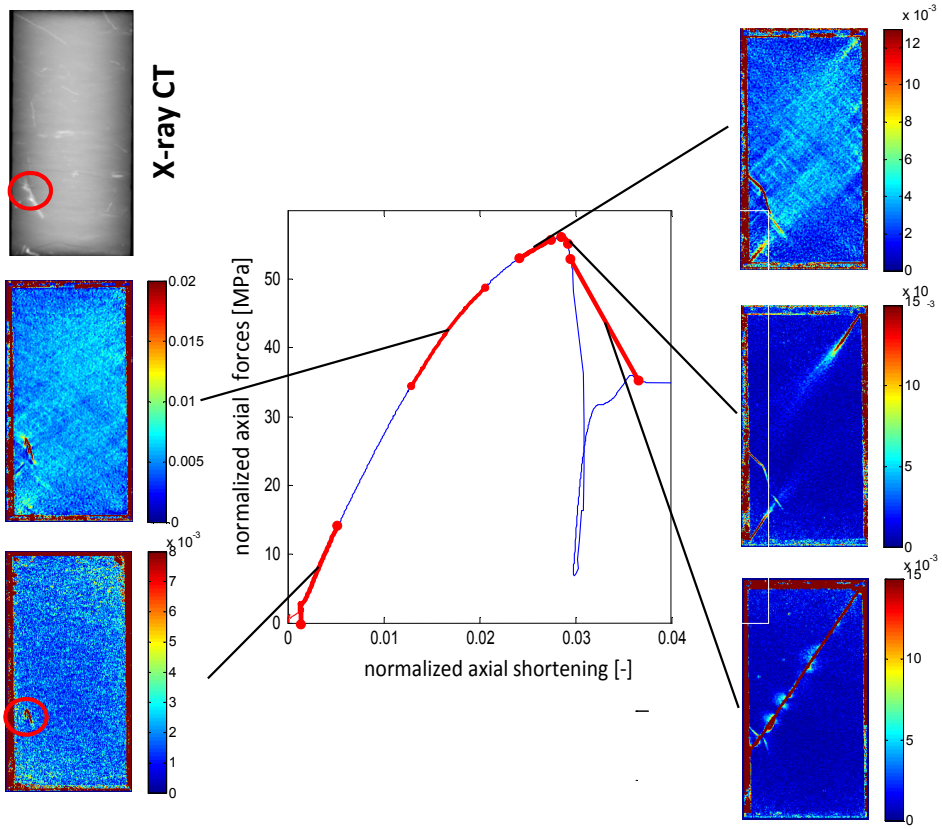

Fig. 17.11: Second invariant of the strain increment . Obtained from digital image correlation of pictures taken during a biaxial compression test on Callovo-Oxfordian claystone at 12 MPa lateral confinement [Bésuelle, 2015]

CONCLUSIONS PART IV

In this Part the developed model was calibrated against the experimental data of available for the Callovo-Oxfordian claystone. Good agreement was obtained with respect to the mechanical properties of material up to the peak response under biaxial/triaxial compression tests, notably for effective Young's modulus, friction angle and cohesion. The model was shown to be capable of reproducing a realistic anisotropy in the peak strength by introducing a weak bedding plane through the preferential direction of grain orientation. However, obtaining perfectly isotropic peak stress responses proves very difficult to obtain with only a limited number of grains in the REV. Nevertheless, anisotropy in the response of the calibrated REV falls within the experimentally observed variation as a combined effect of anisotropy and reproducibility of the experimental test results.

The application of the calibrated model (including the heterogeneity of the grain stiffness for the simulation of inclusions embedded in a clay matrix) in the modelling of biaxial compression of a sample has demonstrated that computational difficulties can prevent an 'advanced' analysis of the post-peak behaviour. Different tools for studying possible instabilities in the macroscale behaviour were demonstrated. Definitive conclusions could not be drawn from these studies, although they gave more insight in the macroscopic complexity of the BVP.

The application of the method in the modelling of gallery excavation problems has demonstrated that the calibrated model does not necessarily reproduce the localization phenomena that were observed in the field. A further investigation into the post-peak behaviour may be required in order to see if fundamental differences in the global material behaviour can explain these discrepancies. The use of a material with a 'conservative' calibration of the material strength was demonstrated to be able to capture the progressive development of shear bands around the gallery. The effect of the post-peak anisotropy, introduced by a combination of material anisotropy and boundary condition orientation, was observed in the shape and orientation of the shear bands. This effect clearly points out the need for a more representative post-peak behaviour.

The application of the model to the simulation of hydromechanical coupling has demonstrated that the build-up and dissipation of (negative) pore pressures can have an important effect on the initiation and progression of both the convergence of the gallery wall and the development of localizations of deformation. The evolution of the hydraulic conductivity is found to be relatively low due to the remaining contact between the grains, which prevents the development of continuous percolation paths through the entire REV. This can be seen as a strong effect of the microscale modelling in 2D.

The introduction of a random distribution of initial REV orientation shows that isotropy can be restored by randomly distributing the orientation-dependent effects of the material anisotropy and the periodic frame. This effect also restored the unpredictability of developing shear bands as the anisotropy no longer con-

strains the reflection of shear bands at the top and the bottom of the domain. The introduction of an intermediate scale of heterogeneity, although directly defined by the finite element dimensions, allows the initiation of multiple localizations of deformation in the post-peak regime of biaxial compression tests, showing good resemblance with experimental observations.

Part V

CONCLUSIONS

Several novelties were presented in this work on the development, implementation and application of a finite element squared (FE^2) model for hydromechanical coupling: An existing microscale model for hydromechanical coupling [Frey, 2010] was modified in order to meet the requirements of consistent computational homogenization. This modified model was used to fill a representative elementary volume (REV) for modelling the local hydromechanical behaviour of a poromechanical continuum at the macroscale. The macroscale response to kinematical loading of this REV was used to provide a numerical constitutive relation and was implemented in a finite element code, coupled to an existing locals second gradient model for hydromechanical coupling Collin et al. [2006]. For this purpose the method of computational homogenization by static condensation was extended to the case of hydromechanical coupling to obtain the consistent tangent operator that relates a variation of the kinematics to a variation of the homogenized response. A simple algorithm was then developed for generating periodic microstructures for a given set of grain shape characteristics. These characteristics were used to calibrate the modified microscale model to the Callovo-Oxfordian claystone, after which the calibrated model was applied in the doublescale numerical simulation of the excavation damaged zone around a gallery excavation, taking into account hydromechanical coupling. The ability to model strain localization effects in was demonstrated in both academic examples and a (simplified) engineering problem.
This Part gives the concluding summary of the work on these contributions and gives in indications for further studies and improvements.

First order computational homogenization by static condensation, commonly used for upscaling in purely mechanical micro-macro computations, was extended in this work to the framework of hydromechanical coupling and formulated to meet the specific characteristics of the micromechanical model. Developments have been detailed for the specific microscale model, although the general approach and formulation can be used for other steady-state microscale models for hydromechanical coupling. Performance tests have demonstrated that the numerical accuracy of this method in the macroscale Newton-Raphson iteration for solving the macroscale nonlinear problem is of the same quality as that of its numerical alternative of finite difference approximations by numerical perturbation. Both theoretical and practical examples have demonstrated a significant gain in computational efficiency.

The developed extension of computational homogenization for hydromechanical coupling was implemented as an independent constitutive relation for local hydromechanical coupled behaviour in a finite element code. The use of the model in combination with a local second gradient constitutive law in a HM-coupled finite element formulation has allowed the modelling of strain localization without mesh dependency.

A micromechanical material description with discontinuous grains and interfaces was used to fill up a REV to provide a computationally homogenized constitutive relation for a macroscale poro-mechanical continuum description. The formulation of the mixture theory of hydromechanical coupling in the poromechanical continuum at the macroscale, which in a classical formulation makes use of a phenomenological expression of the behaviour of the mixture of both the solid and the fluid phase, is now obtained by modelling the solid and and fluid

phases separately at the microscale and using the homogenization of the response to kinematical variations to obtain the constitutive relations. By this approach the poromechanical formulation of the macroscale hydromechanical coupling is obtained in a natural way and the description can therefore be based on physical considerations of micromechanical interactions between the solid and fluid phase rather than expressing the the hydromechanical coupling by phenomenological laws. The evolution of pore space (leading to fluid storage) and permeability as an effect of (micromechanical) deformation is controlled by the mechanical part of the REV, as the pore channel network evolves under deformation of the REV. This gives the means of modelling the anisotropic evolution of permeability as a response to material deformation, based on specific configuration of the material microstructure.

Examples have demonstrated that enforced deformation of the REV can lead to an evolution of the hydraulic properties by means of a traceable evolution of the pore channel network. The physical changes in the pore channel network form the basis of the alteration of the fluid system of equations.

Although diffusive flow in the grains has been introduced to take into account transport of fluid mass through the clay matrix, the main advantage of the presented model is the ability of modelling hydromechanical coupling based on the interaction between solid and fluid phases rather than modelling a poromechanical mixture. For the modelling of fluid transport through the (undamaged) clay matrix, the diffusive flow model has to be interpreted as the homogenized result of the underlying microstructure of clay particles and platelets. As the microstructure of the clay matrix is defined at a smaller scale than the microstructure of the embedded inclusions, the clay matrix microstructure should either be taken into account by separate REVs at a smaller scale (introducing a third scale to take into account) or by a phenomenological law to represent the homogenized effects of the microstructure on the (coupled) hydromechanical behaviour. As the introduction of a third level of computations is unrealistic, the latter option is chosen and a (uncoupled) description of a continuum with hydromechanical behaviour is used to represent the homogenized behaviour of the clay matrix.

The approach of modelling the material as an assembly of grains that can interact at their interfaces allows (in addition to a natural way of obtaining hydromechanical coupling in a poromechanical continuum formulation) the introduction of anisotropy in the mechanical behaviour based on the geometry of the grains that form the microstructure. Although a further specification of anisotropy would be possible by a variation of microscale constitutive relations, it was shown that anisotropy in (initial) macroscale stiffness, peak strength and softening response can be obtained by a variation of the average grain size and shape only. However, the anisotropy introduced by the material interferes with the anisotropy introduced by the periodic frame in case of softening behaviour. First by the constraint of the low number of possible localizations passing the REV boundaries (in case of REVs with a low number of grains) and later by the periodic frame effect through the orientation of the periodic constraints on possible microscale localizations of interface damage.

The application of the microscale model has demonstrated that the basic geometrical distributions of the spaces of the inclusions can be easily reproduced by means of a Voronoï-based microstructure and that REVs of restricted complexity

can be calibrated against experimental data with respect to post-peak stiffness and peak strength. This reproduction of the basic geometrical characteristics of inclusions is of importance for the model to be useful in sensitivity analysis of the material model and the influence of the variation of these characteristics could be obtained by numerical simulations.

The doublescale modelling approach was successfully applied in doublescale simulations of biaxial compression tests in both purely mechanical and hydromechanical formulations. Although the micromechanical constitutive relations, the microstructure in the REV and the macroscale boundary value problem were relatively limited in complexity, the results serve as a good proof of concept for the application of the finite element squared method for hydromechanical coupling to academic problems. Its application to the modelling of gallery excavations has demonstrated that the method can be applied to engineering problems when a good balance between microstructural detail and computational efficiency is taken into account, although the increased computational cost introduced by the microscale computations remains an issue. With respect to the computational cost it must be noted that significant reduction in net computation time can be made in case (massively) parallel computation is implemented. As the REV boundary value problem has to be solved for each macroscale integration point individually, the FE^2 method is very suitable for parallel processing.

The simulation of the gallery excavations has demonstrated that localized strain response around the gallery is not evidently obtained with the microscale model calibrated against experimental data, indicating that certain characteristics of the material behaviour are not properly simulated and further development of the model (on the microscale model as well as the doublescale framework) is required. For future applications and development of the method, the following points need consideration: Both the size and the orientation of the periodic boundaries of the REV were statistically demonstrated to have an influence on the post-peak behaviour, making the periodicity of the boundary conditions an inherent property of the constitutive behaviour as soon as the periodicity of the material is lost. This is one of the consequences of maintaining a continuum description in the post-peak regime of deformation, and a sound way of maintaining a continuum approach is not readily available: Coupling between a microscale with discontinuous microstructure and a macroscale poro-mechanical continuum in the post-peak domain without relying on additional constraints such as the (artificial) regularization by the periodic boundary conditions remains a major challenge in the fully consistent application of the presented doublescale approach. In the meantime, the periodic boundary conditions are used as the regularization of the micromechanical behaviour. For further development of the method, the following points can be formulated to serve as recommendations:

- A first point is to assess the issue of post-localized dependency of the REV response on the periodic boundary conditions. A consistent and objective way of maintaining the continuum approach is required for a proper use with the second gradient model. A certain enhancement will be required for this purpose, replacing the boundary conditions as a method for local regularization.

- For a certain phenomenon (either mechanical or hydraulic) to be present in the macroscale behaviour, a micromechanical process must be present to locally initiate these phenomena at the microscale. Plasticity in the macroscale response was given as an example of these phenomena, for which the introduction of a plasticity model at the interfaces was suggested instead. In analogy with this example, additional characteristics of the material behaviour need to be represented at the microscale and the microscale constitutive relations should be modified to take these effects into account.

- It was demonstrated that the doublescale modelling of localizations around gallery excavations can be obtained with the presented model. It is clear that the given examples do not contain the required level of detail at the macroscale due to restrictions with respect to the mesh size and that the micromechanical model gives a too strong variability with orientation. A pragmatic approach for more realistic results would be to increase the number of elements at the macroscale and the complexity of the REV at the microscale. This will have consequences on the computational load and asks for a more time-efficient architecture of the code. In a first stage, this can be obtained by a parallelization of the computations of the boundary value problems on the individual REVs. Other approaches that can reduce the total computational cost without such as adaptive remeshing, a combination with reduced-basis methods, or the combination of the doublescale model with a phenomenological model in regions of lower degrees of deformation.

- For a more progressive evolution of the permeability under material deformation, the incorporation of additional effects that better capture the three-dimensional nature of the development of connected pore channels is required. These effects need to account for connected interface openings throughout the REV, which currently are prevented due to the normal grain contacts. The change from 2D to 3D in the formulation of the REVs might contribute to the more realistic representation of the model, although this will have a major impact on he computational load of the REV boundary value problem, both through the increase in the number of degrees of freedom and the interconnectivity of these degrees of freedom, which reduces the sparseness of the systems of equations to be solved.

BIBLIOGRAPHY

E. Alonso, L. R. Alejano, F. Varas, G. Fdez-Manin and C. Carranza-Torres. Ground response curves for rock masses exhibiting strain-softening behaviour. *International Journal for Numerical and Analytical Methods in Geomechanics*, 27(13):1153–1185, 2003. ISSN 1096-9853. URL `http://dx.doi.org/10.1002/nag.315`. [Cited on page 193]

F. Alonso-Marroquín, S. Luding, H. J. Herrmann and I. Vardoulakis. Role of anisotropy in the elastoplastic response of a polygonal packing. *Phys. Rev. E*, 71:051304, May 2005. URL `http://dx.doi.org/10.1103/PhysRevE.71.051304`. [Cited on page 126]

Andra. Dossier 2005 argile : Synthèse : Evolution phénoménologique du stockage géologique. Technical report, ANDRA, France, 2005a. [Cited on page 3, 8, 9, 153, 187]

Andra. Dossier 2005 referentiel du site meuse/haute-marne tome 2. Technical report, ANDRA, France, 2005b. [Cited on page 3, 9]

Andra. Synthèse Générale du Programme 2007-2011 du Groupement de Laboratoire Géomécanique. Report Andra no C.RP.AMFS.11.0066. Technical report, ANDRA, France, 2011. [Cited on page 8]

Andra. Action Modèles transverse au GL Géomécanique et au Programme de simulation de l'Andra (UPS4) - Phase 3: modélisation des ouvrages. CG.RP.AMFS.13.0031. Technical report, ANDRA, France, 2013. [Cited on page xi, 8, 9, 157, 158, 193]

S. Andrieux, Y. Bamberger and J.J Marigo. Un modèle de matériaux microfissurés pour les roches et les bétons. *J. Méc. Théor. Appl.*, 5:471 – 513, 1986. [Cited on page 13]

G. Armand, A. Noiret, J. Zghondi and D.M. Seyedi. Short- and long-term behaviors of drifts in the Callovo-Oxfordian claystone at the Meuse/Haute-Marne Underground Research Laboratory. *Journal of Rock Mechanics and Geotechnical Engineering*, 5(3):221 – 230, 2013. URL `http://dx.doi.org/10.1016/j.jrmge.2013.05.005`. [Cited on page 157]

G. Armand, F. Leveau, C. Nussbaum, R. de la Vaissiere, A. Noiret, D. Jaeggi, P. Landrein and C. Righini. Geometry and properties of the excavation-induced fractures at the meuse/haute-marne url drifts. *Rock Mechanics and Rock Engineering*, 47(1):21–41, 2014. URL `http://dx.doi.org/10.1007/s00603-012-0339-6`. [Cited on page xi, xix, 9, 10, 11, 12, 196]

C. Arson and B. Gatmiri. A mixed damage model for unsaturated porous media. *Comptes Rendus Mécanique*, 337(2):68 – 74, 2009. ISSN 1631-0721. URL http://dx.doi.org/10.1016/j.crme.2009.03.005. [Cited on page 13]

C. Auvray. Essais géomécaniques, ouvrage EST361, laboratoire de recherche souterrain meuse/haute-marne. report andra no c.rp.0eng.04.0500. Technical report, ANDRA, France, 2011. [Cited on page 8]

J. Bai. *A homogenization based continuum plasticity-damage model for ductile fracture of materials containing heterogeneities*. PhD thesis, The Ohio State University, 2008. [Cited on page 15]

F. Barbe, L. Decker, D. Jeulin and G. Cailletaud. Intergranular and intragranular behavior of polycrystalline aggregates. part 1: F.E. model. *International Journal of Plasticity*, 17(4):513 – 536, 2001a. URL http://dx.doi.org/10.1016/S0749-6419(00)00061-9. [Cited on page 125, 126]

F. Barbe, S. Forest and G. Cailletaud. Intergranular and intragranular behavior of polycrystalline aggregates.part 2: Results. *International Journal of Plasticity*, 17(4):537 – 563, 2001b. URL http://dx.doi.org/10.1016/S0749-6419(00)00062-0. [Cited on page 125]

I. Benedetti and M.H. Aliabadi. A three-dimensional cohesive-frictional grain-boundary micromechanical model for intergranular degradation and failure in polycrystalline materials. *Computer Methods in Applied Mechanics and Engineering*, 265(0):36 – 62, 2013. URL http://dx.doi.org/10.1016/j.cma.2013.05.023. [Cited on page 126]

A. Bensoussan, J-L. Lions and G. Papanicolaou. In *Asymptotic Analysis for Periodic Structures*, volume 5 of *Studies in Mathematics and Its Applications*, pages ii – iii. Elsevier, 1978. URL http://dx.doi.org/10.1016/S0168-2024(08)70192-9. [Cited on page xxvii]

P. Bésuelle. personal communication, 2014. [Cited on page xi, 7]

P. Bésuelle. personal communication, 2015. [Cited on page xvii, 205, 207]

P. Bésuelle and J.W. Rudnicki. Localization: shear bands and compaction bands. *International Geophysics*, 89:219–321, 2003. [Cited on page 177]

P. Bésuelle, R. Chambon and F. Collin. Switching deformation modes in post-localization solutions with a quasibrittle material. *J. Mech. Mat. Str.*, 1:1115 – 1134, 2006. URL http://dx.doi.org/10.2140/jomms.2006.1.1115. [Cited on page 16, 20]

P. Bésuelle, G. Viggiani, N. Lenoir, J. Desrues and M. Bornert. X-ray micro ct for studying strain localization in clay rocks under triaxial compression. In *Advances in X-ray Tomography for Geomaterials*, pages 35–53. ISTE, 2010. ISBN 9780470612187. doi: 10.1002/9780470612187.ch2. URL http://dx.doi.org/10.1002/9780470612187.ch2. [Cited on page 7]

G. Bilbie. *Modélisation multi-échelle de l'endommagement et de la rupture dans les milieux (quasi-) fragiles*. PhD thesis, Université Joseph Fourier - Grenoble 1, 2007. [Cited on page 31]

G. Bilbie, C. Dascalu, R. Chambon and D. Caillerie. Micro-fracture instabilities in granular solids. *Acta Geotechnica*, 3(1):25–35, 2008. URL http://dx.doi.org/10.1007/s11440-007-0046-8. [Cited on page xxix, 34, 129]

M.A. Biot. General theory of threedimensional consolidation. *Journal of Applied Physics*, 12(2):155–164, 1941. URL http://dx.doi.org/10.1063/1.1712886. [Cited on page 112]

J. Bonet and R. D. Wood. *Nonlinear continuum mechanics for finite element analysis*. Cambridge University Press, 2000. ISBN 0 521 57272 X. [Cited on page 140]

M. Bornert, F. Valès, H. Gharbi and D. Nguyen Minh. Multiscale full-field strain measurements for micromechanical investigations of the hydromechanical behaviour of clayey rocks. *Strain*, 46(1):33–46, 2010. ISSN 1475-1305. URL http://dx.doi.org/10.1111/j.1475-1305.2008.00590.x. [Cited on page 7]

E. Brown, J. Bray, B. Ladanyi and E. Hoek. Ground response curves for rock tunnels. *Journal of Geotechnical Engineering*, 109(1):15–39, 1983. doi: 10.1061/(ASCE)0733-9410(1983)109:1(15). URL http://dx.doi.org/10.1061/(ASCE)0733-9410(1983)109:1(15). [Cited on page 193]

S. Cariou, L. Dormieux and F. Skoczylas. An original constitutive law for callovo-oxfordian argillite, a two-scale double-porosity material. *Applied Clay Science*, 80 - 81(0):18 – 30, 2013. URL http://dx.doi.org/10.1016/j.clay.2013.05.003. [Cited on page 13]

R. Chambon. Numerical methods in non linear continuum mechanics. *Lecture notes, Laboratoire 3S-R Grenoble Université Joseph Fourier, Institut National Polytechnique, CNRS UMR 5521, Grenoble, France*, 2008. [Cited on page 67]

R. Chambon and D. Caillerie. Existence and uniqueness theorems for boundary value problems involving incrementally non linear models. *International Journal of Solids and Structures*, 36(33):5089 – 5099, 1999. ISSN 0020-7683. URL http://dx.doi.org/10.1016/S0020-7683(98)00212-1. [Cited on page 171, 174, 175]

R. Chambon, D. Caillerie and N. El Hassan. One-dimensional localisation studied with a second grade model. *European Journal of Mechanics - A/Solids*, 17 (4):637 – 656, 1998. ISSN 0997-7538. URL http://dx.doi.org/10.1016/S0997-7538(99)80026-6. [Cited on page 17]

R. Chambon, D. Caillerie and T. Matsuchima. Plastic continuum with microstructure, local second gradient theories for geomaterials: localization studies. *International Journal of Solids and Structures*, 38(46–47):8503 – 8527, 2001. URL http://dx.doi.org/10.1016/S0020-7683(01)00057-9. [Cited on page xxviii, xxix, 16]

R. Charlier. *Approche unifiée de quelques problémes non linéaires de mécanique des milieux continus par la méthode des éléments finis (grandes déformations des métaux et des sols, contact unilatéral de solides, conduction thermique et écoulements en milieu poreux)*. PhD thesis, Université de Liège, Belgium, 1987. [Cited on page xxviii, 85]

R. Charlier, F. Collin, B. Pardoen, J. Talandier, J-P. Radu and P. Gérard. An unsaturated hydro-mechanical modelling of two in-situ experiments in callovo-oxfordian argillite. *Engineering geology*, 165:46–63, 2013. [Cited on page 13]

E.W.C. Coenen, V.G. Kouznetsova and M.G.D. Geers. Novel boundary conditions for strain localization analyses in microstructural volume elements. *Int. J. for Num. Meth. in Eng.*, 90:1 – 21, 2011a. [Cited on page 15]

E.W.C. Coenen, V.G. Kouznetsova and M.G.D. Geers. Enabling microstructure-based damage and localization analyses and ubscaling. *Modelling Simul. Mater. Sci. Eng.*, 19:1 – 15, 2011b. [Cited on page 15]

F. Collin, R. Chambon and R. Charlier. A finite element method for poro mechanical modelling of geotechnical problems using local second gradient models. *International Journal for Numerical Methods in Engineering*, 65(11):1749–1772, 2006. URL `http://dx.doi.org/10.1002/nme.1515`. [Cited on page i, iv, xxviii, xxix, 18, 19, 27, 213]

E. Cuthill and J. McKee. Reducing the bandwidth of sparse symmetric matrices. In *Proceedings of the 1969 24th National Conference*, ACM '69, pages 157–172, New York, NY, USA, 1969. ACM. URL `http://doi.acm.org/10.1145/800195.805928`. [Cited on page 89, 140]

J. Desrues and R. Chambon. Shear band analysis for granular materials: The question of incremental non-linearity. *Ingenieur-Archiv*, 59(3):187–196, 1989. ISSN 0020-1154. doi: 10.1007/BF00532249. URL `http://dx.doi.org/10.1007/BF00532249`. [Cited on page 171]

L. Dormieux, A. Molinari and D. Kondo. Micromechanical approach to the behavior of poroelastic materials. *Journal of the Mechanics and Physics of Solids*, 50 (10):2203 – 2231, 2002. ISSN 0022-5096. URL `http://dx.doi.org/10.1016/S0022-5096(02)00008-X`. [Cited on page 13]

L. Dormieux, D. Kondo and F-J. Ulm. A micromechanical analysis of damage propagation in fluid-saturated cracked media. *Comptes Rendus Mécanique*, 334 (7):440 – 446, 2006. doi: http://dx.doi.org/10.1016/j.crme.2006.05.007. [Cited on page 13]

A.P. van den Eijnden, F. Collin, P. Bésuelle and R. Chambon. A double-scale modelling approach for hydromechanical coupling. *Proceedings of the Third International Conference on Computational Geomechanics, COMGEO III*, 183: 309–330, 2013. [Cited on page 251]

J. D. Eshelby. The determination of the elastic field of an ellipsoidal inclusion, and related problems. *Proceedings of the Royal Society of London A: Mathematical, Physical and Engineering Sciences*, 241(1226):376–396, 1957. ISSN 0080-4630. URL `http://dx.doi.org/10.1098/rspa.1957.0133`. [Cited on page xxvii]

F. Feyel and J-L. Chaboche. FE^2 multiscale approach for modelling the elastovis-coplastic behaviour of long fibre sic/ti composite materials. *Computer Methods in Applied Mechanics and Engineering*, 183(3-4):309 – 330, 2000. URL `http://dx.doi.org/10.1016/S0045-7825(99)00224-8`. [Cited on page xxvii, 14, 68]

B. François, V. Labiouse, A. Dizier, F. Marinelli, R. Charlier and pages=71-86 language=English Collin, F. Hollow cylinder tests on boom clay: Modelling of strain localization in the anisotropic excavation damaged zone. *Rock Mechanics and Rock Engineering*, 47(1), 2014. ISSN 0723-2632. URL http://dx.doi.org/10.1007/s00603-012-0348-5. [Cited on page 184]

J. Frey. *Modélisation multi-échelle de l'endommagement hydroméchanique des roches argileuses*. PhD thesis, Université de Grenoble, 2010. [Cited on page i, iii, xxviii, xxix, xxx, 20, 23, 24, 27, 31, 52, 213, 245, 254]

J. Frey, R. Chambon and C. Dascalu. A two-scale poromechanical model for cohesive rocks. *Acta Geotechnica*, 8(2):107–124, 2013. doi: 10.1007/s11440-012-0173-8. URL http://dx.doi.org/10.1007/s11440-012-0173-8. [Cited on page xi, 20, 22, 245]

F. Fritzen, T. Böhlke and E. Schnack. Periodic three-dimensional mesh generation for crystalline aggregates based on Voronoï tessellations. *Computational Mechanics*, 43(5):701–713, 2009. URL http://dx.doi.org/10.1007/s00466-008-0339-2. [Cited on page 126]

M.G.D. Geers, V.G. Kouznetsova and W.A.M. Brekelmans. Multi-scale computational homogenization: Trends and challenges. *Journal of Computational and Applied Mathematics*, 234(7):2175 – 2182, 2010. URL http://dx.doi.org/10.1016/j.cam.2009.08.077. [Cited on page 15, 69]

P. Germain. La méthode des puissances virtuelles en mécanique des milieux continus. *J. Mécanique*, 12:235–274, 1973. [Cited on page 16, 17, 33]

S. Ghosh, J. Bai and P. Raghavan. Concurrent multi-level model for damage evolution in microstructurally debonding composites. *Mechanics of Materials*, 39(3):241 – 266, 2007. URL http://dx.doi.org/10.1016/j.mechmat.2006.05.004. [Cited on page 15]

I.M. Gitman, H. Askes and L.J. Sluys. Representative volume: Existence and size determination. *Engineering Fracture Mechanics*, 74(16):2518 – 2534, 2007. ISSN 0013-7944. URL http://dx.doi.org/10.1016/j.engfracmech.2006.12.021. [Cited on page 34, 125]

G. Gudehus. A comparison of some constitutive laws for soils under radially symmetric loading and unloading. *Proceedings of 3rd Int. Conf. on Numerical Methods in Geomechanics*, pages 1309 – 1323, 1979. [Cited on page 168]

R. Hill. A general theory of uniqueness and stability in elastic-plastic solids. *Journal of the Mechanics and Physics of Solids*, 6(3):236 – 249, 1958. ISSN 0022-5096. URL http://dx.doi.org/10.1016/0022-5096(58)90029-2. [Cited on page 175]

R. Hill. Elastic properties of reinforced solids: Some theoretical principles. *Journal of the Mechanics and Physics of Solids*, 11(5):357 – 372, 1963. URL http://dx.doi.org/10.1016/0022-5096(63)90036-X. [Cited on page 34]

R. Hill. A self-consistent mechanics of composite materials. *Journal of the Mechanics and Physics of Solids*, 13:213 – 222, 1965. [Cited on page xxvii, 14, 62]

E. Hoek and E.T. Brown. Practical estimates of rock mass strength. *International Journal of Rock Mechanics and Mining Sciences*, 34(8):1165 – 1186, 1997. URL http://dx.doi.org/10.1016/S1365-1609(97)80069-X. [Cited on page 9]

E. Hoek, C. Carranza-Torres and B. Corkum. Hoek-brown failure criterion-2002 edition. *Proceedings of NARMS-Tac*, pages 267–273, 2002. [Cited on page 9]

R. Jänicke, S. Diebels, H-G. Sehlhorst and A. Düster. Two-scale modelling of micromorphic continua. *Continuum Mechanics and Thermodynamics*, 21(4):297–315, 2009. URL http://dx.doi.org/10.1007/s00161-009-0114-4. [Cited on page 15]

R. Jänicke, B. Quintal and H. Steeb. Numerical homogenization of mesoscopic loss in poroelastic media. *European Journal of Mechanics - A/Solids*, 49(0): 382 – 395, 2015. ISSN 0997-7538. URL http://dx.doi.org/10.1016/j.euromechsol.2014.08.011. [Cited on page 16]

D. Kolymbas. An outline of hypoplasticity. *Archive of Applied Mechanics*, 61(3), 1991. [Cited on page 13]

V. Kouznetsova, W. A. M. Brekelmans and F. P. T. Baaijens. An approach to micro-macro modeling of heterogeneous materials. *Computational Mechanics*, 27(1):37–48, 2001. URL http://dx.doi.org/10.1007/s004660000212. [Cited on page i, iii, xxvii, xxviii, xxix, 14, 31, 69]

V. Kouznetsova, M. G. D. Geers and W. A. M. Brekelmans. Multi-scale constitutive modelling of heterogeneous materials with a gradient-enhanced computational homogenization scheme. *International Journal for Numerical Methods in Engineering*, 54(8):1235–1260, 2002. ISSN 1097-0207. doi: 10.1002/nme.541. URL http://dx.doi.org/10.1002/nme.541. [Cited on page 15]

V.G. Kouznetsova, M.G.D. Geers and W.A.M. Brekelmans. Multi-scale second-order computational homogenization of multi-phase materials: a nested finite element strategy. *Comp. Methode Appl. Mech. Engg*, 193:5525–5550, 2004. [Cited on page 15]

M. G. Kulkarni, K. Matous and P. H. Geubelle. Coupled multi-scale cohesive modeling of failure in heterogeneous adhesives. *International Journal for Numerical Methods in Engineering*, 84(8):916–946, 2010. URL http://dx.doi.org/10.1002/nme.2923. [Cited on page 15]

Patrizia Lanatà. *Full-field experimental characterization of mechanical behaviour and failure in a porous rock in plane strain compression: homogeneous deformation and strain localization.* PhD thesis, Université de Grenoble, 2015. [Cited on page 206]

K. Lee and S. Ghosh. Multiple scale analysis of heterogeneous elastic structures using homogenization theory and Voronoï cell finite element method. *International Journal for Solids and Structures*, 32:27–62, 1995. [Cited on page xxvii, 14, 126]

K. Lee and S. Ghosh. Small deformation multi-scale analysis of heterogeneous materials with the Voronoï cell finite element model and homogenization theory. *Computational Material Sciences*, 7:131–146, 1996. [Cited on page xxvii, 14]

Y-K. Lee and S. Pietruszczak. A new numerical procedure for elasto-plastic analysis of a circular opening excavated in a strain-softening rock mass. *Tunnelling and Underground Space Technology*, 23(5):588 – 599, 2008. URL http://dx.doi.org/10.1016/j.tust.2007.11.002. [Cited on page 193]

N. Lenoir, M. Bornert, J. Desrues, P. Bésuelle and G. Viggiani. Volumetric digital image correlation applied to x-ray microtomography images from triaxial compression tests on argillaceous rock. *Strain*, 43(3):193–205, 2007. URL http://dx.doi.org/10.1111/j.1475-1305.2007.00348.x. [Cited on page 7]

D.J. Luscher, D.L. McDowell and C.A. Bronkhorst. A second gradient theoretical framework for hierarchical multiscale modeling of materials. *International Journal of Plasticity*, 26(8):1248 – 1275, 2010. ISSN 0749-6419. URL http://dx.doi.org/10.1016/j.ijplas.2010.05.006. Special Issue In Honor of Lallit Anand. [Cited on page 15]

J. Mandel. Plasticité classique et viscoplasticité. *CISM lecture notes*, 97, 1972. [Cited on page 14, 62]

F. Marinelli. *Comportement couplé des géomatériaux: deux approches de modélisation numérique*. PhD thesis, Université de Grenoble, 2013. [Cited on page xxix, 24, 31, 68, 69, 111, 245]

F. Marinelli, Y. Sieffert and R. Chambon. Hydromechanical modeling of an initial boundary value problem: Studies of non-uniqueness with a second gradient continuum. *International Journal of Solids and Structures*, 54(0):238 – 257, 2015. ISSN 0020-7683. URL http://dx.doi.org/10.1016/j.ijsolstr.2014.10.012. [Cited on page 184, 189]

T. J. Massart, R. H. J. Peerlings and M. G. D. Geers. An enhanced multi-scale approach for masonry wall computations with localization of damage. *International Journal for Numerical Methods in Engineering*, 69(5):1022–1059, 2007. URL http://dx.doi.org/10.1002/nme.1799. [Cited on page 15]

T.J. Massart and A.P.S. Selvadurai. Stress-induced permeability evolution in a quasi-brittle geomaterial. *Journal of Geophysical Research*, 117:1–15, 2012. [Cited on page 16, 65, 196]

T.J. Massart and A.P.S. Selvadurai. Computational modelling of crack-induced permeability evolution in granite dilatant cracks. *International Journal of Rock Mechanics and Mining Sciences*, 70:593–604, 2014. [Cited on page 16, 65]

T. Matsushima, R. Chambon and D. Caillerie. Large strain finite element analysis of a local second gradient model: application to localization. *Int. J. for Num. Meth. in Eng.*, 54:499–521, 2002. [Cited on page 16, 17, 19]

B.C.N. Mercatoris, T.J. Massart and L.J. Sluys. A multi-scale computational scheme for anisotropic hydro-mechanical couplings in saturated heterogeneous porous media. *In: J.G.M. Van Mier, G. Ruiz, C. Andrade, R.C. Yu and X.X. Zhang (Eds). Proceedings of the VIIIth International Conference on Fracture Mechanics of Concrete and Concrete Structures - FraMCoS-8*, 2014. [Cited on page 16]

C. Miehe and A. Koch. Computational micro-to-macro transitions of discretized microstructures undergoing small strain. *Archive of Applied Mechanics*, 72: 300–317, 2002. [Cited on page 14]

R.D. Mindlin. Micro-structure in linear elasticity. *Archive for Rational Mechnaics and Analysis*, 16:51–78, 1964. [Cited on page 19]

R.D. Mindlin. Second gradient of strain and surface-tension in linear elasticity. *Int. J. of Solids and Structures*, 1:417–438, 1965. [Cited on page 16, 17]

H.B. Muhlhaus and E.C. Alfantis. A variational principle for gradient plasticity. *International Journal of Solids and Structures*, 28(7):845 – 857, 1991. URL `http://dx.doi.org/10.1016/0020-7683(91)90004-Y`. [Cited on page 16]

T.K. Nguyen. *Modélisation multi-échelle des matériaux granulaires frotant-cohésifs*. PhD thesis, Université de Grenoble, 2013. [Cited on page 189]

V.-D. Nguyen and L. Noels. Computational homogenization of cellular materials. *International Journal of Solids and Structures*, 51(11-12):2183 – 2203, 2014. URL `http://dx.doi.org/10.1016/j.ijsolstr.2014.02.029`. [Cited on page 15]

V.D. Nguyen. *Computational homogenization of cellular materials capturing micro-buckling, macro-localization and size effects*. PhD thesis, Université de liège, 2014. [Cited on page 15]

V.P. Nguyen, O. Lloberas-Valls, M. Stroeven and L.J. Sluys. Homogenization-based multiscale crack modelling: From micro-diffusive damage to macro-cracks. *Comput. Methods Appl. Mech. Engrg.*, 200:1220 – 1236, 2011. [Cited on page 15]

H. Niandou, J.F. Shao, J.P. Henry and D. Fourmaintraux. Laboratory investigation of the mechanical behaviour of tournemire shale. *International Journal of Rock Mechanics and Mining Sciences*, 34(1):3 – 16, 1997. URL `http://dx.doi.org/10.1016/S1365-1609(97)80029-9`. [Cited on page 150]

İ Özdemir. *Multi-scale Modelling of Thermal Shock Damage in Refractory Materials*. PhD thesis, Technische Universiteit Eindhoven, 2009. [Cited on page 65]

I. Özdemir, W. A. M. Brekelmans and M. G. D. Geers. Computational homogenization for heat conduction in heterogeneous solids. *International Journal for Numerical Methods in Engineering*, 73(2):185–204, 2008a. URL `http://dx.doi.org/10.1002/nme.2068`. [Cited on page xxviii, xxix, 16, 31]

I. Özdemir, W.A.M. Brekelmans and M.G.D. Geers. FE^2 computational homogenization for the thermo-mechanical analysis of heterogeneous solids. *Comput. Methods Appl. Mech. Engrg.*, 198:602–613, 2008b. [Cited on page 16]

P. Pellenard and J-F. Deconinck. Mineralogical variability of callovo-oxfordian clays from the paris basin and the subalpine basin. *Comptes Rendus Geoscience*, 338(12-13):854 – 866, 2006. URL `http://dx.doi.org/10.1016/j.crte.2006.05.008`. [Cited on page 4]

V. Pensée, D. Kondo and L. Dormieux. Micromechanical analysis of anisotropic damage in brittle material. *J. Eng. Mech.*, 128:889 – 897, 2002. [Cited on page 13]

Q.T. Pham, F. Valès, L. Malinsky, D. Nguyen Minh and H. Gharbi. Effects of desaturation - resaturation on mudstone. *Physics and Chemistry of the Earth, Parts A/B/C*, 32(8-14):646 – 655, 2007. ISSN 1474-7065. URL `http://dx.doi.org/10.1016/j.pce.2006.03.012`. Clay in natural and engineered barriers for radioactive waste confinement - Part 2. [Cited on page 8]

G. Pijaudier-Chabot and Z. Bažant. Nonlocal damage theory. *J. Eng. Mech.*, 113:1512 – 1533, 1987. [Cited on page 16, 17]

W.H. Press, S.A. Teukolsky, W.T. Vetterling and B.P. Flannery. *Numerical Recipes in FORTRAN; The Art of Scientific Computing*. Cambridge University Press, New York, NY, USA, 2nd edition, 1993. ISBN 0521437164. [Cited on page 140]

J-C. Robinet. *Minéralogie, porosité et diffusion dans l' argilite du Callovo-Oxfordien de Bure (Meuse/Haute-Marne,France) de l'échelle centimétrique à micrométrique*. PhD thesis, Université de Poitiers, 2008. [Cited on page iii, 3, 4, 5, 153]

J-C. Robinet, P. Sardini, D. Coelho, J-C. Parneix, D. Prêt, S. Sammartino, E. Boller and S. Altmann. Effects of mineral distribution at mesoscopic scale on solute diffusion in a clay-rich rock: Example of the callovo-oxfordian mudstone (Bure, France). *Water Resources Research*, 48(5), 2012. ISSN 1944-7973. URL `http://dx.doi.org/10.1029/2011WR011352`. [Cited on page i, xi, xv, xix, 4, 5, 6, 7, 153, 155, 156]

P. Royis and T. Doanh. Theoretical analysis of strain response envelopes using incrementally non-linear constitutive equations. *Int. Journ. Num. Anal. Methods in Geomechanics*, 22:97–132, 1998. [Cited on page 168]

J.W. Rudnicki and J.R. Rice. Conditions for the localization of deformation in pressure-sensitive dilatant materials. *Journal of the Mechanics and Physics of Solids*, 23(6):371 – 394, 1975. URL `http://dx.doi.org/10.1016/0022-5096(75)90001-0`. [Cited on page 171, 177]

E. Sanchez-Palencia. Non-homogeneous media and vibration theory. *Lecture notes in Physics*, 127:45 – 128, 1980. [Cited on page xxvii]

J. Schröder. A numerical two-scale homogenization scheme: the FE^2–method. In *Plasticity and Beyond*, volume 550, pages 1–64. Springer, 2014. [Cited on page 14]

J.F. Shao, Y. Jia, D. Kondo and A.S. Chiarelli. A coupled elastoplastic damage model for semi-brittle materials and extension to unsaturated conditions. *Mechanics of Materials*, 38(3):218 – 232, 2006. URL `http://dx.doi.org/10.1016/j.mechmat.2005.07.002`. [Cited on page 13]

Y. Sieffert, S. Al Holo and R. Chambon. Loss of uniqueness of numerical solutions of the borehole problem modelled with enhanced media. *International Journal of Solids and Structures*, 46(17):3173 – 3197, 2009. URL `http://dx.doi.org/10.1016/j.ijsolstr.2009.04.014`. [Cited on page 184]

R. J. M. Smit, W. A. M. Brekelmans and H. E. H. Meijer. Prediction of the mechanical behavior of nonlinear heterogeneous systems by multi-level finite element modeling. *Comput. Methods Appl. Mech. Eng.*, 155:181 – 5192, 1998. [Cited on page 14]

B. Sonon, B. François and T.J. Massart. A unified level set based methodology for fast generation of complex microstructural multi-phase {RVEs}. *Computer Methods in Applied Mechanics and Engineering*, 223-224(0):103 – 122, 2012. URL `http://dx.doi.org/10.1016/j.cma.2012.02.018`. [Cited on page 126]

F. Su, F. Larsson and K. Runesson. Computational homogenization of coupled consolidation problems in micro-heterogeneous porous media. *Int. J. for Num. Meth. in Eng.*, 88:1198–1218, 2011. [Cited on page 16]

P.M. Suquet. Local and global aspects in the mathematical theory of plasticity. *Plasticity today: modelling, methods and applications*, pages 279–310, 1985. [Cited on page xxvii]

K. Terada, M. Hori, T. Kyoya and N. Kikuchi. Simulation of the multi-scale convergence in computational homogenization approaches. *International Journal of Solids and Structures*, 37(16):2285–2311, 2000. [Cited on page 14, 34]

K. Terzaghi. *Theoretical soil mechanics*. J. Wiley, New York, 1943. [Cited on page 112]

C-F. Tsang, F. Bernier and C. Davies. Geohydromechanical processes in the excavation damaged zone in crystalline rock, rock salt, and indurated and plastic clays in the context of radioactive waste disposal. *International Journal of Rock Mechanics and Mining Sciences*, 42(1):109 – 125, 2005. ISSN 1365-1609. URL `http://dx.doi.org/10.1016/j.ijrmms.2004.08.003`. [Cited on page xxviii]

C. Geuzaine V.-D. Nguyen, E. Béchet and L. Noels. Imposing periodic boundary condition on arbitrary meshes by polynomial interpolation. *Computational Materials Science*, 55:390–406, 2012. URL `http://dx.doi.org/10.1016/j.commatsci.2011.10.017`. [Cited on page 34]

O. van der Sluis, P.J.G. Schreurs, W.A.M. Brekelmans and H.E.H. Meijer. Overall behaviour of heterogeneous elastoviscoplastic materials: effect of microstructural modelling. *Mechanics of Materials*, 32(8):449 – 462, 2000. URL `http://dx.doi.org/10.1016/S0167-6636(00)00019-3`. [Cited on page 14, 34]

F. Varas, E. Alonso, L.R. Alejano and G. Fdez.-Manin. Study of bifurcation in the problem of unloading a circular excavation in a strain-softening material. *Tunnelling and Underground Space Technology*, 20(4):311 – 322, 2005. URL `http://dx.doi.org/10.1016/j.tust.2004.12.003`. [Cited on page 189]

I. Vardoulakis. Shear band inclination and shear modulus of sand in biaxial tests. *International Journal for Numerical and Analytical Methods in Geomechanics*, 4(2):103–119, 1980. URL `http://dx.doi.org/10.1002/nag.1610040202`. [Cited on page 178]

C.V. Verhoosel and M.A. Gutiérrez. Modelling inter- and transgranular fracture in piezoelectric polycrystals. *Engineering Fracture Mechanics*, 76(6):742 – 760, 2009. ISSN 0013-7944. URL http://dx.doi.org/10.1016/j.engfracmech.2008.07.004. Multi-scale analysis of evolving interfaces in (multi) materials Multi-scale Analysis. [Cited on page 126]

P.A. Vermeer and R. de Borst. Non-associated plasticity for soils, concrete and rock. *Heron*, 29(3):1–64, 1984. [Cited on page 13]

L.L. Wang, M. Bornert, E. Héripré, S. Chanchole, A. Pouya and B. Halphen. The mechanisms of deformation and damage of mudstones: A micro-scale study combining esem and dic. *Rock Mechanics and Rock Engineering*, 2014. URL 10.1007/s00603-014-0670-1. [Cited on page 7]

B. Yven, S. Sammartino, Y. Géraud, F. Homand and F. Villieras. Mineralogy, texture and porosity of callovo-oxfordian argillites of the meuse/haute-marne region (eastern paris basin). *Mém. Soc. géol. France*, 178:73–90, 2007. [Cited on page 4, 7, 8]

A. Zervos, P. Papanastasiou and I. Vardoulakis. Modelling of localisation and scale effect in thick-walled cylinders with gradient elastoplasticity. *International Journal of Solids and Structures*, 38(30/31):5081 – 5095, 2001. URL http://dx.doi.org/10.1016/S0020-7683(00)00337-1. [Cited on page 184]

F. Zhang. *Comportement mécanique des argillites de MHM - influences de la saturation, de la composition minéralogique et de la température*. PhD thesis, Université de Lille I, 2011. [Cited on page 8]

O.C. Zienkiewicz and R. L. Taylor. *The finite element method, Fifth edition*. Butterworth-Heinemann, 2000. ISBN 0 7506 5049 4. [Cited on page 140]

APPENDIX

A. REV ROTATION

Between the definition of the macroscale strain state in the form of macroscale deformation gradient tensor $\boldsymbol{F}^M$ and its application in the periodic boundary conditions of the REV, the following corrections are made;

- application of initial REV deformation $\boldsymbol{F}^0$ related to the initial stress state $\boldsymbol{\sigma}^0(\boldsymbol{F}^{M,0} = \boldsymbol{I}) \neq \boldsymbol{0}$.
- the (rate-objective) rotation of the REV with respect to the global axis by angle θ^I
- the decomposition into a symmetric stretch tensor $\boldsymbol{U}^{REV}$ and rotation $\boldsymbol{R}^{REV}$

The different transitions are schematically presented in Figure A.1.

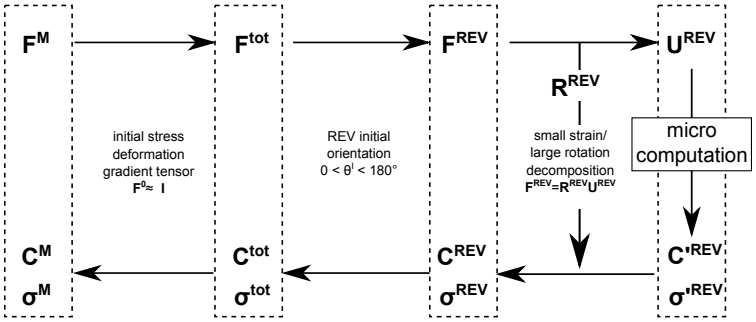

Fig. A.1: Schematic representation of local deformation gradient transformation before application on the REV and the associated stress definitions

In the following three sections, the different operators with respect to deformation gradient tensor $\boldsymbol{F}$, stress tensor $\boldsymbol{\sigma}$ and tangent operator ${}^4\boldsymbol{C}$ are given.

A.1 Initial stress deformation

The initial deformation gradient tensor $\boldsymbol{F}^0$, related to the initial stress state, is taken into account by defining the total deformation gradient $\boldsymbol{F}^{tot}$ as the macroscale deformation applied on the REV in initial state of deformation:

$$F_{ij}^{tot} = F_{ik}^{M} F_{kj}^{0} \tag{A.1}$$

Under the assumption that $\boldsymbol{F}^0 \approx \boldsymbol{I}$, no geometrical correction is required for the transformation of the stress state and

$$\boldsymbol{\sigma}^M \approx \boldsymbol{\sigma}^{tot} \tag{A.2}$$

To be fully consistent in the linearization, the tangent operator is corrected for the initial state of deformation:

$$C^M_{ijkl} = C_{ijkm} F^0_{lm} \tag{A.3}$$

Note: in the main part of this work, the correction for initial stress state was kept out and a direct transformation between $[]^M$ and $[]^R EV$ was made, which corresponds to the case where $\boldsymbol{F}^0 = \boldsymbol{I}$ and $\boldsymbol{\sigma}^0 = \boldsymbol{0}$

A.2 Initial REV rotation

The REV is rotated with respect to the macro scale frame by an initial rotation angle θ^I. For numerical simplicity, not the actual REV is rotated, but the deformation gradient that is enforced on its boundaries. This means a rotated deformation gradient tensor $F^{REV}_{\gamma\delta}$ is defined, corresponding to the rotation of F^{tot}_{kl} by angle θ^I, thereby introducing a reference frame are the macroscale and one at the microscale.

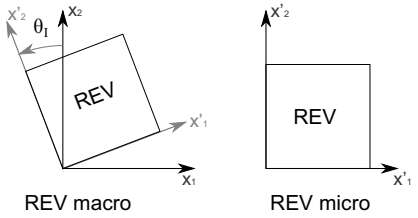

Fig. A.2: REV in the macro coordinate system (left) and the same REV as evaluated in the micro scale (right). The transformation operation is the rotation by angle θ^θ of the enforced deformation (macro to micro) and the same rotation in opposite direction of the resulting stress and tangent stiffness matrix (micro to macro).

Defining a macroscale vector $\vec{z}^M$ and a microscale vector $\vec{z}^{REV}$, the rotation of the deformation is defined by the rotation tensor $\boldsymbol{R}^\theta$ as

$$\vec{z}^M = \boldsymbol{R}^\theta \vec{z}^{REV} \tag{A.4}$$

with

$$\boldsymbol{R} = \begin{bmatrix} \cos(\theta) & -\sin(\theta) \\ \sin(\theta) & \cos(\theta) \end{bmatrix} \tag{A.5}$$

This leads to the following transformation of deormation gradient and stress tensor;

$$\boldsymbol{F}^{REV} = {\boldsymbol{R}^\theta}^T \boldsymbol{F}^{tot} \boldsymbol{R}^\theta \tag{A.6}$$

$$\boldsymbol{\sigma}^M = \boldsymbol{R}^\theta \boldsymbol{\sigma}^{REV} {\boldsymbol{R}^\theta}^T \tag{A.7}$$

Note here that in this rotation the stress is rate-objective, since the rotation $\boldsymbol{R}^\theta$ is constant. This allows a straightforward rotation of the tangent operator:

$$C^{tot}_{ijkl} = R^\theta_{i\alpha} R^\theta_{j\beta} C^{REV}_{\alpha\beta\gamma\delta} R^\theta_{k\gamma} R^\theta_{l\delta} \tag{A.8}$$

A.3 Polar decomposition for small strain-large rotation

A small strain-large rotation assumption is adopted at the micro level in order to avoid difficulties with the continuity of stress state in and around the interfaces. This means that for the evaluation, the macro deformation gradient F_{ij} (formulated in large strain and therefore non-symmetric) is decomposed in a pure rotation R_{ik} and a symmetric stretch U_{kj} according to

$$F_{ij} = R_{ik}U_{kj} \tag{A.9}$$

A variation of the components of the deformation gradient tensor $\boldsymbol{F}$ now becomes

$$\delta F_{ij} = \delta R_{ik}U_{kj} + R_{ik}\delta U_{kj} \tag{A.10}$$

When the stress σ_{ij}^{M} corresponds to the deformation gradient F_{ij} we can define the rotated stress state $\sigma_{ij}^{'REV}$ that corresponds to the stretch U_{ij}. The relation between the two stress states is given by

$$\sigma_{ij}^{REV} = R_{ik}\sigma_{kl}^{'REV}R_{jl} \tag{A.11}$$

and so;

$$\dot{\boldsymbol{\sigma}} = \dot{\boldsymbol{R}}\boldsymbol{\sigma}'\boldsymbol{R}^T + \boldsymbol{R}\dot{\boldsymbol{\sigma}}'\boldsymbol{R}^T + \boldsymbol{R}\boldsymbol{\sigma}'\dot{\boldsymbol{R}}^T \tag{A.12}$$

When we define the tangent moduli

$$C_{ijkl} = \frac{\partial \sigma_{ij}}{\partial F_{kl}} \qquad or \qquad \dot{\sigma}_{ij} = C_{ijkl}\dot{F}_{kl} \tag{A.13}$$

$$C'_{\alpha\beta\gamma\delta} = \frac{\partial \sigma'_{\alpha\beta}}{\partial U_{\gamma\delta}} \qquad or \qquad \dot{\sigma}'_{\alpha\beta} = C'_{\alpha\beta\gamma\delta}\dot{U}_{\gamma\delta} \tag{A.14}$$

we can find the relation between C_{ijkl} and $C'_{\alpha\beta\gamma\delta}$ by several substitutions using the equations above. After some tedious algebra [Mathematica] we find that; ori :

$$C_{ijkl} = R_{i\alpha}R_{j\beta}C'_{\alpha\beta\gamma\delta}\frac{\partial U_{\gamma\delta}}{\partial F_{kl}} - R_{i\beta}\frac{\partial R_{\alpha\beta}}{\partial F_{kl}}\sigma_{\alpha j} - R_{j\beta}\frac{R_{\alpha\beta}}{\partial F_{kl}}\sigma_{\alpha i} \tag{A.15}$$

$$\dot{\boldsymbol{\sigma}} = \left(\frac{\partial \boldsymbol{R}}{\partial \boldsymbol{F}} : \dot{\boldsymbol{F}}\right)\boldsymbol{\sigma}'\boldsymbol{R}^T + \boldsymbol{R}\left[{}^{4}\boldsymbol{C}' : \left(\frac{\partial \boldsymbol{U}}{\partial \boldsymbol{F}} : \dot{\boldsymbol{F}}\right)\right]\boldsymbol{R}^T + \boldsymbol{R}\boldsymbol{\sigma}'\left(\frac{\partial \boldsymbol{R}}{\partial \boldsymbol{F}} : \dot{\boldsymbol{F}}\right)^T \tag{A.16}$$

or:

$$C_{ijkl} = \frac{\partial R_{i\alpha}}{\partial F_{kl}}\sigma'_{\alpha\beta}R_{j\beta} + R_{i\alpha}C'_{\alpha\beta\gamma\delta}\frac{\partial U_{\gamma\delta}}{\delta F_{kl}}R_{j\beta} + R_{i\alpha}\sigma'_{\alpha\beta}\frac{\partial R_{j\beta}}{\partial F_{kl}} \tag{A.17}$$

with:

$$\frac{\partial U_{\gamma\delta}}{\partial F_{kl}} = \frac{1}{I_1}\frac{\partial R_{kl}}{\partial \theta}\left(\left(\delta_{\gamma 2} - \delta_{\gamma 1}\right)\delta_{\gamma\delta}U_{12} + (1 - \delta_{\gamma\delta})(\delta_{l2}U_{11} - \delta_{l1}U_{22})\right) + \delta_{\gamma l}\delta_{\delta l}R_{kl}$$

(A.18)

scratch

$$\frac{\partial U_{\gamma\delta}}{\partial F_{kl}} = \frac{1}{I_1}\frac{\partial R_{kl}}{\partial \theta}\left(\left(\delta_{\gamma 2} - \delta_{\gamma 1}\right)\delta_{\gamma\delta}U_{12} + (1-\delta_{\gamma\delta})(\delta_{l2}U_{11} - \delta_{l1}U_{22})\right) + \delta_{\gamma l}\delta_{\delta l}R_{kl} \tag{A.19}$$

and

$$\frac{\partial R_{i\alpha}}{\partial F_{kl}} = \frac{1}{I_1}\frac{\partial R_{i\alpha}}{\partial \theta}\frac{\partial R_{kl}}{\partial \theta} \tag{A.20}$$

where I_1 is the first strain invariant $tr(\boldsymbol{U})$, δ_{ij} is the Kronecker delta and θ is the angle of rotation represented by $\boldsymbol{R}$.
With the symmetric stretch $U_{\gamma\delta}$ enforced on the micro REV the resulting stress $\sigma'_{\alpha\beta}$ and tangent moduli $C'_{\alpha\beta\gamma\delta}$ can be rotated back to the correct orientation with equations (A.11) and (A.15) to correspond to the deformation gradient F_{kl}.

Following the same procedure, the hydraulic tangent operator and the coupling tangent operators can be rotated from the symmetric configuration $[]^R EV$ to the macroscale configuration $[]^M$.

B. STEREOGRAPHICAL PROJECTIONS OF LOADING INCREMENTS LEADING TO NEGATIVE SECOND ORDER WORK

On the following page, the stereographical projection of the loading orientations leading to negative second order work or $\Delta\varepsilon : \Delta\boldsymbol{\sigma} < 0$ is given for the integration points along cross sections $A' - A''$ and $B' - B''$ (Figure B.1) are given. The figure gives $\det(\boldsymbol{A}) < 0$ to indicate the approximate position of the shear band.

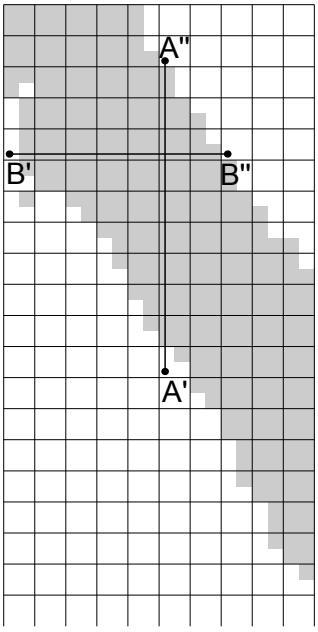

Fig. B.1: Crosssection along which the evaluation of negative second order work and $\Delta\varepsilon : \Delta\boldsymbol{\sigma} < 0$

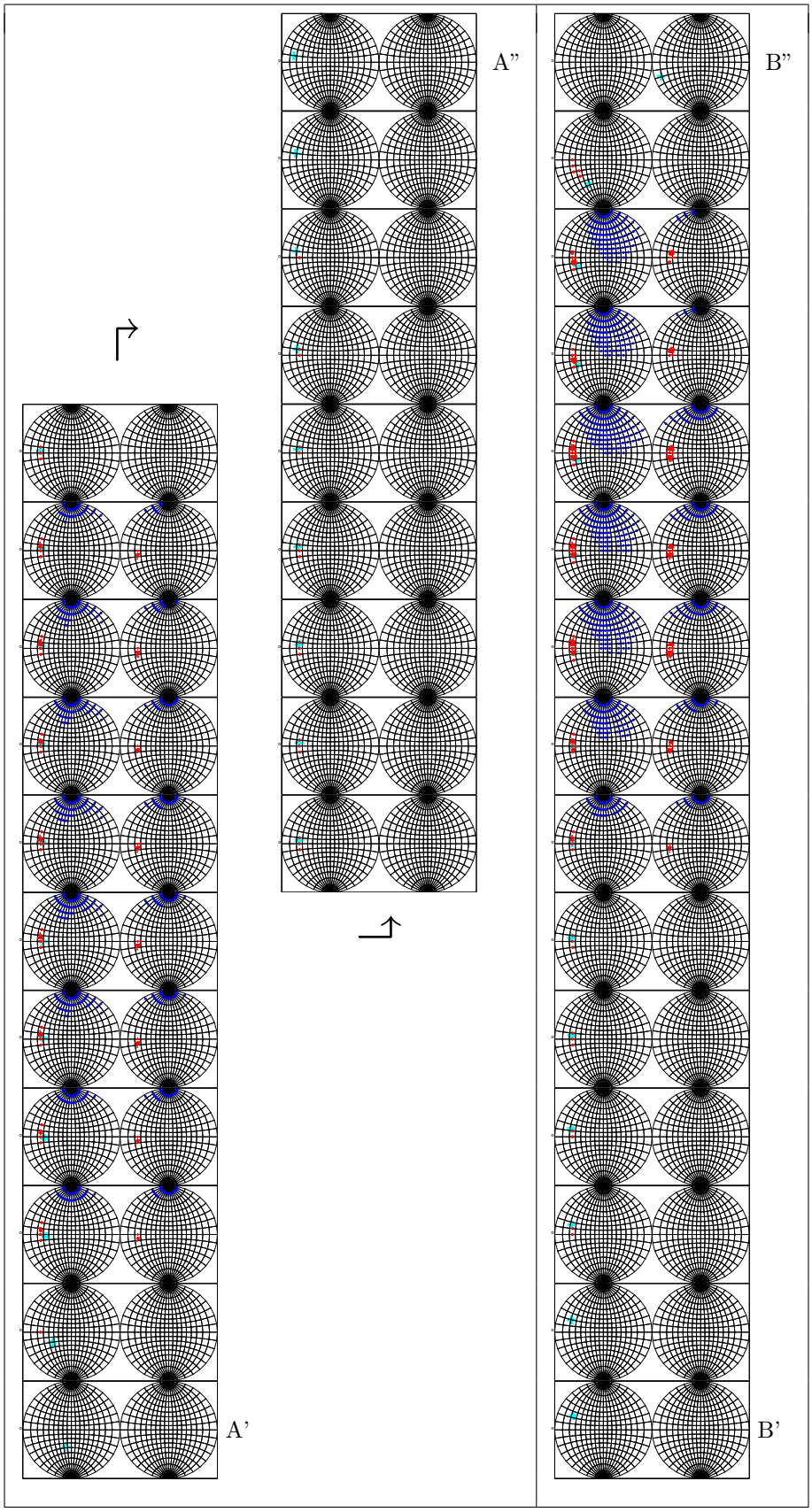
A”
B”
A’
B’

C. INTRODUCTION OF DIFFUSIVE FLOW IN THE FREY MODEL

For the developement of the diffusive flow in the grains, we will consider the following :

- Fluid is compressible: $\rho^t = \rho_0 \exp(p^t/k^w)$
- Grain pore volume is constant (small strain assumption)
- grain permeability is constant

This means that the solid part of the hydraulic problem does not change and only pressure p is a variable, but the problem is nonlinear due to fluid compressibility.

The introduction of diffusive flow in the grains, requires to redefine the hydraulic problem and write it in a purely nonlinear problem that is solved iteratively.

We define the following:

φ = grain porosity (constant)
ρ^w = fluid density
Q = sink term
$\dot{M}$ = fluid storage term $[kg\ m^{-3}s^{-1}]$

In this chapter, all variables etc. are at the micro scale.

A short description of the introduction of double porosity at the micro level. The new fluid system to be solved includes the original system of interfaces with compressible fluid (no changes). In addition to that, a flui pressure degree of freedom is defined in each node inside the grains. Diffusive flow of compressible fluid inside each grain is taken into account. Interaction between the flow in the grains and the flow in the interfaces is allowed by means of a 'connecting channel', basically a large connectivity term prescribing quasi-equal pressures on opposite sides of the interface (see Figure C.1).

In the new fluid system, all nodes i_i and n_i shown in Figure C.1 have fluid degrees of freedom. Nodes n_i are the nodes that are part of the mechanical system as well. Nodes i_i are the interface nodes, existing only in the fluid interface elements.

Three types of hydraulic elements are distinguished;

- 2D porous elements for the grains, bounded by nodes n_i (green surfaces)
- 1D fluid channel elements for the interfaces, bounded by nodes i_i (blue thick lines)
- 1D connection channel elements, connecting the interface channel system with the grain porous media, between elements i_i and n_i (blue lines)

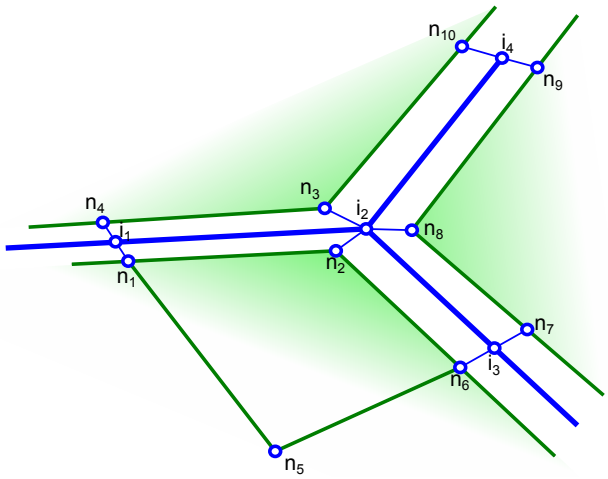

Fig. C.1: Hydraulic finite element discretization with nodes n part of the poromechanical elements and nodes i in the interface channel network. Connection elements between the grains and the interfaces are defined connecting n and i.

C.1 2D porous elements

Developments for diffusive flow in grains We start with the balance of momentum for the fluid phase :

$$\frac{\partial p^t}{\partial x_i} + F_i^{S/W,t} + \rho^{w,t} g_i = 0 \tag{C.1}$$

and the mass balance equation for the fluid :

$$\int_\Omega \left(\dot{M}^t p^\star - m_i^t \frac{\partial p^\star}{\partial x_i} \right) \mathrm{d}\Omega = \int_\Omega Q^t p^\star \mathrm{d}\Omega - \int_{\Gamma_q} \bar{q}^t p^\star \mathrm{d}\Gamma \tag{C.2}$$

with Q a sink term and $\dot{M}$ the storage term. Because we are in steady state, this will reduce to

$$\int_\Omega m_i^t \frac{\partial p^\star}{\partial x_i} \mathrm{d}\Omega = \int_{\Gamma_q} \bar{q}^t p^\star \mathrm{d}\Gamma \tag{C.3}$$

The mass flux m_i^t is defined as a function of the true fluid velocity with respect to the solid phase $V_i^{W/S,t}$:

$$m_i^t = \rho^{w,t} \varphi V_i^{W/S,t} \tag{C.4}$$

The constitutive law for the fluid reads:

$$\dot{\rho}^{w,t} = \frac{\rho^{w,t}}{k^w} \dot{p}^t \tag{C.5}$$

Computation of the fluid mass flow, for the moment leaving out the gravtational forces gives

$$m_i^t = -\rho^{w,t} \frac{\kappa}{\mu} \left(\frac{\partial p^t}{\partial x_i} + \rho^{w,t} g_i \right) = -\rho^{w,t} \frac{\kappa}{\mu} \frac{\partial p^t}{\partial x_i} \tag{C.6}$$

Fluid mass density is given by

$$M_\Omega^t = \rho^{w,t}\varphi \tag{C.7}$$

$$\bar{q}^t = m_i^t n_i \qquad\qquad on\ \Gamma_q^t \tag{C.8}$$

Let's continue, for iteration from $\tau 1$ to $\tau 2$:

$$\int_\Omega m_i^{\tau 1}\frac{\partial p^\star}{\partial x_i}\mathrm{d}\Omega - \int_{\Gamma_q^{\tau 1}} \bar{q}^{\tau 1} p^\star \mathrm{d}\Gamma^{\tau 1} = R^{\tau 1} \tag{C.9}$$

$$\int_\Omega \frac{\partial p^\star}{\partial x_l}\left(m_l^{\tau 2} - m_l^{\tau 1}\right)\mathrm{d}\Omega = -W^{\tau 1} \tag{C.10}$$

under the assumption that $\bar{q}$ does not change... We can further rewrite this into

$$\int_\Omega \rho^{\tau 1}\frac{\kappa}{\mu}\frac{\partial p^{\tau 1}}{\partial x_i}\frac{\partial p^\star}{\partial x_i}\mathrm{d}\Omega - \int_{\Gamma_q} \bar{q}^{\tau 1} p^\star \mathrm{d}\Gamma = W^{\tau 1} \tag{C.11}$$

$$\int_\Omega \frac{\partial p^\star}{\partial x_l}\left(\rho^{\tau 2}\frac{\kappa}{\mu}\frac{\partial p^{\tau 2}}{\partial x_i} - \rho^{\tau 1}\frac{\kappa}{\mu}\frac{\partial p^{\tau 1}}{\partial x_i}\right)\mathrm{d}\Omega... = -W^{\tau 1} \tag{C.12}$$

We now define :

$$\begin{aligned}
\mathrm{d}p^{\tau 1} &= p^{\tau 2} - p^{\tau 1} && \text{(C.13)}\\
\mathrm{d}\rho^{w,\tau 1} &= \rho^{w,\tau 2} - \rho^{w,\tau 1} && \text{(C.14)}\\
\mathrm{d}\varphi^{\tau 1} &= \varphi^{\tau 2} - \varphi^{\tau 1} = 0 && \text{(C.15)}\\
\mathrm{d}u_i^{\tau 1} &= u_i^{\tau 2} - u_i^{\tau 1} = 0 && \text{(C.16)}
\end{aligned}$$

Taylor expansion and disregarding all second-and-higher order terms gives:

$$\int_\Omega \frac{\partial p^\star}{\partial x_j}\left(\mathrm{d}\rho^{w,\tau 1}\frac{\kappa}{\mu}\frac{\partial p^{\tau 1}}{\partial x_l} + \rho^{w,\tau 1}\frac{\kappa}{\mu}\frac{\partial \mathrm{d}p^{\tau 1}}{\partial x_l}\right)\mathrm{d}\Omega = -R^{\tau 1} \tag{C.17}$$

where all terms related to volume deformation are ignored. Because we know that

$$\mathrm{d}\rho^{w,\tau 1} = \frac{\rho^{w,\tau 1}}{k^w}\mathrm{d}p^{\tau 1} \tag{C.18}$$

we can further rewrite into

$$\int_\Omega \frac{\partial p^\star}{\partial x_j}\left(\frac{\rho^{w,\tau 1}}{k^w}\frac{\kappa}{\mu}\frac{\partial p^{\tau 1}}{\partial x_l}\mathrm{d}p^{\tau 1} + \rho^{w,\tau 1}\frac{\kappa}{\mu}\frac{\partial \mathrm{d}p^{\tau 1}}{\partial x_l}\right)\mathrm{d}\Omega = -R^{\tau 1} \tag{C.19}$$

We now write in matrical form:

$$\int_{\Omega} [P^{\star\tau 1}_{(x,y)}]^T [W^{\tau 1}][\mathrm{d}P^{\tau 1}_{(x,y)}]\mathrm{d}\Omega = -R^{\tau 1} \tag{C.20}$$

with

$$[\mathrm{d}P^{\tau 1}_{(x,y)}] = \begin{bmatrix} \frac{\partial \mathrm{d}p^{\tau 1}}{\partial x_1} \\ \frac{\partial \mathrm{d}p^{\tau 1}}{\partial x_2} \\ \mathrm{d}p^{\tau 1} \end{bmatrix} \qquad [P^{\star\tau 1}_{(x,y)}] = \begin{bmatrix} \frac{\partial p^{\star\tau 1}}{\partial x} \\ \frac{\partial p^{\star\tau 1}}{\partial y} \\ p^{\star\tau 1} \end{bmatrix} \tag{C.21}$$

$$[W^{\tau 1}] = \begin{bmatrix} \rho^{w,\tau 1}\frac{\kappa}{\mu} & 0 & \frac{\rho^{w,\tau 1}}{k^w}\frac{\kappa}{\mu}\frac{\partial p^{\tau 1}}{\partial x_1} \\ 0 & \rho^{w,\tau 1}\frac{\kappa}{\mu} & \frac{\rho^{w,\tau 1}}{k^w}\frac{\kappa}{\mu}\frac{\partial p^{\tau 1}}{\partial x_2} \\ 0 & 0 & 0 \end{bmatrix} \tag{C.22}$$

Finite element discretization on 4-node quadrilateral elements will give

$$\begin{aligned} [P^{\star}_{node}]^T \int_{-1}^{1}\int_{-1}^{1} [B]^T [T^{\tau 1}]^T [W^{\tau 1}][T^{\tau 1}][B]\mathrm{d}\xi\mathrm{d}\eta[\mathrm{d}P^{\tau 1}_{node}] &= -W^{\tau 1} \\ [P^{\star}_{node}]^T [K^{elem}][\mathrm{d}P^{\tau 1}_{node}] &= -W^{\tau 1} \end{aligned} \tag{C.23}$$

with

$$[\mathrm{d}P^{\tau 1}_{(x,y)}] = [T^{\tau 1}][\mathrm{d}P^{\tau 1}_{(\xi,\eta)}] \tag{C.24}$$

$$[\mathrm{d}P^{\tau 1}_{(\xi,\eta)}] = [B][\mathrm{d}P^{\tau 1}_{node}] \tag{C.25}$$

and

$$[\mathrm{d}P^{\tau 1}_{node}] = \begin{bmatrix} \mathrm{d}p^{\tau 1}_{(-1,-1)} \\ \mathrm{d}p^{\tau 1}_{(+1,-1)} \\ \mathrm{d}p^{\tau 1}_{(+1,+1)} \\ \mathrm{d}p^{\tau 1}_{(-1,+1)} \end{bmatrix} \tag{C.26}$$

The out-of-balance residual is calculated as:

$$-W^{\tau 1} = -[P^{\star}_{node}]^T \int_{-1}^{1}\int_{-1}^{1} [B]^T [T^{\tau 1}][\sigma^{\tau 1}]\mathrm{d}\xi\mathrm{d}\eta = [P^{\star}_{node}]^T [f^{\tau 1}_{HE}] \tag{C.27}$$

$$[\sigma^{\tau 1}] = \begin{bmatrix} -m_1^{\tau 1} \\ -m_2^{\tau 2} \\ \dot{M}^{\tau 1} \end{bmatrix} \tag{C.28}$$

$$[F^{\tau 1}_{HE}] = \begin{bmatrix} q_1^{\tau 1} \\ q_2^{\tau 2} \\ Q^{\tau 1} \end{bmatrix} \tag{C.29}$$

q_i and Q are the nodal residual terms.

shape function :

$$N^{(i)} = \frac{1}{4}(1+\xi_1^{(i)}\xi_1)(1+\xi_2^{(i)}\xi_2), \qquad x_i = N^{(i)}x_i^{(i)} \tag{C.30}$$

$$\frac{\partial N^{(i)}}{\partial \xi_i} = \frac{1}{4}\xi_i^{(i)}(1+\xi_{3-i}^{(i)}\xi_{3-i}) \tag{C.31}$$

$$\begin{bmatrix} \frac{\partial p}{\partial \xi_1} \\ \frac{\partial p}{\partial \xi_2} \end{bmatrix} = \begin{bmatrix} \frac{\partial N^{(1)}}{\partial \xi_1} & \frac{\partial N^{(2)}}{\partial \xi_1} & \frac{\partial N^{(3)}}{\partial \xi_1} & \frac{\partial N^{(4)}}{\partial \xi_1} \\ \frac{\partial N^{(1)}}{\partial \xi_2} & \frac{\partial N^{(2)}}{\partial \xi_2} & \frac{\partial N^{(3)}}{\partial \xi_2} & \frac{\partial N^{(4)}}{\partial \xi_2} \end{bmatrix} \begin{bmatrix} p^{(1)} \\ p^{(2)} \\ p^{(3)} \\ p^{(4)} \end{bmatrix} \qquad \texttt{eledb(2:3)} \tag{C.32}$$

C.2 1D fluid channel elements

This type of elements are the elements that were present in the original version of the code, modelling the flow between smooth quasi-parallel platens by means of a 1D channel. The mass flow $\bar{\omega}^{i_i i_j}$ in the channel between nodes i_i and i_j $(i \neq j)$ on position s is given by

$$\bar{\omega}(s) = -\rho(s)\kappa(s)\frac{\partial p(s)}{\partial s} \tag{C.33}$$

with $\rho(s) = \exp\left(p(s)/k^w\right)$ the fluid density, $\kappa(s)$ the hydraulic conductivity of the crossesction of the channel at location s. Mass conservation in the channel requires that $\bar{\omega}(s)$ is constant over the element and with the assumption of constant pressure gradient over the interface it can be found that

$$\bar{\omega}^{i_i i_j} = \frac{k^w \rho_0}{\exp\left(\frac{p_0}{k^w}\right)\int_{i_i}^{i_j}\frac{1}{\kappa(s)}ds}\left(\exp\left(\frac{p^{i_i}}{k^w}\right) - \exp\left(\frac{p^{i_j}}{k^w}\right)\right) \tag{C.34}$$

with $\bar{\omega}^{i_i i_j}$ the flux *from* node i_i *to* node i_j (mind the difference with what has been written before...). This expression is summarised as

$$\bar{\omega}^{i_i i_j} = \phi^{i_i i_j}\left(\lambda^{i_i} - \lambda^{i_j}\right) \tag{C.35}$$

When we want to solve only the fluid system of equations, the variable ϕ is constant (κ is only dependent on $u_i^{n_i}$). This means that the variational expression for $\delta\bar{\omega}^{i_i i_j}$ will become

$$\delta\bar{\omega}^{i_i i_j} = \frac{\phi^{i_i i_j}}{k^w}\left(\lambda^{i_i}\delta p^{i_i} - \lambda^{i_j}\delta p^{i_j}\right), \qquad \delta\bar{\omega}^{i_i i_j} = \frac{\phi^{i_i i_j}}{k^w}\begin{bmatrix}\lambda^{i_i} & -\lambda^{i_j}\end{bmatrix}\begin{Bmatrix}\delta p^{i_i} \\ \delta p^{i_j}\end{Bmatrix} \tag{C.36}$$

If we now want to build a 'element stiffness matrix' for the variation of fluxes δq^{i_i} *away* from nodes i_i, we get:

$$\begin{Bmatrix}\delta q^{i_1} \\ \delta q^{i_2}\end{Bmatrix} = \begin{bmatrix} \frac{\phi^{i_1 i_2}}{k^w}\lambda^{i_1} & -\frac{\phi^{i_1 i_2}}{k^w}\lambda^{i_2} \\ -\frac{\phi^{i_1 i_2}}{k^w}\lambda^{i_1} & \frac{\phi^{i_1 i_2}}{k^w}\lambda^{i_2} \end{bmatrix}\begin{Bmatrix}\delta p^{i_1} \\ \delta p^{i_2}\end{Bmatrix} \tag{C.37}$$

to compute the net flow away from the nodes (for the residual in Newton-scheme), the flow away from the nodes can be computed as

$$\begin{Bmatrix} q^{i_1} \\ q^{i_2} \end{Bmatrix} = \begin{Bmatrix} \bar{\omega}^{i_1 i_2} \\ -\bar{\omega}^{i_1 i_2} \end{Bmatrix} \tag{C.38}$$

C.3 1D connection elements

For the coupling of the flow in the porous grains and the channel interfaces, connection ellements are used for the exchange of fluid between the mechanical nodes n_i on the boundaries of the solid grains and the interface fluid nodes i_i. An arbitrary (large with respect to the interface channel conductivity) conductivity is used for this type of channels, to allow large fluid exchange with a low pressure gradient. Without defining the dimensions of the channel, the fluid mass flow in the channel is given by

$$\bar{\omega} = -k\rho(s)\frac{\partial p(s)}{\partial s} \tag{C.39}$$

because we will choose k such that the pressure gradient is small and the length of the channel is small as well, we can assume a constant density $\rho(s) = \rho$. Conservation of fluid mass now requires the pressure gradient to be constant as well, whichallows to write

$$\bar{\omega} = -\frac{k\rho}{l}(p^{n_i} - p^{i_i}) \tag{C.40}$$

with l the length of our connection element. We now define a single parameter K^C such that

$$\bar{\omega}^{i_i n_i} = -K^C(p^{n_i} - p^{i_i}) \tag{C.41}$$

K^S is chosen such hat it is large compared to the conductivity of the interface elements connected to node i_i. In this way the assumption of a small pressure gradient can be justified. In this way we can write the variational equation for the fluid mass flow from i_i to n_i as

$$\delta\bar{\omega}^{i_i n_i} = -K^C(\delta p^{n_i} - \delta p^{i_i}) = \begin{bmatrix} K^C & -K^C \end{bmatrix} \begin{Bmatrix} \delta p^{i_i} \\ \delta p^{n_i} \end{Bmatrix} \tag{C.42}$$

for the variation of the fluxes away from the nodes we can write the element 'stiffness' matrix as

$$\begin{Bmatrix} \delta q^{i_1} \\ \delta q^{n_1} \end{Bmatrix} = \begin{bmatrix} K^C & -K^C \\ -K^C & K^C \end{bmatrix} \begin{Bmatrix} \delta p^{i_1} \\ \delta p^{n_1} \end{Bmatrix} \tag{C.43}$$

C.4 Boundary conditions

The boundary conditions are enforced as follows;
At the beginning of each iteration, the pressure in the nodes at the top boundary and left boundary are updated:

$$p^+ = p^- + \Delta p^{REV} \tag{C.44}$$

After this, the element system of equations is build, the fluxes are computed and the global system of equations is assembled. Equilibrium is checked based on fluid flux. Convergence criterium is the norm of the residual fluxes (taking into account periodicity) divided by the norm of the fluxes on the REV boundaries (without periodicity). When the convergence criterium is not met in the curent configuration $p^{\tau 1}$, an update $\delta p^{\tau 1}$ is computed to correct for the residual nodal fluxes $q^{res,\tau 1}$.

The degrees of freedom on the top and right boundary are reduced from the system of equations using the following relations:

$$\delta p^{+} = \delta p^{-} \qquad \delta q^{+} = -\delta q^{-} \tag{C.45}$$

The reduced system is solved for the pressure update $\delta p^{\tau 1}$ and the pressure DOFs (including the reduced DOFs) are updated to find $p^{\tau 2}$.

1. Initiate arrays
2. Gather info on boundary conditions and inclusions : `LDEXT`
3. set `PPEN = P_X(1)`
4. LOOP to solve average pressure: `WHILE |DP_AV| >1E-6`
   (a) LOOP to solve fluid problem: `WHILE convnorm` $\leq$ `1E-6`
      i. ZERO arrays
      ii. Update porepressure difference: `P_top = P_bottom + DP_I`
      iii. Build integration point SOE's solid elements: `W`
      iv. Integrate SOE to solid element stiffness matrix: `GELEM`
      v. Build interface element stiffness matrix: `GELEM`
      vi. Compute solid integration point fluxes
      vii. Integrate fluxes to find element nodal fluxes
      viii. Assemble global system of equations
         - for solid elements : `GELEM`$\rightarrow$ `GFLUID`
         - for interface elements : `GELEM` $\rightarrow$ `GFLUID`
         - for connection ellements : `T` $\rightarrow$ `GFLUID`
      ix. Assemble residual fluxes: FRES $\rightarrow$ RFLUID
         - for solid elements : `FRES` $\rightarrow$ `RFLUID`
         - for interface elements : `FRES --> RFLUID`
         - for connection ellements : `expression --> GFLUID`
      x. penalize porepressure: `GFLUID(n,n)+1`, `RFLUID(n)+PPEN`
      xi. Reduce system of equations
         - transport follow DOFs to lead DOFs in `GFLUID` and `RFLUID`
         - annul follow DOFs and fixed DOFs
         - remove follow DOFs and DOFs: `GFLUID` $\rightarrow$ `G, RFLUID` $\rightarrow$ `FLUID`
      xii. Compure residual norm: `CONVNORM`
      xiii. Check convergence
      xiv. Solve fluid system `[G]{dp} = fluid` LU-decomposition and back-substitution

xv. copy lead DOFs to follow DOFs : `FLUID` → `RFLUID`

xvi. update porepressure

(b) END LOOP

(c) compute average pressure

(d) compute pressure diff: `DP_AV`

(e) update penalization pressure: `PPEN = PPEN + DP_AV`

5. END LOOP

6. pass info to existing module arrays

7. `PPORE` → `QB`

8. compute fluid mass M

9. `M` → `SIGMB`

D. COMPUTATIONAL HOMOGENIZATION FOR CONSISTENT TANGENT OPERATORS OF THE FREY MODEL

The modifications of the Frey model into the model presented in this work has been performed in several stages and several modifications were only made after the full development of several transitional versions. One of these versions contains only the adoption of small strain/large rotation for the mechanical system and treats the hydraulic system in the original way of linearization in the exponential of the fluid pressure $\lambda = \exp(p/k^w)$ and including the effective pressure gradient over the REV and the drag forces acting on the grain boundaries. This appendix covers the condensation routine for the computational homogenization of the HM-coupled tangent stiffness matrix for this transitional version of the microscale model. Not all details of the Frey model are repeated here and for the details of the hydraulic system and its coupling with the mechanical system, reference is made to the thesis by Frey [2010], see also Frey et al. [2013], Marinelli [2013].

First, some equations are repeated to state the relations between the macro scale problem and the micro scale problem. These equations are used later on to link the condensed rigidity matrix to the variables that link the micro and macro scales . The computations for the condensation are described in different steps. Parts of the code of the most time-consuming steps are given to show the code and the non-zero profiles of the matrices involved in the condensation are given. The computation time of the different steps of the condensation routine are given. They show which parts of the routine take the most computational effort.

In addition to the presented approach for condensation, an alternative way is described as Method 2. The different approach to the condensation of this Method 2 avoids the problems that make Method 1 so slow.

D.1 Preliminaries

The microstructure that will be used for the examples is given in figure D.1. To deal with the renumbering of all types and subsets of degrees of freedom we define the following notation, which corresponds to the

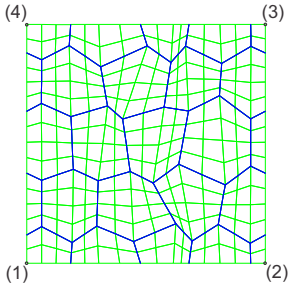

Fig. D.1: 120-elements REV mesh used as example.

variable		value		indice notation
`NITI`	no. of fluid nodes	120		it,jt,kt,...
`NICO`	no. of interface elements	128		ic,jc,kc,...
`NELEM`	total no. of elements	384		ie,je,ke,...
`NGAUC`	no. of int. point interface el.	2		igi,jgi,kgi,...
`NPOIN`	no of nodes mechanic	441		ip,jp,kp,...
`NNODE`	no. of mechanical nodes per element	4		in,jn,kn,...
`NNODF`	no. of hydraulic nodes per element	2		if,jf,kf,...
`NDGOF`	no. of mech. deg. of freedom	882		id,jd,kd,...

To address nodes that are located at the boundaries, an additional letter is added:

t : top boundary
b : bottom boundary
r : right boundary
l : left boundary

In this way, the displacement of a mechanical node on the top boundary will be either u_i^{ipt} or u^{idt}, the fluid pressure on a hydraulic node on the right boundary will be p^{icr}.
In addition, the following sets of DOFs will be used:

d : dependent DOFs : located on the top and right boundary and corner node (3)
i : independent DOFs : all but the dependent DOF's
p : prescribed DOFs : located on the corner nodes (1), (2) and (4)
f : free DOF's : all independent DOFs except the corner nodes

The indices for nodes and elements will be written in superscript, a comma will be used to separate these indices. The indices for dimensions $(i, j, k, ...)$ will be written in subscript. To give an example, the variation of the interface element volume as a function of the variation of the displacement of its corner nodes can be written as:

$$\frac{\partial V^{ic}}{\partial u_i^{ic,in}} \tag{D.1}$$

Matrices will be written as $[A]$ with components $A^{i,j}$, column vectors as $\{A\}$, the combination of column vector $\{A\}$ and $\{B\}$ as $\begin{Bmatrix} A \\ B \end{Bmatrix}$, a vector as $\vec{a}$ with components a_i, a second order tensor as $\boldsymbol{a}$ with components a_{ij}, a fourth order

tensor as ${}^4\boldsymbol{A}$ with indices A_{ijkl}.

List of variables

$\vec{f}$	(nodal) force
$\vec{F}_p$	(nodal) normal force on interface boundary by fluid pressure in the global frame
$\vec{f}_t$	(nodal) tangential force on interface boundary by fluid pressure gradient in the global fram
$\vec{g}$	gravitational acceleration
m_i	fluid mass flux in direction i (macro)
p	(nodal) fluid pressure
$\bar{p}$	REV average fluid pressure
p^M	macro level fluid pressure ($= \bar{p}$)
Δp	fluid pressure difference between opposite REV boundaries
$q^i t$	net fluid flow at fluid node it: nonzero at boundaries
$Q = [Q^L; Q^B]$	boundary fluxes; first component is fluid flux over left REV boundary, second over right
u_i	(nodal) displacement
$\vec{x}$	(nodal) position vector
$[C_{sym}]$	7×7 consistent tangent stiffness matrix in coordinate system x
CTE^{ic}	$1/\kappa$
F_{ij}	Deformation gradient tensor component
M	fluid mass per volume (macro)
$\dot{M}$	fluid mass variation per unit volume (macro)
R_{ij}	Rotation tensor component
U_{ij}	Stretch tensor component
V	volume in general
$V^{ic,igi}$	fluid volume related to interface integration point
V^w	total fluid volume
V^{REV}	total volume of the REV
ϕ	element conductivity term
$\kappa^{ic,ig}$	element conductivity
λ	exponential fluid pressure term $\lambda = exp(p/k^w), \lambda^{\Delta p} = exp(\Delta p/k^w)$,...
ρ	density
ρ^w	fluid density
σ_{ij}^M	Cauchy stress components at macro level
σ_{ij}^m	Cauchy stress components at micro level
ω	interface element fluid mass flux from node 1 to node 2
Δu_n	normal opening of interfaces
Γ	boundary domain
Γ^{int}	internal boundary domain: interface boundaries
Γ^{ext}	external boundary domain: boundaries of the REV
Ω	general volumetric domain
Ω^w	fluid domain

D.2 Balance equations and definitions before condensation

Stress

The definitions of the homogenized quantities that form the coupling between the macro scale and the micro scale are defined here, starting from the balance

equation

$$\frac{\partial \sigma_{ij}}{\partial x_j} = 0 \tag{D.2}$$

when no external (body) forces are considered. The definition of the macro stress $\boldsymbol{\sigma}^M$ as the integral over the micro stress $\boldsymbol{\sigma}^m$ is written as a result of the small-strain assumption:

$$\boldsymbol{\sigma}^M = \frac{1}{V^{REV}} \int\limits_{\Omega^{REV}} \boldsymbol{\sigma}^m dV \tag{D.3}$$

Application of the divergence theorem provides an integral of the boundary traction over the domain boundaries:

$$\boldsymbol{\sigma}^M = \frac{1}{V} \int\limits_{\Omega} \boldsymbol{\sigma}^m dV = \frac{1}{V} \left(\int\limits_{\Gamma^{ext}} (\vec{f}^{ext} \vec{x}) ds + \int\limits_{\Gamma^{int}} (\vec{f}^{int} \vec{x}) ds \right) \tag{D.4}$$

with Γ^{ext} the REV external boundary and Γ^{int} the internal boundaries on which internal forces are acting. These internal boundaries are the grain boundaries. Because of the small strain assumption and antisymmetry of the cohesive and normal fluid forces, the only internal forces that need te be taken into account are the fluid drag forces $\vec{f}_D$, acting on both interface sides. The other forces acting on the interface boundaries are antisymmetric and therefore cancel out under small strain assumption. When the integral above is discretized, the following equation for the macro stress is found;

$$\sigma_{ij}^M = \frac{1}{V^{REV}} \left(\sum_{ip \in \Gamma^{ext}} f_i^{ip} x_j^{ip} + \sum_{ip \in \Gamma^{int}} f_{t_i}^{ip} x_j^{ip} \right) \tag{D.5}$$

Under small strain assumption, variation of this expression gives:

$$\delta\sigma_{ij}^M = \frac{1}{V^{REV}} \left(\sum_{ip \in \Gamma^{ext}} \delta f_i^{ip} x_j^{ip} + \sum_{ip \in \Gamma^{int}} \delta f_{t_i}^{ip} x_j^{ip} \right) \tag{D.6}$$

Fluid terms

The flux ω^{ic} in interface element ic from fluid node 1 to fluid node 2 is calculated by

$$\phi^{ic}(\lambda^2 - \lambda^1) = \omega^{ic} \tag{D.7}$$

with $\phi = \phi(u_i^{in})$ the element conductivity term dependent on the displacements u_i^{in} of interface element nodes in and $\lambda^{if} = exp(p^{if}/k^w)$ the pressures in interface element fluid nodes if. ω is the flux in terms of fluid mass.

Conservation of fluid mass in the steady state micro problem requires that the sum of the fluxes towards any fluid node is zero, which gives the conservation of fluid mass in the fluid nodes as

$$\sum_{icon} \omega^{icon} = q^{it} = 0 \tag{D.8}$$

with *icon* the interface elements connected to the fluid node it. For the fluid nodes on the boundaries, the sum of the opposite fluid nodes equals zero. The fluid mass fluxes Q^L and Q^B over the left and bottom REV boundaries are defined as the sum over the nodal fluxes q^{it} on these boundaries;

$$Q^L = \sum_{itl \in \Gamma^L} q^{itl} \tag{D.9}$$

$$Q^B = \sum_{itb \in \Gamma^B} q^{itb} \tag{D.10}$$

with Γ^L and Γ^B the left and bottom boundaries of the REV.
The fluid mass per volume M is defined as

$$M = \frac{1}{V^{REV}} \int_{\Omega^w} \rho^w dV \qquad\qquad M = \frac{1}{V^{REV}} \sum_{ic,igi} V^{ic,igi} \rho^{ic,igi} \tag{D.11}$$

with Ω^w the fluid domain and V^{REV} the REV volume. The volume $V^{ic,igi}$ is the volume corresponding to the normal hydraulic opening Δu_h at the integration point igi in interface element ic.

Variation of equations (D.9),(D.11) gives

$$\delta M = \sum_{ic,igi} \sum_{ip} \rho^{ic,igi} \frac{\partial V^{ic,igi}}{\partial u_i^{ip}} \delta u_i^{ip} + \sum_{jt} \sum_{ic,igi} V^{ic,igi} \frac{\partial \rho^{ic,igi}}{\partial p^{jt}} \delta p^{jt} \tag{D.12}$$

$$\delta Q^L = \sum_{ip} \sum_{itl \in \Gamma^L} \frac{\partial q^{itl}}{\partial u_j^{ip}} \delta u_j^{ip} + \sum_{jt} \sum_{itb \in \Gamma^L} \frac{\partial q^{itl}}{\partial p^{jt}} \delta p^{jt} \tag{D.13}$$

$$\delta Q^B = \sum_{ip} \sum_{itb \in \Gamma^B} \frac{\partial q^{itb}}{\partial u_j^{ip}} \delta u_j^{ip} + \sum_{jt} \sum_{itb \in \Gamma^B} \frac{\partial q^{itb}}{\partial p^{jt}} \delta p^{jt} \tag{D.14}$$

Input/Output variables

From the periodicity conditions and the coupling between the macrolevel and the micro level, we have the following relations with on the left hand side the micro scale variables and on the right hand side the macro scale variables. :

$$\delta u_i^{(c)} / x_j^{(c)} = \delta U_{ij}^M \tag{D.15}$$

$$\delta \Delta p_1 / x_1^{(2)} = \delta \frac{\partial p^M}{\partial x_1} \tag{D.16}$$

$$\delta \Delta p_2 / x_2^{(4)} = \delta \frac{\partial p^M}{\partial x_2} \tag{D.17}$$

$$\delta \left(\frac{1}{V^w} \int_{\Omega^w} p dV \right) = \delta \bar{p} = \delta p^M \tag{D.18}$$

U_{ij}^M is the stretch $\frac{\partial x_i}{\partial x_{0_j}}$ at the macro level . $\bar{p}$ is the REV average fluid pressure at the micro level, which is equal to the local fluid pressure at the macro level. Δp_1 is the pressure difference between the right and the left boundary. Δp_2 is

the pressure difference between the top and bottom boundary of the REV. Note that on the left hand side $x_1^{(2)}$ and $x_2^{(4)}$ are constant (small strain assumption) but that V^w can evolve with time.

The flux over the boundaries Q^L and Q^B can be related to the macro flux $\vec{m}$ by

$$Q^L = m_1(x_2^{(4)} - x_2^{(1)}) - m_2(x_1^{(4)} - x_1^{(1)}) \tag{D.19}$$

$$Q^B = m_2(x_1^{(2)} - x_1^{(1)}) - m_1(x_2^{(2)} - x_2^{(1)}) \tag{D.20}$$

$$\tag{D.21}$$

With $x_1^{(1)} = x_2^{(1)} = 0$, small strain assumption and some rewriting this gives;

$$m_1 = \frac{1}{V^{REV}} \left({x_0}_1^{(2)} Q^L + x_1^{(4)} Q^B \right) \tag{D.22}$$

$$m_2 = \frac{1}{V^{REV}} \left({x_0}_2^{(2)} Q^L + x_2^{(4)} Q^B \right) \tag{D.23}$$

The variation of the fluid mass with time $\dot{M}$ is computed as the finite difference approximation over the time step. For a time step Δt from t^n to t^{n+1} we have:

$$\dot{M}^{t^{n+1}} = \frac{M^{t^{n+1}} - M^{t^n}}{\Delta t} \tag{D.24}$$

Because M^{t^n} does not change, the variation of this equation gives

$$\delta\dot{M}^{t^{n+1}} = \frac{\delta M^{t^{n+1}}}{\Delta t} \tag{D.25}$$

Because the time step is not part of the computations at the micro level, the devision by the time step is done at the macro level. The output of the micro level therefore only contains terms for $M$and not $\dot{M}$.
The relation between σ^M and the micro-scale variables is given above.

Combined

The goal is to find the 7×7 consistent tangent stiffness matrix $[A_{(7\times7)}]$ for the macro scale that holds the relation:

$$[A_{(7\times7)}] \begin{Bmatrix} \frac{\partial \delta u_k}{\partial x_l} \\ \frac{\partial \delta p^M}{\partial x_l} \\ \delta p^M \end{Bmatrix} = \begin{Bmatrix} \delta\sigma_{ij} \\ \delta m_i \\ \delta\dot{M} \end{Bmatrix} \tag{D.26}$$

Subscript x is used here to indicate that this is the consistent tangent stiffness matrix with respect to the x-coordinate system in which the deformation of the REV is symmetric. Equations (D.15)-(D.18) will link the left hand side to the nodal variables. Equations (D.6),(D.11), (D.22) and (D.23) will link the right hand side to the nodal reactions.

D.3 HM-coupled condensation: Method 1

Based on the definitions of homogenized macro response in the section above, the first homogenization procedure for the tangent operators is given in this section. This method was introduced in Eijnden et al. [2013] and repeated here in detail with focus on the numerical implementation. The method is presented in 8 subsequent steps in order to demonstrate the computation time, which can become a major drawback of this method.

Step 1 : initialization

Declare dimensions of matrices, memory, etc. This part only concerns the programing part of the code.

Step 2 : assembly of partial derivatives

A preparational part of the subroutine computes the following partial derivatives that will form the building blocks of the matrices used in the condensation. These equations are written in discretized form, directly relating the nodal degrees of freedom and nodal reactions. These partial derivatives concern the hydraulic and coupled terms. The mechanical system of equations has already been obtained while solving the micro problem.
The following matrices of derivatives are constructed:

$$\frac{\partial V^{ic,ig}}{\partial u_i^{ic,j}} \qquad \texttt{dVdu\_e(ic,ig,j,i)} \tag{D.27}$$

$$\frac{\partial \Delta u_n{}^{ic,ig}}{\partial u_i^{ic,j}} \qquad \texttt{dDUndu\_e(ic,ig,j,i)} \tag{D.28}$$

$$\frac{\partial V^{w}}{\partial u^{id}} \qquad \texttt{dVdu(id)} \tag{D.29}$$

$$\frac{\partial CTE^{ic}}{\partial \kappa^{ic}} \qquad \texttt{dCTEdKAP(ic)} \tag{D.30}$$

$$\frac{\partial \kappa^{ic}}{\partial \Delta u_n{}^{ic,ig}} \qquad \texttt{dKAPdDUn\_e(ic,ig)} \tag{D.31}$$

$$\frac{\partial \phi^{ic}}{\partial u_i^{ic,j}} \qquad \texttt{dphidu\_e(ic,j,i)} \tag{D.32}$$

$$\frac{\partial \phi^{ic}}{\partial u^{id}} \qquad \texttt{dphidu(ic,id)} \tag{D.33}$$

$\frac{\partial \omega^{ic}}{\partial p^{ic,if}}$	`dwdp_e(if,ic)`	(D.34)
$\frac{\partial \omega^{ic}}{\partial u^{ic,in,i}}$	`dwdu_e(in,i,ic)`	(D.35)
$\frac{\partial Q_i}{\partial u^{id}}$	`dQdu(i,id)`	(D.36)
$\frac{\partial Q_i}{\partial p^{it}}$	`dQdp(i,it)`	(D.37)
$\frac{\partial \rho^{ico,ig}}{\partial p^{it}}$	`drhodp(ic,ig,it)`	(D.38)
$\frac{\partial M}{\partial u^{id}}$	`dMMdu(id)`	(D.39)
$\frac{\partial M}{\partial p^{it}}$	`dMMdp(it)`	(D.40)
$\frac{\partial F_{p_i}^{\ ic,in}}{\partial p^{ic,if}}$	`dfndp_e(ic,in,i,if`	(D.41)
$\frac{\partial F_p^{\ id}}{\partial p^{it}}$	`dfndp(id,it)`	(D.42)
$\frac{\partial f_{t_i}^{ic,in}}{\partial u_j^{ic,jn}}$	`dfDdu_e(ic,in,i,jn,j)`	(D.43)
$\frac{\partial f_t^{\ id}}{\partial u^{jd}}$	`dfDdu(id,jd)`	(D.44)
$\frac{\partial f_{t_i}^{ico,in}}{\partial p^{ico,if}}$	`dfDp_e(ico,in,i,if)`	(D.45)
$\frac{\partial f_t^{\ id}}{\partial p^{it}}$	`dfDdp(id,it)`	(D.46)

Step 3 : build global system of equations

From the mechanical part of the code, a complete mechanical system of equations is available;

$$G_{mech}^{id,jd} = \frac{\partial f_{mech}^{id}}{\partial u^{jd}} \tag{D.47}$$

in matrix notation, this will give:

$$[G_{mech}] \cdot \{\delta u\} = \{\delta f_{mech}\} \tag{D.48}$$

with dimensions
$[G_{mech}]$: $NDGOF \times NDGOF$
$\{\delta u\}$: $NDGOF$
$\{\delta f_{mech}\}$: $NDGOF$
The forces f_{mech}^{id} contain the nodal stress equivalent forces and the interface cohesive forces. Using the partial derivatives defined in Step 2, this mechanical system of equations is extended into a HM-coupled system of equations $[G]$:

$$[G] \begin{Bmatrix} \delta u \\ \delta p \end{Bmatrix} = \begin{Bmatrix} \delta f \\ \delta M \\ \delta Q \end{Bmatrix} \tag{D.49}$$

$$[G] = \begin{bmatrix} \left[\frac{\partial f^{mech}}{\partial u} - \frac{\partial f_D}{\partial u}\right] & \left[-\frac{\partial f_n}{\partial p} - \frac{\partial f_D}{\partial p}\right] \\ \left[-\frac{\partial M}{\partial u}\right] & \left[-\frac{\partial M}{\partial p}\right] \\ \left[-\frac{\partial Q}{\partial u}\right] & \left[-\frac{\partial q^{L,B}}{\partial p}\right] \end{bmatrix} \tag{D.50}$$

Dimensions :
$[G]$: `NDGOF`+3×`NDGOF`+`NITI`
$\{u\}$: `NDGOF`
$\{p\}$: `NITI`
$\{f\}$: `NDGOF`
$\{M\}$: 1
$\{Q\}$: 2
This assembly of the coupled global matrix includes the summation for obtaining Q_i and M.

Step 4 : Compute transformation matrix T_p

A transformation matrix is needed to eliminate the pressure degrees of freedom p from the system of equations. This transformation matrix $[T_p]$ is the incremental relation between the nodal fluid pressures p^{it} on one side and the mechanical nodal displacements u^{id}, REV pressure difference $\Delta\bar{p}_i$ and REV average pressure $\bar{p}$ on the other:

$$[T_p] \{\delta p\} = \begin{Bmatrix} \delta u \\ \delta \Delta p \\ \delta \bar{p} \end{Bmatrix} \tag{D.51}$$

This means that $[T_p]$ has dimensions $\texttt{NDGOF} + 3 \times \texttt{NITI}$. In the original code, the following hydraulic system of equations is solved [Frey, 2010]:

$$[\Phi]\{\lambda\} = ([\Phi_\omega] + [\Phi_\Delta])\{\lambda\} = \{0\} \tag{D.52}$$

Matrix $[\Phi]$ has dimensions $[NITI \times NITI]$ and contains 2 types of equations. This system therefore can be written as a sum of two matrices, each containing one type of equations. In this way we have;

- $[\Phi_\omega]$: containing terms ϕ^{ic} for equations $\phi^{ic}(\lambda^{ic,2} - \lambda^{ic,1}) = 0$ with $\sum_{ic \text{ connected to } it} \omega^{ic} = 0$

- $[\Phi_\Delta]$: containing the constraints on boundary conditions : $\lambda^{itb}\lambda^{\Delta p2} - \lambda^{itt} = 0$, $\lambda^{itl}\lambda^{\Delta p1} - \lambda^{itr} = 0$

ω is the flux in the interface element from local hydraulic node 1 to 2. Equation (D.52) is the singular system for which one value of λ needs to be fixed by penalization in order to have one solution. For the homogenization, this penalization will not be used. Instead, an additional incremental relation for the average fluid pressure is added to the system. With ϕ^{ic} the conductivity terms of the interface elements and λ^{it} the exponential pressure terms at the fluid nodes ($\lambda = exp(p/k^w)$) we have; $\Phi_\omega = \Phi_\omega(\phi)$ and $\Phi_\Delta = \Phi_\Delta(\lambda^{\Delta p})$. Variation of equation D.52 gives:

$$[\delta\Phi]\{\lambda\} + [\Phi]\{\delta\lambda\} = ([\delta\Phi_\omega] + [\delta\Phi_\Delta]])\{\lambda\} + [\Phi]\{\delta\lambda\} = \{0\} \tag{D.53}$$

This can be written as

$$\sum_{ic,jt,id} \left(\frac{\partial \Phi_\omega^{it,jt}}{\partial \phi^{ic}} \frac{\partial \phi^{ic}}{\partial u^{id}} \delta u^{id} + \frac{\partial \Phi_\Delta^{it,jt}}{\partial \lambda_i^\Delta} \frac{\partial \lambda_i^\Delta}{\partial \Delta \bar{p}_j} \delta \Delta \bar{p}_j \right) \lambda^{jt} + \sum_{jt,kt} \Phi^{it,jt} \frac{\partial \lambda^{jt}}{\partial p^{kt}} \delta p^{kt} = 0 \tag{D.54}$$

This singular system needs one additional equation in order to be solved and this equation is given by the definition of the average pressure. The average pressure $\bar{p}$ is calculated as the integral of the fluid pressure over the fluid domain divided by the fluid volume. Discretization gives

$$\bar{p} = \frac{\sum_{ic} \sum_{ig} V^{ic,ig} p^{ic,ig}}{V^w} \tag{D.55}$$

variation of the average fluid pressure can be written as

$$\begin{aligned} \delta \bar{p} = & - \frac{1}{(V^w)^2} \sum_{ic,ig,id} \left(\frac{\partial V^w}{\partial u^{id}} \delta u^{id} p^{ic,ig} V^{ic,ig} \right) \\ & + \frac{1}{V^w} \sum_{ic,ig,it} \left(\frac{\partial p^{ic,ig}}{\partial p^{it}} \delta p^{it} V^{ic,ig} \right) \\ & + \frac{1}{V^w} \sum_{ic,ig,id} \left(p^{ic,ig} \frac{\partial V^{ic,ig}}{\partial u^{id}} \delta u^{id} \right) \end{aligned} \tag{D.56}$$

or

$$\frac{1}{V^w}\sum_{id}\left(\sum_{ic,ig}\left(p^{ic,ig}\frac{\partial V^{ic,ig}}{\partial u^{id}}\right)-\bar{p}\frac{\partial V^w}{\partial u^{id}}\right)\delta u^{id}+\frac{1}{V^w}\sum_{ic,ig,it}\left(V^{ic,ig}\frac{\partial p^{ic,ig}}{\partial p^{it}}\right)\delta p^{it}=\delta\bar{p} \tag{D.57}$$

This equation is added to one of the equations in (D.54), preferably the equation that was previously used to penalize one nodal pore pressure. This will be fluid node $it = it_{pen}$. When we now switch over to matrix notation, equation D.54 can be written as :

$$[A_1]\begin{Bmatrix}\delta u\\ \delta\Delta p\\ \delta p\end{Bmatrix}=\{0\} \tag{D.58}$$

Matrix $[A_1]$ has dimensions $\texttt{NITI}\times\texttt{NITI}+\texttt{NDGOF}+3$. In the same way, using the partial derivatives given above, equation D.57 can be written as

$$[A_2]\begin{Bmatrix}\delta u\\ \delta\Delta p\\ \delta p\end{Bmatrix}=\delta\bar{p} \tag{D.59}$$

'Matrix' $[A_2]$ has dimensions $1\times\texttt{NDGOF}+2+\texttt{NITI}$. Adding $[A_2]$ to $[A_1]$ will give $[A_3]$:

$$[A_3]\begin{Bmatrix}\delta u\\ \delta\Delta p\\ \delta p\end{Bmatrix}=\begin{Bmatrix}0\\ \vdots\\ 0\\ \delta\bar{p}\\ 0\\ \vdots\\ 0\end{Bmatrix} \tag{D.60}$$

Partitioning $[A_3]=\begin{bmatrix}A & B & C\end{bmatrix}$ gives

$$\begin{bmatrix}[A] & [B] & [C]\end{bmatrix}\begin{Bmatrix}\delta u\\ \delta\Delta p\\ \delta p\end{Bmatrix}=\{D\}\delta\bar{p} \qquad \{D\}=\begin{Bmatrix}0\\ \vdots\\ 0\\ 1\\ 0\\ \vdots\\ 0\end{Bmatrix} \tag{D.61}$$

with dimensions

$[A]$	:	$\texttt{NITI}\times\texttt{NDGOF}$
$[B]$	:	$\texttt{NITI}\times 2$
$[C]$	:	$\texttt{NITI}\times\texttt{NITI}$
$[D]$	:	$\texttt{NITI}$

isolating $\{\delta p\}$ gives:

$$\{\delta p\} = [C]^{-1} \begin{bmatrix} -[A] & \{D\} & -[B] \end{bmatrix} \begin{Bmatrix} \delta u \\ \delta \bar{p} \\ \delta \Delta p \end{Bmatrix} \tag{D.62}$$

which means that $[T_p]$ can be defined as

$$[T_p] = [C]^{-1} \begin{bmatrix} -[A] & \{D\} & -[B] \end{bmatrix} \tag{D.63}$$

The fluid pressure DOFs are eliminated using the matrix $[T_p]$;

$$[K] = [G] \begin{bmatrix} [I] \, [0] \\ [T_p] \end{bmatrix} \qquad [K] \begin{Bmatrix} \delta u \\ \delta \bar{p} \\ \delta \Delta p \end{Bmatrix} = \begin{Bmatrix} \delta f \\ \delta M \\ \delta m \end{Bmatrix} \tag{D.64}$$

with

$[I]$	:	$[NDGOF \times NDGOF]$	:	identity matrix
$[0]$	:	$[NDGOF \times 3]$	:	zero matrix
$[K]$	:	$[NDGOF + 3 \times NDGOF + 3]$	:	matrix for new system of equations

Step 5 : Elimination of dependent DOFs

This step starts from system of equations

$$[K] \begin{Bmatrix} \delta u \\ \delta \bar{p} \\ \delta \Delta p \end{Bmatrix} = \begin{Bmatrix} \delta f \\ \delta M \\ \delta Q \end{Bmatrix} \tag{D.65}$$

The periodicity conditions for displacements are:

$$\begin{aligned} u_i^{ipt} &= u_i^{ipb} + u_i^{(4)} - u_i^{(1)} \\ u_i^{ipr} &= u_i^{ipl} + u_i^{(2)} - u_i^{(1)} \\ u_i^{(3)} &= u_i^{(2)} + u_i^{(4)} - u_i^{(1)} \end{aligned} \tag{D.66}$$

with *ipt*, *ipb*, *ipr* and *ipl* the nodal numbering for nodes on the top, bottom, right and left boundary of the REV and (i) the numbering of the corner nodes given in Figure D.1. These conditions are used for the elimination of the dependent degrees of freedom (those on the top and right boundary and corner node (3)). This elimination entails the distribution of the dependent left hands side of (D.67) over their three dependencies at the right hand side of (D.67), which makes the dependent variables obsolete in the system of equations.

For the forces, the periodicity conditions read:

$$\delta f_i^{ipt} = -\delta f_i^{ipb} \tag{D.67}$$

$$\delta f_i^{ipr} = -\delta f_i^{ipl} \tag{D.68}$$

and for the homogenized macroscale stress tensor, the following summation is required as constraining condition;

$$\delta \sigma_{ij}^{REV} = \int_{\Gamma} \delta f_i x_j d\Gamma \tag{D.69}$$

with Γ the boundary of the REV, f_i the traction forces acting on the boundaries and x_j the coordiates at which the traction forces act. After discretization, this corresponds to the summation of the nodal forces f_i^{ipt},f_i^{ipb}, ..., $f_i^{(4)}$ and their corresponding coordinates x_j^{ipt},x_j^{ipb}, ..., $x_j^{(4)}$. Because of the periodic boundary conditions, the second term in the integral disappears ($f_i^{ipt}\delta x_j^{ipt} = -f_i^{ipb}\delta x_j^{ipb}$, $f_i^{ipr}\delta x_j^{ipr} = ...$). Parts of the first term of the right hand side of equation (D.69) can be written as

$$\delta f_i^{ipt} x_j^{ipt} = \delta f^{ipt}(x_i^{ipb} + x_i^{(4)} - x_i^{(1)}) \tag{D.70}$$

$$\delta f_i^{ipr} x_j^{ipt} = \delta f^{ipr}(x_i^{ipl} + x_i^{(2)} - x_i^{(1)}) \tag{D.71}$$

$$\delta f_i^{(3)} x_j^{(3)} = \delta f^{(3)}(x_i^{(4)} + x_i^{(2)} - x_i^{(1)}) \tag{D.72}$$

$$\tag{D.73}$$

This means we can add the dependent boundary forces to the independent boundary forces without changing the result of equation D.69 and in the meantime eliminate the variation in reaction forces by defining a reduced reaction force column vector $\{f^\star\}$:

$$\begin{aligned}
\delta f_i^{\star ipt} &= \delta f^{ipt} + \delta f^{ipb}\ (\approx 0)\\
\delta f_i^{\star ipr} &= \delta f^{ipr} + \delta f^{ipl}\ (\approx 0)\\
\delta f_i^{\star ipb} &= \delta f^{ipb} + \delta f^{ipt}\ (\approx 0)\\
\delta f_i^{\star ipl} &= \delta f^{ipl} + \delta f^{ipr}\ (\approx 0)\\
\delta f_i^{\star(1)} &= \delta f^{(1)} - \delta f^{(3)} - \sum_{ipt} \delta f_i^{ipt} - \sum_{ipr} \delta f_i^{ipr}\\
\delta f_i^{\star(4)} &= \delta f^{(4)} + \delta f^{(3)} + \sum_{ipt} \delta f^{ipt}\\
\delta f_i^{\star(2)} &= \delta f^{(2)} + \delta f^{(3)} + \sum_{ipr} \delta f^{ipr}
\end{aligned} \tag{D.74}$$

In this way, the variation of the dependent boundary forces are taken into account in the $\{\delta f^\star\}$ and the dependent DOFs are eliminated from the system of equations when the same additions are done for the rows of $[K]$ in equation (D.65). The result is the reduced system of equations containing only independent variables and reaction:

$$[K^\star]\{\delta U^I\} = \{\delta F^{\star I}\} \tag{D.75}$$

with $\{U^I\}$ the independent DOF's (all except top/right boundary and corner 3), the average fluid pressure $\bar{p}$ and the pressure difference over the REV Δp_i. The column vector $\{\delta F^I\}$ contains the variation of the independent nodal forces, the variation of the mass in the REV δM and the variation of the mass flux over the boundaries δQ_i.

Step 6 : The actual condensation

$\{\delta U^I\}$ and $\{\delta F^I\}$ are partitioned in prescribed ($^{\mathrm{p}}$) and free ($^{\mathrm{f}}$) DOF's:

$$\begin{bmatrix} K^{\star \mathrm{pp}} & K^{\star \mathrm{pf}} \\ K^{\star \mathrm{fp}} & K^{\star \mathrm{ff}} \end{bmatrix} \begin{Bmatrix} U^{\mathrm{p}} \\ U^{\mathrm{f}} \end{Bmatrix} = \begin{Bmatrix} \delta F^{\star \mathrm{p}} \\ \delta F^{\star \mathrm{f}} \end{Bmatrix} = \begin{Bmatrix} \delta F^{\star \mathrm{p}} \\ 0 \end{Bmatrix} \tag{D.76}$$

with

$$\{\delta F^{\star \mathrm{p}}\} = \begin{Bmatrix} \delta f_1^{\star(1)} \\ \delta f_2^{\star(1)} \\ \delta f_1^{\star(2)} \\ \delta f_2^{\star(2)} \\ \delta f_1^{\star(4)} \\ \delta f_2^{\star(4)} \\ \delta \Delta \bar{p}_1 \\ \delta \Delta \bar{p}_2 \\ \delta \bar{p} \end{Bmatrix} \qquad \{\delta U^{\mathrm{p}}\} = \begin{Bmatrix} \delta u_1^{(1)} \\ \delta u_2^{(1)} \\ \delta u_1^{(2)} \\ \delta u_2^{(2)} \\ \delta u_1^{(4)} \\ \delta u_2^{(4)} \\ \delta Q^L \\ \delta Q^B \\ \delta M \end{Bmatrix}$$

The partitioning is actually taken into account in the numbering of the DOF's and therefore does not take any special operations in the code.

In a balanced REV, the nodal forces on the free nodes $\{F^{\star \mathrm{f}}\}$ are equal to zero. This enables the condensation on the prescribed DOFs to

$$[S]\{\delta U^{\mathrm{p}}\} = \{\delta F^{\star \mathrm{p}}\} \tag{D.77}$$

with

$$[S] = [K^{\star \mathrm{pp}}] - [K^{\star \mathrm{pf}}][K^{\star \mathrm{ff}}]^{-1}[K^{\star \mathrm{fp}}] \qquad [K_{temp}] = [K^{\star \mathrm{ff}}]^{-1}[K^{\star \mathrm{fp}}] \tag{D.78}$$

To find $[S]$, first the matrix $[K_{temp}] = [K^{\star \mathbf{ff}}]^{-1}[K^{\star \mathbf{fp}}]$ is computed by solving $[K^{\star \mathrm{ff}}][K_{temp}] = [K^{\star \mathrm{fp}}]$. This is done using LU-decomposition and backsubstitution. Once the term $[K_{temp}]$ is calculated, the nodal stiffness matrix $[S]$ is found by a simple mulpiplication:

$$[S] = [K^{\star pp}] - [K^{\star pf}] * [K_{temp}] \tag{D.79}$$

Solving the system to find $[K_{temp}]$ is the main cause of the high computation cost of the condensation routine. Looking at the profile of the matrices involved (see figure below), makes clear why; matrix $[K^{\star ff}]$ has hardly any zero values. For this reason the computational homogenization procedure above is a computational inefficient way to obtain the consistent tangent operators for the hydromechanical coupling (see below).

Step 7 : system of equations for drag forces

A matrix for the system of equations for the fluid drag forces is build:

$$[G_D] \begin{Bmatrix} \delta u \\ \delta p \end{Bmatrix} = \{\delta f_D\} \tag{D.80}$$

This is done using the partial derivatives `dfDdu(id,jd)` and `dfDdp(id,it)` defined in Step 2

Using elimination matrix $[T_p]$ defined above, the pressure DOFs are eliminated just like we've seen before:

$$[K_D] = [G_D] \begin{bmatrix} [I] & [0] \\ [T_p] \end{bmatrix} \qquad [K_D] \begin{Bmatrix} \delta u \\ \delta \\ \Delta \bar{p} \\ \delta \bar{p} \end{Bmatrix} = \{\delta f_D\} \tag{D.81}$$

The dependent displacements can be eliminated from system of equations $[K_D]$ using the periodicity conditions of the boundaries similar to Step 5. Partitioning in prescribed and free DOFs then gives the following equation

$$\begin{bmatrix} K_D^{\star p} & K_D^{\star f} \end{bmatrix} \begin{Bmatrix} \delta U^p \\ \delta U^f \end{Bmatrix} = \{\delta f_D\} \tag{D.82}$$

with $\{\delta U^f\}$ and $\{\delta U^p\}$ as defined above. The programming for this elimination of the dependent DOFs is exactly the same as described in Step 5.
The condensation in Step 6 has shown that

$$\{\delta U^f\} = -[K_{temp}]\{\delta U^p\}. \tag{D.83}$$

This means that we can substitute for $\{\delta U^f\}$ to find $[S_D]$ as

$$[S_D] = [K_D^{\star p}] - [K_D^{\star f}][K_{temp}] \qquad [S_D]\{\delta U^p\} = \{\delta f_D\} \tag{D.84}$$

the dimensions of $[S_D]$ is $NDGOF \times 9$.

Step 8 : find the tangent stiffness

From above we have the relation

$$\delta\sigma_{ij}^M = \frac{1}{V^{REV}} \int\limits_{\Gamma^{ext}} \delta f_i^{ext} x_j d\Gamma + \frac{1}{V^{REV}} \int\limits_{\Gamma^{int}} \delta f_i^{int} x_j \Gamma \tag{D.85}$$

After discretization, f_i^{ext} is given by the prescribed forces $f_i^{\star(1,2,4)}$ in $\{F^{\star p}\}$ in equation D.77, f_i^{int} is given by the drag forces ${f_D}_i^{ip}$ in equation D.84. This means we have;

$$\delta\sigma_{ij}^M = \frac{1}{V^{REV}} \sum_{c=1,2,4} \delta f_i^{\star(c)} x_j^{(c)} + \frac{1}{V^{REV}} \sum \delta {f_D}_i^{ip} x_j^{ip} \tag{D.86}$$

with corner node forces $f_i^{\star(c)}$ as the only external boundary forces and ${f_D}_i^{ip}$ as the only internal boundary forces. Substitution of $\delta f_i^{\star(c)}$ and δf_{D_i} using equations (D.77) and (D.84) will give the relation between $\delta\boldsymbol{\sigma}^M$ and δU^p. Using equations (D.15)-(D.18) allows to substitute the components of δU^p for the variables of the macro scale (stretch U_{ij}, pressure gradient $\nabla_{sym} p$ and average pressure $\bar{p}$).
For the mass flux Q^L and Q^B, equations (D.22) and (D.23) give the relation with the macro scale mass flux $\vec{m}$.

To repeat all relations, we have:

$$\delta u_1^{(1)} = \delta U_{11}^M x_{0_1}^{(1)} + \delta U_{12}^M x_{0_2}^{(1)} \tag{D.87}$$

$$\delta u_2^{(1)} = \delta U_{21}^M x_{0_1}^{(1)} + \delta U_{22}^M x_{0_2}^{(1)} \tag{D.88}$$

$$\delta u_1^{(2)} = \delta U_{11}^M x_{0_1}^{(2)} + \delta U_{12}^M x_{0_2}^{(2)} \tag{D.89}$$

$$\delta u_2^{(2)} = \delta U_{21}^M x_{0_1}^{(2)} + \delta U_{22}^M x_{0_2}^{(2)} \tag{D.90}$$

$$\delta u_1^{(4)} = \delta U_{11}^M x_{0_1}^{(4)} + \delta U_{12}^M x_{0_2}^{(4)} \tag{D.91}$$

$$\delta u_2^{(4)} = \delta U_{21}^M x_{0_1}^{(4)} + \delta U_{22}^M x_{0_2}^{(4)} \tag{D.92}$$

$$\delta \Delta p_1 = \frac{\partial p^M}{\partial x_1^M} x_{0_1}^{(2)} + \frac{\partial p^M}{\partial x_2^M} x_{0_2}^{(2)} \tag{D.93}$$

$$\delta \Delta p_2 = \frac{\partial p^M}{\partial x_1^M} x_{0_1}^{(4)} + \frac{\partial p^M}{\partial x_2^M} x_{0_2}^{(4)} \tag{D.94}$$

$$\tag{D.95}$$

$$\delta \sigma_{11}^M = \frac{1}{V^{REV}} \left(\delta f_1^{\star(1)} x_{0_1}^{(1)} + \delta f_1^{\star(2)} x_{0_1}^{(2)} + \delta f_1^{\star(4)} x_{0_1}^{(4)} \right) \tag{D.96}$$

$$\delta \sigma_{12}^M = \frac{1}{V^{REV}} \left(\delta f_1^{\star(1)} x_{0_2}^{(1)} + \delta f_1^{\star(2)} x_{0_2}^{(2)} + \delta f_1^{\star(4)} x_{0_2}^{(4)} \right) \tag{D.97}$$

$$\delta \sigma_{21}^M = \frac{1}{V^{REV}} \left(\delta f_2^{\star(1)} x_{0_1}^{(1)} + \delta f_2^{\star(2)} x_{0_1}^{(2)} + \delta f_2^{\star(4)} x_{0_1}^{(4)} \right) \tag{D.98}$$

$$\delta \sigma_{22}^M = \frac{1}{V^{REV}} \left(\delta f_2^{\star(1)} x_{0_2}^{(1)} + \delta f_2^{\star(2)} x_{0_2}^{(2)} + \delta f_2^{\star(4)} x_{0_2}^{(4)} \right) \tag{D.99}$$

$$\delta m_1 = \frac{1}{V^{REV}} \left(Q^L x_{0_1}^{(2)} + Q^B x_{0_1}^{(4)} \right) \tag{D.100}$$

$$\delta m_2 = \frac{1}{V^{REV}} \left(Q^L x_{0_2}^{(2)} + Q^B x_{0_2}^{(4)} \right) \tag{D.101}$$

When using the symmetry in the Cauchy stress tensor, the substitutions mentioned above can be performed by the multiplication with a transformation matrix $[T_x]$:

$$[C_{sym}] = \frac{1}{V^{REV}} [T_x]^T [S] [T_x] + \frac{1}{V^{REV}} [x_0]^T [S_D] [T_x] \tag{D.102}$$

with

$$[x_0] = \begin{bmatrix} x_{0_1}^1 & x_{0_2}^1 & 0 & 0 \\ 0 & 0 & x_{0_1}^1 & x_{0_2}^1 \\ x_{0_1}^1 & x_{0_2}^1 & 0 & 0 \\ 0 & 0 & x_{0_1}^2 & x_{0_2}^2 \\ \cdot & & & \\ \cdot & & & \\ x_{0_1}^{N-1} & x_{0_2}^{N-1} & 0 & 0 \\ 0 & 0 & x_{0_1}^{N-1} & x_{0_2}^{N-1} \\ x_{0_1}^N & x_{0_2}^N & 0 & 0 \\ 0 & 0 & x_{0_1}^N & x_{0_2}^N \end{bmatrix} \qquad N = NPOIN \tag{D.103}$$

and

$$[T_x] = \begin{bmatrix} x_1^{(1)} & x_2^{(1)} & 0 & 0 & 0 & 0 & 0 \\ 0 & 0 & x_1^{(1)} & x_2^{(1)} & 0 & 0 & 0 \\ x_1^{(2)} & x_2^{(2)} & 0 & 0 & 0 & 0 & 0 \\ 0 & 0 & x_1^{(2)} & x_2^{(2)} & 0 & 0 & 0 \\ x_1^{(4)} & x_2^{(4)} & 0 & 0 & 0 & 0 & 0 \\ 0 & 0 & x_1^{(4)} & x_2^{(4)} & 0 & 0 & 0 \\ 0 & 0 & 0 & 0 & x_1^{(2)} & x_2^{(2)} & 0 \\ 0 & 0 & 0 & 0 & x_1^{(4)} & x_2^{(4)} & 0 \\ 0 & 0 & 0 & 0 & 0 & 0 & 1 \end{bmatrix} \tag{D.104}$$

Note that the matrix $[S_D]$ only concerns the first four (related to the stress) lines of stiffness matrix $[C_{sym}]$, the zeros are added to make the matrices fit. Furthermore, for a rectangular REV with two boundaries on the axes most of the terms in $[T_x]$ will be zero.
Once consistent tangent stiffness matrix $[C_{sym}]$ is determined, it is rotated back to the macro coordinate system in a separate routine, together with the resulting stress and fluid flux.

D.4 HM-coupled condensation: Method 2

Using the partial derivatives defined in the Step 2 above, the following matrices can easily be assembled:

$$\delta M = \begin{bmatrix} [G^{Mm}] & [G^{Mh}] \end{bmatrix} \begin{Bmatrix} \delta u \\ \delta p \end{Bmatrix} \tag{D.105}$$

$$\delta \bar{p} = \begin{bmatrix} [G^{pm}] & [G^{ph}] \end{bmatrix} \begin{Bmatrix} \delta u \\ \delta p \end{Bmatrix} \tag{D.106}$$

$$\begin{bmatrix} [G^{mm}] & [G^{mh}] \\ [G^{hm}] & [G^{hh}] \end{bmatrix} \begin{Bmatrix} \delta u \\ \delta p \end{Bmatrix} = \begin{Bmatrix} \delta f \\ \delta q \end{Bmatrix} \tag{D.107}$$

Dimensions:

$\bar{p}$	: 1
M	: 1
$\{f\}$	: $NDGOF$
$\{q\}$	: $NITI$
$\{u\}$	: $NDGOF$
$\{p\}$	: $NITI$
$[G^{Mm}]$	: $1 \times NDGOF$
$[G^{Mh}]$	: $1 \times NITI$
$[G^{pm}]$	: $1 \times NDGOF$
$[G^{ph}]$	: $1 \times NITI$
$[G^{mm}]$	: $NDGOF \times NDGOF$
$[G^{mh}]$	: $NDGOF \times NITI$
$[G^{hm}]$	: $NITI \times NDGOF$
$[G^{hh}]$	: $NITI \times NITI$

Fig. D.2: Non-zero profile of matrix $[K]$ to condense on corner nodes in Method 2. The non-zero values that lay outside the band currently prevent efficiency of the solver. A better numbering of the DOFs that better takes into account the coupling between the hydraulic and mechanical DOFs is needed to solve this.

with q^{it} the nodal fluid imbalance; non-zero values represent a source at the node... The combination of these three equations gives:

$$\begin{bmatrix} [G^{pM}] & [G^{ph}] \\ [G^{Mm}] & [G^{Mh}] \\ [G^{mm}] & [G^{mh}] \\ [G^{hm}] & [G^{hh}] \end{bmatrix} \begin{Bmatrix} \delta u \\ \delta p \end{Bmatrix} = \begin{Bmatrix} \delta \bar{p} \\ \delta M \\ \delta f \\ \delta q \end{Bmatrix} \tag{D.108}$$

Using periodicity equations

$$\begin{aligned} u^{ipt} &= u^{ipb} + u^{(4)} - u^{(1)} \\ u^{ipr} &= u^{ipl} + u^{(2)} - u^{(1)} \\ p^{itt} &= p^{itb} + p^{(4)} - p^{(1)} \\ p^{itr} &= p^{itl} + p^{(2)} - p^{(1)} \\ f_i^{ipt} &= -f_i^{ipb} \\ f_i^{ipr} &= -f_i^{ipl} \\ q^{itt} &= -q^{itb} \\ q^{itr} &= -q^{itl} \end{aligned} \tag{D.109}$$

and equilibrium condition (residual forces and mass fluxes are zero at all nodes that are not involved in the periodic boundary conditions) the dependent DOFs (top boundary, right boundary and upper-right corner node) can be eliminated from this system of equations as was done before for forces only. This gives us a system with the independent DOFs $\{u^i\}$ and $\{p^i\}$:

$$\begin{bmatrix} [K^{\star pm}] & [K^{\star ph}] \\ [K^{\star Mm}] & [K^{\star Mh}] \\ [K^{\star mm}] & [K^{\star hm}] \\ [K^{\star hm}] & [K^{\star hh}] \end{bmatrix} \begin{Bmatrix} \delta u^i \\ \delta p^i \end{Bmatrix} = \begin{Bmatrix} \delta \bar{p} \\ \delta M \\ \delta f^{\star i} \\ \delta q^{\star i} \end{Bmatrix} \tag{D.110}$$

The fact that $[K^\star]$ is build directly from $[K]$, means that it maintains its sparcity and a proper renumbering of the DOFs can reduce the band width of the matrix $[K]$ significantly. Only the dependent DOFs have been eliminated to find $[K^\star]$, which meand the size of $[K]$ is still in the order of the number of DOFs in the total REV. Figure D.2 shows the matrix $[K]$ without renumbering and with a renumbering including the fluid terms. The system $[K]$ can now be condensed on mechanical corner nodes (c) and artificial hydraulic nodes (g), located at the mechanical corner nodes. This is done in the same way as before, but now for both forces and fluxes. The condensation gives:

$$\begin{bmatrix} [S^{\star pm}] & [S^{\star ph}] \\ [S^{\star Mm}] & [S^{\star Mh}] \\ [S^{\star mm}] & [S^{\star hm}] \\ [S^{\star hm}] & [S^{\star hh}] \end{bmatrix} \begin{Bmatrix} \delta u^{(c)} \\ \delta p^{(g)} \end{Bmatrix} = \begin{Bmatrix} \delta \bar{p} \\ \delta M \\ \delta f^{\star(c)} \\ \delta q^{\star(g)} \end{Bmatrix} \tag{D.111}$$

with (c) indicating the prescribed corner nodes (1), (2) and (4). (g) indicates the 'ghost'-points for the fluid system located at the mechanical points (1), (2) and (4). This means we now have a system of 11 equations of which equation nine is directly dependent on equations ten and eleven ($\delta q^{(1)} = -\delta q^{(2)} - \delta q^{(4)}$). From the first equation and the variation of the pressure difference over the opposite boundaries $\delta\Delta p_1 = \delta p^{(2)} - \delta p^{(1)}$, $\delta\Delta p_2 = \delta p^{(4)} - \delta p^{(1)}$ it the following transformation matrix can be built:

$$[S^{\star\star}] \begin{Bmatrix} \delta u_1^{(1)} \\ \delta u_2^{(1)} \\ \delta u_1^{(2)} \\ \delta u_2^{(2)} \\ \delta u_1^{(4)} \\ \delta u_2^{(4)} \\ \delta p^{(1)} \\ \delta p^{(2)} \\ \delta p^{(3)} \end{Bmatrix} = \begin{Bmatrix} \delta u_1^{(1)} \\ \delta f_2^{(1)} \\ \delta f_1^{(2)} \\ \delta f_2^{(2)} \\ \delta f_1^{(4)} \\ \delta f_2^{(4)} \\ \delta\Delta p_1 \\ \delta\Delta p_2 \\ \delta\bar{p} \end{Bmatrix} \tag{D.112}$$

with $[S^{\star\star}]$ the following matrix:

$$\begin{bmatrix} 1 & 0 & 0 & 0 & 0 & 0 & 0 & 0 & 0 \\ 0 & 1 & 0 & 0 & 0 & 0 & 0 & 0 & 0 \\ 0 & 0 & 1 & 0 & 0 & 0 & 0 & 0 & 0 \\ 0 & 0 & 0 & 1 & 0 & 0 & 0 & 0 & 0 \\ 0 & 0 & 0 & 0 & 1 & 0 & 0 & 0 & 0 \\ 0 & 0 & 0 & 0 & 0 & 1 & 0 & 0 & 0 \\ 0 & 0 & 0 & 0 & 0 & 0 & -1 & 1 & 0 \\ 0 & 0 & 0 & 0 & 0 & 0 & -1 & 0 & 1 \\ S^{\star pm}(1) & S^{\star pm}(2) & S^{\star pm}(3) & S^{\star pm}(4) & S^{\star pm}(5) & S^{\star pm}(6) & S^{\star ph}(1) & S^{\star ph}(2) & S^{\star ph}(3) \end{bmatrix} \tag{D.113}$$

We define matrix $[T_p]$ as the inverse of this matrix to find the same matrix $[S]$ as in Method 1 as :

$$[S] = \begin{bmatrix} [S^{\star mm}] & [S^{\star hm}] \\ [S^{\star hm}] & [S^{\star hh}] \\ [S^{\star Mm}] & [S^{\star Mh}] \end{bmatrix} [T_p] \tag{D.114}$$

Note that the seventh equation ($q^{(1)}$) is fully dependent on the eighth' and equation nine ($q^{(2)}$ and equation 10 ($q^{(4)}$) because of the periodic boundary conditions. This seventh equation can therefore be left out of the system of equations and the result is a 9 by 9 matrix $[S]$ like we've seen before in Method 1.
For the drag forces, the exact same procedure can be followed; first condensation on corner nodes (c) and ghost nodes (g), followed by transformation matrix $[T_p]$ to find matrix $[S_D]$. Once $[S]$ and $[S_D]$ are found, the consistent tangent stiffness matrix is easily found following Step 8 from the method 1.

The big advantage of this method is that renumbering of the DOFs will lead to a sparce matrix with relatively small band width such thet term that we used to call $[K_{temp}]$ in the foregoing can be computed efficiently.